

MAGNESIUM ALLOYS AS A BIORESORBABLE  
IMPLANT MATERIAL

A THESIS  
SUBMITTED TO THE UNIVERSITY OF MANCHESTER  
FOR THE DEGREE OF  
DOCTOR OF ENGINEERING (ENGD)  
IN THE FACULTY OF ENGINEERING AND PHYSICAL SCIENCES

ROBERT THORNTON

SCHOOL OF MATERIALS  
2010





# CONTENTS

<b>Abstract</b>	<b>19</b>
<b>Declaration</b>	<b>21</b>
<b>Copyright</b>	<b>23</b>
<b>Acknowledgements</b>	<b>25</b>
<b>1 Introduction</b>	<b>27</b>
1.1 Magnesium Elektron . . . . .	27
1.2 Magnesium as a Biomaterial . . . . .	29
1.2.1 Orthopaedics . . . . .	29
1.2.2 Cardiovascular Stents . . . . .	30
<b>2 Literature Review</b>	<b>33</b>
2.1 The effect of implants . . . . .	33
2.1.1 Magnesium in the body . . . . .	35
2.1.2 Magnesium in bone . . . . .	37
2.1.3 Osteoblasts . . . . .	37
2.2 Magnesium as a biomaterial . . . . .	41
2.2.1 A history of work pre 2000 . . . . .	41
2.2.2 Recent developments . . . . .	43
2.3 Corrosion . . . . .	47
2.3.1 Corrosion of Magnesium in Simple Electrolytes . . . . .	47
2.3.2 Corrosion of Magnesium in Biological Electrolytes . . . . .	51
2.4 New Alloy Development . . . . .	57
2.4.1 Magnesium alloy systems and their uses . . . . .	57
2.4.2 Biocompatibility of Alloying Elements . . . . .	59
2.4.3 Biomedical Alloys Already Investigated . . . . .	59
2.5 Surface Treatments . . . . .	62
2.5.1 Biological surface treatments . . . . .	64

<b>3</b>	<b><i>In vitro</i> testing of Magnesium alloys</b>	<b>71</b>
3.1	Introduction . . . . .	71
3.2	Materials and methods . . . . .	72
3.3	Results and Discussion . . . . .	75
3.3.1	Problems with <i>in vitro</i> testing techniques . . . . .	86
3.4	Conclusions . . . . .	92
3.5	Further work . . . . .	92
<b>4</b>	<b>Microstructure considerations</b>	<b>95</b>
4.1	Introduction . . . . .	95
4.2	Worked microstructures . . . . .	95
4.2.1	Materials and Methods . . . . .	96
4.2.2	Results and discussion . . . . .	99
4.2.3	Conclusions . . . . .	102
4.2.4	Further work . . . . .	104
4.3	Sub solidus heat treatments for improved corrosion resistance . . . . .	104
4.3.1	Material and methods . . . . .	104
4.3.2	Results . . . . .	105
4.3.3	Conclusions . . . . .	112
4.3.4	Further Work . . . . .	112
4.4	Stress corrosion cracking . . . . .	113
4.4.1	Materials and methods . . . . .	113
4.4.2	Results and Discussion . . . . .	115
4.4.3	Conclusions . . . . .	119
4.4.4	Further Work . . . . .	119
<b>5</b>	<b>New alloy compositions for biomedical applications</b>	<b>121</b>
5.1	Introduction . . . . .	121
5.2	Materials and methods . . . . .	124
5.3	Results and discussion . . . . .	125
5.3.1	Characterisation . . . . .	125
5.3.2	Mechanical properties . . . . .	127
5.3.3	Corrosion rates . . . . .	129
5.3.4	Corrosion analysis . . . . .	130
5.3.5	Heat treatment . . . . .	136
5.3.6	Cell culture . . . . .	137
5.4	Conclusions . . . . .	139
5.5	Further work . . . . .	140

<b>6 Strategies To reduce initial Corrosion rate and alter biocompatibility using surface modifications</b>	<b>143</b>
6.1 Introduction . . . . .	143
6.2 Carboxyl Ended Self Assembled Monolayers . . . . .	145
6.2.1 Materials and Methods . . . . .	145
6.2.2 Results and Discussion . . . . .	146
6.3 Silanes . . . . .	148
6.3.1 Materials and Methods . . . . .	148
6.3.2 Results and discussion . . . . .	150
6.3.3 Silane Modification . . . . .	154
6.4 Magnetron Sputtered Hydroxyapatite . . . . .	159
6.4.1 Materials and Methods . . . . .	159
6.4.2 Results and Discussion . . . . .	161
6.5 Conclusions . . . . .	167
6.6 Further Work . . . . .	168
6.6.1 Silanes . . . . .	168
6.6.2 Magnetron Sputtered Hydroxyapatite . . . . .	169
<b>7 Erbium additions to Yttrium Rare Earth Alloys for reduced corrosion rate</b>	<b>171</b>
7.1 Introduction . . . . .	171
7.2 Material and methods . . . . .	171
7.3 Results and Discussion . . . . .	173
7.4 Conclusions . . . . .	183
7.5 Further Work . . . . .	183
<b>8 Final conclusion</b>	<b>185</b>
<b>Bibliography</b>	<b>187</b>



## LIST OF FIGURES

1.1	Mechanical properties of current strutral implant materials alongside AZ31 magnesium alloy. AZ31 appears to have properties closer to bone than the other metals and is also stronger than Poly-L-Lactide Acid (PLLA), which is deemed too weak for many structural applications . . . . .	30
1.2	An example of stress shielding. A, Preoperative image. B, Image obtained directly after surgery. C, Image of the same patient after 7 years of follow-up. Arrow indicates region of cortical bone resorption [8] . . . . .	30
2.1	Representation of events at the bone-implant interface. (a) Protein adsorption (b) protein desorption, (c) material release, (d) inflammatory and connective tissue cells approach, (e) release of matrix proteins and selected adsorption of proteins (f) formation of lamina limitans and adhesion of osteogenic cells, (g) bone deposition on exposed bone and implant surfaces, (h) remodeling of newly formed bone [15] . . . . .	34
2.2	Summary of segmental magnesium absorption along the nephron within the kidney[24] . . . . .	36
2.3	Model of the relationship between proliferation and differentiation during the rat osteoblast developmental sequence. Commitment periods and restriction points, designated within broken vertical lines. A functional relationship between the down-regulation of proliferation and the initiation of extracellular matrix maturation and development is based on stimulation of alkaline phosphatase (AP) and osteopontin (OP) gene expression when proliferation is inhibited, but the developmental sequence is induced only to the second transition point. Growth of the osteoblast under conditions that do not support mineralization confirms the day 20 restriction point since the developmental sequence proceeds through the proliferation and the extracellular matrix development/maturation periods, but not further. DNA, DNA synthesis; col I, collagen Type I; OC; osteocalcin [25] . . . .	38
2.4	Representation of the cell proteins involved in cell adhesion on biomaterial[16] . . . . .	39

2.5	Publications and conference proceedings on the subject of biological applications of Magnesium or its Alloys against year. 2010 calculated pro-rata	43
2.6	Subcutaneous gas bubbles observed on postoperative radiographs for 4 weeks during magnesium implant degradation [11]. . . . .	44
2.7	Potential-pH (Pourbaix) diagram for the system of magnesium and water at 25C, showing the theoretical domains of corrosion, immunity, and passivation.[63] . . . . .	49
2.8	Effect of iron content on the corrosion rate of commercially pure magnesium subjected to alternate immersion in 3% NaCl.[63] . . . . .	50
2.9	Electrochemical potential against time for AZ31 in four salt solutions. It is shown that the alloy is passivated with time in the carbonate containing solutions [75] . . . . .	54
2.10	Impedance spectroscopy of AZ31 in SBF with increasing time. The loops increase with time (maximum at 24 hours), before decreasing with the low frequency loop turning into a inductive component [87] . . . . .	56
2.11	Left shows Nyquist plots from Impedance spectroscopy of WE43 in SBF with increasing time. Right shows the corresponding polarisation resistance against time. The alloy's polarisation resistance rises sharply at first before steadying and then rising again. . . . .	56
3.1	Experimental setup for hydrogen evolution tests. . . . .	76
3.2	Cell numbers against time after seeding at $4 \times 10^4$ cells $\text{ml}^{-1}$ on various biomaterials and 5 magnesium alloys. $n = 6$ , error = SD . . . . .	76
3.3	Optical images of osteoblast on tissue culture plastic alongside titanium (right) and WE43 (left). Scale bar = $200 \mu\text{m}$ . . . . .	77
3.4	Alkaline phosphatase production per cell on five magnesium alloys and three controls at day 8. Both commercial alloys show better performance than the binary alloys and are comparable with glass and titanium. * (675) and ** (WE43) indicates a statistical difference by single factor anova between the two commercial alloys and all three of the binaries (* $p < 0.05$ , $n = 4$ and ** $p < 0.05$ , $n = 4$ ) . . . . .	77
3.5	SEM images of osteoblasts cultured on WE43 after 24 hours. Osteoblasts are encased in the rapidly developed reaction layer, left. Osteoblasts in clusters grow on top of the layer and spread well, right. Scale bar = $50 \mu\text{m}$ .	78
3.6	Average cell number counted from Live/Dead images over 7 days. Osteoblasts were seeded at $10 \times 10^4$ cells $\text{ml}^{-1}$ on WE43 and glass ( $t=2$ ). $n = 20$ , error = SD . . . . .	80

3.7	Fluorescence images of osteoblasts seeded on WE43 at various timepoints stained with Live/Dead reagent. t=2 image is osteoblasts on glass to give true seeding density without material related losses. There is a large loss in cell number within the first 4 hours, which is recovery and the cells repopulate. Scale bar = 200 $\mu\text{m}$ . . . . .	80
3.8	Average magnesium concentration from all alloys in cell culture media with corrosion time measured by ICP. Concentration rises steeply within the first 4 hours before steadying. n = 16, error = SD . . . . .	81
3.9	pH against time for WE43 in cell culture media. . . . .	81
3.10	Cell number calculated by Hoechst DNA staining against the corrosion time. A sharp decline is seen at low corrosion times. n = 16, error = SD. . . . .	83
3.11	Individual alloy plots of Hoechst DNA staining against the corrosion time. Alloy to alloy differences are not apparent. n = 4, error = SD. . . . .	83
3.12	Cell activity was measured using alamar blue assay. This showed a slight decline in cellular metabolism with magnesium corrosion time. n = 16, error = SD. . . . .	84
3.13	Osteoblasts on magnesium alloy WE43 (left) and glass (right), seeded at 10 times the density previously. The cells appear unilaterally stretched on WE43. Scale bar = 50 $\mu\text{m}$ . . . . .	84
3.14	Osteoblasts seeded on untreated and pre-corroded WE43 after 24 hours quantified by Live/Dead imaging. Top shows phalloidin/DAPI stained cells at the same time point. Osteoblasts appear rounded on the untreated compared to spread and attached on the pre-corroded sample. Scale bar = 100 $\mu\text{m}$ . . . . .	85
3.15	Example of an alamar blue trial with results that defy expectation and vary with repeats, prompting studies to assess the assay's suitability. n = 6, error = SD . . . . .	87
3.16	Alamar blue readings against number of magnesium discs in the cell culture media and also pH. Both show positive trends with increasing magnesium corrosion n = 4, error = SD . . . . .	88
3.17	The reduction of resazurin salt to resorufin. . . . .	88
3.18	Hoechst DNA assay readings against the number of magnesium discs in the media and their corresponding pH. The trend appears to be linked to magnesium concentration and not pH. n = 4, error = SD. . . . .	89
3.19	Hoechst DNA assay reading against Magnesium concentration modified by additions of $\text{MgCl}_2$ . Magnesium appears to inhibit Hoechst readings . . . . .	89
3.20	An example of alloy to alloy differences experienced with alamar blue which appear to be independent of both magnesium concentration and pH. n = 4, error = SD . . . . .	90

3.21	Cell numbers against time after seeding at $2 \times 10^5$ cells $\text{ml}^{-1}$ on ML4 and Glass using the modified protocol. Cell numbers were measured by both visual counting with Live/Dead and also by absorption with DNA hoestch staining. Differences are seen between tests within sample types, but sample vs sample shows test agreement. . . . .	91
3.22	Fluorescent micrograph showing the effect of Prolong Gold® anti fade regeant on magnesium. The mountant causes corrosion of magnesium and therefore hydrogen bubble formation which interfere with image processing. The surface is generally unusable after 30 minutes. Scale bar = $100 \mu\text{m}$ . . . . .	92
4.1	Optical micrographs taken by Magnesium Elektron of the front (right) and rear (left) of extruded 6.4 mm rods. The front of the extrusion gives a worked microstructure and corrosion and apparent higher corrosion rates. The back of the extrusions appear closer in microstructure to the 9 mm extrusion (bottom image). In all cases the 6.4 mm rods are high in corrosion and inconsistent comparated to the 9 mm WE43 rod. Scale bars = $50 \mu\text{m}$ . . . . .	96
4.2	Optical micrographs taken of a 6.4 mm extruded rod from front (A) to back (G). The microstructure progressively turns from a worked unrecrystallised structure to the normal recrystallised structure expected. Scale bars = $200 \mu\text{m}$ . . . . .	99
4.3	Right: Eight optical micrographs taken mid way through the extrusion and combined showing the worked structure distributes to one outer section of the rod. Circle demonstrates outer circumference of the 6.4 mm extrusion. Left: the worked structure's relative postion out of the die (Mid way through bar). . . . .	100
4.4	Ram displacement against pressure and temperature of a typical extrusion with a billet temperature of $350^\circ\text{C}$ [144]. Extrusion pressure initially increases rapidly, known as the breakthrough pressure before declining. Temperature increases with ram displacement due to work on the material. . . . .	100
4.5	SBF bath corrosion results from the worked and normal structures of both 675 and WE43 alongside a 9 mm control. SBF corrosion seems unaffected by the microstructure. * and ** indicates no statistical difference by single factor anova (* $p > 0.05$ , $n = 6$ and ** $p \gg 0.05$ , $n = 6$ ) . . . . .	101
4.6	Potentiodynamic polarisation curves of the worked and normal structures in SBF (left) and 0.1M NaCl (right). Corrosion in SBF shows no correlation with microstructure, whereas in NaCl the worked struture is shown to increase the alloys corrosion protential. The alloy used in 675 after 30 minutes corrosion. . . . .	102



4.7	SBF bath corrosion data after annealing. The original worked structures appear unaffected by the heat treatment. The control however shows a $\sim 45\%$ drop at $400^\circ\text{C}$ . Worked samples $n = 3$ , WE43 $n = 1$ , error = SD. . . . .	103
4.8	Micrographs of the annealed samples. Standard microstructure is the as extruded sample with no further heat treatments. Further structures are post treatment, which was the stated temperature for 4 hours. The worked microstructure is fully recrystallised when heated to $500^\circ\text{C}$ or above. Annealing took place for 4 hours. Scale bars = $50\ \mu\text{m}$ . . . . .	103
4.9	Corrosion data from three SBF baths showing temperature and time against corrosion rate as a percentage of the control. All three baths differ with the magnitude the heat treatment decreases corrosion rate as well as the optimal condition. . . . .	106
4.10	The mean from the data shown in figure 4.9. The optimum condition is shown to be 8 hours at $350^\circ\text{C}$ , which lowers corrosion rate by over $30\%$ . . . . .	107
4.11	Potentiodynamic polarisation curves of the normal against heat treated condition (8 hours at $350^\circ\text{C}$ ). The treatments positively shifts the $E_{\text{corr}}$ value. . . . .	107
4.12	Optical micrographs of ML4 showing coarsening of the grain boundaries and twinning plans after 8 hours at $350^\circ\text{C}$ . Scale bar = $50\ \mu\text{m}$ . . . . .	107
4.13	SEM using secondary electrons. After 8 hours at $350^\circ\text{C}$ ML4 appears to have the second phase aligned at the grain boundaries. Scale bar = $20\ \mu\text{m}$ . . . . .	108
4.14	Back scattered electron micrographs show that the heavy elements (white) have migrated from within grains and the matrix to boundaries and stressed regions. Scale bar = $20\ \mu\text{m}$ . . . . .	108
4.15	Positions from which the EDX values in table 4.7 were taken. . . . .	109
4.16	Original and post heat treatment microstructures, Scale bar = $10\ \mu\text{m}$ . The post treatment samples shown represent the best replication of the structure seen in figure 4.12 from a range of conditions trialled. . . . .	111
4.17	Hydrogen evolution in SBF for the stents in their post drawn state and after optimal heat treatments. No improvement is seen. . . . .	112
4.18	Top shows the design of both the single and double notched samples. Bottom; a schematic of the static load rig used to test both single and double notched samples. . . . .	114
4.19	Time to failure against stress as a percentage of UTS while submerged in SBF. 675 fails at far lower % stress than WE43 and Elektron 21 + Gd. Samples marked as 1000 hours, were taken off test without failure. . . . .	114
4.20	Optical micrographs taken at the edge of the fracture from three magnesium alloys. Scale bar = $200\ \mu\text{m}$ . . . . .	116
4.21	Pitting at the surviving notch from a double notched WE43 sample after corrosion in SBF. Scale bar = $100\ \mu\text{m}$ . . . . .	116

4.22	Transgranular cracking at the surviving notch from a double notched 675 sample after corrosion in SBF. Scale bar = 50 $\mu\text{m}$ . . . . .	117
4.23	Four combined optical micrographs highlighting the extent of cracking in 675 alloy. Scale bar = 500 $\mu\text{m}$ . . . . .	117
5.1	Phase diagram for magnesium and Gadolinium. . . . .	122
5.2	Phase diagram for magnesium and Calcium. . . . .	123
5.3	Phase diagram for magnesium and Erbium. . . . .	124
5.4	Scanning electron micrographys of the new alloys microstructure. Scale bar = 50 $\mu\text{m}$ . . . . .	126
5.5	Microstructure of ML4(MI0009) taken by SEM with BSE, scale bar = 50 $\mu\text{m}$ . The table shows the chemistry in wt% of the spot points indicated by arrows A-D. . . . .	127
5.6	Microstructures of alloys MI0010-MI0014 taken by SEM with BSE, scale bar = 50 $\mu\text{m}$ . The table shows the corresponding chemistry in wt% at the spot points indicated by arrows A-D. . . . .	128
5.7	Tensile properties of MI0010-MI0029 against the ML4 standard. . . . .	129
5.8	Mass loss after 7 days in either NaCl salt fog or SBF bath. MI0029 shows corrosion rates over 10 times less than ML4 in SBF. . . . .	130
5.9	Polarisation resistance from the surface film off MI0010-MI0014 alloys after 24 hours in SBF (table 5.3) against mass loss from the SBF baths in figure 5.9. Note, a inverse relationship indicating strong surface films are an important aspect for lower corrosion rates. . . . .	131
5.10	Potentiodynamic polarisation curves obtained in SBF from MI0009 to MI0014 alloys. Black = 0 hrs, red = 2 hrs and blue = 24 hrs. . . . .	133
5.11	Nyquist plots obtained in SBF from MI0009 to MI0014 alloys. Black = 0 hrs, red = 2 hrs and blue = 24 hrs. . . . .	134
5.12	Chemical composton through the corrosion reaction layer investiged by GDOS. Corrosion occured in SBF for 15 minutes. 0 sputtering time represents the expected surface. . . . .	135
5.13	MI0010 to MI0014 heat treated for 4 and 8 hours 300-450 $^{\circ}\text{C}$ in an attempt to further the corrosion rate loss as achieved by ML4 in Chapter 4 . . . .	138
5.14	Cell density MI0009 to MI0029 compared to titanium and glass control. Calculated by DNA hoectsh staining after 14 days culture. n = 4, error = SD. . . . .	139
5.15	Fluorescence micrography of osteoblasts seeded on magnesium discs for 14 days, stained with phalloidin for F-actin and DAPI for the nuclei. Scale bar = 200 $\mu\text{m}$ . . . . .	141
6.1	hydrogen evolution of ML4 discs in SBF at 37 $^{\circ}\text{C}$ . . . . .	143

6.2	Water droplets on the surface of WE43 coated with sodium stearate (left and uncoated (right)). . . . .	147
6.3	Water contact angle measurements after degradation in water. SAM coatings show poor adhesion . . . . .	147
6.4	Mass loss of magnesium discs coated with SAMs in SBF over 7 days. $n = 6$ , error = SD . . . . .	148
6.5	FTIR spectra for Octadecyl-trimethoxy-silane coated (red) and uncoated ML4 (black). . . . .	150
6.6	FTIR spectra for ML4 coated with APS, APS + stearate acid, APS + Fmoc-Asp and APS + $\alpha$ -lipoic acid. . . . .	151
6.7	FTIR spectra for ML4 coated in GOPTS, GOPTS and PEG and uncoated . . . . .	151
6.8	Degradation of octadecyltrimethoxysilane in ethanol over 9 days. Measured by contact angle $n = 4$ , error = SD. . . . .	152
6.9	Mass loss of magnesium discs coated with octadecyltrimethoxysilane and uncoated after 7 days in SBF. $n = 12$ , error = SD . . . . .	153
6.10	Hydrogen evolved from coated and uncoated magnesium discs in SBF at 37 °C. $n = 12$ , error = SD . . . . .	153
6.11	Potentiodynamic polarization in SBF after 5 minutes submersion. ODTMS shifts the rest potential less negative and to a lower current density. . . . .	154
6.12	Nyquist Plot in SBF after 5 minutes of both samples. The uncoated shows only a single time phase, whereas the ODTMS coated shows a low frequency effect. . . . .	155
6.13	Chemical structures of APS (left) GOPTS (right). Note, the oxygen groups can react sideways with other silane molecules forming a 2D network in a monolayer. . . . .	155
6.14	Osteoblasts seeded for 24 hours on four surfaces stained with Phalloidin for F-actin green and DAPI for nuclei (blue). The PEG coating demonstrates the non-fouling properties of this surface Scale bar = 200 $\mu$ m. . . . .	157
6.15	PEG repels proteins by steric hindrance. Protein adsorption using the Pierce protein assay shows lower adsorbed albumin than the uncoated samples. $n = 4$ , error = SD . . . . .	158
6.16	SEM images of both coated (right) and uncoated AZ31 (left). The surface shows no difference after the coating, with Magnesium oxide appearing over the surface of both samples Scale bar = 500 nm . . . . .	161
6.17	Cross Section through HA layer (left) to substrate (right) using GDOS. . . . .	162
6.18	X ray diffraction of the coated sample after sintering at 530 °C for 3 hours. Unlabelled are the three large characteristic magnesium peaks. Labelled with $\blacktriangle$ are hydroxapatite peaks, $\bullet$ represent $Mg_2Ca$ , and $\square$ second phase yttrium and neodymium peaks. . . . .	163

6.19	SEM of Magnetron Sputtered HA on ML4 after 530 °C sinter. Scale bar = 50 $\mu$ m. . . . .	163
6.20	H <sub>2</sub> evolution against time with HA Coating and uncoated alloy when submerged in SBF. n = 6, error = SD . . . . .	164
6.21	Potential against time for HA coated and uncoated alloy. The Uncoated shows the characteristic passivation with time. Whereas the HA coated sample shows a large increase in corrosion potential before staying constant. .	164
6.22	Electrochemical potentials for HA coating and uncoated sample in SBF. The coating shifts the rest potential over 0.6 mV less negative. . . . .	165
6.23	Nyquist Plot of the HA layer in SBF over time in SBF. The low frequency inductive loop becomes a capacitance loop as the surface coating breaks down. . . . .	165
6.24	Degradation of the hydroxyapatite surface after 24 hours in cell culture media. The surface shows peeling of the coating, which appears to flake .	166
6.25	Schematic of the proposed breakdown of the HA coating, concluded from the various electrochemical and visual investigations above. Left hand side represents the point of exposure to SBF, with the stages of breakdown progressing further right with time. . . . .	167
6.26	SEM images of osteoblasts on uncoated and magnetron sputtered hydroxyapatite coated magnesium after 24 hours culture, scale bar = 20 $\mu$ m . . .	168
7.1	ML4 (left) and ML4+Er (right) microstructures shown with optical, etched in 5% Nitol, scale bar = 40 $\mu$ m. . . . .	173
7.2	ML4 (left) and ML4+Er (right) using SEM Secondary Electrons, scale bar = 50 $\mu$ m. . . . .	173
7.3	ML4 (left) and ML4+Er (right) microstructures shown with Back Scattered Electrons, scale bar = 10 $\mu$ m. . . . .	174
7.4	Back scattered electron image of MI0029 with EDX composition points. Arrow A; erbium cuboid particle. Arrow B; second phase. Arrow C; matrix.	174
7.5	Grazing X-Ray Diffraction plots of MI0009 and MI0029. Insert highlights the triple Mg HCP lattice peaks and shows the shift in diffraction angle caused by lattice stretching due to Er. Labelled with $\square$ representing magnesium, $\blacktriangle$ for Mg <sub>x</sub> Nd <sub>y</sub> peaks and $\bullet$ for Mg <sub>x</sub> Er <sub>y</sub> peaks. . . . .	175
7.6	Hydrogen evolved from both alloys in SBF at 37 °C. MI0029 corrodes at 7 times less than ML4 over the 7 day period. n = 8, error = SD . . . . .	176
7.7	Potentiodynamic polarisation curves obtained in SBF over time with both alloys; MI0009 (black) and MI0029 (red). MI0029 grows an anodic shoulder within the first hours, ML4 takes 16 hours to replicate. . . . .	177
7.8	Nyquist plots of ML4 (left) and MI0029 (right) in SBF with increasing time. . . . .	177

7.9	Hydrogen evolution for ML4 and MI0029 in both 0.1M NaCl and SBF. The curves show that MI0029 only offers greater corrosion resistance in SBF and not NaCl. $n = 4$ , error = SD. . . . .	178
7.10	Polarisation and impedance plots for both alloys (ML4 black and MI0029 red) in NaCl (left) and SBF (right). MI0009 appears more corrosion resistant in NaCl, but less in SBF). . . . .	179
7.11	Rest potential against time of ML4 and MI0029 in NaCl and SBF. . . . .	179
7.12	Polarisation and impedance plots in 1mM $\text{KH}_2\text{PO}_3$ + 0.1M NaCl (left) 28mM $\text{NaHCO}_3$ + 0.1M NaCl (right) for both alloys. MI0029 gives higher potentials and polarisation resistance in both solutions than ML4. The opposite seen in NaCl. . . . .	181
7.13	GDOS cross sections through MI0009 (left) and MI0029 (right) in NaCl (top) and SBF (bottom). The reaction layers in NaCl appear to consist of Mg, O and C from the atmosphere. In SBF phosphate is in the layer. Both MI0029 samples show the presence of Er within the layer as well. . . . .	182
7.14	Cross section of Er through the reaction layer and substrate after corrosion in SBF (red) and NaCl (Black) . Er is more intense when incorporated in with the carbonate and phosphate of the SBF reaction layer. . . . .	182



## LIST OF TABLES

2.1	Serum concentrations of magnesium with their symptoms in humans. . .	36
2.2	Gene expression of U2-OS (osteoblast) cells cultured in different magnesium conditions[29] . . . . .	40
2.3	Standard reduction potentials . . . . .	48
2.4	Ion concentrations of human plasma and synthetic solutions, mM [71]. . .	52
2.5	The ASTM design magnesium alloys consists of not more than two letters representing the major alloying elements. These arranged in order of descending wt%, followed by the respective wt% rounded to the whole number. For example an alloy of 96.2wt%Mg, 3.1wt%Al, 0.7wt%Zn would be abbreviated to AZ31. . . . .	58
2.6	A brief summary of the toxicology and pathophysiology of some alloying elements and impurities[93] . . . . .	60
3.1	Chemical composition of alloys given by wt%. Heavy Rare Earths (HRE) are given individually where appropriate or as a combined mix as specified in WE43's composition. Total impurities equates to the combined composition of Fe, Ni and Cu. . . . .	72
3.2	Corrosion rate in SBF of five magnesium alloys over 7 days. 675 corrodes at 75% the rate of WE43 . . . . .	79
3.3	Cell numbers on magnesium alloy WE43 and glass after seeding at $4 \times 10^5$ cells $\text{ml}^{-1}$ and 24 hours culture . . . . .	84
4.1	Chemical composition of alloys given by wt%. Total impurities equates to the combined composition of Fe, Ni and Cu. . . . .	97
4.2	Mechanical properties from both microstructures of 675 6.4 mm rods. . .	97
4.3	Concentrations of salt solutions used to make 1 litre of SBF. . . . .	98
4.4	Specification of ML4 given by wt%. Total impurities equates to the combined composition of Fe, Ni and Cu. . . . .	105
4.5	Preliminary mass loss results for heat treated ML4 . . . . .	105
4.6	Mechanical properties before and after the heat treatment. The alloy strength lowers considerably . . . . .	109

4.7	Compositions found by EDX analysis of the heat treated sample. . . . .	109
4.8	Corrosion rates of stent tubing in R91 and V09 condition found by hydrogen evolution in SBF after 18 hours. . . . .	111
4.9	Alloy compositions given by wt%. Total impurities (Fe, Ni, Cu) are less than 0.006 wt% for all three alloys. . . . .	113
4.10	Ultimate tensile strength when tested in ambient air by static loading. . .	113
5.1	Mass loss of various alloys based on Elekton 21 with added amounts of Gd. 1.3wt% is standard. Corrosion took place in cell culture media. . . . .	122
5.2	Alloy composition used in the chapter. Additions on Gd, Ca and Er were added to ML4 and Elektron 21. Heavy Rare Earths (HRE) are added combined in ML4. Total impurities (TI) equates to the sum of Fe, Ni and Cu. . . . .	125
5.3	Tafel extrapolation values from the potentiodynamic polarisation curves shown in figure 5.10 and polarisation resistances from medium and low frequency loops obtained from figure 5.11. All corrosion in SBF . . . . .	132
6.1	Chemical composition of WE43 given by wt%. Total impurities equates to the combined composition of Fe, Ni and Cu. . . . .	146
6.2	Mean water contact angles for silane modified magnesium surfaces. . . .	147
6.3	Specification of ML4 and AZ31 given by wt%. Total impurities equates to the combined composition of Fe, Ni and Cu. . . . .	149
6.4	Hydrogen evolution after 7 days corrosion in SBF $\text{mlcm}^{-1}$ . . . . .	156
6.5	Specification of ML4 and AZ31 given by wt%. Total impurities equates to the combined composition of Fe, Ni and Cu. . . . .	160
6.6	$R_p$ values in SBF for coated and uncoated AZ31 after a 430 °C sinter . . .	161
7.1	Alloy composition used of ML4 and ML4 + Er given by wt%. Total impurities equates to the combined composition of Fe, Ni and Cu. . . . .	172
7.2	Particle chemistry of MI0029 established by EDX in wt%. The area analysed by EDX is shown in figure 7.4. . . . .	174
7.3	Tafel exploration values from the potentiodynamic polarisation curves obtained in SBF from MI0009 and MI0029 alloys. . . . .	176
7.4	Polarisation Resistance values obtained from figure 7.8. . . . .	178



## ABSTRACT

The use of magnesium as a bioresorbable implant material has been gaining large amounts of interest over the last five years. Mg alloys by nature corrode rapidly comparative to other engineering metals, Mg is also naturally found in the body, meaning it offers a potential degradable material which can support far higher stresses than the current biodegradable polymers. Magnesium Elektron wanted to gain an understanding of how Mg alloys would work in this new environment and find a potential alloy fit for purpose. This thesis outlines the progress the author and Magnesium Elektron have made in achieving those goals.

Initially, to form an understanding of what occurs when Mg is implanted into the body. Osteoblast trials were used to determine *in vitro* responses and effects on the various Mg alloys. These studies showed that high corrosion rates initially seen when Mg alloys are placed in cell culture medium have a lower cell numbers. Most likely due to local pH rise. The effect is inherent to all Mg alloys irrespective of their overall corrosion rate. However, after the initial corrosion spike, surviving cells on the surface would proliferate and attach well. The attached cells on Mg also showed a phenotype expression change compared to those on glass.

It was then established that lowering the corrosion rate of the current Mg alloys was now key. Initially this involved modifications to current alloys. Annealing ML4 at 350 °C for 8 hours was found optimal and lowered corrosion rates by 20-30%. Further work looked at modifying alloys by changes to chemical composition. It was discovered that additions of 8wt% Er to ML4 made corrosion rates drop by 6-8 times in SBF. Additions of Gd in ML4 also gave low corrosion, 2 times less than ML4. Calcium also lowered corrosion rates slightly.

The modifications to the Mg surface was also looked into to lower the initial corrosion rate and potentially alter the biocompatibility of the alloys. Two successful techniques were found. Firstly organo-silanes were found to protect Mg for around 4 days, with reductions in corrosion rate of 6 times in the first hours. Silanes were also successfully used as anchors to graft polythene glycol to create a non fouling surface, which could potentially lower stent restenosis Secondly, Magnetron sputtered hydroxyapatite was used to lower corrosion rates by 6 times in the first 24 hours with no visible hydrogen gas being evolved in the first hours.



# DECLARATION

**The University of Manchester**  
*PhD by published work Candidate Declaration*

**Candidate Name:** Robert Thornton

**Faculty:** Engineering and Physical Sciences

**Thesis Title:** Magnesium Alloys as Bioresorbable Implant Materials

**Declaration to be completed by the candidate:**

I declare that no portion of this work referred to in this thesis has been submitted in support of an application for another degree or qualification of this or any other university or other institute of learning.

Signed:

Date: April 7, 2011



## COPYRIGHT

The author of this thesis (including any appendices and/or schedules to this thesis) owns any copyright in it (the "Copyright")<sup>1</sup> and s/he has given The University of Manchester the right to use such Copyright for any administrative, promotional, educational and/or teaching purposes.

Copies of this thesis, either in full or in extracts, may be made only in accordance with the regulations of the John Rylands University Library of Manchester. Details of these regulations may be obtained from the Librarian. This page must form part of any such copies made.

The ownership of any patents, designs, trade marks and any and all other intellectual property rights except for the Copyright (the "Intellectual Property Rights") and any reproductions of copyright works, for example graphs and tables ("Reproductions"), which may be described in this thesis, may not be owned by the author and may be owned by third parties. Such Intellectual Property Rights and Reproductions cannot and must not be made available for use without the prior written permission of the owner(s) of the relevant Intellectual Property Rights and/or Reproductions.

Further information on the conditions under which disclosure, publication and exploitation of this thesis, the Copyright and any Intellectual Property Rights and/or Reproductions described in it may take place is available from the Head of School of Materials (or the Vice-President) and the Dean of the Faculty of Engineering and Physical Sciences, for Faculty of Engineering and Physical Sciences candidates.

---

<sup>1</sup>This excludes material already printed in academic journals, for which the copyright belongs to said journal and publisher. Pages for which the author does not own the copyright are numbered differently from the rest of the thesis.



## ACKNOWLEDGEMENTS

I would first like to thank Magnesium Elektron and the EPSRC for granting me the chance to work on this project. Without their funding it would not be possible. Special thanks must go to Paul Lyon at Magnesium Elektron and Dr. Julie Gough at the University of Manchester who supervised me through the 4 years of this doctorate. I'd like to acknowledge the team at Magnesium Elektron who have helped me in every way possible, specifically Tony Boden who worked with me closely throughout this investigation. At the university, Dr. Nicolas Stevens gave me greatly appreciated help on all aspects of corrosion, as did Dr. Simon Todd for help regarding surfaces. I'd also like to thank David Stanley at the EngD centre for facilitating the course throughout the 4 years.





## INTRODUCTION

### 1.1 Magnesium Elektron

Magnesium Elektron is part of the Luxfer Group, an international manufacturer of high performance engineering materials including magnesium alloys, zirconium products and high pressure lightweight gas cylinders. The group employs approximately 1,600 people in 26 countries and operates 17 manufacturing plants in 6 countries; UK, USA, France, Czech Republic and Canada. Magnesium Elektron specialises in the development, manufacture and supply of magnesium products and services to technology industries worldwide and is regarded as the world leading innovator. It employs approximately 500 people operating in Manchester (UK), New Jersey and Pennsylvania (USA), Ontario (Canada) and Litvinov (Czech Republic).

The company was founded by A. G. Farben and F. A. Hughes in 1936 who previously were solely involved in importing and distributing magnesium from Germany. Pre war, Magnesium Elektron produced pure magnesium as its sole product, but at the start of World War Two it started producing war goods. Then after, the vast quantities of scrap were used to create scrap metal products before Magnesium Elektron then turned attention to its current speciality; the design and manufacture of new innovative alloys.

Magnesium Elektron's first range of alloys were the highly successful Zirconium based range, which could withstand higher temperatures and were used for the first jet engines. The Mg-RE-Zn-Zr alloy RZ5, first patented by Magnesium Elektron has been hugely popular for a large range of casting applications[1]. The yttrium based alloys were then developed, including WE43 and WE54 which are still the world leading high strength alloys for both cast and wrought applications[2][3]. Other noteworthy contributions include the magnox alloys used for nuclear power stations, the development of sheet magnesium batteries for torpedoes and life jackets.

Today, Magnesium Elektron continues to develop new alloys for a vast range of applications and actively looks to keep its research and development diverse. Currently, Elektron alloys are used for aerospace, defence, automotive, electronics and power generation. Company strategy has always placed Magnesium Elektron at the low volume,

high technology end of the market, as the company can not compete on the same scale as magnesium producers from China. Because of this, Magnesium Elektron aims to keep a large and wide spanning customer base which gives a number of benefits. Mainly that it can trade through and adapt during difficult periods which are expected with a relatively small volume material like magnesium. For example in 2006, the Formula 1 industry, which was a high profit market for materials ruled the use of magnesium illegal in certain areas of the car[4]. It also means that Magnesium Elektron can act as ambassadors for the material and encourage new industries and companies to take on alloys for applications that would normally be designed with aluminium or steel in mind. This also goes hand-in-hand with another company strategy, which is to form partnerships with new customers and supply service and expertise. Magnesium Elektron is not just a material provider, but helps the development of the company's new magnesium alloy based products.

Magnesium Elektron is actively involved the drive towards lightweight armoured military personnel carriers and lightweight commercial aerospace cabin components, markets that had previously avoided the use of magnesium due to its combustible and corrosive reputation. Without effort from Magnesium Elektron to provide service and expertise, these areas would never have been developed. Markets that are commonly thought of today as a main stay of the magnesium industry, such as investment casting and wrought products, are now processed in mass by high production companies and would not have been feasible if not for the development service provided by Magnesium Elektron. It is the service driven nature of Magnesium Elektron along with their reputation of excellence that caused the biotechnology market to approach them when wanting to trial magnesium *in vivo*.

Magnesium Elektron have been regarded as a world leader in nearly all applications its alloys are used for. Its aim is to investigate the suitability of the biomedical market. Success is no easy exercise due to the vast competition in the biotechnology market and the new found interest in biomagnesium, therefore collaboration with world leading biomedical companies will be the necessary to fulfil this.

Magnesium Elektron commonly sell material per tonne to its customers, an arrangement which would clearly be inappropriate for such small scale biomedical components where only a few kilograms will be needed. From a research perspective, this is one the the first development routes where magnesium Elektron does not have the facilities needed, which for this product line will be full in vivo and vitro testing access. On the other hand, biotechnology companies have no knowledge or infrastructure to design, develop and create magnesium alloys. These reasons point towards a commercial partnership for product development through to the full scale production of the finalised product range in the future.

This Engineering Doctorate project was created at the time when Magnesium Elektron was first analysing the market and determining the feasibility of the idea. The project follows from previous work from the same author, again with Magnesium Elektron, which

was an undergraduate fourth year research project titled 'Magnesium as a resorbable bio-material' started in 2005. The outcome of this project along with the increased interest from biotechnology companies was the stimulus for creating the Doctorate project with the aim to aid the development of biomedical alloys alongside technical staff and increase Magnesium Elektron's understanding of biomedical research.

## 1.2 Magnesium as a Biomaterial

The proposal to use magnesium alloys as a biomaterial are based upon three logical points: Firstly, Magnesium corrodes at a very fast rate, so could be biodegradable *in vivo*, secondly as an element Magnesium is already abundant in the body, and finally its strength would out perform all current biodegradable polymers. This is a market niche of huge potential, and could have a large impact on the metallic medical devices industry. There have been two key areas where a biodegradable metallic implant has been identified for potential impact; orthopaedic trauma devices (such as screws, plates, pins and staples); and cardiovascular stents.

### 1.2.1 Orthopaedics

There are several approved and commonly used metallic biomaterials for use as orthopaedic trauma devices, including stainless steels, titanium and cobalt-chromium based alloys. The orthopaedics industry has been using these materials for decades and are now widely used in medical procedures. However, these permanent devices have limitations preventing a more widespread use and commonly introduce the need for further surgery, compromising the patient's health.

Prominent metallic biomaterials have been shown to release toxic metallic ions and/or particles through corrosion or wear processes. These can lead to inflammatory responses and induce tissue loss [5]. Furthermore, the high elastic moduli of these metals are upwards of 20 times greater than that of bone [6](figure 1.1 shows mechanical properties of current popular implant materials). Implantation of metallic implants with high elastic moduli causes an affect called stress shielding, which is the result of much stronger implants taking the various loading stresses for the bone [7]. Stress shielding leads to lower amounts of new bone growth and bone remodelling to smaller, weaker forms due to its apparent redundancy [8]. To overcome this, implants are commonly removed during a second surgical procedure after the tissue has healed. This causes discomfort and further medical problems, as well as increasing health care costs.

Degradable materials have been identified as the solution to the problems described above, hence biodegradable polymers, particularly the new synthetic polymers have been used for the last twenty years in large numbers [9]. Polymers such as poly (lactic acid), poly (glycolic acid) and poly ( $\epsilon$ -caprolactone) can solve some of the problems associated with permanent metallic implants, due to their low modulus and adjustable degradation

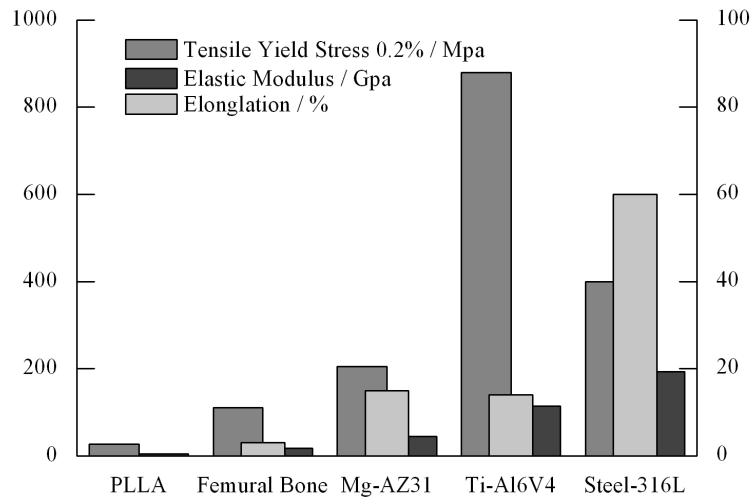


**Figure 1.1:** Mechanical properties of current structural implant materials alongside AZ31 magnesium alloy. AZ31 appears to have properties closer to bone than the other metals and is also stronger than Poly-L-Lactide Acid (PLLA), which is deemed too weak for many structural applications

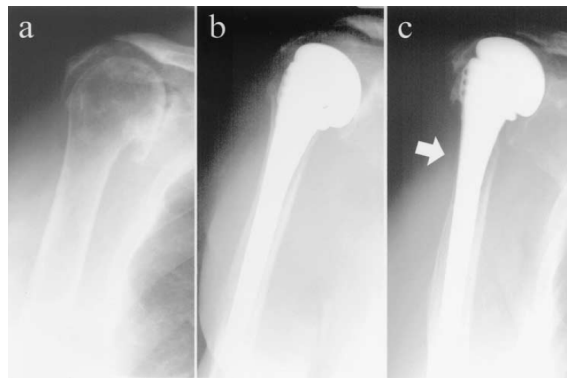


**Figure 1.2:** An example of stress shielding. A, Preoperative image. B, Image obtained directly after surgery. C, Image of the same patient after 7 years of follow-up. Arrow indicates region of cortical bone resorption [8]

rates. Often, the by-products of degradation are acidic which can lead to further degradation of the implant and also trigger inflammation pathways [10]. Polymers have limited applications as biodegradable load bearing implants as they rarely achieve sufficient strength for orthopaedic procedures [11]. Poly-L-lactic acid demonstrates tensile strength three fold less than that of the femoral bone [11].

## 1.2.2 Cardiovascular Stents

The uses of permanent stents can cause similar problems observed with orthopaedic implants. Limitations include stent thrombosis, which requires prolonged antiplatelet therapy, and stent-vessel size mismatch which often results in a smaller lumen after stent implantation [12]. Therefore the use of degradable stents is appealing as once they are bioabsorbed, degradable stents leave behind only the healed natural tissue, allowing

restoration of vasoreactivity with the potential of vessel remodelling. Late stent thrombosis is unlikely since the stent is no longer there, and prolonged antiplatelet therapy will potentially be no longer necessary. Bioabsorbable stents can also be suitable for complex anatomy where stents would impede vessel geometry and morphology causing a likelihood of crushing and fractures, such as is seen in saphenous femoral and tibial arteries [13].

Polymers have been used in this application with good results. Popular bioabsorbable stents are typically made from Poly-L-lactic acid, polyglycolic acid, polycaprolactone and poly (D, L-lactide/glycolide) copolymer [13]. Studies have shown that thrombosis and restenosis rates were lower than with steel stents [14]. Vascular remodelling in a Porcine model was also seen with decreased lumen cross sectional area [14].

The limitations of polymeric biodegradable stents are their lower strength and stiffness when compared to metallic stents, which can result in early recoil post implantation. They can have a recoil rate of approximately 20%, which requires thick struts that can impede their profile and delivery capabilities, especially in small vessels[13]. Polymer stents are associated with a significant degree of local inflammation[13]. The bioabsorption rate is relatively slow, and still results in restenosis, albeit less than steel. Polymer stents are also radiolucent, which can make positioning hard [13].

Magnesium demonstrates the ability to overcome the limitations of polymers, whilst having the mechanical properties of metals. However, magnesium is not visible by radiography.



## LITERATURE REVIEW

### **2.1 The effect of implants**

The performance of biomaterials comprises two components, the response of the host to the implant and the behaviour of the material in the host[15]. The almost immediate event that occurs upon implantation of metals, as with other biomaterials, is adsorption of proteins[16]. These proteins first come from blood and tissue fluids at the wound site and later from cellular activity in the periprosthetic region. A large body of work has been completed on the subject concluding the kinetics of the adsorption to be a matter of milliseconds [17].

The bonding of proteins to the implant depends on the nature of the surface, with hydrophilicity being an important parameter[17]. It is widely assumed that no specific covalent attachment occurs between proteins and implant surfaces but adsorption is the product of thermodynamic mechanisms, the ambivalent polar/non-polar characteristics of proteins and thirdly, protein's limited solubility meaning adsorption increases as the solubility decreases[18]. The amount that adsorbs varies; variations from 0.005 to 0.144 $\mu\text{gcm}^{-2}$  for albumin and 0.283 to 0.512 $\mu\text{gcm}^{-2}$  for fibrinogen were found to adsorb under steady state conditions on to polymers ranging from hydrophilic to hydrophobic in character [19].

Once on the surface, proteins can desorb (native or denatured, intact or fragmented) or remain to mediate tissue-implant interactions. In fact, the nature of this conditioning film deposited on biomaterials is believed to be responsible for the host response [15].

#### **Cardiovascular stents**

Following the implantation of a cardiovascular stent and the initial protein adsorption there are four stages of response. First is thrombosis, which caused the failure of early stents (over 40%)[20]. Today this has reduced to under 1%, however thrombosis remains a feature of every stent, albeit insignificant in terms of lumen encroachment, but occurs at the strut walls enough for mural thrombus deposition. This effect is within 1-3 days of implantation. Thrombi that form at the struts as well as on the vessel wall between

struts provide the site of the second phase of repair, a brief inflammatory reaction. During this stage the area is covered in leukocytes, with the number greatly affecting the rate of proliferation later on with the developed lesion. These leukocytes decrease in number from day 3 to 7 and are replaced by macrophages[20].

The third phase is intimal cell proliferation of smooth muscle cells along with monocytes that have migrated to the thickened layer of arterial wall (neointima). These proliferate and form the metabolic and architectural framework of the hyperplastic lesion. The number of monocytes per artery determines the extent of arterial intimal growth in a linear relationship[20].

The last stage is remodelling of the artery. Here, increased collagen and fibrosis deposition causes the artery to shrink. Also, the arterial wall may be squeezed through the stent strut interstices. Because the artery is dynamic and responsive, it opposes the strain imposed by the stent struts through increased collagen deposition, marked destruction of elastin, and persistent inflammation[20].

## Orthopaedics

The host response to implants placed in bone involves a series of cell and matrix events, ideally resulting in intimate apposition of bone to biomaterial called osteointegration. For this intimate contact to occur, gaps between bone and implant must be filled, and bone damaged during preparation of the implant site must be repaired[15].

Initially the adsorption and remodelling of proteins along with the release of material or reaction productions occurs. After which is the approach of inflammatory and connective tissue cells. These adhere to the surface along with targeted matrix proteins such as bone sialoprotein (BSP), osteopontin (OPN) and  $\alpha$ 2HS-glycoprotein[15].

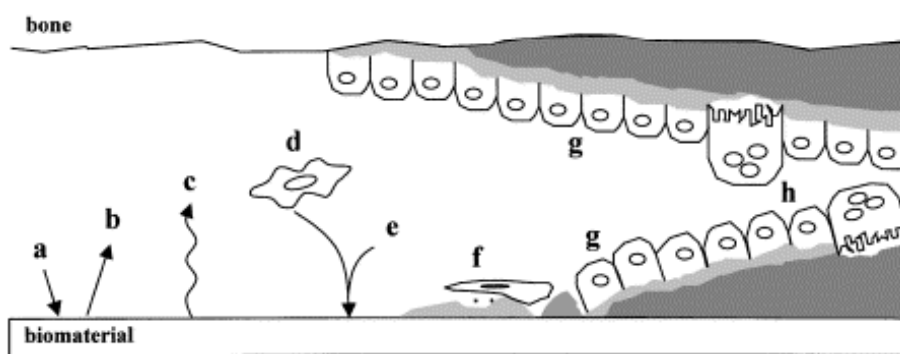


**Figure 2.1:** Representation of events at the bone-implant interface. (a) Protein adsorption (b) protein desorption, (c) material release, (d) inflammatory and connective tissue cells approach, (e) release of matrix proteins and selected adsorption of proteins (f) formation of lamina limitans and adhesion of osteogenic cells, (g) bone deposition on exposed bone and implant surfaces, (h) remodeling of newly formed bone [15]

This matrix formation is the first step of the formation of the lamina limitans and allows the adhesion of osteogenic cells. The interfacial zone now formed is absent of serum proteins, such as albumin. This means the protein adsorption thus far is a selective accumulation/deposition of specific molecules. The afibrillar interfacial zone there on



becomes populated with osteogenic cells and new bone is deposited. During this phase it has been shown that osteoblasts, osteoid, and mineralised matrix are present adjacent to the lamina/limitans-like layer. This suggests bone is deposited directly on the surface of the implant, extending outward from the biomaterial. Therefore, bone formation in the interface region occurs in two directions; not only does the healing bone approach the biomaterial, but bone also extends from the implant toward the healing bone. The new bone growth is remodelled to mature bone structures[15].

### **2.1.1 Magnesium in the body**

Magnesium in the human body ranks fourth in overall abundance of inorganic compounds, an estimated 1 mol of magnesium is stored in the body of a normal 70kg adult. Within cells, magnesium concentration is higher, second only to potassium. Between 60-65% of magnesium is found in bone, the remainder stored largely within muscle cells[21].

Magnesium is involved in over 300 enzymatic reactions in the body including glycolysis, the Krebs cycle, creatine phosphate formation, nucleic acid synthesis, amino acid activation, cardiac and smooth muscle contraction, cyclic AMP formation, and protein synthesis[22].

Magnesium and calcium are constantly linked within the body, with a number of mechanisms involved in their homeostasis, Magnesium is a nonspecific, natural calcium channel blocker. Renal homeostasis maintains the magnesium serum level (figure 2.2 shows a schematic of the processes within the kidney). Magnesium within the blood enters the kidney where it is ultrafiltrated through the blood kidney interface, the glomerulus. Here about 70% of total magnesium concentration is filtered through the glomerular membrane into the nephron by means of the bowmans capsule[23]. Once in the nephron only 10-15% of the filtered magnesium is reabsorbed in the proximal tubule, the major part, roughly 60-70% is reabsorbed in the ascending limb of the loop of Henle. Here magnesium is reabsorbed by a paracellular mechanism involving paracellin-1[23].

The remaining 10-15% is reabsorbed in the distal convoluted tubule[24]. In the distal convoluted segment magnesium is absorbed by an active transcellular mechanism. This absorption is under the control of special divalent cation sensing receptors; elevated plasma magnesium concentrations inhibit reabsorption of magnesium from the distal convoluted tubule, leading to an increased loss of magnesium from the body[23]. This system is the main regulator of the excretion of magnesium as there is little magnesium reabsorption beyond the distal tubule. If magnesium blood levels rise, divalent cation sensing receptors are activated on the peritubular side of the cells of the distal tubule. Activation of these receptors reduces response to hormones such as parathyroid hormone, calcitonin, glucagon and arginine vasopressin (magnesium conserving hormones) on the hormone mediated magnesium uptake into the cells of the distal tubule. Subsequently less magnesium is transported through the cells leading to an increased urinary magnesium excretion[23].

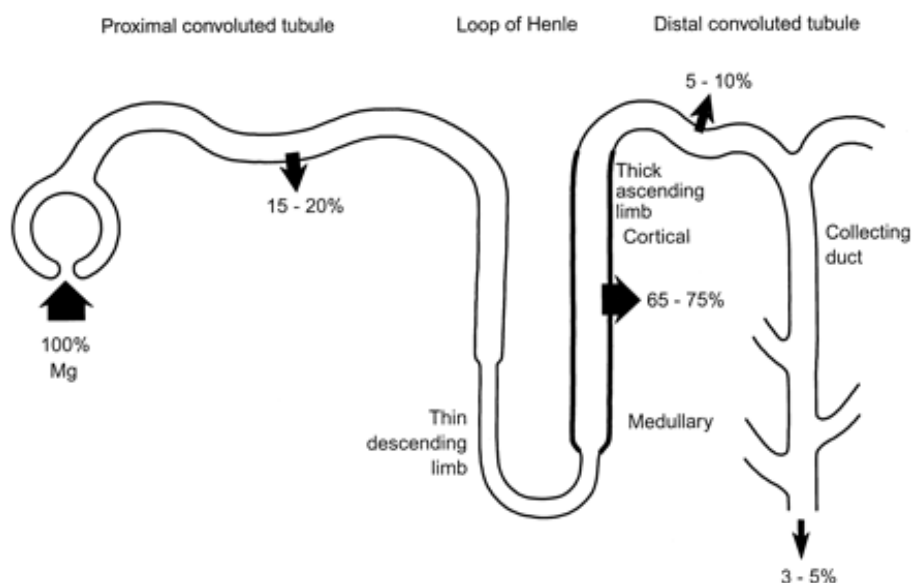


**Figure 2.2:** Summary of segmental magnesium absorption along the nephron within the kidney[24]

Serum Mg Level		Effect
mg/dL	mmol/L	
1.7-2.4	0.7-1.05	Normal Serum Level
5-8	2-3.5	Nausea, flushing, headache, lethargy
9-12	4-5	Somnolence, loss of deep tendon reflexes, prolongation of QRS, PR, QT intervals, bradycardia and hypotension
>15	>6	Complete heart block, respiratory paralysis, coma, shock
>20	>8	Asystole, death

**Table 2.1:** Serum concentrations of magnesium with their symptoms in humans.

### Clinically high levels of Magnesium

Clinically significant hypermagnesemia is rare in individuals with normal renal function, and its cause is often the result of medical intervention. Hypermagnesemia is frequently subtle and nonspecific and often the symptoms are attributed to other illnesses. Hypermagnesemia is associated with a high morbidity and may be life threatening.

Mild hypermagnesemia has been observed in patients receiving a range of treatments which actively modify homoeostasis of magnesium, such as lithium therapy, hyperparathyroidism and hypothyroidism.

The most common cause is prescribed excessive intake of magnesium containing laxatives, cathartics, or supplements, or concomitant use of anticholinergic and narcotic agents and multiple doses of magnesium-containing cathartic therapy given in conjunction with activated charcoal.

Nausea, headache, flushing, warmth, and lightheadedness characterise minor elevations of serum magnesium. The cardiovascular, respiratory, and neuromuscular systems are affected at higher doses. In large doses, magnesium acts like the poison curare at

the neuromuscular junction and a parasympathetic blocking agent. Temporary intestinal paralysis has been reported. Although the correlation between symptoms, signs, and serum level can be extremely variable and dependent on the presence of one or more disorders states, in most cases respiratory failure precedes cardiac collapse. Muscle weakness, an abnormal electrocardiogram and altered mental status with a CT scan should suggest hypermagnesemia. The highest published serum magnesium level in a patient who survived was 10.65 mmol/L (26.0 mg/dL).

### 2.1.2 Magnesium in bone

The majority of the body's magnesium is located in bone. The magnesium adsorbed on the bone's surface is in equilibrium with the extracellular magnesium[22]. At reduced plasma concentrations magnesium can be rapidly released from the bone surface and at increased plasma concentrations magnesium is bound to the surface[22].

In an investigation into the kinetic model of magnesium metabolism, the movement of stable isotopes  $^{25}\text{Mg}$  and  $^{26}\text{Mg}$  were studied. It was found that 24% of the human total magnesium exchanges rapidly from bone to blood. Bone magnesium, therefore, represents a magnesium reservoir that buffers extracellular magnesium concentration. In humans this magnesium buffering capacity is reduced with increasing age as over lifetime nearly half of the magnesium content of bone is lost [22].

### 2.1.3 Osteoblasts

The focus of this study with regard to understanding the biological aspects of the research is centred around the orthopaedic market. The *in vitro* models chosen to investigate the magnesium-bone relationship are based on human osteoblast cells. These cells as mentioned earlier are fundamental to implant success, as they are responsible for new bone growth.

Fundamental to the growth of new bone tissue is the way in which the osteoblast cells behave. This is determined by a progressive and interdependent series of biochemical events within the cells known as the cell cycle, which affects the cell genetically [25]. First, the expression of cell growth and subsequently a series of tissue-specific genes. The changes in gene expression can be monitored and are used to define the developmental sequence now thought of as osteoblast's three distinct periods; Proliferation, matrix development and maturation, finally followed by mineralisation [25].

Owen *et al* investigated in great depth the relationship between osteoblast gene expression, activity and time. The basis of the Owen model (shown in figure 2.3) is that genetic modifications throughout the cells life produce the three stages. It is reported that there are genetic restrictions on the sequence between the phases, meaning cells can progress but not pass without the appropriate signals. Genes involved in the production and deposition of the extracellular matrix must be expressed during the first phase of proliferation.

If not, the cells will not differentiate and stay in a proliferative state. It is also reported that the onset of extracellular matrix synthesis is the cause of the shutdown of the proliferative gene pathways. The maturation and organisation of the matrix shutting down proliferation is the tissue's way of determining the matrix is ready for mineralisation. It is therefore important for these gene pathways to be expressed so that new bone growth can occur. These gene pathways are externally influenced by the conditions of the cell.

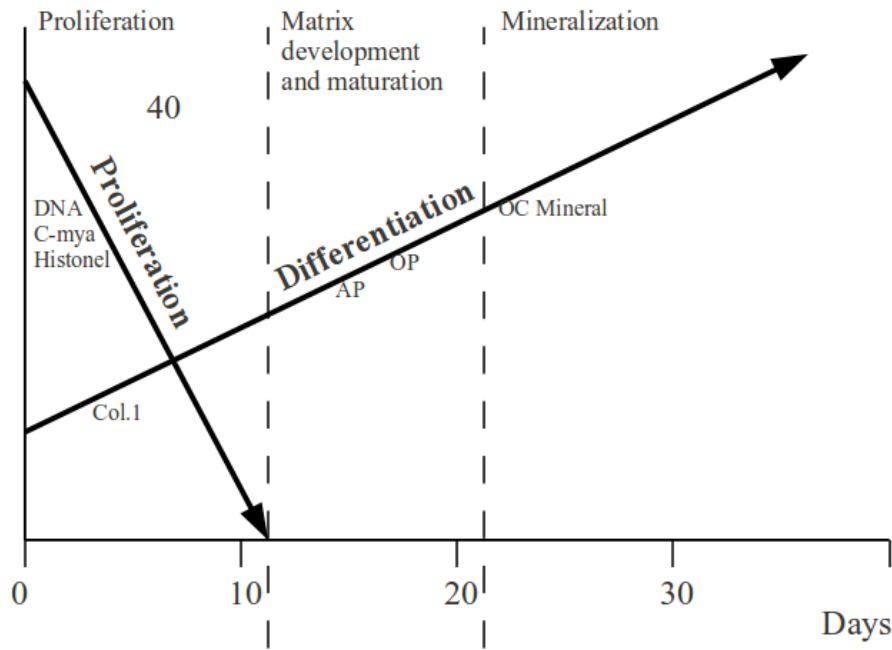


**Figure 2.3:** Model of the relationship between proliferation and differentiation during the rat osteoblast developmental sequence. Commitment periods and restriction points, designated within broken vertical lines. A functional relationship between the down-regulation of proliferation and the initiation of extracellular matrix maturation and development is based on stimulation of alkaline phosphatase (AP) and osteopontin (OP) gene expression when proliferation is inhibited, but the developmental sequence is induced only to the second transition point. Growth of the osteoblast under conditions that do not support mineralization confirms the day 20 restriction point since the developmental sequence proceeds through the proliferation and the extracellular matrix development/maturation periods, but not further. DNA, DNA synthesis; col I, collagen Type I; OC; osteocalcin [25]

One factor that influences cell function is how its attached to its surrounding environment. Cells are attached to the extra-cellular matrix by molecules in their cell membranes called Integrins. It has been documented that integrins can regulate gene expression[16]. Integrins along with cadherins, which are used in cell-cell attachment have direct interactions with a-actinin, talin and catenins, linking to the cell's cytoskeleton meaning a direct affect on cell shape. The signals mediated by cell shape may be processed by the nuclear matrix, which is physically linked to the cytoskeleton via the nuclear lamins. Subsequently, adhesion activation is essential for signal transduction through to regulation of gene expression. Extracellular matrix-mediated changes in cell shape can modify the nuclear matrix and therefore modify gene expression. Extracellular matrix-mediated changes in cell shape initiate a switch between the proliferative and differentiative state. For example, as osteoblasts shift from a proliferative to a rounded differentiated state, its been shown that the nuclear matrix protein NMP-2 is produced. NMP-2 binds to the

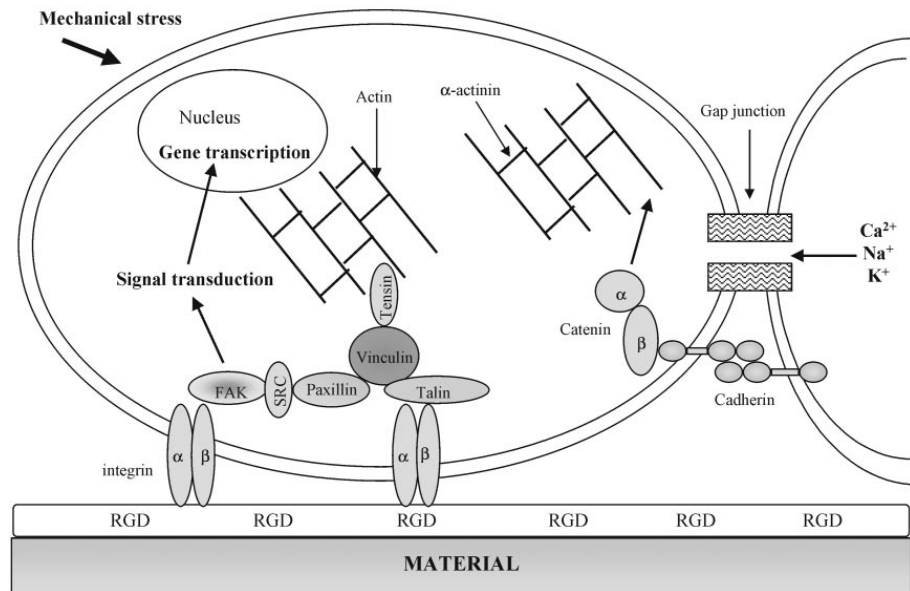


**Figure 2.4:** Representation of the cell proteins involved in cell adhesion on biomaterial[16]

osteocalcin gene promoter and induces an expression[26]. Recent work has been conducted on osteoblast adhesion to fibronectin which is a protein commonly found in the extra cellular matrix. It was shown that the specific fibronectin receptor ( $\alpha 5 \alpha 1$ -integrin) and  $\beta 1$ -integrin were reported to promote osteoblastic differentiation. It was found that amplification of  $\alpha 5 \alpha 1$ -integrin was associated with increased mineralisation of bone cells in culture[16].

### Osteoblasts and Magnesium

Several publications have shown that bone growth is stimulated by the presence of a degrading magnesium implant. Witte reported increased bone growth at the surface of implants within rabbits and Zijian reported increased numbers of osteoblasts and osteoclasts around corroding Mg-1wt%Ca pins[27]. There are several hypotheses to explain why this could happen. Electrical current has been suggested, along with increased local pH. But logical reasoning would be that Magnesium corrosion,  $Mg^{2+}$  could be stimulating osteoblast function[27].

Janning used magnesium hydroxide cylinders in rabbits to look at its affect on surrounding bone[28]. It was reported that not only was there an increase in osteoblast activity, but also in the first 4 weeks, the number of osteoclasts lowered. It was concluded as no metal alloy was present, only the magnesium ions could have produced this result as electrochemical effects, metal surface properties or the effect of alloying elements were removed from the model[28].

At concentrations close to normal physiological conditions, it has been reported that lowering the amount of magnesium reduced osteoblast proliferation. This was the result of increase TRPM7 expression[30]. TRPM7 proteins are melastatin-like transient receptor potential which have been associated with cell proliferation and survival. It was found

	CTR (1mM)	Mg (0mM)	Mg (10mM)	Mg (100mM)
Growth-related genes				
Ki67	100	9	41	63
PCNA	100	55	86	75
Apoptosis-related genes				
DFF-40	100	93	143	177
DFF-45	100	80	164	207
Bcl2	100	38	120	90
Bcl-XL	100	75	137	243
Inflammation-related genes				
IL-8	100	159	72	200
PDGF	100	74	129	133
TGF-beta1	100	62	151	276
Angio1	100	24	23	91
bFGF	100	108	258	241
VEGF	100	58	98	168
ET-1	100	91	114	210
CXCR-1	100	33	43	54
HIF-1a	100	110	288	160
Migration-related genes				
uPA	100	34	791	1100
MMP2	100	142	194	279
MMP9	100	148	197	124
TIMP-1	100	159	431	214

**Table 2.2:** Gene expression of U2-OS (osteoblast) cells cultured in different magnesium conditions[29]

that increasing magnesium concentration from 0 mM through to 0.8 mM gave cell proliferation increases proportional to concentration[30].

Using higher concentrations, predicted to be similar to those found around the implant surface, YeoHeung looked at genetic responses in osteoblasts to changes in magnesium concentration. Osteoblasts were cultured in 0, 1, 5, 10, 100 and 200 mM magnesium[29]. The results are shown in table 2.2. Average growth, apoptosis, inflammation and migration regulators all increase with Mg concentration. Proliferation results showed that cell number increased with magnesium until 5mM, but above this value it became detrimental. This was the same result seen with mineralisation[29].

The modification of hydroxyapatite with magnesium and other divalent ions has also shown osteoconductive effects. Surface modification of bioceramics with  $Mg^{2+}$  substantially affects the phenotype of osteoblast cells *in vivo* and *in vitro* [31][32]. Modifying biomaterials with divalent cations such as  $Mg^{2+}$  results in an increase in osteoblast adhesion to the altered substrate using integrin mediated mechanisms. Although the specific role of  $Mg^{2+}$  in this process remains to be determined, a possible consequence of bioceramic modification with  $Mg^{2+}$  was suggested to be the result of alterations in cell-matrix interaction[31][33]. This was shown when integrin expression was changed as a result of the magnesium surface modification. The osteoblasts grow on the  $Mg^{2+}$  modified

bioceramic with higher expression levels of  $\beta 1$ ,  $\alpha 5$ ,  $\alpha 5\alpha 1$ , and  $\alpha 3\beta 1$ -integrin receptors, compared to the  $Mg^{2+}$  free bioceramic. It was suggested that the  $\alpha 5\alpha 1$ -integrin were found to be regulated by divalent cations and extracellular changes in these ions modify integrin affinity to their respective ligands[33].

## 2.2 Magnesium as a biomaterial

### 2.2.1 A history of work pre 2000

The use of magnesium-based materials as biomaterials has been researched and used in experimental surgery before, the first recorded case was in the first half of the 20th century. The pioneer was Lambotte whose unsuccessful experiment in 1907 utilized a plate of pure magnesium fixed with gold-plated steel nails to try and secure a lower leg fracture. The result was an implant that corroded completely within 8 days and produced a large amount of gas beneath the skin [34].

In 1938, McBride reported on the use of a magnesium-aluminium-manganese alloy to make screws, pegs, plates and bands to secure 20 fractures and bone grafts. The report showed a typical magnesium aluminium manganese 1g screw would completely dissolve in 120 days [35]. The patients showed no reactions to the use of magnesium alloys and no inflammatory responses adjacent to the implant [35]. During repair, McBride reported that there was no effect on the cancellous bone tissues, but there was a positive effect on the periosteal tissue and deposits of the osseous callous were reported [35].

The second world war then provided the catalyst for a large amount of work. In 1944, Troitskii and Tsitrin, used a magnesium-cadmium alloy to make plates and screws for 34 patients with various fractures[36]. The results showed that the implants stimulated hard callouses at the fracture sites. They would also produce hydrogen gas in the form of large cysts, these were overcome by drawing off the gas with a subcutaneous needle[36]. The implant is reported to have maintained mechanical integrity for 6-8 weeks, with complete resorption occurring in 10-12 months. Some implants only lasted 3-5 weeks, which was attributed to increased acidity. In all patients (44 total), no distinct inflammatory reactions to the implant were observed [36].

Znamenski used a magnesium-aluminum alloy (10%Al) to treat gunshot wounds [37]. The two patients treated both had their fractures fused in 6 weeks, with the magnesium plate no longer detectable after 6 weeks, and the pins no longer detected after 4 weeks[37]. Both patients were considered a success, with no inflammatory reactions or problems.

In 1972 a patent was granted for two biomagnesium alloys for Stroganov, who observed lower corrosion rates by using rare earths (0.4-4wt%) and cadmium (0.05-1.2wt%) in the first and rare earth (0.4-4wt%) and aluminium (0.05-1.2wt%) in the second. Both alloys had traces of manganese, silver, zirconium or silicon, [38]. It was reported that pins of 3mm diameter lasted for 5 months, and pins 8mm in diameter for 11 months *In vivo* [38].

Since the early pioneering surgical investigations, to the author's knowledge no work was carried out until the 21st century. Most likely due to the success and advances in modern surgical techniques with inert metals such as steel 316L and titanium Ti6Al4V in that time. Meanwhile the use of biodegradable polymers had become widespread in research and clinically [39], these addressed a number of problems regarding permanent implants and made biodegradable materials an in-demand asset to surgical operations. Biomedical polymers also highlighted the short-fall with present metallic implant materials which were still burdened by their need for repeated procedures and lasting complications.

Concurrently magnesium's lightweight nature meant that it was becoming more demanded by the automotive and aerospace industry and therefore large advances in corrosion and mechanical properties were required and ultimately were delivered by the magnesium suppliers. Specifically the WE alloys and high grade AZ alloys which gave great improvements in strength and corrosion resistance [40].

Both factors have breed a new interest in biomagnesium research, hoping to utilize the new magnesium alloys available. The first known paper of recent times to utilise the new technology was by DiMario in 2004, working alongside the Swiss medical devices company Biotronik[41]. The first study used a total of 20 patients (10 diabetics), who underwent angioplasty for critical lower limb ischemia using magnesium drug eluting stents. A total of 23 stents with two lengths, 10 and 15 mm were used. No adverse events were reported during the procedures and no early recoil was seen. One-month follow-up with Doppler and MRI showed that normal flow was present in 18 patients, while indices suggested 30-40% stenosis in two patients[41].

Biotronik subsequently named the absorbable metal stent (AMS), Magic. It is pre-mounted on a fast-exchange delivery system, compatible with 6 Fr introducer systems. The stent is tubular, slotted, balloon-expandable and is sculpted by laser from a single tube of WE43. The stent design was specifically developed with respect to the mechanical characteristics of the magnesium alloy in order to achieve a radial force comparable to conventional metal stents. The AMS rapidly proved itself to be remarkably successful. 12 absorbable (AMS) and 6 conventional metal stents (control) were implanted in the main coronary arteries of mini-pigs. Quantitative coronary angiography revealed significant higher minimal lumen diameter values for the AMS (1.50 mm) than the control stents (1.26 mm) at 4 weeks follow-up and values of 1.55 mm versus 1.09 mm at 8 weeks follow-up, respectively. Histomorphometric analysis at 8 weeks showed significantly reduced intimal proliferation for the AMS in comparison with the control stent, indicating a reduced mechanical irritation of surrounding tissue as well as possible anti-proliferative effects of the stent material. No stent-related adverse events occurred during the study. No thrombotic effects and acceptable local inflammation response were observed. In a short-term trial, endothelialisation of the AMS struts was almost complete after a few days. Mechanical integrity of the AMS did not change appreciably within this time frame under *in vivo* conditions. These initial studies have prompted far greater research into the



cardiovascular area[42].

In 2005 Frank Witte used four magnesium alloys including WE43 to investigate their effects by placing rods in Guinea pig femurs. The Witte and Biotronik investigations were classed as successful by the authors as the new magnesium alloys show great potential, with no adverse affects, and an implant life much greater than previously seen [11].

### 2.2.2 Recent developments

The Biotronik and Witte work showed modern magnesium alloy's huge potential and further *in vivo* investigative work was carried out with the aim of confirming whether bioresorbable magnesium was purely academic or had real-world potential [43–46] Since these initial trials, research in the area has ballooned exponentially as figure 2.5 shows; only three publications were made in 2005, compared to over 60 in 2009.

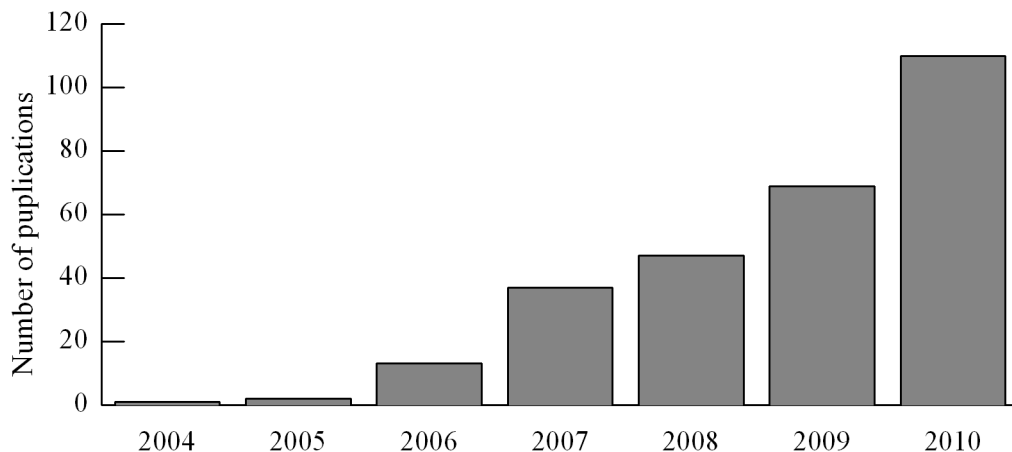


**Figure 2.5:** Publications and conference proceedings on the subject of biological applications of Magnesium or its Alloys against year. 2010 calculated pro-rata

The very first *in vivo* work had demonstrated that modern magnesium alloys could work, but also their prominent flaw; they still corroded too rapid for most applications. This gave rise to the next area of research; biological corrosion of magnesium and its alloys. This was mainly *in vitro* work using solutions representative of the body and looked into how and why magnesium was corroding at the rates seen.

Work looking into potential ways to overcome the corrosion rate issue was then started, with the surface treatments and coatings the quickest way to give improvements. Most recently it has been alloy development taking precedent, with a move to stop modifying existing aerospace and automotive alloys and design a specifically formulated biomagnesium alloy. This work has been compiled and split into respective groupings.

### *In vivo* studies

Being the most complete form of investigation, it was *in vivo* studies that were first conducted to give an overall indication whether magnesium would work as a biodegradable metallic implant. In 2005, Witte *et al.* used WE43 along with three other alloys to investigate the degradation mechanism at the bone-implant interface, specifically to determine the alloy's effect on the surrounding bone [11]. Witte report had five sample rods 20.0 mm length and 1.5 mm diameter, made of from four magnesium alloys and a degradable polymer as a control implanted intramedullary into the femora of Guinea pigs. WE43, AZ31, AZ91 and LAE442 were used, with the control made from poly-96L/4D-lactide.



**Figure 2.6:** Subcutaneous gas bubbles observed on postoperative radiographs for 4 weeks during magnesium implant degradation [11].

The samples were radiographed regularly to look at the implants integrity. Synchrotron-radiation-based microtomography was used to analyse the degradation characteristics. The report made two important observations, the first that there was a significant increase in bone mass observed with the magnesium-based implants in comparison to the polymer control. The second that the rare earth elements were shown to gather in the corrosion layer and were not detected in the surrounding bone. The report also stated that gas build up seen in faster corroding alloys of past were only observed after 1 week. These were removed using a syringe, and after a 2-3 week period, gas bubbles were not seen [11]. As noticed in previous work, gas bubbles had no adverse effects.

The increased bone mass seen in Witte's study was demonstrated in three *in vivo* studies following. Kaya compared autologous bone tissue with autologous bone tissue with inserted magnesium particles for osterolateral spinal fusions in sheep spines. They noted far better quality bone fusion when the Mg particles were present[47]. Waselau M used magnesium phosphate against calcium phosphate cement in bone fractures[48]. The

Mg based cement secured fragments closer and the remodelling and healing of the bone was significantly greater. The bone formed adjacent to the cement was observed to be more woven than the next to the standard cement. In Duygulus' study, AZ31 rods were implanted into sheep and after three months, Ca and P were shown to be prevalent on the surface, Duygulu concluded that this was new bone formation[49].

Promotion of bone formation is a common theme among *in vivo* studies of Mg implants, with every publication noting an improvement over controls. [43–46, 49, 50] This is attributed to two factors, the first that magnesium alloy corrosion, even at high rates [51] does not initiate a immunoresponse [52] and secondly, that the reaction products such as Mg ions and the reaction layer are osteoconductive [46, 52]

The first point is shown clearly when Witte used a magnesium foam scaffold for cartilage and bone repair in rabbits. The large surface area meant that the magnesium alloy corroded within three months which was at a much greater rate than seen in previous modern studies. This meant that the primary function of the trial failed as the implant was not able to provide significant support for long enough, but it did show the effects of magnesium corrosion at the highest rates. Hydrogen gas was visible for the first two weeks, but none at following time points. The rabbits gave no indication of pain or irritation during the study. Histological staining post-mortem, showed no enhanced cell inflammation, instead a fibrous matrix enclosing the scaffold and later the scaffold remnants. There was no osteolytic change seen, and only a small phagocytic response was noted removing the Mg particles[51, 53]. Overall, this concluded that at even ultra high corrosion rates, magnesium initiates only a small immunoresponse.

When corrosion rates are not excessive however, no response is seen other than as an effect of the surgery itself [52]. Mg-Zn-Mn rods were implanted perpendicular in femurs crossecting the marrow and cortical bone and into the surrounding muscle. The implants corroded at a rate of 55% over 26 weeks, which meant no hydrogen gas was observed. Unlike Witte's foam, this implant give rise to no fibrous capsule and on a cellular level; no macrophage, leukocytic or giant cells were seen at all. External to the implant site serum levels of magnesium were not increased meaning the kidneys can adequately cope with the corrosion[52]. He 2009, demonstrated this in greater detail, with no affects seen on the heart, kidneys, liver, spleen of rabbits implanted with magnesium rods which corroded at a slightly faster rate (87% in 14 weeks) [54]

Along with presenting the near zero levels of immunoresponse, these studies demonstrated much higher bone response and activity. Witte's foam gave rise to greater osteoid density around the implant, a higher bone to tissue ratio and a much more mature bone structure. This was suggested to be the result of increased osteoblast and osteoclast density and a greater mineral apposition rate. The latter due to the regeneration affect of  $Mg^{2+}$  ions on alkaline phosphatase, which in turn is directly related to bone remineralisation [55]. Zhang concluded that the increased bone activity was due to the reaction layer of the corroding magnesium in blood/plasma (determined to be Calcium magnesium phosphate

based) being osteoconductive and that the ions released gave rise to no immunoresponse meaning no fibrous capsule slowed the rate of bone growth and remodelling [52].

### ***In vitro* Cell studies**

Using cell cultures to replicate the *in vivo* conditions gives the advantages of not having to use animal or human subjects and that the conditions are set by the user so can be more specific. The obvious disadvantage is the large discrepancies between *in vitro* and *in vivo* results. Nevertheless, work has been carried out on magnesium alloys with human cell lines for various investigations. The first being by Pietak in 2007 who concluded that despite the said disadvantages of *in vitro* work, it could still be a useful tool in screening alloy characteristics [56]. Since, bone activity, cell viability, cell toxicology, inflammatory response, corrosion rate and corrosion morphology have all been characteristics studied by *in vitro* means.[56–61]. On top off these, various publications, reviewed later, looked at alloy compositions and surface treatments using *in vitro* studies to validate their findings.

Every study has shown that cells can be supported on the surface or neighboring cell culture media of magnesium and magnesium alloy samples and that the cells will all have lower viability than plastic or glass controls in the initial time points (<3 days). The types of cell used are dominated by the perceived applications of magnesium alloys, i.e. smooth muscles cells (SMC) replicating conditions for the cardiovascular stents and osteoblasts for orthopedics. Using osteoblasts, it was shown that culturing these magnesium discs gave increased alkaline phosphatase activity and compared to a polymer control, far greater bone like matrix formation [56].

Work on smooth muscle cells has shown that in high magnesium corrosion environments, 50% of cells will be lost and the remaining viable cells will produce less vimentin, caldesmon and alpha actin [57]. It was argued that this could decrease the probability of SMC proliferating and thrombosis. Looking at the heavy metal additives used in common magnesium alloys, Drynda used SMC to show that it was only at large concentrations (70 $\mu$ g/ml), that cell numbers decreased [60]. These concentrations were concluded to be far too high to represent stent conditions, as stents only weigh roughly 10 mg. Although, whether a concern for orthopedic applications where masses used are three or four orders of magnitude higher was not mentioned. The rare earth metals were shown to be responsible for the induced mRNA expression of IL-6, IL-8 and ICAM-1, plus a increased expression of chemo-attractant factors. All of which will lead to an inflammation response. Out of the elements neodymium, an element commonly used in WE43 was the most potent[60].

Other work has looked at fibroblast, 3T3 cells and their hemolysis rates on magnesium alloys. It was found that with a low corrosion rate alloy (using increased zinc content, 5%) compared to commonly used magnesium zinc manganese alloys, only 3.4% of the cells died. This was reported to be lower than the 5% hemolysis rate that the ISO 10993-4:2002

standard for materials toxicology for stent applications had set[61].

## 2.3 Corrosion

### 2.3.1 Corrosion of Magnesium in Simple Electrolytes

Magnesium as an engineering alloy is widely and some times unfairly known for its poor corrosion resistance. It has been this factor the has stopped the wider use of its alloys in the areas where its high strength to weight ratio would be of great benefit. Conversely, although it is widely regarded as a very poorly corrosion resistant material, in almost any atmospheric conditions; from rural through to marine and industrial, magnesium alloys have better resistance than mild steel and in some cases, better than aluminium. For instance, the die cast alloy AZ91 can give a salt spray corrosion performance that is good to excellent when compared to steel and aluminium [62]. However, this stigma is sometimes justified. Magnesium alloys offer very poor corrosion in chloride containing solutions.

There are two problems with magnesium alloys that stop its overall corrosion resistance in these environments, first is it's oxide layer. With aluminium and titanium and other engineering alloys, their oxide forms in the environment which is then stable and acts as a protective barrier between the electrolytes and the metal and also the metal dissolving into the solution[63]. Magnesium generally forms magnesium hydroxide,  $Mg(OH)_2$ . This is easily broken down or reacted away in most corrosive environments. The second factor is magnesium itself. It has a low standard potential (the lowest of all common metals) so that it acts and an anode to any internal impurity or second phase creating micro-galvanic cells within the material[63].

High purity magnesium alloys have been a recent development, alloys made before impurities were below threshold concentrations suffered rapid attack in nearly all moist conditions. High purity alloys exhibit resistance to salt water more than ten-fold that of low purity, which shows the significances of micro-galvanic corrosion in magnesium alloys. Typically the impurities responsible are metals such as iron, nickel and copper, a by product from poor production standards [64].

#### Corrosion mechanism

Magnesium reacts with water in aqueous environments by the following electrochemical reaction. It is therefore not affected by oxygen content like some other metals. The reaction is the product of micro-galvanic coupling of cathodic and anodic components of the microstructure [62].

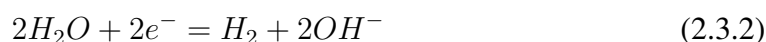
Anodic reaction



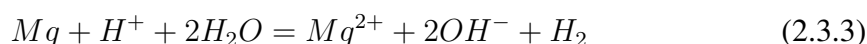
Electrode	Potential V
Li	-3.02
K	-2.92
Na	-2.71
Mg	-2.37
Al	-1.71
Zn	-0.76
Fe	-0.44
Cd	-0.40
Ni	-0.24
Sn	-0.14
Cu	0.34
Ag	0.80

**Table 2.3:** Standard reduction potentials

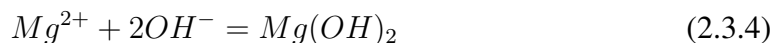
Cathodic reaction



Overall reaction



Product formation



The result of the redox reaction is a standard potential of pure magnesium in 25 C water of -2.37 V, which is the lowest of all engineering alloys [62]. But this potential is only theoretical as the product formation step means the layer of  $Mg(OH)_2$  protects the surface and a true potential of -1.7 V is normally seen. Comparisons to other metals (Table 2.3) shows why magnesium can corrode at such high rates.

The hydroxide layer formed in aqueous solutions is not thermodynamically stable, and therefore only offers slight protection to corrosion. The thermodynamics which govern the stable forms of magnesium are described by Pourbaix diagram (figure 2.7), which states that at pH below 10,  $Mg^{2+}$  is the stable form and therefore corrosion occurs. But at higher pH  $Mg(OH)_2$  is stable and offers very good protection against electrochemical breakdown.

Unfortunately, in real terms, chlorides are generally the main threat to magnesium and at normal pH when magnesium hydroxide is unstable, it reacts to form  $MgCl_2$  which is soluble and therefore offers even less protection than  $Mg(OH)_2$  meaning corrosion rates accelerate. Although if the surface area to solution volume is high enough, or there is little movement of the surrounding solution, pH can build up as a product of equation 2.3.2 and this can enhance the protective nature of  $Mg(OH)_2$ .

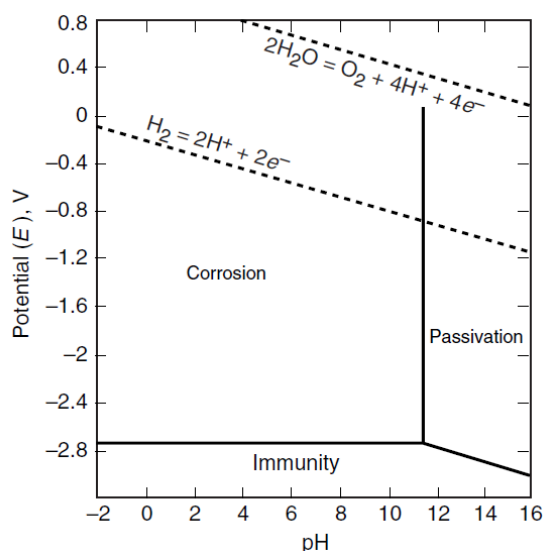


**Figure 2.7:** Potential-pH (Pourbaix) diagram for the system of magnesium and water at 25°C, showing the theoretical domains of corrosion, immunity, and passivation.[63]

For pure and single phase magnesium, the potential of free corrosion is more positive than that of the pitting potential. Meaning localised corrosion is the mechanism by which these materials breakdown. This is because no galvanic coupling can occur as with reactions 2.3.1 and 2.3.2. Generally this is an academic observation as all magnesium is used in double or multiple phase form whether this is due to alloying components or through bad manufacturing and the inclusion of impurities.

Impurities as previously stated are bad for magnesium as they act as cathodic sites to facilitate the reaction 2.3.2. Hanawalt *et al.* studied 14 different types of common impurity and found four were particularly bad for corrosion rates; iron, nickel, copper and cobalt [65]. It was later shown that these four elements had a linear inverse relationship with their content and corrosion rate, but only to a point. When concentrations lowered to a critical amount, they had very little effect on corrosion rate. This is called the tolerance limit, Figure 2.8 shows the limit for iron.

This affect is explained by the contaminants having very poor solid-solubility in magnesium so form particles when concentrations are above the tolerance limit. These in turn form the cathodic sites that help breakdown the alloy [62].

The addition of large amounts of other elements to form an alloy have a number of affects dependant on the element. The most widely used elements for alloying are aluminium, zirconium, zinc, yttrium and heavy rare earths (HRE), which is a group name for elements such as gadolinium and various other Lanthanoids. The additions are put in for three reasons, either to form second phase particulates, dissolve within the magnesium in solid solution or just to form compounds with potential impurities so they change characteristics in the alloy or are removed before casting. Zirconium is the most widely used example of the latter, as it forms dense compounds with iron and nickel which fall to the bottom of the crucible and are therefore not cast. It also has the advantage of being a grain refiner which adds strength[62].

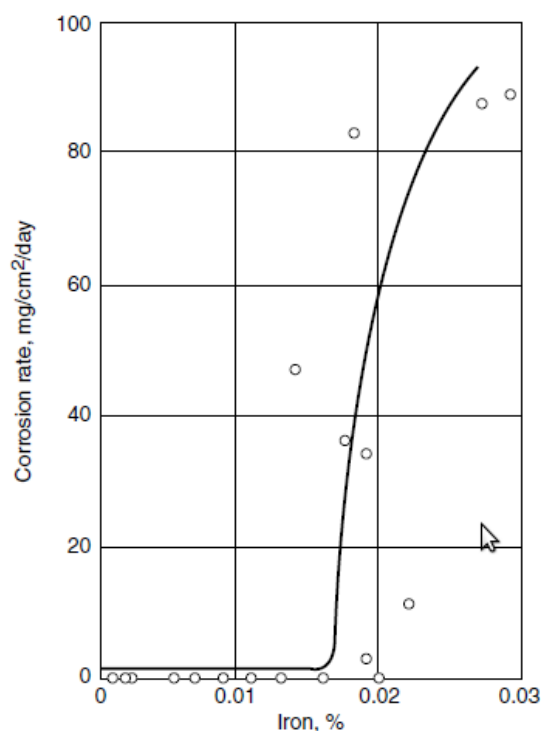


**Figure 2.8:** Effect of iron content on the corrosion rate of commercially pure magnesium subjected to alternate immersion in 3% NaCl.[63]

Second phase has two affects on corrosion, first they act as cathodic sites for the reaction 2.2.2, which is detrimental to the overall corrosion rate. This is generally the case with most second phase that is formed, as it is likely to have a more positive potential than the magnesium matrix around it. The second affect is that if this phase forms a protective film over its surface, and therefore creates a barrier to cathode and stops the reduction of water at these site. This is called an anodic barrier[62].

Aluminium is found partly in solid solution and party in the second phase  $Mg_{17}Al_{12}$  called  $\beta$ -Phase. Additions of aluminium can be good or detrimental to the corrosion rate, and this has been found to be a product of the concentration of beta phase. Higher amounts have been shown to decrease corrosion rate . A potential problem with the use of aluminium is that it lower the tolerance limit of iron, so production standards have to be far greater[62].

Zinc on the other hand increases tolerance limits and is generally used in conjunction with aluminium in popular alloys. Common corrosion mechanisms of aluminium and zinc alloys are pitting at the second phases particles due to the micro-galvanic corrosion cells created [62].

With additions of yttrium and rare earths, pitting is not seen at the phases present (found to be  $Mg_{41}(Y,Nd)_5$  and  $Mg_{24}(Y,Nd)_5$  in neodymium based rare earth alloys[66], but instead at the grain boundaries. Corrosion rate as a consequence is related to the gain size and structure [66]. The pits formed are also smaller, Geary reported that WE43 had the lowest maximum pit depth of all the Mg alloys tested. Yttrium and rare earth alloys are generally far less corrosive than aluminium and zinc alloys. Nakatsugawa found that



Mg-RE alloys have a corrosion resistance about four times higher than that of AZ91D[67]. Unsworth showed that WE54 alloy had a corrosion resistance comparable to that of A356 and A347 aluminium alloys [68].

### Corrosion films

In many cases, metal corrosion is governed by the characteristics of its surface film[62]. However, the nature of the surface film on magnesium is still not well understood. As described earlier the reaction layer on magnesium in most environments is composed mainly of  $\text{Mg}(\text{OH})_2$ . The film is generally regarded to be crystalline. It has been proposed that the oxide layer first forms from magnesium oxide which then slowly hydrate to form the hydroxide which is harder and has lower solubility[62].

In aluminium and zinc alloys the reaction layer is affected by the extra components, and it has been found that these enrich the reaction layer. Aluminium increases the resistance to breakdown of the layer. The film formed has three layers, a inner  $\text{Al}_2\text{O}_3$  rich layer, a middle with  $\text{MgO}$  and the outer which is  $\text{Mg}(\text{OH})_2$ . It is thought the presence of the aluminium oxide, which is much more stable than its magnesium counterparts, is the route of its passivity [62].

In rare earth alloys, the formation of a lanthanide-doped layer helps form a more stable protective film has been shown [69]. In Yttrium containing alloys, the corrosion of Y means it can incorporate in the surface film in the form of  $\text{Y}_2\text{O}_3$  and partly  $\text{Y}(\text{OH})_3$ . This can improve the corrosion resistance of the surface film. However, with these films, the oxide is still largely  $\text{Mg}(\text{OH})_2$  and therefore protection is very limited [70].

### 2.3.2 Corrosion of Magnesium in Biological Electrolytes

The early research on magnesium as a biodegradable implant material all came to the same conclusion; that it would be viable if the corrosion rate could be lowered or controlled *in Vivo*. No knowledge of how magnesium reacts in biological solutions had been sought at the point of these early clinical trials, so it was shortly after that a large quantity of publications to help answer the questions raised.

Biological corrosion testing on metals is obviously no new feat, as work has been carried out on titanium alloys, stainless steels and so on for decades. Therefore the experimental tests were already in place for magnesium to be studied. This is in main the solutions to replicate the body's electrolyte content. These were first developed in 1880, with Ringer's solution, then followed by Earle's balanced salt solution in 1943 and Hank's balanced salt solution in 1949. The balanced salt solutions were modified and Kakubo developed SBF in 1990 which is designed to mimic the acellular human blood plasma [71]. EBSS and HBSS have gone on to be widely available commercial products with additions of amino acids, glucose and vitamins to be used for cell culture and tissue engineering.

The main differences between these biological fluids (composition shown in table 2.4)

	Human plasma	Ringer	EBSS	HBSS	Kokubo-SBF
Na <sup>+</sup>	142	130	143.6	138	142
K <sup>+</sup>	5	4	5.37	6.14	5
Ca <sup>2+</sup>	2.5	1.4	1.8	1.26	2.5
Mg <sup>2+</sup>	1.5		0.81	0.81	1.5
Cl	103	109	125.3	144.8	147.8
HCO <sup>3</sup>	27		26.2	4.2	4.2
HPO <sub>4</sub> <sup>2</sup>	1		1	0.78	1
SO <sub>4</sub> <sup>2</sup>	0.5		0.81	0.81	0.5
Ca/P	2.5		1.8	1.62	2.5
Buffer					Tris
pH	7.4	6.5	7.2-7.6	6.7-6.9	7.4

**Table 2.4:** Ion concentrations of human plasma and synthetic solutions, mM [71].

and the simple sodium chloride salts used in normal corrosion conditions, is firstly the additions of various phosphates, carbonates and sulphates, and secondly the addition of buffers which are used to keep the pH at *in vivo* ranges. The buffer first used was Tris (tris-hydroxymethyl-aminomethane), but in recent years, HEPES (2-(4-(2-hydroxyethyl)-1-piperazinyl)ethane sulphonic acid) has been more widely used [71].

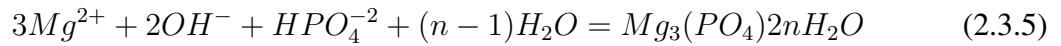
Before 2005, no research had been conducted looking at how magnesium alloys corroded in environments containing these combinations of electrolytes. Witte 2005 was the first study to try and compare lab based corrosion conditions to *in vivo* results, but used marine salt water (ASTM-D1141-98) instead of a true biological solution[44]. This contains sulphates and calcium, but no phosphates, carbonates or buffer. Lopex later in 2005 used SBF to compare heat treatments and surfaces conditions to try and lower corrosion rates of pure magnesium[72]. It was noted that the corrosion rate is much higher than normal salt solutions and there was evidence that hydroxyapatite was formed in the reaction layer[72]. The differences between SBF and NaCl solutions was investigated by Song in 2006[73]. It was found that the polarisation curves of pure magnesium in the two solutions were similar, but the impedance plots showed that there were clearly a large number of dissolution steps with SBF. Also reported was the massive pH raise seen in SBF, Song showed a 1cm<sup>3</sup> cube of magnesium could raise the pH of 250ml SBF (starting 7.4) to 10 in 15 hours. Only speculations of why SBF was causing such differences compared to NaCl were made[73].

Detailed mechanisms of the corrosion process have been studied since as the ever increased popularity of the subject evolved. Certain publications in particular; Rettig 2007[73] and 2008[74], Xin 2008[75] and Song 2009[76] have given great insight into how these biological fluids effect magnesium alloys. These papers looked primarily at three things, what new corrosion mechanisms the extra electrolytes were activating at the magnesium surface, the new reaction layer formed, and the effect of both of these in terms of the corrosion rate.

The proposed corrosion mechanisms *in vitro* suggested by the work are discussed be-

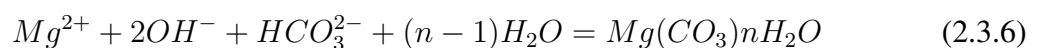
low. As shown earlier, the reaction in water with Mg forms  $Mg(OH)_2$  and that in a solution containing chlorides such as a NaCl, the layer will be reacted to form  $MgCl_2$ , which is soluble and results in the breakdown of the layer. All the investigations with biological solutions have shown this to be the overriding mechanism in this instance too, especially in the early stages. Liu 2007 used SBF and determined that in the very early stages, the pH around the surface would drop with the formation of  $Mg(OH)_2$ , but would then steadily increase thereafter due to the hydroxide released by its chlorinated breakdown [77]. Immediately after the mechanism is altered, phosphate reacts with the magnesium to form  $Mg_3(PO_4)_2$  on the surface. This stops chloride having such an affect as it can only breakdown the  $Mg(OH)_2$  in the reaction layer[77].

The effect of phosphates in the layer is the first change seen in the corrosion mechanisms of magnesium *in vitro*. Its affect has been demonstrated systemically by Xin 2008 who added  $K_2HPO_4$ ,  $K_2HPO_4 + CaCO_3$  and  $K_2HPO_4 + CaCO_3 + MgSO_4$  to NaCl and compared the differences. It was shown that by adding phosphate, corrosion rates were lowered, less pitting was seen on the surface and the reaction layer incorporated  $Mg_2(PO_4)_2$  as well as hydroxide [75]. Studying reaction rates against time, the phosphate-containing solution initially corroded the samples in a similar manner to the solution without, the 12 hour time point showed no difference. But at 24 hours, the rate lowered to less than half when phosphate was added, and this stayed as such for the remainder of the trial (168hrs)[75].



The reaction layer formed is amorphous unlike the crystalline  $Mg(OH)_2$  surface seen with NaCl solution [78]. The distribution of phosphates within the layer is homogeneous [79] which would help to explain why it appears to stabilise the surface; Retting [78] and Xin [75] both show increases in polarisation resistance with phosphates containing solutions. The formation of this layer means that the effects of the chloride attack are weakened and corrosion events like pitting, normally associated with chloride attack at vulnerable areas of the microstructure are not seen on the surface [75].

The effect of carbonates on corrosion are also beneficial to magnesium alloy's corrosion rate, Quach 2008 [80] and Xin 2008 [75] both compared solutions with and without carbonate to find carbonate lowered the corrosion rate after an initial spike. Carbonated solutions form an amorphous reaction layer with no pitting [74][79]. The reaction at the surface (eqn.2.3.6) causes the corrosion rate to rise massively in the first few hours, Xin shows a 300% increase after 12 hours. This is due to the consumption of magnesium and also hydroxide at the surface, meaning the pH increase at the surface which passivates the hydroxide surface is stopped.



After the initial period the corrosion rate lowered to less than that of a non carbonate solution, this period was shown to be around 72 hours [75]. At this point the carbonate precipitates in the reaction layer and has a stabilising affect. Xin presents current density against time (figure 2.9), and after 50 h, the magnesium alloy in the carbonated solutions have become more passive than in the standard solution. Unfortunately the electrochemical impedance spectroscopy data only go up to 24 hours and not past 50 h, so Xin was unable to show this with impedance loops. Polarisation curves show that although carbonated NaCl solution is less noble than the non carbonated solution, its anodic region displays a large shoulder, indicating the magnesium is now harder to breakdown[75].

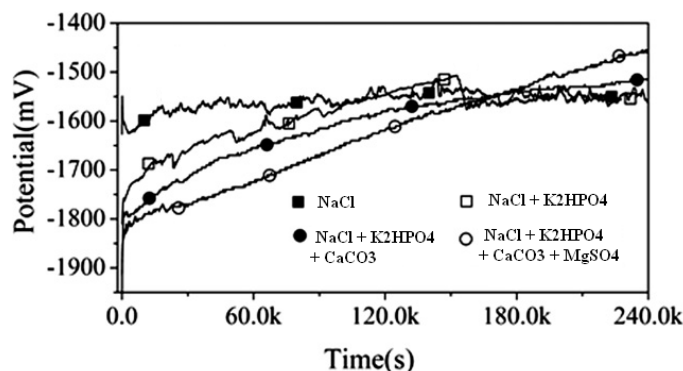


**Figure 2.9:** Electrochemical potential against time for AZ31 in four salt solutions. It is shown that the alloy is passivated with time in the carbonate containing solutions [75]

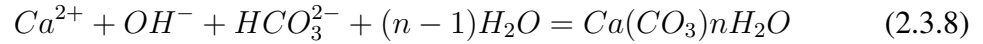
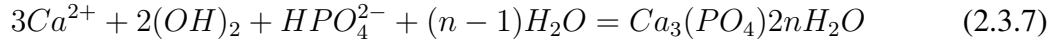
Other than phosphate and carbonate, SBF contains only sulphur and calcium. The affect of sulphur is only known to the extent that it increases the corrosion rate of magnesium alloys[75]. Xin reports that the addition of 0.5mmol/L  $\text{SO}_4^-$  increases the initial (<36 hours) corrosion rate by 25% over the  $\text{NaCl} + \text{CO}_3 + \text{PO}_4$  solution. No sulphur has been reported to be found within the reaction layer [78, 79, 81, 82], and electrochemical testing has shown no discrepancies with that of the non-sulphur solution in terms of polarisation resistance and impedance [75].

Calcium on the other hand has an interesting affect, especially when considering the potential applications of these alloys. Initial publications observed that corrosion in SBF, formed participates on the reaction layer that were; hydroxyapatite-like [72], calcium or magnesium phosphate [79, 82, 83], and carbonated calcium/magnesium phosphate apatite [74, 78], all of which are bone like ceramics, meaning the corrosion products are potentially highly biocompatible. The differences between publications is most likely due the reaction layer being highly heterogeneous and various forms of precipitates being found across the surface.

Calcium is mainly found in precipitates at localised areas when in phosphate form, but have been found homogeneously distributed within the reaction layer as calcium carbonate [79]. Xin also shows that the distribution of calcium deposits is found around passive areas in the microstructure, for example, the  $\beta$ -Phase ( $\text{Mg}_{17}\text{Al}_{12}$ ) in AZ91.

The formation of calcium phosphate is the same as magnesium phosphate, at the surface of the magnesium alloy calcium's concentration will be much lower than that of free

magnesium due to fast corrosion, therefore magnesium phosphate is reported in much higher concentrations [74] [79]. Calcium phosphate only develops when the concentration of magnesium is low enough to favour calcium, therefore only after corrosion rates have stabilised and in local regions where corrosion is still not prevalent.



The formation of calcium carbonate is shown in reaction 2.3.9 which is reported by Xin 2009 as a probable component of the reaction layer. This was suggested due to XPS results which showed a divalent carbonate compound. Xin suggested a combination of Calcium and magnesium carbonate for this peak[79]. Although this is contradicted by Retting [78] who's study used no phosphate in a solution with carbonates and calcium. It was found that calcium could only be precipitated with the presence of phosphate to form  $(Mg, Ca)_x(PO_4)_y(CO_3)_z(OH)_i$  and no calcium was detected (using EDX) on the surface without phosphate, therefore reaction 2.3.9 could not occur and the X-ray Photoelectron Spectroscopy (XPS) peak seen by Xin for the divalent carbonate peak was all magnesium.

In summary, the reaction layer is created in a number of complex reactions that occur in various stages of the corrosion of magnesium. This observation was first noted by Song in 2006, comparing the impedance loops of magnesium in SBF and NaCl to show the differences in complexity between the two [73]. It was also noted that the dynamics of the corrosion with SBF and other biological fluids is different from using NaCl, in that the reaction layer and reaction products are non linear in formation. Magnesium corrodes as a function only of pH when corroded in NaCl [78], where the corrosion rate stays fairly constant until the hydroxide concentration at the surface starts to stabilise the  $Mg(OH)_2$ . Corrosion dynamics in SBF have been shown to be much more complex.

When corroded in SBF corrosion rates are shown to be ever decreasing [84][85][86] which can be attributed to the reaction layer previously discussed. It has been shown that the reaction layer ( $Mg(OH)_2$ ) starts to form in patches as early as 15 minutes and after 5 days the layer is 20-40 $\mu m$  thick [74] where it has matured into the complex magnesium/calcium phosphate carbonate layer.

The formation of a corrosion resistant layer appears to happen in 3 stages, first is a quick increase in passivation (upto 24 hours), then a drop (around 36-48 hours), before a stabilisation [78] [87]. Song uses electrochemical impedance spectroscopy to show this (using AZ31). After 2 hours a twin high and low frequency loop is seen, with the high frequency being the electric double layer and the low the surface film. It has been shown that the size of both loops increases dramatically up to 24 hours. The loops then halve in size toward 48 hours, before the low frequency loop turns into an induction loop at 72

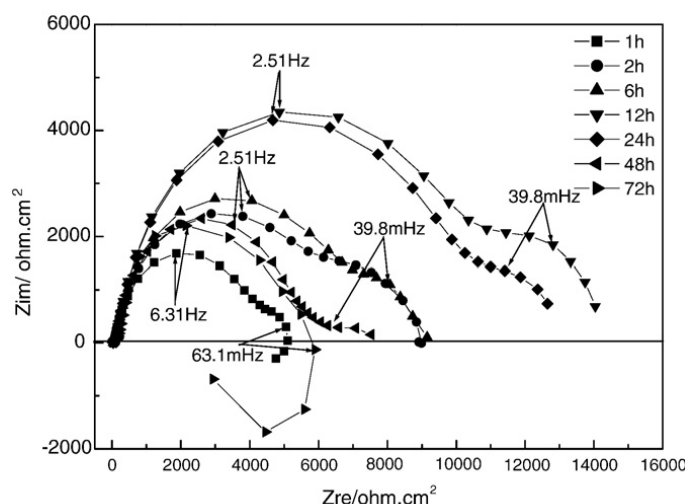


**Figure 2.10:** Impedance spectroscopy of AZ31 in SBF with increasing time. The loops increase with time (maximum at 24 hours), before decreasing with the low frequency loop turning into an inductive component [87]

hours. Song concludes that the first part is due to compaction of the reaction layer, the second due to adoption of chloride so that  $\text{MgCl}_2$  is formed and dissolved. The inductive loop is an indicator of the surface either pitting or peeling. Retting sees a similar trend but due to using a more corrosion resistant alloy (WE43) it is less dramatic, with no inductive loop seen, and the impedance loops only slightly decrease in size after their increase. The point to note in this study is that this trend is shown to be a product of phosphate [78]. This coincides with the study by Xin, who showed that  $\text{NaCl} + \text{HPO}_4$  had a very high corrosion rate which lowers sharply at 24 hours, before the rate fell before that of magnesium in NaCl [75]. Therefore it can be concluded that it is phosphates that are the driving force for the dynamic changes in corrosion rate in biological fluids.

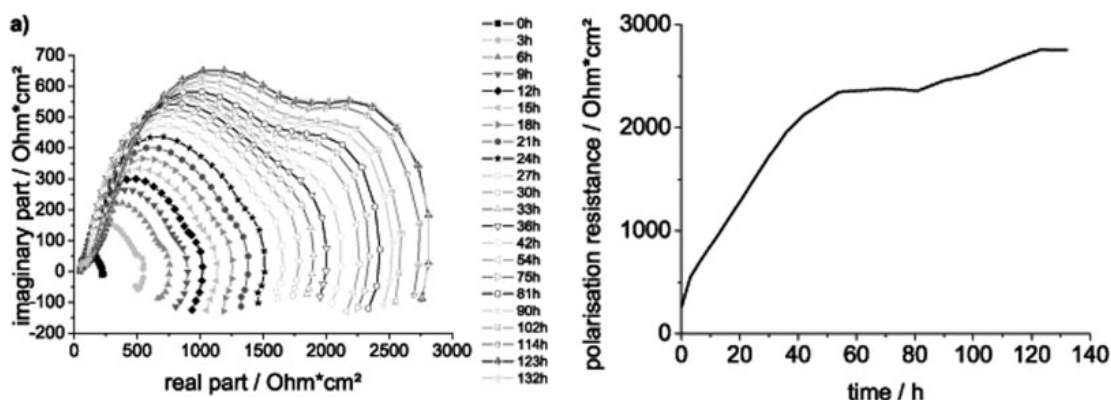


**Figure 2.11:** Left shows Nyquist plots from Impedance spectroscopy of WE43 in SBF with increasing time. Right shows the corresponding polarisation resistance against time. The alloy's polarisation resistance rises sharply at first before steadying and then rising again.

So far biological fluids have been discussed in regard to their electrolyte composition. But biological fluids have huge numbers organic molecules such as proteins, sugars, cells, enzymes and so on comprised within them. From an *in vitro* aspect it is difficult to replicate this, so *in vivo* studies have been used to look at degradation on a complete level, but

biological solutions can lessen the gap by adding various components. Studies such as Lui [77] and Gu [88] have added protein to analyse its affect on magnesium corrosion.

It has been found that by the addition of protein (bovine serum albumin, BSA) to SBF the corrosion rate is lowered, pitting is retarded and the reaction layer is fortified and is stopped from peeling as heavily [77, 88, 89]. Yamamoto reports a reduction in corrosion rate of half compared to Eagles minimum essential medium (MEM) without fetal bovine serum (FBS) on pure magnesium [89]. As with all metals, proteins will adsorb to the surface on magnesium by a combination of van der Waals, hydrophobic and electrostatic interactions and hydrogen bonding creating a complete layer. Previously studied metals such as titanium have shown this layer to have had an affect on corrosion rate when the titanium has to repassivate in BSA containing solutions. With titanium, as with magnesium the corrosion rate is heavily influenced by the adjacent pH, and the addition of BSA stopped this influence. It could therefore be expected that the BSA would stop the localised pH influence on magnesium alloys and cause an increase in rates, but this is not the case. In fact the protein layer disrupts the charge transfer process in the electric double layer, decreasing current density, changing the anodic polarisation and making the magnesium far more passive [77, 88]. It is known as a blocking affect, the adsorbed proteins influence the electric field on the metal surface because they are polarised at different potentials by the dissociation of their amino acid residue. Lui suggests the divalent Mg cations interact with proteins in this layer, which depresses the further dissolution of magnesium[77].

The effect proteins have on the corrosion rate has been shown to be influenced by alloying chemistry and is a result of oxide Z-potentials. Aluminium oxide for instance has a greater potential than magnesium hydroxide, therefore proteins adhere more strongly to the surface[90] This is reported by Gu, where AZ91 had a higher reduction in corrosion rate with the addition of BSA than pure magnesium or Mg-Ca and even AZ31[88]. This could explain the retardation of pitting seen, as pits are associated with second phase regions, but as these will be more highly protected by the protein blocking layer, micro galvanic corrosion and thus pitting lowered.

## **2.4 New Alloy Development**

### **2.4.1 Magnesium alloy systems and their uses**

The first studies looking at magnesium as a biomaterial all used commercial alloys available at the time. As previously stated, in the early years pre 21<sup>st</sup> century the performance of these in biomedical application was very poor and excluded magnesium's use from the body completely. But with the arrival of better production techniques and alloy compositions, corrosion rates meant the initial studies this century showed potential, albeit, still a long way from perfect. [11, 41]. It was concluded that these magnesium alloys developed originally for automotive and aerospace applications needed updating

ASTM Nomenclature	
A - Aluminum	M - Manganese
B - Bismuth	N - Nickel
C - Copper	P - Lead
D - Cadmium	Q - Silver
E - Rare Earth	R - Chromium
F - Iron	S - Silicon
G - Magnesium	T - Tin
J - Phosphorus	K - Zirconium
L - Beryllium	W - Yttrium
Y - Antimony	Z - Zinc

**Table 2.5:** The ASTM design magnesium alloys consists of not more than two letters representing the major alloying elements. These arranged in order of descending wt%, followed by the respective wt% rounded to the whole number. For example an alloy of 96.2wt%Mg, 3.1wt%Al, 0.7wt%Zn would be abbreviated to AZ31.

or changing. The two methods for this are surface coatings and modifications which offer instant benefits on already developed and trusted alloying systems, or compositional changes to the bulk alloy to create alloys specifically for *in vivo* applications. The latter of course being the longer term option but also requiring the greater effort in development.

Commercial magnesium alloys today offer the framework by which new biomedical alloys can be made. They represent years of research creating stronger, more formable and less corrosive materials. Currently, the alloys can be split into three distinct groups; pure magnesium, aluminium containing and non aluminium alloys[62]. These are designated by the abbreviation system listed in table 2.5. By far the most popular are the aluminium containing varieties, these include common systems like the AZ (zinc), AM (manganese), AS (silicon) and AJ (strontium), with the AZ alloys being the most common out of these, including the ASTM (American Society for Testing and Materials) listed AZ31 and AZ91 alloys[91].

The non aluminium containing alloys are more recent developments and included WE systems (yttrium and heavy rare earths) such as WE43 and WE54, ZM (zinc, manganese) and EV (heavy rare earths, zirconium)[66] alloys such as the recent Elektron 21[92]. These alloys offer high strength and high temperature resistance as well as increased corrosion resistance in salt spray tests, out performing AZ alloy at most attributes. Because of this, the first of recent trials [11][41] used WE43 as their starting point for *in vivo* analysis of magnesium.

Tuning these alloys or creating new systems offers a new challenge for metallurgists as the *in vivo* environment is an entirely new obstacle. Present day alloys have been created to perform in atmosphere or moist situations, so their compositions and microstructures are based around countering the affects of these normal conditions. Therefore additions of certain elements that are used and perform well for say automotive applications may cause an entirely new corrosion or failure mechanism *in vivo*. However the basic principles of



how certain elements affect an alloy's attributes are still valid. Elements additions will still be regarded with the same factors in mind; effects on mechanical properties and corrosion characteristics, as well as now the additional attribute, biocompatibility.

### 2.4.2 Biocompatibility of Alloying Elements

Biocompatibility of potential elements is summarised in the table 2.6 taken from Witte 2009[93]

The table shows that almost all commonly used elements are either already present in the body as traces, or have little affect when used at low concentrations. The only major concerns come about Aluminium, as research as found a link with its presence in the body and Alzheimer's. Zinc and manganese are shown to have neurotoxin properties is at high concentrations[93].

Regarding heavy rare earth additions, Drynda [94] used trivalent chlorides of various rare earths including every lanthanide as well as scandium and yttrium on smooth muscle cells *in vitro* to determine affects of these metals on the blood vessels. It was reported that only large concentrations ( $70\mu\text{L/ml}$ ) would cause cell number to decrease. Inflammation genes were expressed though, indicating that these elements are a problem at high concentrations. The element that showed most inflammation was Neodymium [94] which showed effects at lower concentrations than the others ( $50\mu\text{L/ml}$ ). The study used quantities over and above the expected release from magnesium corrosion from an average sized implant.

Feyerabend also used Metal chlorides to investigate biocompatibility on rat macrophages, human osteosarcoma (MG63) and human stem cells[59]. A variety of magnesium additions were looked at, which included zirconium, calcium, lithium and magnesium chlorides as well as the rare earths (yttrium, neodymium, dysprosium, praseodymium, gadolinium, lanthanum, cerium and europium). Splitting these into three categories, Feyerabend found that low solubility (Nd, La, Ce, Pr and Eu) RE's had the greatest affect, with highly soluble RE's (Y, Gd and Dy) generally being acceptable[59]. Calcium, lithium and zirconium were concluded to be no risk due to positive results in this trial and their history of clinical use already. Within the low solubility elements Cerium and lanthanum showed high influences of cell viability and high toxicology, these were concluded to be the only rare earths that were a risk at standard alloying concentrations. Many high solubility elements increased the viability of the cell lines and demonstrated low toxicology[59].

### 2.4.3 Biomedical Alloys Already Investigated

Witte 2005 was the first publication to compare alloys *in vivo* with the intention of understanding metallurgical properties for this application [11]. The study used common AZ alloys, AZ31 and AZ91 alongside the stronger more corrosion resistant WE43 [66] and the lithium containing LAE442. It was reported that only the lithium containing alloy

Element	Pathophysiology/toxicology
Calcium	Normal serum level 0.919-0.993 mg/L Most abundant mineral in the human body (1-1.1 kg) Mainly stored in bone, teeth Is tightly regulated by homeostasis of skeletal, renal and intestinal mechanism
Aluminium	Normal blood serum level 2.1-4.8 $\mu\text{g/L}$ Established alloying element in titanium implants Risk factor in generation of Alzheimer's disease Can cause muscle fiber damage Decrease osteoclast viability In magnesium alloys: mild foreign body reactions were observed in vivo
Zinc	Normal blood serum level 12.4-17.4 $\mu\text{mol/L}$ Trace element Essential for the immune system Co-factor for specific enzymes in bone and cartilage Neurotoxic at higher concentrations
Manganese	Normal blood serum level <0.8 $\mu\text{g/L}$ Essential trace element Important role in metabolic cycle of e.g. lipids, amino acids and carbohydrates Influences the function of the immune system, bone growth, blood clotting, cellular energy regulation and neurotransmitter synthesis Scavenger of free radicals in the manganese superoxide dismutase Neurotoxic in higher concentration (manganism)
Lithium	Normal blood serum level 2-4 ng/g Compound of drugs for treatment of psychiatric disorders Overdosage causes nephrological or lung dysfunctions Possible teratogenic effects
Rare earth elements	Many rare earth elements exhibit anti-cancerogenic properties
Impurities	
Nickel	Normal blood serum level 0.05-0.23 $\mu\text{g/L}$ Strong allergenic agent which can induce metal sensitivity Carcinogenic and genotoxic
Beryllium	Toxic dosage >2 $\mu\text{g/m}^3$ Induces metal sensitivity, highly carcinogenic
Iron	Normal blood serum level 5.0-17.6 g/L Essential for life and metabolically regulated and stored Generator of age related diseases by reactive oxygen species
Copper	Normal blood serum level 74-131 $\mu\text{mol/L}$

**Table 2.6:** A brief summary of the toxicology and pathophysiology of some alloying elements and impurities[93]

out performed the rest, this contradicted industry standards which suggest that WE43 would have a lower corrosion rate than the AZ alloys [66]. Witte has since gone on to use LAE442 for the basis of much more *in vivo* alloy development[95].

Calcium containing alloys seem to be the most popular. This is an obvious addition when considering orthopaedic applications and osteo-conductivity, but Mg-Ca alloys have also shown good corrosion properties [27, 50, 96–101]. This is at odds with current research in general salt spray and atmosphere conditions where calcium is seen as detrimental at conditions above its solid solution point, highlighting that *in vivo* alloys need to be designed specifically for the purpose.

Additions of calcium in current commercial alloys have shown decreases in strength but increases in corrosion resistance[96, 97, 100]. AZ91 with 1 wt% Ca gave significant corrosion rate improvements over AZ91, demonstrating surface film 5 time more resistant to SBF[96]. 1% Ca resulted in AZ91 shown on polarisation curves becoming 140 mv more noble with a lower iCorr. The breakdown potential was similar to that of the standard alloy, but the surface film was shown to be more resistive to general corrosion and pitting. Kannan made the conclusion that calcium additions make the surface film more uniform[96]. This also resulted in less susceptibility to stress corrosion cracking. Calcium added to magnesium-silicon alloys has also shown lower corrosion rate [101]. 0.2 wt% and 0.4 wt%Ca were added to Mg-0.6 wt%Si. The latter increased corrosion resistance considerably compared to 0.2 wt%, with a decrease in corrosion rate from 0.39 to 0.15  $\text{mg}^{-1}\text{cm}^{-2}\text{day}^{-1}$ . It was also shown again that additions of calcium lower mechanical properties.

In binary alloy form, calcium lowers corrosion resistance as the formation of  $\text{Mg}_2\text{Ca}$  precipitates cause micro galvanic corrosion. Calcium forms a  $\text{Mg}_2\text{Ca}$  phase when above solid solubility [97]. When added with silicon these form  $\text{CaMgSi}$  phase which has been shown to be a dot shaped polygonal precipitate which has lower surface area than the  $\text{Mg}_2\text{Ca}$  phase which in turn lowers the galvanic coupling effect [101].

The addition of zinc is popular in non-biomedical alloys due to its positive effects on strength, grain size and reduction of cathodic contaminants[62]. For biomedical alloys additions of zinc have been shown to lower corrosion rates in SBF with low amounts of yttrium [102], manganese [103] and silicon [101]. Zinc refines second phases particles that it belongs to and also has the effect of making the matrix more noble, these factors both act to lower galvanic coupling [102]. Optimum additions of zinc appear to be in the 1-2 wt% range. Zhang used 2 wt% Zn with various yttrium amounts to lower corrosion and increase strength [100–102], Yin showed that 1-2% would increase corrosion resistance, but above this would be detrimental [103]. Yin speculated that keeping to these amounts helped form a more stable passive surface film which has been previously demonstrated Zhang by Zn enrichment of the film. Above the 2 wt% point and cathodic second phases become a problem[102].

Yttrium addition appears to decrease the nobility of the alloys [102, 104], but its affect

on surface film are more protective. Yttrium has been shown to lower pitting potential and polarisation curves comparing Mg-Zn-Mn-Y alloys to non Y alloys show shoulder points on the anodic slope indicating a stable passive film [104]. Zhang demonstrated that when added to zinc containing alloys, yttrium affects are best at low Zn/Y ratios to produce the zinc rich, Y poor 'I' Phase.

Other than these three elements, only lithium and aluminium have been used as alloying additives in great amounts. Aluminium is most likely going to be phased out of biomedical magnesium development due to its long term risks with Alzheimer's [93]. But Lithium in the form on LAE442 has constantly performed well in *in vivo* and *in vitro* studies [11, 44, 93].

## 2.5 Surface Treatments

The need for lower corrosion rates to make magnesium a viable option as an implant material has lead to the development of new alloy designs as discussed previously. But an immediate alteration to current alloys is to use a surface modification or coating. These can act as barriers to the body's electrolytes and slow the corrosion process giving increased corrosion resistance. Surface treatments can also have a dual affect, by not only lowering corrosion rate, but also changing the bodies response to the implant material by making it more biocompatible for the tissue the implant is designated for[105].

The use of surface treatments has been around for many years in the magnesium industry as lowering corrosion rate has always been one of the industry's main tasks to make it more appealing to the engineering market. There are many patented and industry standard coatings and surface modifications on the market. The most widely used are electrochemical plating, conversion coating, hydride coating, anodizing, gas-phase deposition (such as chemical vapour and physical vapour) and polymer coatings[106].

Electrochemical plating is one of the most cost effective and simple techniques for introducing a metallic coating. This is where metal salt in solution is reduced to its metallic form, and via an electric current, applied on the surface of the magnesium substrate. Plating of magnesium has been shown to be useful in a number of applications. Cu-Ni-Cr plating has been shown to have good corrosion resistance in interior and mild exterior environments [106]. However, a plating method has not been developed that can produce coatings to withstand marine or salt splash conditions, thereby limiting the use of magnesium in the automotive, aerospace and marine industries and would be of no use *in vivo*[106].

The use of surface cleaning/pickling to change the corrosion dynamics of the bulk material are the main stay of the magnesium and metal industry[107]. For magnesium it is common to use acid dips to remove the outer layer of the casting or extrusion, thus lowering the number of potential cathodic sites (generally iron) picked up from the manufacturing process. The use of a hydrofluoric acid dip, not only removes the outer surface,

but creates a magnesium fluoride surface to the material which is much less reactive than MgO or  $\text{Mg}(\text{OH})_2$  [107].

Conversion coatings are a level above the simple acid etches used to pre-treat the magnesium. These are produced by chemical or electrochemical treatment of the magnesium surface to produce a superficial layer of substrate metal oxides, generally used are chromates, phosphates. These coatings provide corrosion protection and good paint-base properties to the metal [106][107]. Conversion coatings protect the magnesium substrate from corrosion by acting as an insulating barrier of low solubility oxides between the metal surface and the environment [106], thus slowing the rate of magnesium oxide/hydroxide breakdown. There are a number of different types of conversion coatings including chromate [107], phosphate/permanganate and fluorozirconate treatments [106]. The disadvantages of these conversion coatings *in vivo* applications is the toxicity, with only phosphate being applicable,

Hydride modifications, are the process of producing magnesium hydride coating on the bulk magnesium alloy by an electrochemical reaction. The magnesium substrate acts as the cathode in an alkaline solution prepared by adding alkali metal hydroxide, ammonium salts or similar alkaline materials. The hydride coating thus produced has been found to decrease the corrosion rate of AZ91D alloy by a third which is comparable to the dichromate conversion treatment, the treatment is has been developed to replace [106]. These are a real possibility for *in vivo* applications.

Anodizing is an electrolytic process for producing a thick, stable oxide film on metals and alloys. These films may be used to improve paint adhesion to the metal, as a key for dyeing or as a passivation treatment. The films have a thin barrier layer at the metal-coating interface followed by a layer that has a cellular structure. These treatments are poor for corrosion purposes alone, but combine well with paints and other coatings, therefore these are not a viable option for the body.

Microarc oxidation (MAO) is a surface treatment originating from the traditional anodizing but uses an electrolytic plasma. MAO allows production of multipurpose ceramic-like coatings with a wide complex of useful properties, namely, with high wear resistance, corrosion resistance, heat-resistance, dielectric and decorative characteristics. Its ability to coat a wide range of ceramics in a dense corrosion resistance has been this a popular technique for biological applications[108–110].

Cathodic electrocoating is a common industrial process generally used to prime steel in motor car bodies and other mass products. It is used in Al alloy in few cases but hardly in magnesium alloy as it easily dissolves in the cathodic electrocoating solution. Further, the  $\text{Mg}(\text{OH})_2$  corrosion product accumulated at the interface can hamper the adherence strength[111]. It works by applying a negative electrical charge to the metal part that attracts the positively charged ceramic particles. Cathodic coatings have been show to have excellent corrosion resistance in steel and aluminium, but very little work has been carried out with magnesium[111].

Chemical vapour deposition (CVD) is a very promising technique on the condition that the process can be controlled to below the melting point of the magnesium alloy as generally the process requires temperatures around  $>600^{\circ}\text{C}$ [106]. CVD is the deposition of refractory materials onto the magnesium substrate, achieving near theoretical density, controlled grain size, orientation, good adhesion and all from temperatures well below the melting points of the oxide coatings. CVD is also not restricted to line of sight like most physical vapour deposition processes and as there is a high deposition, thick coatings can be produced[106].

Physical vapour deposition (PVD) is used to modify the surface by either changing the surface microstructure or adding another element to the surface in a new alloyed microstructure [106]. Success has been found by using depositing elements such as Ce, Mn, Ti, Zr and various others to create binary Mg-X alloys on the surface which are highly corrosion resistant[106]. Both CVD and PVD are real possibilities for the protection of magnesium implants, potential ceramic coatings, such as hydroxyapatite could be used to lower the corrosion rate of magnesium alloys while stimulating a osteoblast response[105].

Polymer coatings in the industrial context are primarily paints and powder coating. Generally using polymers not suitable for *in vivo* applications. Sol-gel coatings are applicable though, as are self assembled monolayers and organo-silanes. Sol-gels involves the hydrolysis and condensation polymerisation of metal alkoxides. The outcome is a polymeric network of inorganic-organic composite materials which are adherent and uniform[106]. The process has been shown to produce corrosion- protective coatings on magnesium alloys in the industrial context. Self assembled monolayers (SAMs) and organo-silanes form a nano-scale polymer barrier on the surface which can be hydrophobic in order to discourage the diffusion of electrolytes to the material surface and therefore lowering corrosion rate[112].

### 2.5.1 Biological surface treatments

Surface modifications needed for the biological applications differ from the automotive and aerospace coatings in that they first have to be biocompatible and non toxic to the body. They also have to be degradable themselves, as a permanent coating will serve the purpose of a magnesium implant void. Finally surface treatments have to be tailored to the vastly more complex chemistry of the body and the complex corrosion processes that occur rather than industrially where protection is sought from marine and salt spray environments[105].

Various *in vitro* and *in vivo* work has been carried out analysing a range of surface treatments for magnesium alloys. These are based upon the industrial surface treatments previously mentioned. They can be categorised into three groups of surface modification; modifications to the bulk material, which use a pre-treatment, or surface state to change the corrosion properties of the magnesium alloy without adding a layer or coating to the

implants surface. Coatings that add a new layer of new material to the surface, these can be split into polymer and ceramic coatings and serve to protect the magnesium simply by placing a barrier between the body and the alloy.

### Surface modifications

Surface modifications could be classed as the simplest of the surface treatments used, but they have been used to great affect with a wide range of ideas to boost corrosion performance. Modifications ranging from manufacturing surface finishes and simple pre-corrosion steps through to ion implantation. All treatments have had affects both on corrosion and biocompatibility.

Xu [113], Lorenz [114] and Gu [115] had success lowering corrosion rate using pre-corrosion steps before corrosion tests. The idea behind the treatments is simple, magnesium alloys form a phosphates/carbonate corrosion layer as protection *in vivo*, therefore create this first before the material is used. Gu used baths of sodium phosphate, sodium carbonate and sodium bicarbonate followed by heating to near solidus temperatures. Gu found thick stable layers were formed with  $\text{Na}_2\text{HPO}_4$  and  $\text{NaHCO}_3$  composed of  $\text{MgNaPO}_3$  (13microns) and  $\text{MgCO}_3/\text{CaCO}_3$  ( $26\mu\text{m}$ ) respectively[115]. With  $\text{Na}_2\text{HPO}_4$  hydrogen evolution dropped from  $0.108 \text{ mlcm}^{-2}\text{h}^{-1}$  to  $0.029 \text{ mlcm}^{-2}\text{h}^{-1}$  and the impedance plots gave corrosion rates dropping from 13.27 to  $2.08 \text{ mmyr}^{-1}$ . Using  $\text{NaHCO}_3$  can achieve similar results with hydrogen evolutions and corrosion rates from impedance at  $0.020 \text{ mlcm}^{-2}\text{h}^{-1}$  and  $2.79 \text{ mmyr}^{-1}$ . Hydrogen evolution trails were conducted for 15 day, therefore demonstrating the treatment has long term benefits[115]. Lorenz used sodium hydroxide and SBF baths with no following treatment to create the protective layer[114]. It was found that although the SBF treatment gave immediate protection, its was broken down and remodelled in the new environment. This gave pH spikes higher than that of the polished control[114]. Xu also used a simple bath, this time made from various phosphate compounds to give corrosion protection[113]. A surface layer of  $\text{CaHPO}_3$  was shown to have formed on the surface which converted to hydroxyapatite in SBF over time. Corrosion resistance improved by an order of magnitude ( $469.5 \Omega\text{cm}^{-2}$  to  $4976 \Omega\text{cm}^{-2}$ )[113].

Denkena used deep rolling manufacturing process to create residual stress in the surface layers of a Mg-Ca alloy. The surfaces were tested in NaCl, even though the publication was aimed at biomedical applications. But there was great reduction in corrosion rate ( $\times 100$ ) measured by galvanometric and actual mass loss over 20 days[116]. These impressive results are tampered by the limitation of the forming process, as deep rolling is slow and difficult to achieve on complex geometries. Van der Hoh looked at sand blasted, smooth and threaded surfaces and reported lower corrosion with the sand blasted surfaces[99].

More complex procedures have been reported with use of plasma immersion ion implantation and deposition to modify the surface into new alloy states. This is a conversion

coating technique proved in the industrial context. Liu used this process to create new more noble metal oxides on the surface of bulk AZ91[84]. Aluminium, zirconium and titanium were implanted and when corroded with the exception of titanium, new metal oxides,  $\text{Al}_2\text{O}_3$  and  $\text{ZrO}_2$  were formed on the surface rather than the native  $\text{Mg}(\text{OH})_2$ . These much more stable oxides increased the polarisation resistance from 92 k $\Omega$  to 1210(Al) and 755(Zr)[84].

### **Ceramic based coatings**

Ceramic-based coatings generally produced with CVD or PVD processes have been by far the most popular of coating routes. Coating magnesium with a biodegradable ceramic can not only act as a barrier layer, but also if the chemistry is correct promote biocompatibility and bone response due to bone's inorganic nature. The use of calcium phosphate based coatings has been used for many years to promote bone integration and implant-bone adhesion on permanent metal implants. There have been a wide range of processes used to fix calcium phosphates to these metal surfaces, including dip coating, sputter coating, thermal spraying, hot isostatic pressing, ion beam sputtering, magnetron sputtering, pulse laser deposition and electrophoretic deposition [117]. Considering thermal spraying, in particular, plasma spraying regarded as the industry standard[118]. Of these coatings, dip coating, hot isostatic pressing and electrophoretic deposition all require high temperature sintering which would be well above the melting point of any magnesium alloys. Plasma sprayed coatings are not popular for magnesium alloys due to the high temperature post processing and poor adhesion. Therefore the majority of publications reporting ceramic based coatings on magnesium have used chemical and physical vapour deposition techniques and chemical conversions.

Using the physical vapour deposition technique, cathodic arc, aluminium [119] and zirconium[120] oxides have been fixed to magnesium surfaces to serve as protection. It was reported that the metal oxides peeled when directly coated on the magnesium substrate. Due to magnesium high galvanic reactivity, Xin used an intermediate layer of aluminium or zirconium before coating with their respective oxides, giving far greater adhesion[119][120]. The layer was shown to be dense and increase the material's potential from -1836 mV to -1540 mV ( $\text{Zr} + \text{ZrO}_3$ )[120]. The layers gave vastly increasing polarisation resistance at 30 minutes, 200 times greater than the uncoated sample. But this decreased to only around double after 18 hours, meaning cathodic arc deposition can only provide short term corrosion protection when used in this way.

Majamdar used thermal oxidation, a form of chemical conversion, to modify AZ91's surface to  $\text{MgO}$  and  $\text{MgO}_2$ . The best results were obtained from experiments conducted in air at 200 °C for 25 hours[121]. Majamdar reported the new surface to be extremely adherent, this is expected as by nature, this is a conversion not a coating. Corrosion work was carried out in SBF and gave large increases in potential, -1.485 mV increasing to -0.412 mV. Galvanometric calculated mass out decreased by 3.088  $\text{mm}^2\text{yr}^{-1}$  to 0.0141



$\text{mmyr}^{-1}$ . These improvements however were only reported at one time point, which was not mentioned, but it will be assumed this was close to  $t=0$  as degradation of the conversation layer was not discussed. Being a layer derived from MgO and MgO<sub>2</sub>, of which are broken down by chlorides, it is probable the long term protection obtained using this process is limited.

Cathodic electrodeposition has also been reported by authors Wen[122] and Song[123]. Both publications only demonstrate short term corrosion protection as would be expected from this process as no interface is possible. Wen deposited hydroxyapatite on AZ31 which was treated in alkaline solutions to form a more stable and less porous coating. Short term corrosion improvements were shown by potential increases from -1.6 mV to -1.42 mV, but with decreases in current density of 3 orders of magnitude [122]. Song deposited dicalcium phosphate dihydrate (DCPD) and B-tricalcium phosphate which was converted to hydroxyapatite after treatment in NaOH. Current density decreased by one order, whereas corrosion potential actually had a small decrease in nobility[123]. Cathodic deposition techniques appear to be limited for biomedical use.

Using micro arc oxidation (MAO), which is similar to the anodising processes used in industry, but with higher potentials creating a plasma which helps form a more stable oxide layer. Shi used this process to create a MgO and MgF<sub>2</sub> surface[108]. This surface is generally porous, to overcome this Shi used a second coating of TiO<sub>2</sub> via a sol-gel process that was shown to seal the pores. The resulting corrosion resistance was 30 times greater. Impressively, the impedance plots show an inductive loop, associated with stable barrier layers was present over 15 days corrosion[108]. Zhongping used MAO in NaOH and Na<sub>2</sub>SiO<sub>3</sub> systems, both with sodium hexametaphosphate and calcium hypophosphite to create oxide layers of 5  $\mu\text{m}$  and 10  $\mu\text{m}$  respectively containing Ca, P, Mg and Al (substrate AZ91)[109]. The best reduction in corrosion rate came with NaOH which decreased corrosion rate by 100 times. But the main purpose of this piece of work was to create an reaction layer with a Ca/P ratio which could be modified by manufacturing techniques close to that of bone, this was successful demonstrated[109]. Wang used a small amount of TiO<sub>2</sub> added to as-deposited coating of MgO and Mg<sub>2</sub>SiO<sub>4</sub> by the addition of titania sol gel[110]. The coatings ranged from thicknesses of 22 to 18  $\mu\text{m}$ . Electrochemical tests showed that the electrochemical potential ( $E_{\text{Corr}}$ ) of Mg substrate positively shifted about 300-500 mV and the electrochemical current ( $I_{\text{Corr}}$ ) lowers more than 100 times after microarc oxidation. However, the TiO<sub>2</sub> modified coatings formed in electrolyte containing 5 and 10 vol% titania sol indicate an increasingly worse corrosion resistance compared with that of the standard MAO coating[110].

Radio frequency (RF) magnetron sputtering is becoming a popular technique for coating titanium alloys with hydroxyapatite (HA). It is an attractive alternative to the usual coating methods as Shinn-Jyh Ding reported; it forms a coating with excellent adhesion, thickness uniformity, and has the ability to coat implants with difficult surface geometries, a limitation of the various line of sight methods also becoming popular in academia such

as ion beam assisted deposition (IBAD)[124]

Coating bond strength play a large part in the lifetime and performance of HA coatings on implants [124]. RF Magnetron sputtering has been shown to have far better bond strength than that of plasma sprays which are industry standard, and is also close in strength to IBAD [124, 125].

RF magnetron sputtering has been used to coat titanium with HA in various studies since the mid 90s[124], but it has never been used for this purpose on magnesium alloys. The process has been used to coat magnesium with titanium nitride [126], chromium [127] nickel [128] and aluminium [129]. Using TiN, Zeng reported corrosion protection in 3.5% NaCl, with the coated samples around +200 mV compared to the blank[126].

Work by Xin, is the only reported use of RF magnetron sputter-coating for biomedical use. A hydrogenated amorphous silicon layer on AZ91[130]. The coating is showed to be 1 mircon thick with no cracks or pores. There is evidence of a strong bond with an area of inter-diffusion between the magnesium and the silicon. Xin concludes this would be in the form of  $Mg_2Si$  which would strengthen the bond of the silicon coating. Corrosion is carried out in SBF and shows a potential shift of +329 mV. Impedance data reviews inductance loops for the coated sample which Rf values 8 times that of the uncoated sample, and these loops are stable until 6 hours when they become slightly smaller with Rf values around half their peak. The layer was shown to be stable there after for 24 hours[130].

### **Polymer based coatings**

There are a large range of polymer coatings used on titanium and other permanent metal implants, but due to the metal's noble corrosion properties these are generally for biocompatibility rather than corrosion protection. Processes included plasma spraying [131], through to attaching polymers via various reactions, such as the use of silanised titania, cysteine residue[132] photochemistry and self-assembled monolayers.([118])

For use with biomedical magnesium, only two techniques have been looked into. Plasma spraying of biodegradable polymers and silane attachment. Many more have been looked into for industry applications for corrosion protection. Wang published a comprehensive study about the coating of polycaprolactone and dichloromethane onto AZ91 using plasma spraying. Corrosion data was reported up to 60 days in regard of electrochemistry, mass loss and structural integrity[133]. Corrosion potential had a huge improvement with  $E_{Corr}$  increasing +1444 mV at the time of coating. Mg ion concentration was used to follow the mass loss over time, the uncoated sample gained 1360 ppm Mg in 60 days, the coated only 238 ppm Mg in comparison. pH gains associated with magnesium corrosion were low at 0.2 compared to 1 for uncoated. The low long term corrosion had a positive effect on the structural performance of the samples. The uncoated sample yielded (compression) at around 50% of it's  $t=0$  strength, whereas the coated 70%. after the 60 days. *In vivo* tests also revealed greater bone growth around the polymer coated samples.

This was attributed to higher magnesium concentrations than without the implant, but less than the mildly toxic levels seen with uncoated AZ91[133]. Plasma coating of biodegradable polymers looks to be a very attractive method of protecting orthopaedic magnesium implants.

The use of self-assembled monolayers has also been reported, using stearic acid bonded to pure magnesium pre-prepared by a stream treatment[134]. By placing the samples in 120 °C stream, magnesium hydroxide was created on the surface giving a bonding site for the stearic acid. This was reacted at 100 °C and 150 °C for 2 hours. The result was a corrosion resistance covalently bonded coating. 30 Day corrosion tests showed the coated sample to be up to 5 orders (Polarisation resistance,  $R_t = 0.03 \text{ k}\Omega\text{cm}^{-2}$  compared to  $700 \text{ k}\Omega\text{cm}^{-2}$ ) more corrosion resistance at  $t=0$ , dropping to 40 times ( $R_t = 2.5 \text{ k}\Omega\text{cm}^{-2}$  to  $107 \text{ k}\Omega\text{cm}^{-2}$ ) greater than the uncoated after 30 days. Breakdown was attributed to the local pH rise and corrosion products causing cracks and de-lamination of the coating[134].



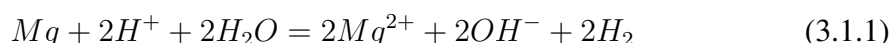
## *IN VITRO* TESTING OF MAGNESIUM ALLOYS

### 3.1 Introduction

The concept of magnesium as a biomaterial has been around for nearly 100 years [34], but to Magnesium Elektron and to modern medicine it was a very new avenue of research. When this investigation was conceived, the biomedical manufacturer Biotronik had requested WE43 material for their initial *in vivo* test and Di Mario had published in 2004 [41]. Other than this the author of this report had finished a small investigation on testing of magnesium alloys *in vitro*. In all this is a very new area of research, with no direction to be drawn from previous work as to how to proceed with developing magnesium as a resorbable biomaterial.

Magnesium Elektron with its new biomedical commercial partners would investigate new alloy and stent design by *in vivo* trials and corrosion testing in simulated biological salt solutions. However there was an obvious gap between these, which could only be filled by *in vitro* testing as in other areas of medical research.

At the start of this investigation no *in vitro* testing had been carried out on magnesium to this author's knowledge, therefore the initial object was to discover if such testing was feasible. If so, then what could be learned from using human cells on magnesium alloys? The two outcomes sought were the basic relationship between magnesium alloys and human bone cells (osteoblasts, as orthopaedics is a primary market for biomedical magnesium), and if this relationship changed depending on alloy composition so that *in vitro* testing could be used to further alloy design?



Magnesium alloys were expected to behave differently other to metals used in medical devices such as titanium and stainless steel due to having a degradation rate many orders higher and with the element being a fundamental component in biological activity[21]. As described in Section 2.3.1, magnesium corrodes in salt water solutions in the overall reaction 3.1.1

This shows that any biological tissue in the vicinity of corroding magnesium will be exposed to increases in pH and evolving hydrogen gas. These affects could potentially be exaggerated by the limited relative volumes of fluid tested *in vitro* compared to the body. It also shows that the  $Mg^{2+}$  will be in greater concentrations after corrosion. The divalent cation is a known osteo-conductor and has been shown to promote osteoblast response: Howlett [31] and Zreiqat [33][32] used magnesium to doped hydroxyapatite and alumina to demonstrate that the surface modification substantially affected the phenotype of osteoblast cells *in vivo* and *in vitro*. The work suggested that this was the result of higher integrin expression increasing cell attachment to the hydroxyapatite surface.

The high concentrations of corrosion products and their bioactivity gives two factors to consider for which a standard non-degradable metal or material do no exist: Therefore the first investigations were to see if these effects could be studied in the lab and if so, what the effects were.

## 3.2 Materials and methods

Compositions of the binary alloys used in the chapter are shown in table 3.1. Elektron WE43 and 674 were also supplied by Magnesium Elektron as commercial product and therefore within company specification, their compositions are also listed below or infomation. The material was made at Magnesium Elektron by melting pure magnesium ingot with the appropriate alloying elements. Once molten, the metal is stirred and a small casting was made for chemical analysis by Optical Emission Spectrometry (OES). If this falls within specifications the metal was ready to cast. Molten metal was then poured from the crucible into the mold. Once solidified and air cooled, the casting was machined into 75 mm diameter billets for extrusion.

The extrusion procedure required, pre heating of the billet, die and billet container to specified temperatures. The material was then extruded into 9 mm bar. These bars are then lathed into 9 mm by 3 mm discs for testing.

**Table 3.1:** Chemical composition of alloys given by wt%. Heavy Rare Earths (HRE) are given individually where appropriate or as a combined mix as specified in WE43's composition. Total impurities equates to the combined composition of Fe, Ni and Cu.

Alloy	Y	Nd	Zr	Gd	Dy	HRE	Total Impurities
WE43	3.7-4.3	2.2-2.5	0.4-1.0	n/a	n/a	0.4-1.9	0.004
675	6	-	0.35-0.4	6.5-7.5	-	n/a	0.006
Mg-8Y	8.00	0.00	0.01	0.09	0.00	n/a	0.005
Mg-3Y	3.73	0.01	0.01	0.00	0.00	n/a	0.004
Mg-6Dy	0.06	0.07	0.57	0.00	6.00	n/a	0.004

Titanium alloy (Ti-6Al-4V) and Stainless Steel (316L) samples were supplied by Goodfellows, (Cambridge, UK) in the form of 0.5mm thick rolled sheet. The sheets were

punched into 9mm diameter discs using a punch press. Glass discs (9mm diameter) were supplied by Chance Glass Ltd (Malvern Link, UK) All the metal discs were ground to a 4000 grit finish on both sides using a silicon carbide grinding wheel. To obtain a mirror finish, the discs were polished using a 10% solution of colloidal silica (OPS), rinsed with in tap water and methanol.

### **Cell Culture**

Primary human osteoblast cells established from a human femur were plated in tissue culture flasks. They were grown to confluence in minimum essential medium (D-MEM + GlutaMAX + Pyruvate, GIBCO-21885-025) supplemented with 10% fetal bovine serum (FBS), 0.85 mM ascorbic acid and 1% penicillin/streptomycin at 37 °C in the presence of 5% CO<sub>2</sub>/air. The medium was changed every second or third day.

At confluence, the medium was removed, cells were washed twice with 10 mL of phosphate-buffered saline (PBS) and subsequently released from the plastic tissue plate surface with trypsin-EDTA standard solution (GIBCO- 25200-072). The released osteoblasts were pelleted at 1500 rpm for 5 min and subsequently resuspended in D-MEM to a density of  $4 \times 10^5$  cells per cm<sup>3</sup>. Samples were placed in 12 well plates (growth area of 3.8 cm<sup>-2</sup> per well) and discs seeded with 3 mL of suspended cell culture medium. Sample were incubated at 37 °C, 5% CO<sub>2</sub>/air with the medium changed every day.

### **Alamar Blue assay**

The cell culture media was removed from each sample and the cells rinsed with PBS. Samples were then removed and placed in a 24 well plate, and 1 ml of fresh cell culture media was added. 200 µL of alamar blue solution (5 mg in 40 ml PBS) was added to each well and samples were incubated for 1.5 hours at 37 °C. 200 µL of the solution was transferred to a 96 well plate and fluorescence was determined using a Fluostar OPTIMA fluorescence plate reader from BMG Latch at a wavelength of 510 nm (excitation) and 590 nm (emission). Cell numbers were calculated by referring to a calibration curve created by seeding set numbers of cells in increments from  $1 \times 10^2$  to  $1 \times 10^7$  cells which were tested using the same procedure 4 hours after seeding.

### **DNA Concentration**

Proliferation values are obtained using the DNA assay which measures the amount of DNA present in any sample. Cell medium was removed from the samples and the cells rinsed in PBS. Five hundred µL of dH<sub>2</sub>O was added to each sample and then freeze-thawed three times at -80 °C. Fifty µL of the sample was aliquoted into a black flat bottom 96-well plate. One hundred µL Hoechst stain solution and 50 µL TNE buffer were then added. Fluorescence was measured using Fluostar OPTIMA fluorescence plate reader from BMG Latch at a wavelength of 355 nm (excitation) and 460 nm (emission).

### **Alkaline Phosphatase assay**

Cell medium was removed from the samples and the cells rinsed in PBS. Five hundred  $\mu\text{L}$  of  $\text{H}_2\text{O}$  was added to each sample and then freeze-thawed three times at  $-80^\circ\text{C}$ . Naphthol AS-MX and TRIS tablets obtained from sigma (SIGMA FASTTM Fast Red TR/Naphthol AS-MX Tablets Set, F4523) were added to 5 mL of distilled water and dissolved at  $37^\circ\text{C}$ . 200  $\mu\text{m}$  of the solution was added to 1 mL of the distilled water from the samples. This was then read every 30 seconds up to 30 minutes at 405 nm on a Ascent Plate reader. The gradient observed over time was calculated to give the alkaline phosphatase concentration.

### **Corrosion product measurements**

Samples were placed in 1 mL of cell culture medium. A pH probe was placed in the media and recorded using a data logger. Magnesium ion concentration was tested by inductively coupled plasma (ICP). Samples were prepared from 0.1 mL of the medium added to 9.9 mL of  $\text{dH}_2\text{O}$ . Standards for the ICP were from Sigma Aldrich (35635-2) and made to concentrations of 10, 20 and 30 ppm and used with pure water to create a standard curve. Magnesium concentration was then measured at 279.553, 280.270 and 285.213 nm absorption. The average of the three readings was taken.

### **Conditioned medium**

Osteoblasts were seeded in 24 well plates and incubated for 1 day at a density of  $4 \times 10^4$  cells  $\text{mL}^{-1}$ . The medium was aspirated and replaced with the 'conditioned' media. This was made by submerging a disc of magnesium alloy in 1 mL of cell culture media per timepoint for 1, 2, 4, 8, 18, 24 and 48 hours at  $37^\circ\text{C}$ , 5%  $\text{CO}_2/\text{air}$ . DNA, alamar blue and alkaline phosphatase assays were then used to determine proliferation and activity.

### **SEM fixation for osteoblast imaging**

In order to observe cell attachment behaviours on discs, chemical fixation of cells was carried out in each sample. After 1, 5 and 8 days of culture, the samples were rinsed twice with PBS and subsequently fixed in 2% glutaraldehyde for 1.5 hours. After which, the samples were rinsed with distilled water and then dehydrated with ascending concentrations of ethanol (twice with 50%, 70%, 90% and 100% ethanol for 5 min each). Finally, the samples were treated with hexamethyldisilazane and kept in a fume hood for air-drying. Dried samples were coated with gold using sputter coating.

### **Phalloidin and DAPI staining**

Cell suspensions were either seeded directly onto magnesium discs or around them on to the tissue culture plastic. The cells were then incubated for set time points. All samples



were thoroughly rinsed with PBS then fixed with a 4% formaldehyde solution over 30 minutes at 4 °C. The samples were then rinsed three times with PBS and permeabilised with 0.1% Triton x100 in PBS (10 minutes at 4 °C.). The samples were again rinsed with PBS and immersed in a 1% solution of bovine serum albumin (BSA) in PBS for 30 minutes at 4 °C. These were then incubated with FITC-conjugated Phalloidin (10 µg /ml) for 20 minutes at 4 °C. which was followed by thorough rinsing and staining with DAPI (10 µg/ml for 5 minutes at 4 °C.). The samples were then mounted onto glass slides with Prolong gold® anti-fade reagent and imaged with the fluorescent microscope.

This procedure was later modified to stop the use of Prolong Gold® anti fade reagent, as explained in section 3.3.1, this damaged the magnesium surface. The new protocol was the same as previous used until after the Phalloidin step, where the samples were stained and protected with a DAPI/Glycerol/Dimethyl sulfoxide (DMSO) mix instead of Prolong. A glass cover slip was then placed over the sample surfaces and the images taken within an hour of glycerol mix being used.

### **Live-Dead Staining**

LIVE-DEAD Viability/Cytotoxicity Kit (L-3224, Molecular Probes, Invitrogen) was used to quantify the viability of osteoblasts on magnesium samples as compared to a glass control. The kit consists of two components: Calcein AM is a fluorogenic esterase substrate that is hydrolyzed to a green-fluorescent product (calcein); thus, green fluorescence is an indicator of cells that have esterase activity as well as an intact membrane to retain the esterase products. Ethidium homodimer-1 (EthD-1) is a high-affinity, red-fluorescent nucleic acid stain that is only able to pass through the compromised membranes of dead cells. Cells were seeded directly into the magnesium surface. An aqueous solution of 2 µM calcein AM and 4 µM EthD-1 in 1.5 mL PBS was used to stain sample surface, by pipetting the solution dropwise onto the magnesium surface. After 5 minutes, the magnesium disc was transferred to a microscope slide and imaged using a fluorescence microscope. Ten to fifteen images were taken of each sample.

### **Hydrogen Evolution**

500 ml of SBF was placed in a beaker with an upturned 100ml measuring cylinder. Air was pumped out of the cylinder so that no air was left present (figure 3.1). Mg discs were coated with Lacomit on the bottom surface. This was then placed under the funnel and the stop watch started. The cylinder was shaken violently to free all small bubbles from the sides pre-measurement.

## **3.3 Results and Discussion**

Initially cell culture trials were carried out with a cell on surface approach by seeding directly onto the magnesium discs in a suspension of cell culture medium. This would

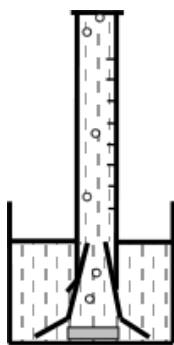


**Figure 3.1:** Experimental setup for hydrogen evolution tests.

give the greatest magnesium-cell interaction and therefore any effects arising from the magnesium would be seen. The alloys used for this study were the two best performing in Magnesium Elektron's product range with regard to strength and corrosion resistance; Elektron 675 and Elektron WE43. Along with these are yttrium and dysprosium binary alloys. These were added to see potential differences in cell behaviour because of alloying. Yttrium has been shown to promote osteoblast activity on Y-doped hydroxyapatite [135].

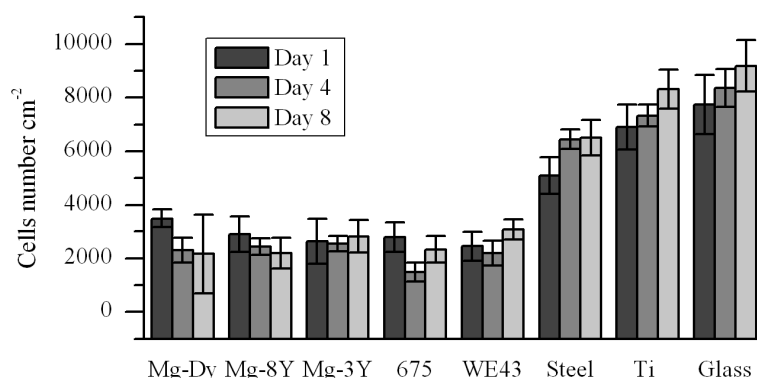


**Figure 3.2:** Cell numbers against time after seeding at  $4 \times 10^4$  cells  $\text{ml}^{-1}$  on various biomaterials and 5 magnesium alloys.  $n = 6$ , error = SD

Cell numbers were measured using DNA quantification (figure 3.21) over 8 days. After the first day around 50% of the cells were measured compared to glass. No losses on the same scale were seen between day 1, 4 and 8 on average across all the magnesium alloys, although on Mg-8Y, 675 and Mg-Dy alloys a further cell loss was shown between day 1 and 4. Differences between alloys in terms of cell loss are negligible, but WE43 and 675 demonstrated cell proliferation after day 1. The cell losses between  $t=0$  and  $t=24$  hours were also seen in optical images taken of the surrounding cells (figure 3.3). Alongside titanium the osteoblasts appear well proliferated, in a confluent cell sheet. Around the WE43 sample, the cells are in clusters, round and poorly spread.

SEM images (figure 3.5) of the seeded cells on the magnesium showed the surface the cells were exposed to in the initial day of seeding. The reaction layer formed in the

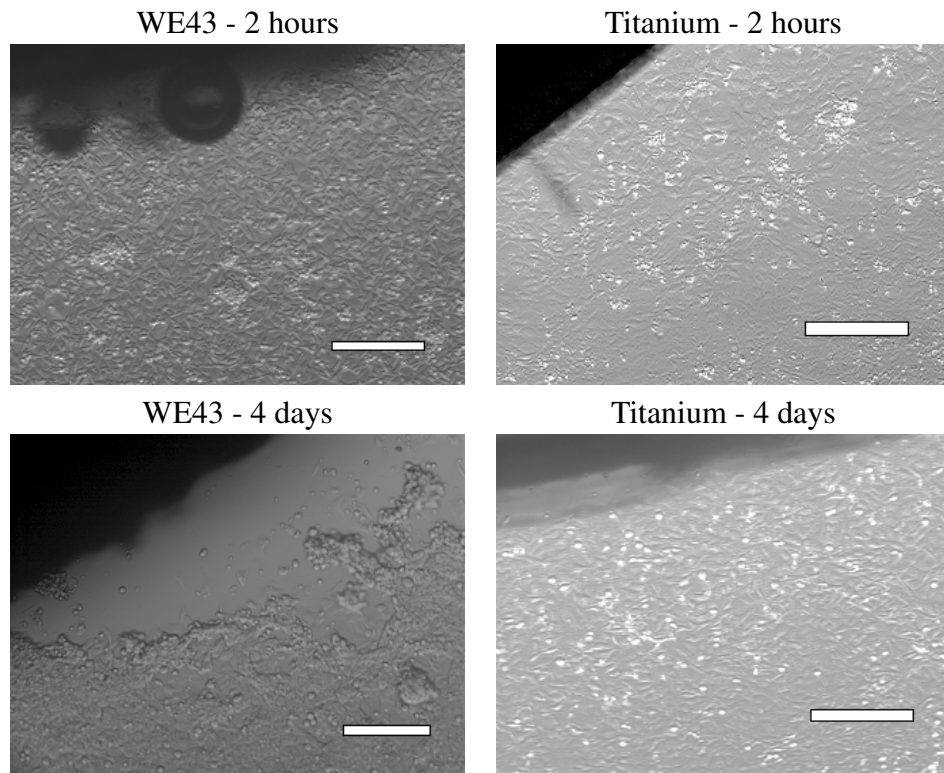


**Figure 3.3:** Optical images of osteoblast on tissue culture plastic alongside titanium (right) and WE43 (left). Scale bar = 200  $\mu\text{m}$

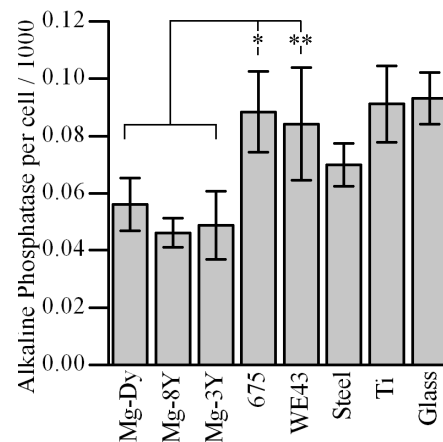


**Figure 3.4:** Alkaline phosphatase production per cell on five magnesium alloys and three controls at day 8. Both commercial alloys show better performance than the binary alloys and are comparable with glass and titanium. \* (675) and \*\* (WE43) indicates a statistical difference by single factor anova between the two commercial alloys and all three of the binaries (\*  $p < 0.05$ ,  $n = 4$  and \*\*  $p < 0.05$ ,  $n = 4$ )

corrosion of the magnesium alloys engulfed some cells so that only the top of these can be seen. This is prevalent over much of the surface, although there are clusters of cells that appear to be able to rise above the reaction layer and grow on the surface. Where this occurs the cells are well spread.

The alkaline phosphatase activity was far lower on the magnesium samples than controls, but using a per cell basis gave comparable results to the glass control (675 and WE43). Alkaline phosphatase activity from osteoblasts is reported in the literature to peak at around day 15 [25], but by day 8 should be present in good quantities to test. The

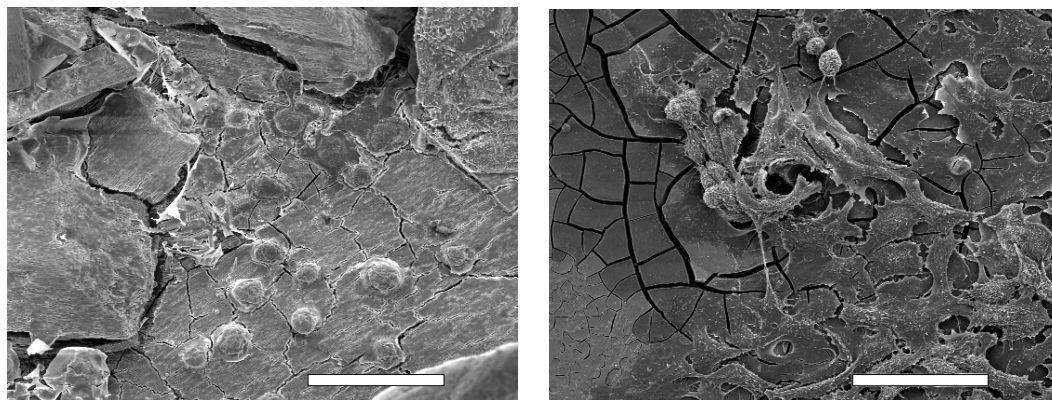


**Figure 3.5:** SEM images of osteoblasts cultured on WE43 after 24 hours. Osteoblasts are encased in the rapidly developed reaction layer, left. Osteoblasts in clusters grow on top of the layer and spread well, right. Scale bar = 50  $\mu\text{m}$ .

results show that in commercial alloy form, magnesium does not enhance (as predicted by *in vivo* work [28][52] [46] nor limit its production, however this does appear the case in the binary alloys. The difference in alkaline phosphatase production between the commercial alloys and the binaries is unknown. The corrosion rates listed in table 3.2 show that 675 corrodes similarly to the binaries. In terms of chemistry there is no trend regarding performance and any particular element concentrations, both commercial alloys include high zirconium (>0.3 wt%), but Mg-6Dy also has zirconium present (0.57 wt%) meaning zirconium and rare earth concentrations in these alloys show no relationship with alkaline phosphatase concentration.

The relationship between magnesium seeding and cell death was then investigated in greater detail. Using the Live/Dead assay, images of cells seeded on the surface were taken at various time points over a week. A true zero timepoint was made by seeding on glass and counting these cells after 2 hours to enable attachment but not proliferation. Five images were taken across four magnesium discs at each time point. The average live cells counts across all 20 images is plotted in figure 3.6. Figure 3.7 shows a selection of Live/Dead images taken on the magnesium samples (2 hours = glass). The original seeding is shown on the glass so that the corrosion effects of magnesium are not a factor, but there is still high cell death seen on the glass surface. This is the result of genuine losses from the stress of the cell seeding process. The zero value however is taken from the number of green cells visible at the point to image capture. The samples were seeded with a high density of  $10 \times 10^4$  cells  $\text{ml}^{-1}$  and this resulted in a coverage density of  $10560$  cells  $\text{cm}^{-2}$ . The conditions the cells were exposed to on the magnesium discs meant after 4 hours this dropped to  $2480$  cells  $\text{cm}^{-2}$  and this difference in cell density is clearly seen in the Live/Dead image. This cell loss could be due to cell death or because cells did not attach. After the initial cell loss, all the following time points showed greater cell densities than previous. The 8 day DNA assay results shown in figure 3.21 do not agree with this, as these are stable from day 1 to 8. This could be the result of the lower seeding densities used for the DNA assay ( $4 \times 10^4$  cells  $\text{ml}^{-1}$  compared to  $10 \times 10^4$  cells  $\text{ml}^{-1}$ ) which would

result in a slower recovery. What is more likely however is the DNA tests' sensitivity to the magnesium corrosion discussed later in the chapter. The Live/Dead test shows with visual certainty, that magnesium causes high death rates to seeded cells on a bare, uncorroded surface. The surface environment must change in the the first hours of seeding (and thus corrosion) to accomodate the cells, after which they recover and proliferate well. The recovery appears to take place from surviving clusters of cells proliferating laterally. The surface at 24 hours is sparingly dotted with areas of cells but with large areas devoid of osteoblasts. This is reflected in figure 3.6 with the large spread of data caused due to high differences, between images. With time these clusters spread out and the surface becomes evenly populated.

As well as highlighting the toxic nature of new corroding magnesium surfaces, the initial trials also highlighted that this *in vitro* technique does not distinguish alloy to alloy differences with regard to alloying additions or corrosion rates. The corrosion rates of these alloys are listed in table 3.2. The alloy 675 corrodes at around three quarters the rate of WE43, and are both alloyed with yttrium and rare earths. Both alloys have insignificant differences in cell loss, the cell numbers seen in subsequent days (figure 3.21) and also alkaline phosphatase production. Regarding alloying differences, yttrium, an element shown to alter osteoblast activity [135] was effectively tested at 0 (Mg-Dy), 3 and 8 wt%. No trend was seen between the alloys in osteoblast activity. It can be determined that cell on surface studies in this format are limited in their information regarding alloying.

**Table 3.2:** Corrosion rate in SBF of five magnesium alloys over 7 days. 675 corrodes at 75% the rate of WE43

Alloy	Corrosion rate /ml H <sub>2</sub>
Mg-3Y	22.37±2.17
Mg-8Y	26.10±3.50
Mg-6Dy	25.92±3.66
675	29.01±4.16
WE43	39.16±5.21

To determine why over 50% of cells died in the first hours after seeding, the environment they were exposed to was studied. The expected result of magnesium corrosion in the cell culture media is a rise in Mg<sup>2+</sup> ions and pH. Figure 3.9 shows the change in pH of WE43 with time in media. Although there are slight discrepancies with corrosion rate between alloys, they all have similar pH curves. This is most likely due to the buffering capacity of the medium. The pH of the media is at 7.4, but this rises sharply in the first hour, reaching 8.3 at after 60 minutes. The pH rises with decreasing rate until it starts to level at around 9.1.

The amount of magnesium leached into the cell culture medium was measured by ICP (figure 3.8). This was seen to follow the same trend with pH with a sharp spike in the first hours, but as this is not rate limited by buffer as with pH, Mg keeps leaching into

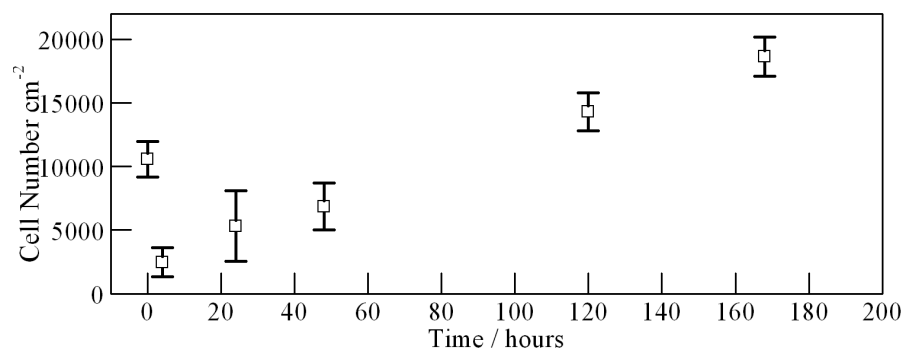


**Figure 3.6:** Average cell number counted from Live/Dead images over 7 days. Osteoblasts were seeded at  $10 \times 10^4$  cells  $\text{ml}^{-1}$  on WE43 and glass ( $t=2$ ).  $n = 20$ , error = SD

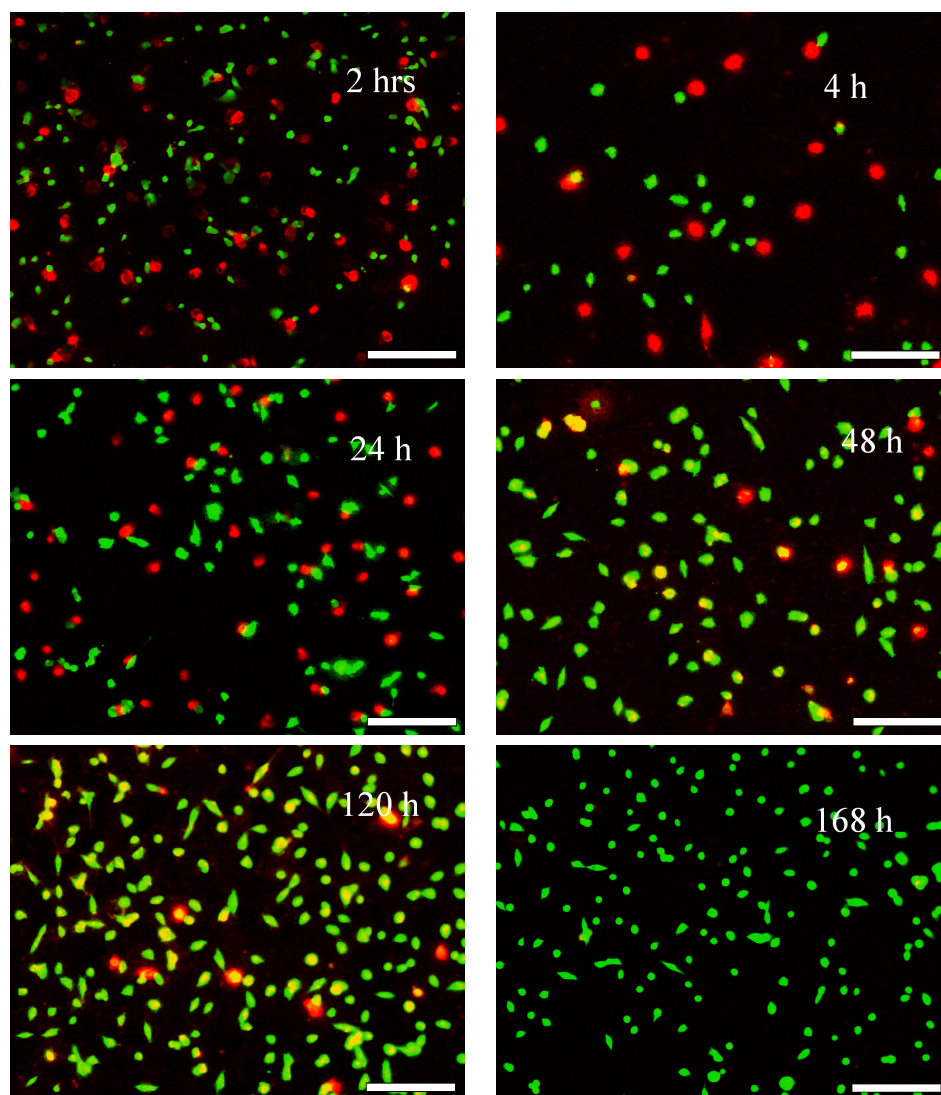


**Figure 3.7:** Fluorescence images of osteoblasts seeded on WE43 at various timepoints stained with Live/Dead reagent.  $t=2$  image is osteoblasts on glass to give true seeding density without material related losses. There is a large loss in cell number within the first 4 hours, which is recovery and the cells repopulate. Scale bar =  $200 \mu\text{m}$

the media at a steady rate after the initial spike. As with the pH curves, alloy to alloy differences could not be distinguished from the ICP measurements. Readings at 0 hours of 20.1 mg/L are similar to the stated concentration of Mg in the medium (21.2 mg/L).

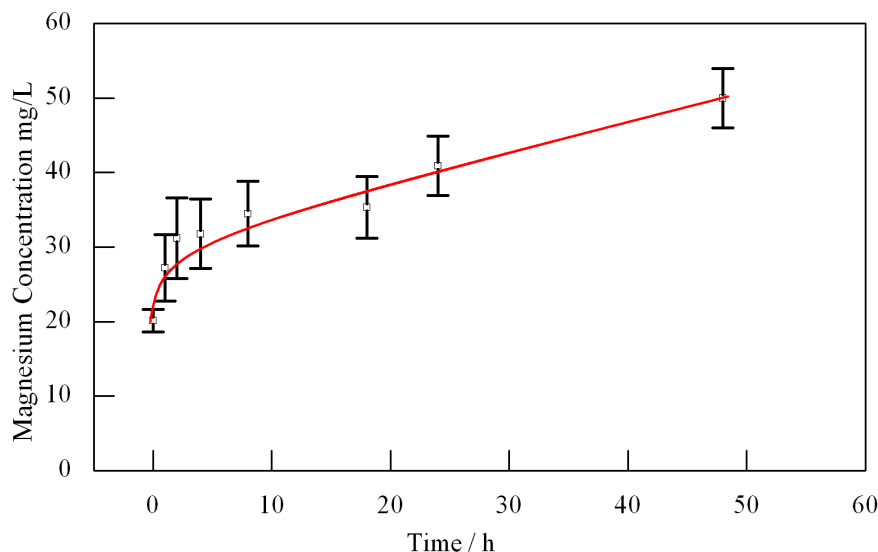


**Figure 3.8:** Average magnesium concentration from all alloys in cell culture media with corrosion time measured by ICP. Concentration rises steeply within the first 4 hours before steadying.  $n = 16$ , error = SD

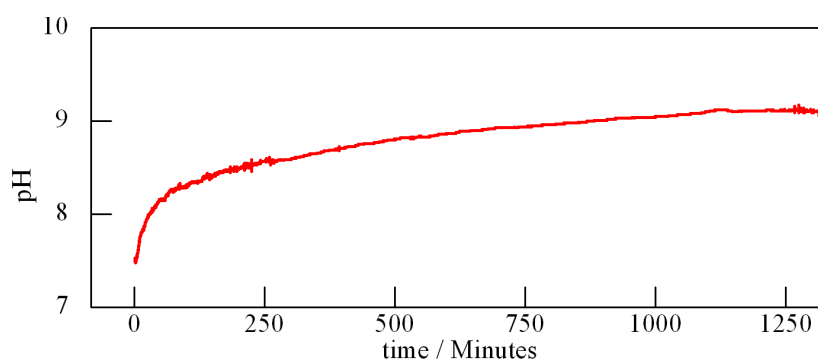


**Figure 3.9:** pH against time for WE43 in cell culture media.

The cell death seen in figures 3.6 and 3.21 could be the result of extremes at the surface, which are buffered or lower in concentration with distance from the magnesium discs. It was thought that if the cells were not exposed to the magnesium directly, but the products of its degradation, the severity of magnesium's alloys effect on cell numbers could be more accurately studied. Also, with less extreme conditions for the osteoblasts, and potentially less cell death, alloy to alloy distinctions might be possible. Thus conditioned medium trials were tested.

The indirect cell culture trial followed the procedure set out in section 3.2. After the Osteoblasts were cultured for 48 hours in the conditioned medium, DNA, alkaline phosphatase and alamar blue were measured to determine cell numbers, mineralisation capacity and comparative metabolism. Cell numbers calculated from DNA are shown against increasing magnesium corrosion in figure 3.10. Cell number declines faster at lower corrosion levels and then slower from 8 hours onwards. Cell loss in media with 48

hours corrosion was 42%. This is close to the 50% seen using the direct surface seeding from the DNA assay, but lower than 76.7% loss visible on the Live-Dead imaging. It is however still high, and therefore the cell death must not be result of extremities at the surface but the corrosion products released. But the 76.7% cell death on the surface only took a matter of hours due to the extreme conditions there. The indirect tests show that if corrosion is great enough, the products will result in similar cell death at distance, but within the body this is likely never to occur due to larger volumes and flow, therefore only a attribute of *in vitro* testing.

The fast decline in cell number at lower corrosion times follows the trend set by the pH and Mg concentrations curves generated. These suggest the largest change in corrosion product concentration would be in the 1-4 hour range. Therefore the high changes in cell loss coincides with the higher increases in pH and corrosion products. It is a fair assumption that magnesium corrosion is having a directly proportional effect on cell death.

The alamar blue assay data (figure 3.12) shows that cell metabolism is only slightly lowered across the corrosion gradient. Cell metabolism could be affected by both the high corrosion products and the magnesium ions, therefore it appears the high concentration of corrosion products is causing cells to lower their activity as magnesium ions should cause as increase [28][31][33].

Overall, across the alloys tested, the conditioned medium trials have shown that even away from the surface, corrosion products can build up and harm cells. The negative influence of corrosion products competes with any potential positive influence on cell behaviour caused by free  $\text{Mg}^{2+}$  ions. The indirect test was also potentially a better test for alloy to alloy comparisons. Figure 3.11 shows the cell number against corrosion time, in all four alloys the trend is similar and any differences are overshadowed by the large spread in the data.

The decline in cell number due to the high initial corrosion is an intrinsic problem with testing magnesium alloys *in vitro* due to; small media volume levels, low cell numbers comparative to the body's resources and in this study and a lack of movement meaning large discrepancies between the surface and the surrounding environment. Without complicating testing procedure with the use of bioreactors to move high volumes of cells and media over the magnesium, two simple solutions were proposed: seeding at very high cell densities (x10 previous) or pre corroding the samples for 24 hours.

Seeding at cell density of  $400,000 \text{ ml}^{-1}$  (shown figure 3.13) will potentially mean even with the same percentage loss, there will be enough cells to form a successful cell layer after the initial corrosion has subsided. SEM images of cell sheets formed on magnesium alloy WE43 show a cell sheet that is still smaller in number than on glass with areas of low coverage. There are areas with very high density and cells here show a completely different cell shape to that on glass. Cells appear elongated and differentiated comparative to the osteoblasts on glass which are spread in what looks like a proliferative state [25]. Cell loss in the first 24 hours on WE43 was calculated by the DNA assay to be 37.1%



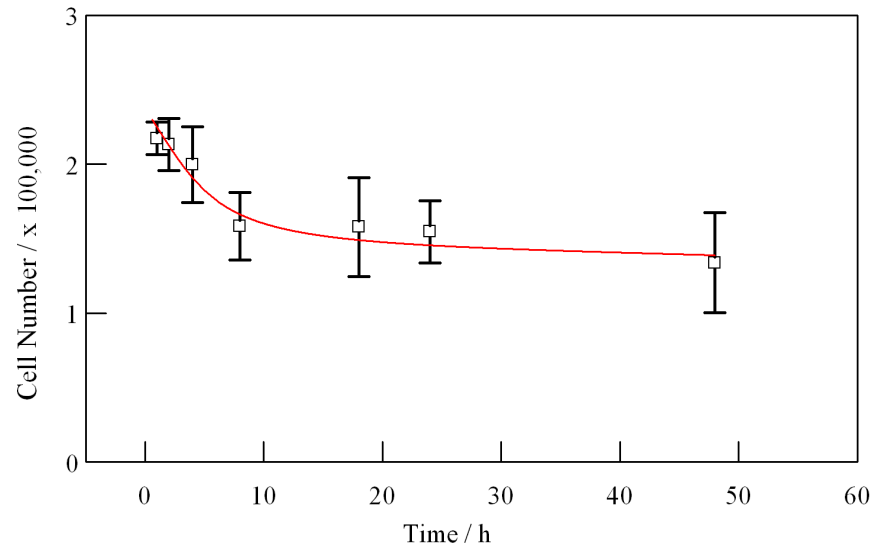


**Figure 3.10:** Cell number calculated by Hoechst DNA staining against the corrosion time. A sharp decline is seen at low corrosion times.  $n = 16$ , error = SD.

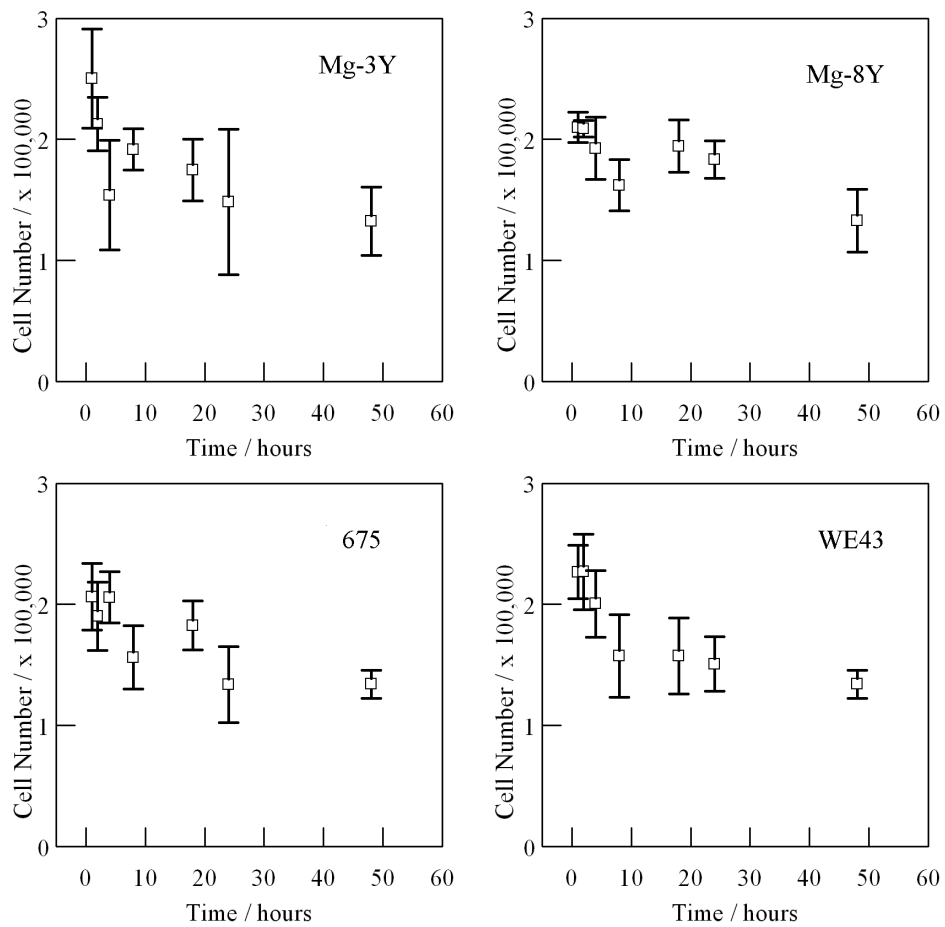


**Figure 3.11:** Individual alloy plots of Hoechst DNA staining against the corrosion time. Alloy to alloy differences are not apparent.  $n = 4$ , error = SD.

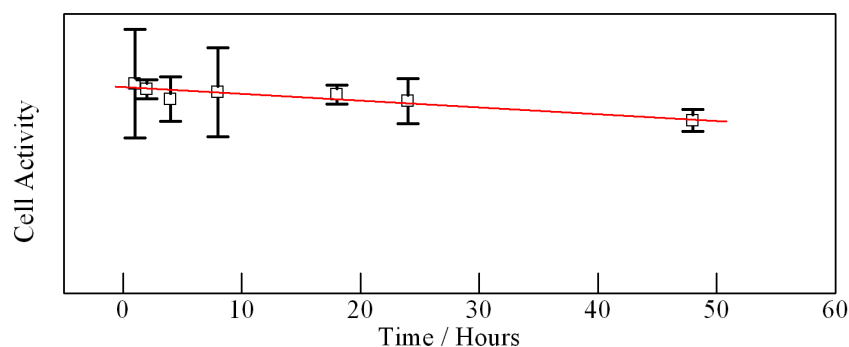


**Figure 3.12:** Cell activity was measured using alamar blue assay. This showed a slight decline in cellular metabolism with magnesium corrosion time.  $n = 16$ , error = SD.

(table 3.3). The loss is lower than when seeded with lower densities. This could be due to a complete coverage of cell slowing corrosion rates, or that they were seeded in such numbers that gaps left by dead cells could be filled by new cells

**Table 3.3:** Cell numbers on magnesium alloy WE43 and glass after seeding at  $4 \times 10^5$  cells  $\text{ml}^{-1}$  and 24 hours culture

WE43	$(149 \pm 37) \times 10^3$
Glass	$(204 \pm 2) \times 10^3$

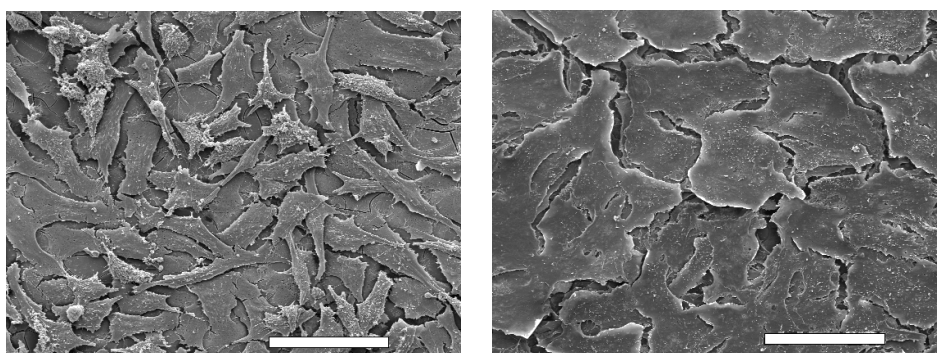


**Figure 3.13:** Osteoblasts on magnesium alloy WE43 (left) and glass (right), seeded at 10 times the density previously. The cells appear unilaterally stretched on WE43. Scale bar =  $50 \mu\text{m}$

Alternatively, pre-treating the magnesium samples was seen as a logical method to reduce cell death and improve *in vitro* testing procedures, a process used for bioactive glasses to also stop cell loss [136]. As shown in the ICP and pH curves against time, the highest corrosion rates are in the first 4-8 hours, with the rate settling after 24 hours. To investigate this, WE43 discs were placed in cell culture media for 24 hours at  $37^\circ\text{C}$ . Osteoblasts were then seeded onto pre-corroded, untreated and glass discs. Figure 3.14 shows cell numbers after 24 hours on both types of surface. Cell death for the untreated samples is slightly higher than previously recorded at 74%. The pre-corroded samples however showed only 12.8% cell death. Fluorescent imaging of cells seeded onto both surfaces shows cells well spread and in greater number on established reaction layer on the pre-treated sample, but rounded on the untreated.

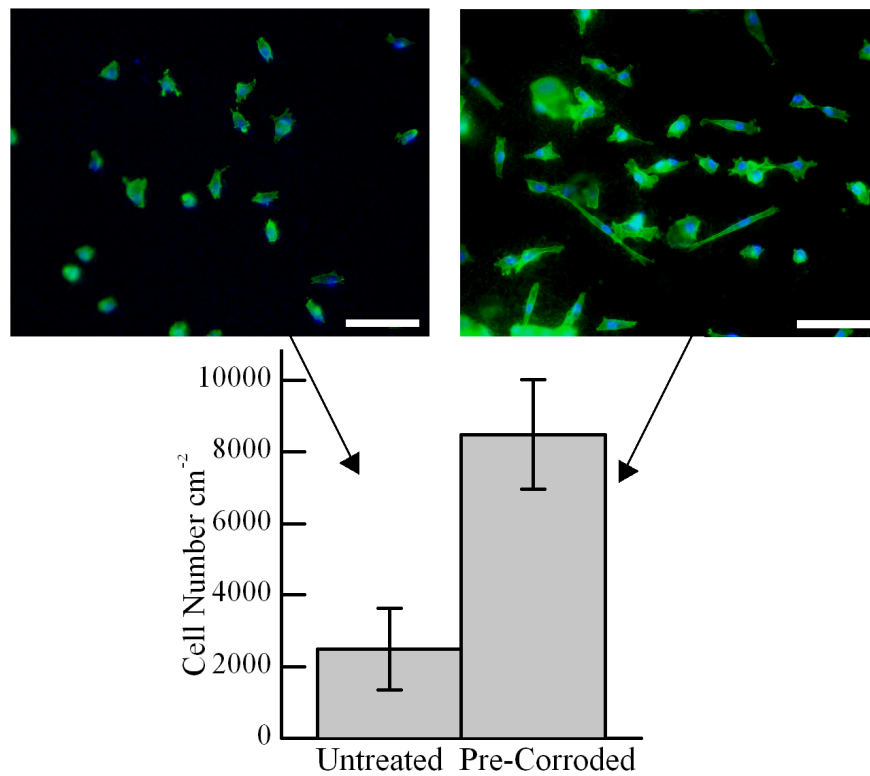


**Figure 3.14:** Osteoblasts seeded on untreated and pre-corroded WE43 after 24 hours quantified by Live/Dead imaging. Top shows phalloidin/DAPI stained cells at the same time point. Osteoblast appear rounded on the untreated compared to spread and attached on the pre-corroded sample. Scale bar = 100  $\mu\text{m}$

The pre-corroding method shows a simple alteration to the *in vitro* testing procedure on magnesium alloys so that cell death and survival is no longer the dominating factor in the cells tested. Pre-corroding has been utilised in a publication by Lorenz in 2009, and it was found that treating in SBF solutions before cell seeding, lowered the cell loss on pure Mg by around 50% compared to glass [114]. This treatment only protected cells for around 24 hours however. Thereafter the reaction layer broke down, most likely due to the discrepancies between cell culture media and SBF meaning a new reaction layer was favourable. This caused cell rounding and some loss in density. In light of this, the use of a pre treatment in media is still the technique used. It was hypothesised that the lower cell death could enhance any positive osteoblast activity and therefore alloy to alloy differentials regarding chemistry could potentially be seen.

The lower cell death and the well spread nature of the cells seen in figure 3.14 on the pre corroded sample strengthens the argument suggested earlier that the high initial corrosion is responsible for cell death. After this, osteoblasts appear to proliferate freely and, as shown in figure 3.13, attach with different morphology than on glass. Since this work many authors have commented on cell death and expression changes due to magnesium alloys *in vitro* and *in vivo*. Pietak [56], Lui [58][57] and Zhang [61] all found cell losses in their investigations. Lui found 40% loss with AM60 with endothelial cells [57], and around 50% loss on AM60 and AZ91 with smooth muscle cells [58]. What was different however from these studies and the one presented here is that Pietak and Lui showed

large differences in cell loss from alloy to alloy. Using various concentrations of calcium, Piekat showed that cell loss was only at 50% when on the highly corrosive Mg-0.8Ca alloy, with the others only around 20% loss [56]. Lui used AZ31, AZ91 and AM60. AZ31 give large cell losses of around 90% compared to AZ91 and AM60 which at most were 50% [58]. The reason for this is most likely to be the result of the alloys used having much greater differences in corrosion rate than the alloys used in this study. WE43 was the fastest corroding alloy presented here and this is still only 20% more corrosive than the best binary alloy.

Aside from cell loss, the change in cell morphology, shown in figure 3.13 and activity indicated in figures 3.21 and 3.12 have also been reported elsewhere. YeoHeung used increasing amounts of magnesium and showed that at higher concentrations, apoptosis, inflammation and migration genes were all expressed [29]. It was also seen that proliferation was enhanced at lower concentrations (<5mM) but reduced above [29]. Smooth muscle cells grown on AM60 were showed to down-regulate  $\alpha$ -actin proteins [58]. Human aortic endothelial cells (HAEC) grown on AM60 had retarded growth and protein expression [57]. Pietak showed lower alkaline phosphatase expression on pure Mg than controls [56]. In all, the majority of *in vitro* testing showed magnesium was detrimental in terms of activity and numbers to that of the controls, as did the results in the investigation presented here. However all *in vivo* work has reported otherwise. Zijan showed greater numbers of osteoblasts around a Mg-1%Ca pin [27], Witte, increased bone growth at surface of magnesium implants of various alloys [53] and Janning, increased osteoblast activity and lower osteoclast numbers[28]. In all the *in vivo* studies, increased bone growth is always shown [43][44][45][46][49][50], even when corrosion rates are very high [51] no immunoresponse is seen. Feyerabend and Zhang reported that the reaction products are osteo-conductive [52] [46].

There is clearly a large difference between the effects of magnesium in the *in vivo* model and the *in vitro*. The most likely reason for this is the upscaling of the biological processes involved. The *in vitro* models use in this investigation along with other reported all use less than 10 ml of culture media, no movement and only one cell type. The body utilises litres of continuously flowing fluids through which the magnesium can dissipate. Magnesium implants are also inserted into tissue, capable of regenerating new cells and tissue coping with any losses that might be caused. *In vitro* models in their current format are therefore shown to be unsuitable for the prediction of bone or artery response to magnesium implants. However, if modified could be used to examine in detail interactions of single cell lines with multiple alloy types and conditions. A process that could not be done *in vivo*.

### 3.3.1 Problems with *in vitro* testing techniques

When approaching this *in vitro* investigation, the experimental methods and procedures followed were based around those used for the majority of other biomaterials, such

as titanium, polymers and glasses. During this investigation it was determined that a number of these assays were not applicable for use with magnesium, or resulted in the protocol being modified.

### Alamar blue

Figure 3.15 shows the alamar blue result for 5 magnesium alloys against three controls. The results suggest that the cell activity on the magnesium alloys is far greater than on glass, titanium or steel. But these results were inconsistent from trial to trial and varied greatly from pre-corroded to untreated states. Magnesium would give readings lower than the controls if the samples were pre-corroded.

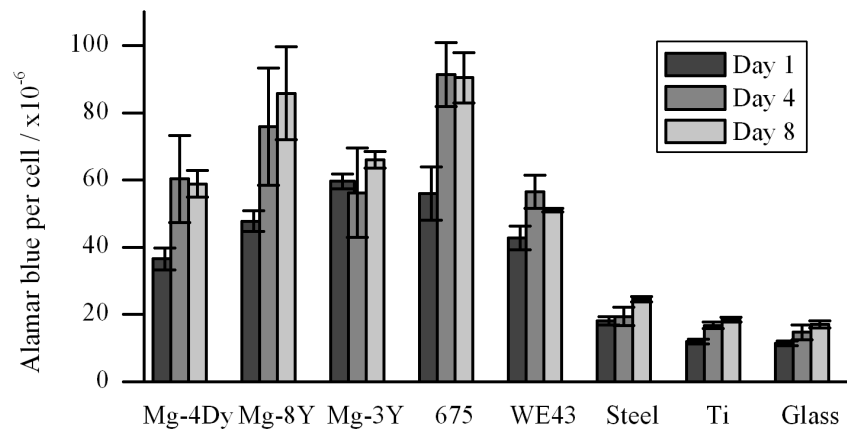


**Figure 3.15:** Example of an alamar blue trial with results that defy expectation and vary with repeats, prompting studies to assess the assays suitability.  $n = 6$ , error = SD

To determine why, the alamar blue assay was conducted on various amounts of magnesium without cells. Figure 3.16 gives the alamar blue readings against the number of magnesium discs placed in media for 24 hours. There is a direct correlation with the number of discs, and by assumption  $Mg^{2+}$  concentration and pH in the media, and the reading.

Taking the pH reading of the media before alamar blue analysis and plotting this against the reading, a direct correlation is seen (figure 3.16). But pH can not be the cause of the increased alamar blue readings. The alamar blue is based on the reduction by biological activity of resazurin salt (which is weakly fluorescent) to resorufin which is strongly fluorescent (figure 3.17)[137]. The reduction potential,  $E_{Red}$  is given by the Nernst equation (3.3.1) and determines the tendency of a chemical species to acquire electrons and thereby be reduced.

$$E_{Red} = E_0 - \frac{RT}{nF} \ln \frac{a_{Red}}{a_{Ox}} \quad (3.3.1)$$

The Nernst equation can be modified to take into account ratio of the number of  $H^+$ ,  $h$  and number of electrons,  $n$  for pH and assuming temperature stays constant at 25 °C, the

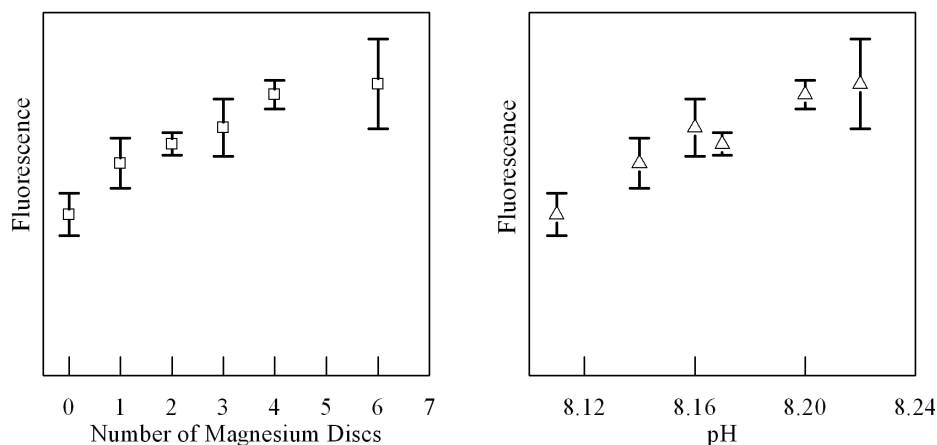


**Figure 3.16:** Alamar blue readings against number of magnesium discs in the cell culture media and also pH. Both show positive trends with increasing magnesium corrosion  $n = 4$ , error = SD

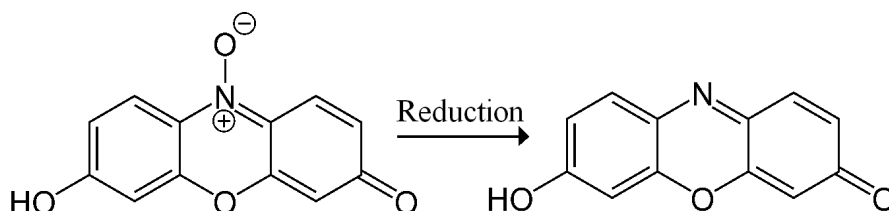


**Figure 3.17:** The reduction of resazurin salt to resorufin.

following equation can be derived.

$$E_{Red} = E_0 - \frac{0.0592}{n} \log \frac{a_{Red}}{a_{Ox}} - \frac{0.0562h}{n} pH \quad (3.3.2)$$

Using this equation for the reduction of resazurin, where  $h = 2$ ,  $n = 2$  and  $E_0 = 380$  mV [138] gives the next equation

$$E_{resazurin} = 380 - \frac{0.0592}{2} \log \frac{a_{resorufin}}{a_{resazurin}} - 0.0562pH \quad (3.3.3)$$

Equation 3.3.3 shows that increasing pH will result in a decrease in  $E_r$  and therefore a decrease in tendency for the resazurin salt to accept electrons and become the fluorescent resorufin. This shows it cannot be the increase in pH resulting in the false readings. An alternative reason for the increased alamar readings is due to a change in reducer. Normally, the reduction process of resazurin salt is carried out by the biological compound Nicotinamide adenine dinucleotide (NADH) [139]. This molecule is an electron carrier, which accepts and donates electrons to enable redox reactions throughout cells. Metal ions are also very strong reducers and accept electrons readily. Magnesium ions formed in the corrosion of the samples are likely to be reducing the resazurin salt into resorufin and thus creating a sample which fluoresces at far greater amounts than it should.

### DNA Hoectsh staining

The same experiment was carried out for the DNA assay, where progressions of magnesium discs were tested without cells. Figure 3.18(left) shows the relationship between the reading and the number of discs and figure 3.18(right) the readings plotted against pH. The analysis of pH was carried out without magnesium, and was simply pH modified TNE buffer added to set concentrations of DNA in dH<sub>2</sub>O. It can be seen that as with alamar blue, there is a direct correlation between magnesium discs and reading. Using buffers of difference pH shows the cause of this is in some part the raise in pH that occurs during the distilled water freeze-thawing process from magnesium corrosion.

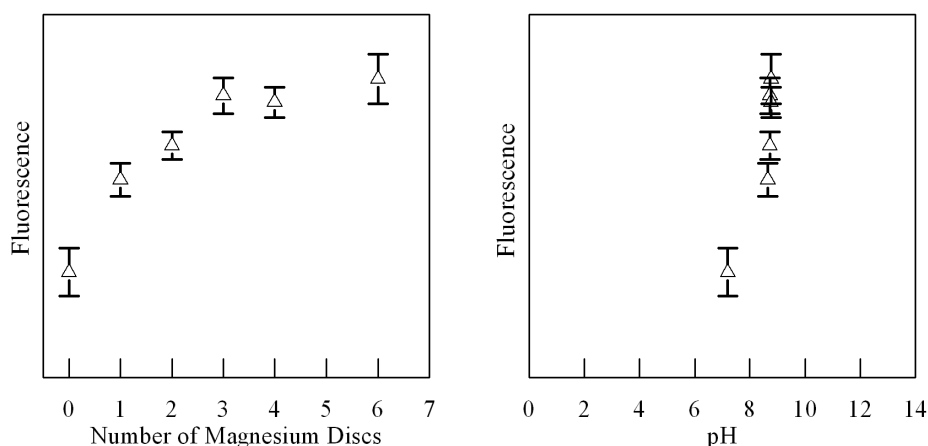


**Figure 3.18:** Hoectsh DNA assay readings against the number of magnesium discs in the media and their corresponding pH. The trend appears to be linked to magnesium concentration and not pH.  $n = 4$ , error = SD.

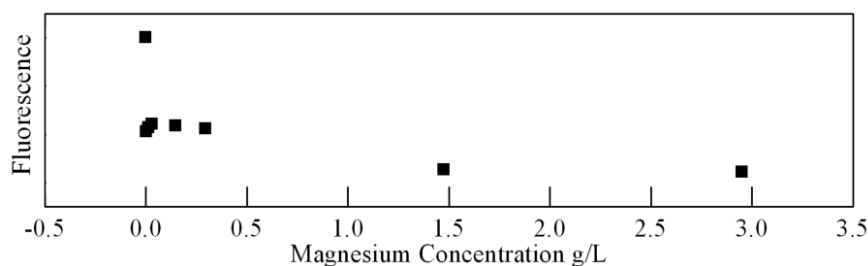


**Figure 3.19:** Hoectsh DNA assay reading against Magnesium concentration modified by additions of MgCl<sub>2</sub>. Magnesium appears to inhibit Hoectsh readings

It has also been shown that magnesium as an ion has an effect on hoectsh results. Figure 3.19 gives magnesium concentration, increased by MgCl<sub>2</sub>, against the respective hoectsh stain fluorescence results. Magnesium ion concentration is shown to have an affect on the reading. Marie *et al* also found that additions on cations to TE buffer (tris and EDTA) raised the intensity of hoectsh readings [140]. Fifty mM MgCl<sub>2</sub> added to TE buffer raised the reading from 0.306 to 0.34 when measuring DNA concentrations of *P. marinus* cells (a protozoan parasite) [140]. The reasons for this effect however are conflicting. Mg cations are a known deleterious to Hoechst 33342 stains, and thus EDTA is often added to chelate them [141]. Magnesium has been shown to act as a nuclease

cofactor [142], and has a role in the shaping oligonucleotides and stabilising them, whereas Calcium due to its lower volume to charge ratio has less of an effect [142]. Hoechst stains are bisbenzimidazole derivatives and work by binding to the minor grooves in DNA. It could be that the extra magnesium causes DNA to form a more regular structure and thus allow the hoechst to form into the minor groove.

So far magnesium has been shown to affect the data given by these two important *in vitro* tests. Alloy to alloy problems have also been noticed. Figure 3.20 gives the data from an alamar blue trial with the new medical grade alloys used in Chapter 5. The alloy MI0029 which contains 8wt% added erbium to the ML4 alloying system. The reading is over 4 times greater than ML4 and glass. This would not be a pH affect as MI0029 corrodes at far lower rates than ML4 and this was measured, so the effect could possibly be due to erbium or its corrosion products.

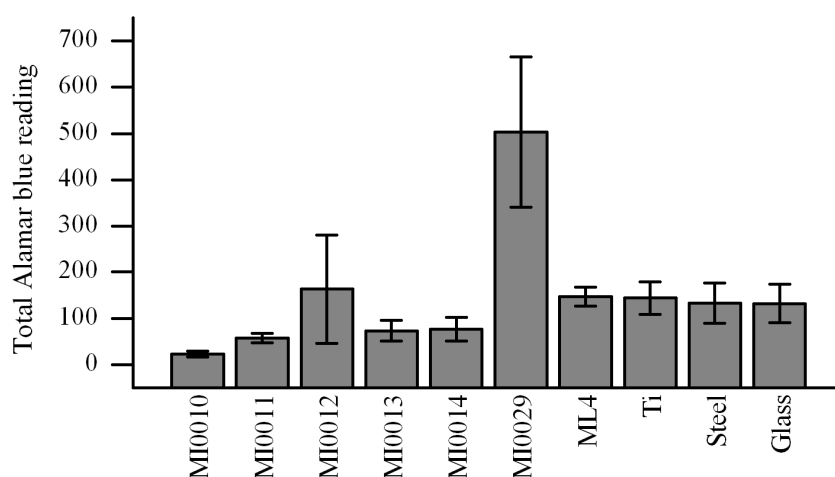


**Figure 3.20:** An example of alloy to alloy differences experienced with alamar blue which appear to be independent of both magnesium concentration and pH.  $n = 4$ , error = SD

### Modified protocols

To overcome these problems a new testing procedure was investigated. The practise of pre-corroding the samples had shown more robust data compared to the assays with cell on cell contact studies. This would be due to lowering the pH and  $Mg^{2+}$  ions transferred into the solution to skew the readings. By removing them further, potentially, the test would become more accurate. For this, no cell on surface studies could be used, as this would always bring the tested solution into contact with corroding magnesium. Conditioned medium studies had previously been used, but for longer term assays, this would mean constantly corroding new magnesium discs in media so supply fresh conditioned media for the media changes carried out every 2 days, therefore, for studies over 1-2 weeks, this is unfavourable.

The approach used was to place magnesium discs in large well plates and seed the cells on the tissue culture plastic around the disc instead of on top. The discs were pre-corroded to stop the high cell death seen previously. To test at a time point, the disc was taken out



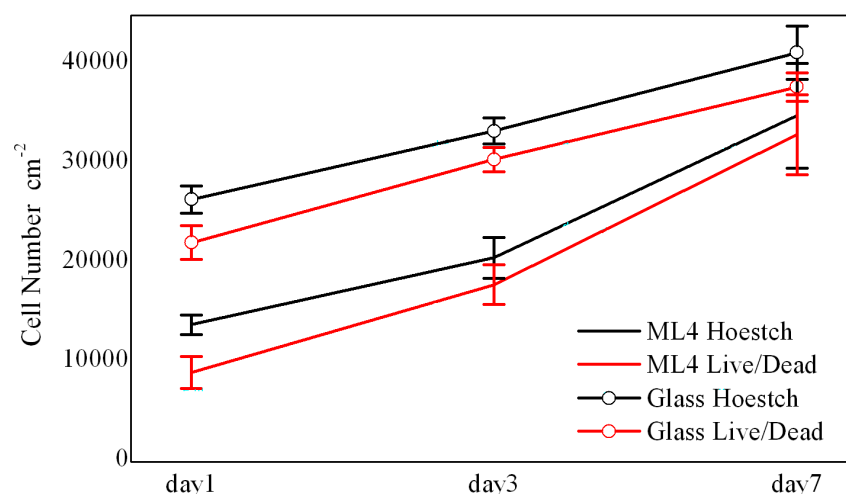


**Figure 3.21:** Cell numbers against time after seeding at  $2 \times 10^5$  cells  $\text{ml}^{-1}$  on ML4 and Glass using the modified protocol. Cell numbers were measured by both visual counting with Live/Dead and also by absorption with DNA hoestch staining. Differences are seen between tests within sample types, but sample vs sample shows test agreement.

and the cells washed twice in PBS. After this step the replicate samples were split in two; half were re-dosed in media to follow the alamar blue, DNA and alkaline phosphatase assays, the other half were used for the Live-Dead staining. After staining the samples were imaged using fluorescence microscopy and 10 images at randomly selected points were taken. The number of cells counted were divided by the total area of the images to give cells  $\text{cm}^{-2}$ . This method gave two readings for cell number which were highly correlated with regard to difference between samples, but side by side the cells  $\text{cm}^{-2}$  value given by the DNA and alamar blue assays were highly dependant on the standard curve made.

### Fluorescent imaging

A powerful tool for cell culture testing is fluorescent imaging of cellular and extra cellular material on surfaces. A popular method is to label F-actin and nuclei with Phalloidin and DAPI stains. The protocol for this is set out in section 3.2, and shows that the final step is to stain and mount the cells with Prolong Gold® + DAPI. This step can be split up into DAPI and then Prolong Gold®, but in both cases the samples have to be mount with Prolong® to preserve the organic tissue from degrading while taking the micrographs. Figure 3.22 shows that Prolong Gold reacts with magnesium and forms hydrogen bubbles, meaning the sample is rendered unusable.

To overcome the mounting step destroying the surface a new anti-fade mount was sought. This was made to the specification listed in section 3.2, and although still slightly reacts with magnesium and forms small bubbles, the surface remains photographable for 4-5 hours, whereas using no mounting step leaves the stain to bleach and results in poor images within minutes.

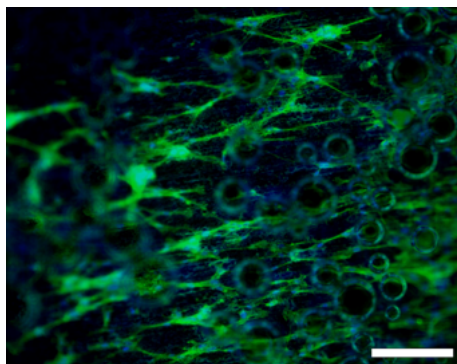


**Figure 3.22:** Fluorescent micrograph showing the effect of Prolong Gold® anti fade reagent on magnesium. The mountant causes corrosion of magnesium and therefore hydrogen bubble formation which interfere with image processing. The surface is generally unusable after 30 minutes. Scale bar = 100  $\mu\text{m}$

### 3.4 Conclusions

The aim of this chapter was to outline an understanding of what occurs when osteoblasts are cultured with magnesium and what can be found from the process. Thus far it has been determined that high corrosion rates initially seen when magnesium alloys are placed in cell culture medium have a detrimental effect on cell numbers. This was determined to be the result of local pH rise and hydroscopic pressure. The effect is inherent to all magnesium alloys irrespective of their overall corrosion rate.

After the initial corrosion spike, the rate lowers and the surviving cells on the sample surface proliferate and attach well. Also, seeding cells on pre-corroded samples to remove the initial corrosion spike show that magnesium is a good osteoblast scaffold. This is in keeping with *in vivo* results which state osteo-conductivity as a result of magnesium implantation. Magnesium shows a clear phenotype expression change in the cells seeded upon its surface compared to glass.

As a testing procedure cell culture based *in vitro* techniques used as in this study are limited for alloy to alloy distinctions, but are worth while to determine the effects of the magnesium-osteoblast interaction. This is due to the high amounts of magnesium comparative to even the largest of alloying additions in these alloys.

Cell culture analysis techniques must be rigorously tested for their dependance on metal cations and pH levels. A new experimental procedure has been set out in this investigation, but results will still be inaccurate if the assay is effected by magnesium corrosion products.

### 3.5 Further work

This chapter has set out the basic mechanisms and ideas for *in vitro* studies of magnesium alloys. The mechanism in which osteoblasts and bone tissue is affected by magnesium ions and corrosion products needs to be tested in greater detail using cell culture. This investigation merely determined that it could be done. A study looking at how such

large magnesium concentrations and high pH spikes affect osteoblast activity, phenotype and bone formation is required. A study looking at cell metabolism was conducted by the author and the company Metabolon (Durham, NC, USA) to answer some of the questions regarding its effect on cellular processes, but this needs to be repeated in greater detail along with gene expression work to show the underlying mechanisms of magnesium alloy corrosion on osteoblasts.

If osteoblast studies are to be continued for alloy to alloy comparisons and development, a true robust testing technique needs to be established. A series of experiments unaffected by pH or cation concentration which lead to highly reproducible data that can statistically distinguish between alloys are required. First steps towards this have started and involve the use of a perfusion bioreactor to cycle large quantities of cell culture media and cells over the magnesium surface. *Ex-vivo* models will also be used. Here bone tissue taken from an animal donor will have magnesium alloy samples placed within and then cultured *in vitro*. This will give a much more accurate model of an orthopaedic implant.



## MICROSTRUCTURE CONSIDERATIONS

### 4.1 Introduction

During the development process of this project, microstructures have had a substantial influence. This chapter outlines some of the development issues and investigations that have taken place centred around the microstructure of alloys, in terms of problems and directions for potential improvements.

The work proceeding this investigation, such as the collaboration with commercial partners, external work now frequently published, and also the initial cell culture chapter (3), had all indicated that bioresorbable magnesium alloys offer huge potential as degradable implant materials if their corrosion rates can be lowered. This was needed to increase product working lifetime, limit hydrogen evolution at the implant surface and also lower localised tissue damage. Therefore future work focused on finding methods to lower corrosion rate *in vitro* and *in vivo*, initially with the alloys available, such as Elektron 21, 675 and WE43, before developing new alloys for this purpose.

### 4.2 Worked microstructures

Standard lower scale extrusions processed for the development department at Magnesium Elektron have always been produced from a 90 mm diameter billet extruded through a 9 mm die at a temperature defined for the specific alloy. To meet the requirements of a biomedical partner, Magnesium Elektron manufactured 6.4 mm extruded rods from Elektron WE43 and Elektron 675 using a six-hole die from 90 mm billets. This was requested by the partner, as the 9mm is normally preferred by Magnesium Elektron. During the batch testing of the extruded material by salt fog cabinet (explained in section 4.2.1), the corrosion rates gave a large spread of data and generally much higher rates than expected (normally less than 12 milli-inch per year (mpy)). Figure 4.1 shows the microstructures of WE43 and 675 extruded to 6.4 mm and their respective corrosion rates under salt fog. WE43 ranged from 9 to 76 mpy and 675; 42 to 192 mpy. The metallography shown in figure 4.1 shows two forms of microstructure; a recrystallised second phase containing

structure normally associated with WE43 and 675 and a highly worked structure. The aim of this investigation was to discover the extent of this worked microstructure across the extrusions, its affects on corrosion in SBF, and whether the microstructure can be removed and the material recovered.

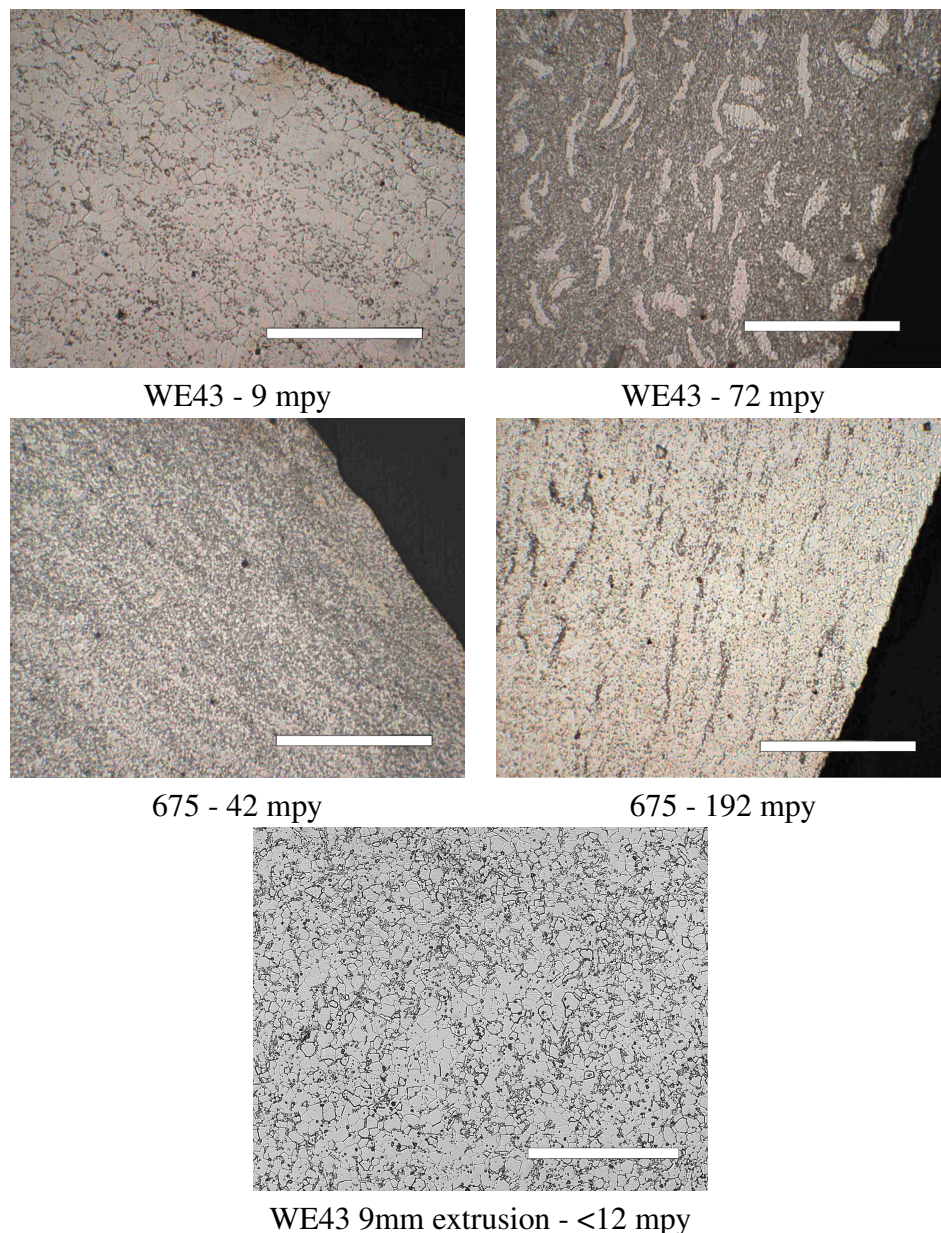


**Figure 4.1:** Optical micrographs taken by Magnesium Elektron of the front (right) and rear (left) of extruded 6.4 mm rods. The front of the extrusion gives a worked microstructure and corrosion and apparent higher corrosion rates. The back of the extrusions appear closer in microstructure to the 9 mm extrusion (bottom image). In all cases the 6.4 mm rods are high in corrosion and inconsistent compared to the 9 mm WE43 rod. Scale bars = 50  $\mu\text{m}$ .

#### 4.2.1 Materials and Methods

Elektron WE43 (DF9441) and Elektron 675 (DF9445), compositions listed in table 4.1,

The material was made at Magnesium Elektron by melting pure magnesium ingot with the appropriate alloying elements. Once molten, the metal is stirred and a small casting was made for chemical analysis by Optical Emission Spectrometry (OES). If this falls within specifications the metal was ready to cast. Molten metal was then poured from the crucible into the mold. Once solidified and air cooled, the casting was machined into 75 mm diameter billets (A and B) for extrusion.

**Table 4.1:** Chemical composition of alloys given by wt%. Total impurities equates to the combined composition of Fe, Ni and Cu.

Alloy	Y	Nd	Zr	Gd	HRE	Total Impurities
WE43	3.7-4.3	2.2-2.5	0.4-1.0	n/a	0.4-1.9	0.005
675	6	-	0.35-0.4	6.5-7.5	n/a	0.005

The extrusion procedure required, pre heating of the billet, die and billet container to specified temperatures. The billets were pushed through a six times 6.4 mm die into rods. These rods had their front and back ends removed up to the point where surface scouring stopped.

Nine mm WE43 rod (DF9527) was also supplied as a control and made with the same procedure. The rods were heat treated for 16 hours at 250 °C (T5). The mechanical properties for the normal and worked structure of DF9445 are listed in table 4.2.

**Table 4.2:** Mechanical properties from both microstructures of 675 6.4 mm rods.

	0.2% Yield /MPa	UTS /MPa	Elongation /%
Standard	280	354	23
Worked	285	358	20

### Corrosion testing

As a standard test to represent a material's ability to withstand corrosive environments, a saltwater fog immersion test is used. The chamber used is specified by the American Society for Testing and Materials, under ASTM B117-94. The rate of corrosion within the seven day test is roughly equal to the material being left twenty five years in a normal atmosphere. Samples were machined from the extruded rod into 30 mm by 6 mm cylinders. The surfaces were then smoothed by pumice. These were weighted and placed in the chamber for seven days. For uniformity of test, samples were spaced to prevent salt solution condensate contaminating other samples. The temperature during testing was set to 35 °C and the concentration of the fog was 5% NaCl. Post-test, the samples were removed and cleaned in 15% chromic oxide solution at 70 °C to remove the magnesium oxide from the surface. Cylinders were then rinsed and dried before being re-weighed to

determine weight loss. The weight loss is given as a function of corrosion penetration (milli-inches) against time in years, referred to as mpy.

SBF testing was conducted using the same sample preparation, but with one end drilled with a thread. These were weighed and attached to a hanging rack via plastic screws at the top end. Oil was placed on the screw before inserting to stop SBF corroding the inside thread. The cylinders were then submerged in SBF for 7 days. Fourteen litres of solution was used per 24 cylinders. SBF solution was made using the protocol below.

### Electrochemistry

Electrochemical measurements were conducted in aerated salt solutions at 37 °C, using an ACM-instruments Gill AC computer-controlled potentiostat. A conventional three electrode cell was employed with a platinum counter electrode and a saturated calomel reference electrode (SCE). The working electrode was the test material with an exposed area of 0.64 cm<sup>2</sup>. For anodic and cathodic potentiodynamic polarisations at a scan rate of 0.3 mVs<sup>-1</sup>, commencing from -3 mV to -0.3 mV with respect to the OCP, respectively.

### Simulated Body Fluid

Five stock solutions were made to concentrations listed in table 4.3. To make 1 litre of SBF, stock solutions were added in the amounts listed in table 4.3, and in the order shown. 23.83 g of 4-(2-hydroxyethyl)-1-piperazineethanesulfonic acid (HEPES) was dissolved into 500 ml dH<sub>2</sub>O. The two were mixed together and the total volume increased to 1000 ml with dH<sub>2</sub>O. The pH was then adjusted to 7.4 with concentrated (32%) NaOH.

**Table 4.3:** Concentrations of salt solutions used to make 1 litre of SBF.

Salt/Buffer	Concentration of Stock Solution /gL <sup>-1</sup>	Stock volume used per litre /mL
KCl	59.64	5
NaCl	116.88	50
NaHCO <sub>3</sub>	45.37	50
MgSO <sub>4</sub> • 7H <sub>2</sub> O	49.30	5
CaCl <sub>2</sub> • 2H <sub>2</sub> O	14.70	25
KH <sub>2</sub> PO <sub>4</sub>	27.22	5
HEPES	23.83	23.83g

### Microstrutural analysis

Surfaces and cross sections of the coatings were examined by field emission gun scanning electron microscopy (FEG-SEM), using a Philips XL30 FEG SEM, equipped with energy-dispersive X-ray (EDX) analysis facilities. Standard secondary electron images were taken with an acceleration voltage of 10 kV and back scattered images at 20 kV.



The cross sections were prepared by grinding, using successive grades of SiC paper, and polishing to  $1/4\ \mu\text{m}$  diamond finish followed by colloidal silica (OPS).

### 4.2.2 Results and discussion

To investigate the extent of the worked microstructure, optical sections were taken along the extruded rods at regular distances from front to back. Figure 4.2 shows the cross sections, and reveals that the worked structure is dominant in the first 3 micrographs taken, a distance from the front of the extrusion of just under a meter. After which the worked structure fades heterogeneously across the rod, staying prominent in one area until the whole of the section is the recrystallized structure normally associated with wrought yttrium-rare earth alloys.

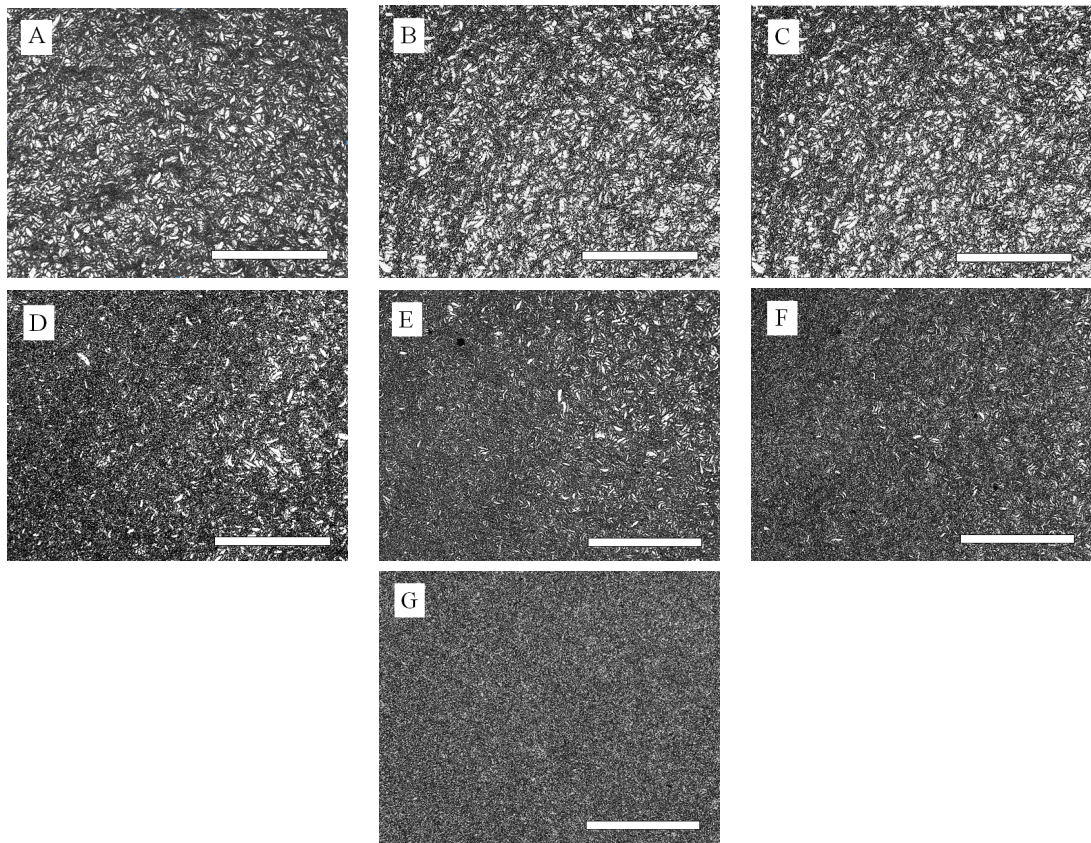


**Figure 4.2:** Optical micrographs taken of a 6.4 mm extruded rod from front (A) to back (G). The microstructure progressively turns from a worked unrecrystallised structure to the normal recrystallised structure expected. Scale bars =  $200\ \mu\text{m}$ .

Micrographs were taken across the entire total cross section at the mid point of the extrusion in all 6 bars (these are combined together in figure 4.3). It can be seen that the worked microstructure is only dominant in one area (shown in figure 4.3 left). If all 6 of the microstructures are positions in their true representation of positions from the die, the areas of worked structure still remaining all face the outer side of the die as demonstrated in figure 4.3(right).

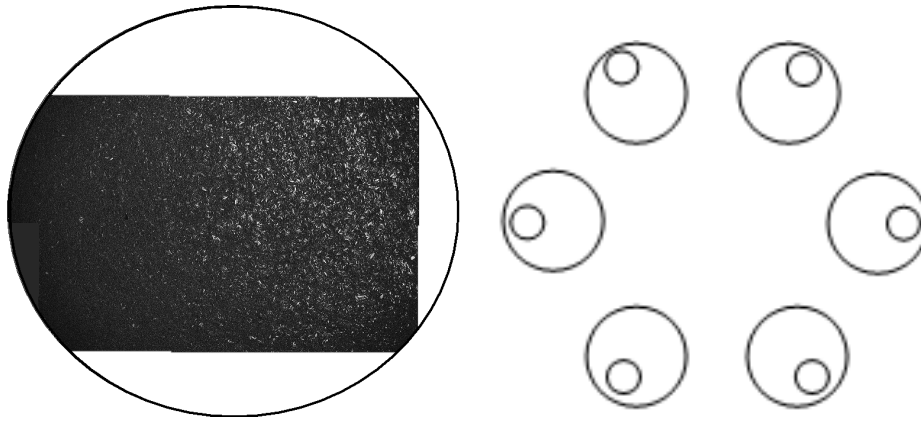


**Figure 4.3:** Right: Eight optical micrographs taken mid way through the extrusion and combined showing the worked structure distributes to one outer section of the rod. Circle demonstrates outer circumference of the 6.4 mm extrusion. Left: the worked structure's relative position out of the die (Mid way through bar).

The worked microstructure resembles the unrecrystallised, worked structures observed when extrusions are warm extruded and not allowed to recrystallise due to the lack of heat. Mehtedi extruded ZM21 magnesium alloy at various temperature and found a similar structure when billet temperatures were below 300 °C, but recrystallised at billet temperature 300 °C or above [143]. The extrusion process received heat by three means, the billet is pre heated as is the die, but final heat transfer occurs from the process of extrusion [144]. The heat transferred is a function of the ram speed, extrusion ratio and the friction between die and material. Figure 4.4 shows a typical pressure / ram displacement diagram for a magnesium alloy [144]. This shows the profile temperature rising rapidly with ram displacement to above 400 °C. The original billet temperature for this diagram is 350 °C, thus demonstrating the transferred heat.

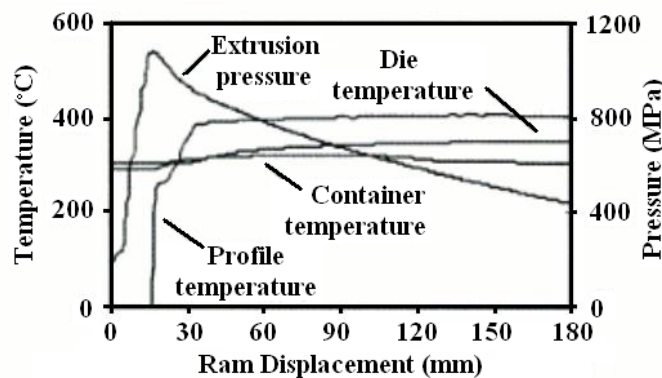


**Figure 4.4:** Ram displacement against pressure and temperature of a typical extrusion with a billet temperature of 350 °C [144]. Extrusion pressure initially increases rapidly, known as the breakthrough pressure before declining. Temperature increases with ram displacement due to work on the material.

Comparing the 9 mm standard extrusions and the 6.4mm diameter 6 hole extrusions, the notable change is the overall extrusion ratio. The surface area of the die outlets has increased from 0.636 cm<sup>2</sup> (extrusion ratio of 69.4) to 2.581 cm<sup>2</sup> (extrusion ratio of 17.1). Therefore the extrusion ratio has dropped by over 3 times. This lowers the transferred heat into the extrusion profile. Chen observed AZ31 extrusions from a range of extrusion

ratios. It was found that a ratio of above 39x was needed to create the recrystallised structure desired [145]. The microstructure observed can therefore be explained by a drop in extrusion temperature due to lower extrusion ratio. The gradient from worked structure to recrystallised is due to the progressive heating of the die with ram displacement as shown in figure 4.4. The extrusion process at Magnesium Elektron has been developed for the 9 mm die, and billet temperature before extrusion is set so that the recrystallised temperature occurs, but the risk of hot cracking and other defects associated with excess heating do not. If future six hole 6.4 mm extrusion were to continue, these should be conducted at higher extrusion ratios and temperatures.

### Corrosion characteristics

Samples were taken from the front of extrusions with the worked structure and tested against the back of the extrusion with the re-crystallised structure. Figure 4.5 gives the corrosion rates from the SBF bath and shows there is no statistical difference between two structures (calculated by single factor anova). Also of note, is that the data spread between samples is low, in contrast to the results from the salt fog cabinet.

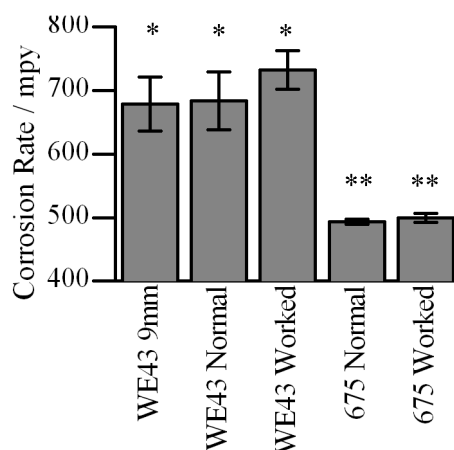


**Figure 4.5:** SBF bath corrosion results from the worked and normal structures of both 675 and WE43 alongside a 9 mm control. SBF corrosion seems unaffected by the microstructure. \* and \*\* indicates no statistical difference by single factor anova (\*  $p>0.05$ ,  $n = 6$  and \*\*  $p>>0.05$ ,  $n = 6$ )

Typical potentiodynamic polarisation curves of both microstructures in SBF and 0.1M NaCl solutions is shown in figure 4.6. As with the SBF bath corrosion, the worked structure seems to have no affect on the corrosion properties. However, in line with the salt fog results, corrosion properties in NaCl solutions are altered. Explanations for this discrepancy in corrosion properties are most likely due to the reaction layer. The unre-crystallised microstructure will cause slightly greater numbers of cathodic particles and therefore greater micro galvanic coupling. Once the structure recrystallises and the cathodic particles group together in their phases, the couplings are reduced. The corrosion dynamics in SBF are controlled in greater effect by the reaction layer formed on its surface than the bulk material (for example the alloys discussed in chapter 7). Therefore slight changes in microstructure should not affect the reaction layer produced in SBF.

However, with such a poor protective layer when corroded in NaCl solutions ( $\text{Mg}(\text{OH})_2$ ), the material is generally always exposed and thus material properties are more influential.

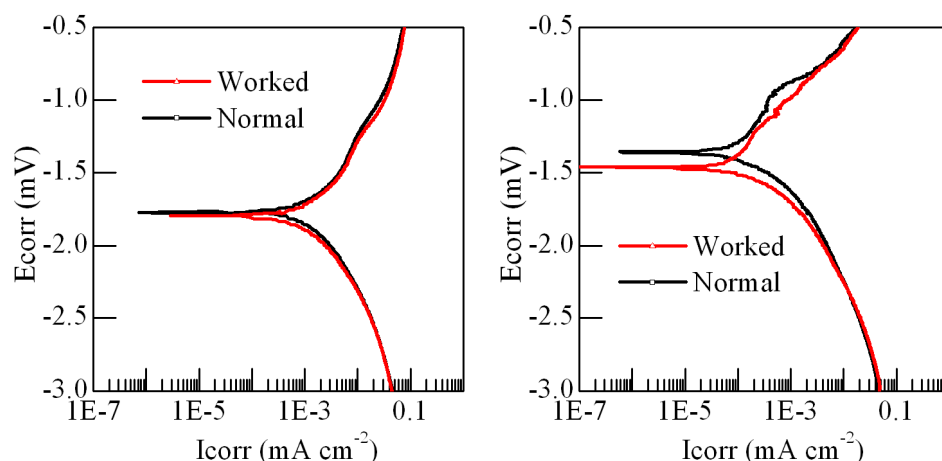


**Figure 4.6:** Potentiodynamic polarisation curves of the worked and normal structures in SBF (left) and 0.1M NaCl (right). Corrosion in SBF shows no correlation with microstructure, whereas in NaCl the worked structure is shown to increase the alloys corrosion potential. The alloy used in 675 after 30 minutes corrosion.

### Microstructure modification

The worked microstructure was sought to be removed and replaced with a recrystalline structure as seen in the back sections of the extrusion. This was for mechanical properties and product uniformity. Even with satisfactory SBF results, the microstructure is still not within specifications for Magnesium Elektron. To remove the worked structure, short term annealing was used in order to give the material the desired energy to recrystallise. Four temperatures were used ( $400^\circ\text{C}$ ,  $450^\circ\text{C}$ ,  $500^\circ\text{C}$ ,  $525^\circ\text{C}$ ) for four hours to anneal magnesium alloy corrosion cylinders of both WE43 and 675 with the worked structure alongside a WE43 9 mm rod standard. The microstructures are shown in figure 4.8. The worked structure was removed from both alloys at  $450^\circ\text{C}$ . Above this temperature a crystalline structure is seen containing large grains, similar to the control at the same temperature. This structure will have poor mechanical properties as the small grains provided ductility and strength. Therefore the annealing process was regarded as a failure. The corrosion data for the heat treated sample is shown in figure 4.7. There is no change with temperature in the worked microstructure samples.

### 4.2.3 Conclusions

The worked microstructure, although not within specifications due to poor salt fog and mechanical data, was comparable to the standard structure in terms of SBF corrosion rate. This was due to magnesium alloy corrosion rates being largely influenced by the reaction layer and not microstructure. The structure was the result of low temperatures at the point of the extrusion die hole leading to insufficient heat to enable recrystallisa-



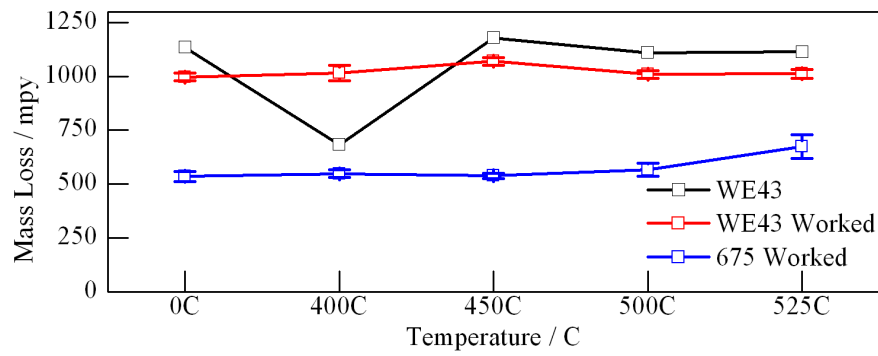


**Figure 4.7:** SBF bath corrosion data after annealing. The original worked structures appear unaffected by the heat treatment. The control however shows a  $\sim 45\%$  drop at  $400\text{ }^{\circ}\text{C}$ . Worked samples  $n = 3$ , WE43  $n = 1$ , error = SD.

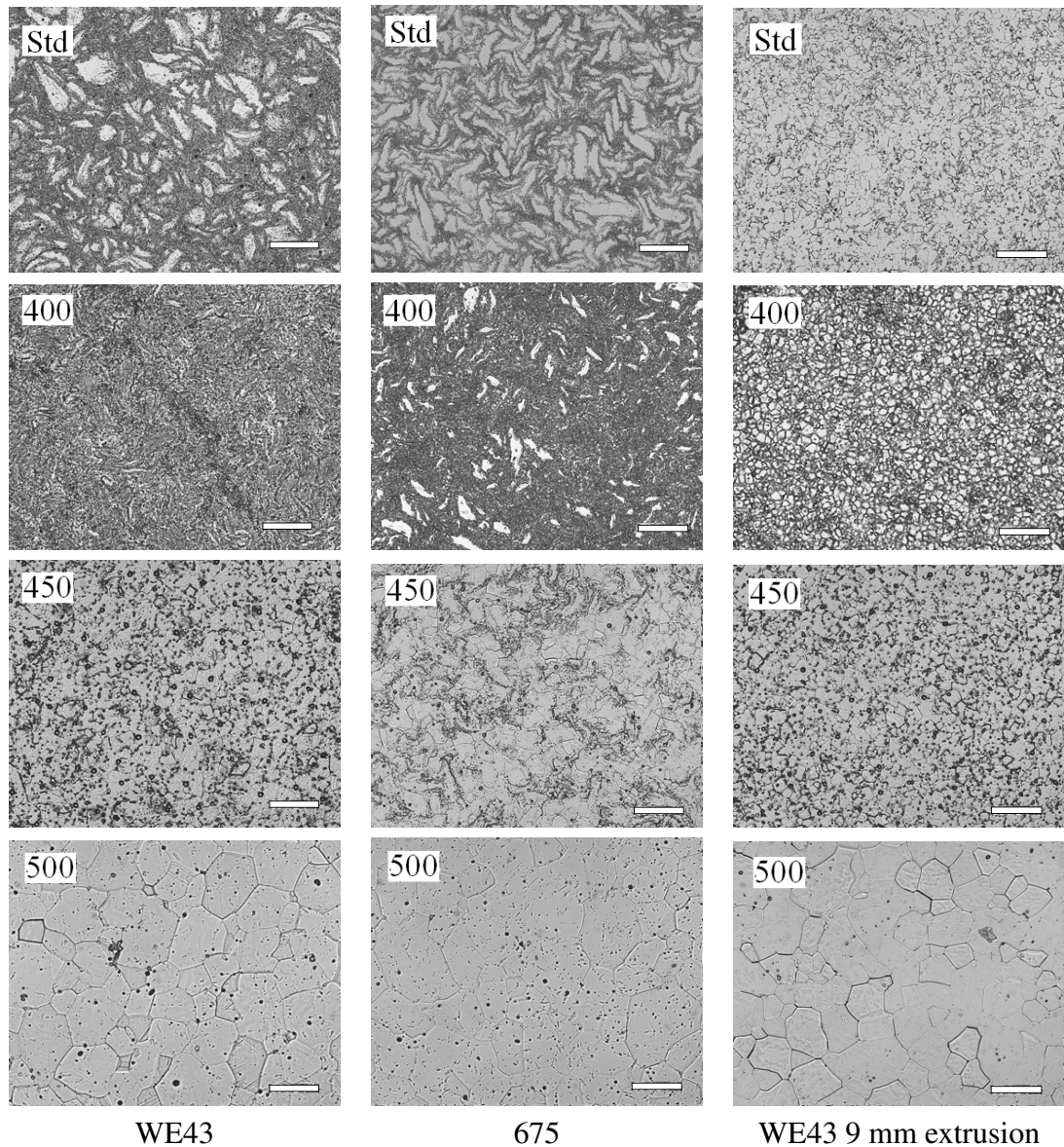


**Figure 4.8:** Micrographs of the annealed samples. Standard microstructure is the as extruded sample with no further heat treatments. Further structures are post treatment, which was the stated temperature for 4 hours. The worked microstructure is fully recrystallized when heated to  $500\text{ }^{\circ}\text{C}$  or above. Annealing took place for 4 hours. Scale bars =  $50\text{ }\mu\text{m}$

tion post extrusion. Compensating for this with heat treatments did not give the desired microstructure.

Too much of the material was therefore scrapped due to the undesired microstructure, and this could not be salvaged by post extrusion processing. Thus all extrusions were determined to be made from 9 mm dies in future work.

### 4.2.4 Further work

Production procedures need to be developed so that extrusions of all die ratios can be produced with the standardised recrystallised structure desired. Recent work has shown that the Mg-Y-RE-Er alloy investigated in Chapter 7 when extruded at normal 9 mm extrusion size can form the worked microstructure and unlike the WE43 alloys in this chapter, the worked structure effects SBF corrosion rates. Billet temperature, extrusion speeds and extrusion ratios need to be investigated in detail so that this microstructure is avoided in all future biomedical alloys.

## 4.3 Sub solidus heat treatments for improved corrosion resistance

While investigating the effects of the worked microstructure on the corrosion properties of WE43 and 675 and whether this structure could be removed by annealing, the control made from 9 mm bar WE43, which was annealed at 400 °C, corroded at a rate 40% lower than the other temperatures including the standard condition (figure 4.7).

WE43 and its various heat treatment processes are well documented. No passivation effect has been reported when WE43 is subjected to commonly used NaCl solutions and salt fog cabinets. Therefore this effect in SBF is novel. This investigation sets out to prove if this effect is repeatable, to optimise the conditions needed, and to analyse why this effect occurs.

### 4.3.1 Material and methods

Magnesium alloy ML4 (DF9193) was used for this investigation. This was supplied in 9 mm extruded rod and created by the procedure outlined previously (section 4.2.1) and cut into 50 mm long sections. These were heat treated at five temperatures (200 °C, 250 °C, 300 °C, 350 °C and 400 °C) for four different time periods (2, 4, 8 and 16 hours). The resulting matrix of heat treated cylinders were machined into 6.4 mm corrosion cylinders and pumiced.

**Table 4.4:** Specification of ML4 given by wt%. Total impurities equates to the combined composition of Fe, Ni and Cu.

	Y	Nd	HRE(misc)	Total impurities
ML4	3.7-4.3	2-2.4	1	0.004

### 4.3.2 Results

First a trial was set up to repeat the result seen previously. A range of temperatures from 200 °C to 400 °C was used for 4 hours on ML4 9mm diameter rod. The results (shown table 4.5) confirmed the effect, but the trial showed a smaller reduction (<20%) in corrosion rate with the lowest rate achieved at 300-350 °C instead of 400 °C as previously observed.

**Table 4.5:** Preliminary mass loss results for heat treated ML4

Temperature / °C	Mass loss vs Std / %
300	48.9
350	57.8
400	49.5
450	40.6

### Optimisation

The cylinders were corrosion tested by SBF baths. Three baths were run side-by-side with one triplicate of each condition in each bath along with standard condition controls. The results of this are shown in figure 4.9. The heat maps show the loss in corrosion rate against both time and temperature for all three baths. The results have been set as a percentage of the standard condition corrosion rate in the same bath. The average of the three is displayed in figure 4.10. Improvements in corrosion rate appear to be dependant on temperature rather than time, although slight increases with time can be seen. Corrosion rate is improved by 20% or more (blue regions) in nearly all conditions at 300 °C or above. In bath 1, 8 hours at 350 °C gave an improvement of 22.3% (551.1 mg mass loss) over the standard condition, in bath 2, 16 hours at 300 °C gave an improvement of 28.5% (464.0 mg loss) and bath 3, 8 hours at 350 °C reduced the rate 51.9% (511.4 mg loss). Figure 4.10 shows the corrosion rates as a percentage of F condition for all temperatures and time lengths. Bath 3 gives greater improvements than both 1 and 2. The large spread of corrosion rates can be seen between baths, but the treatments that appear optimal (8-16 hours at 300-350 °C) are consistent in all three tests.

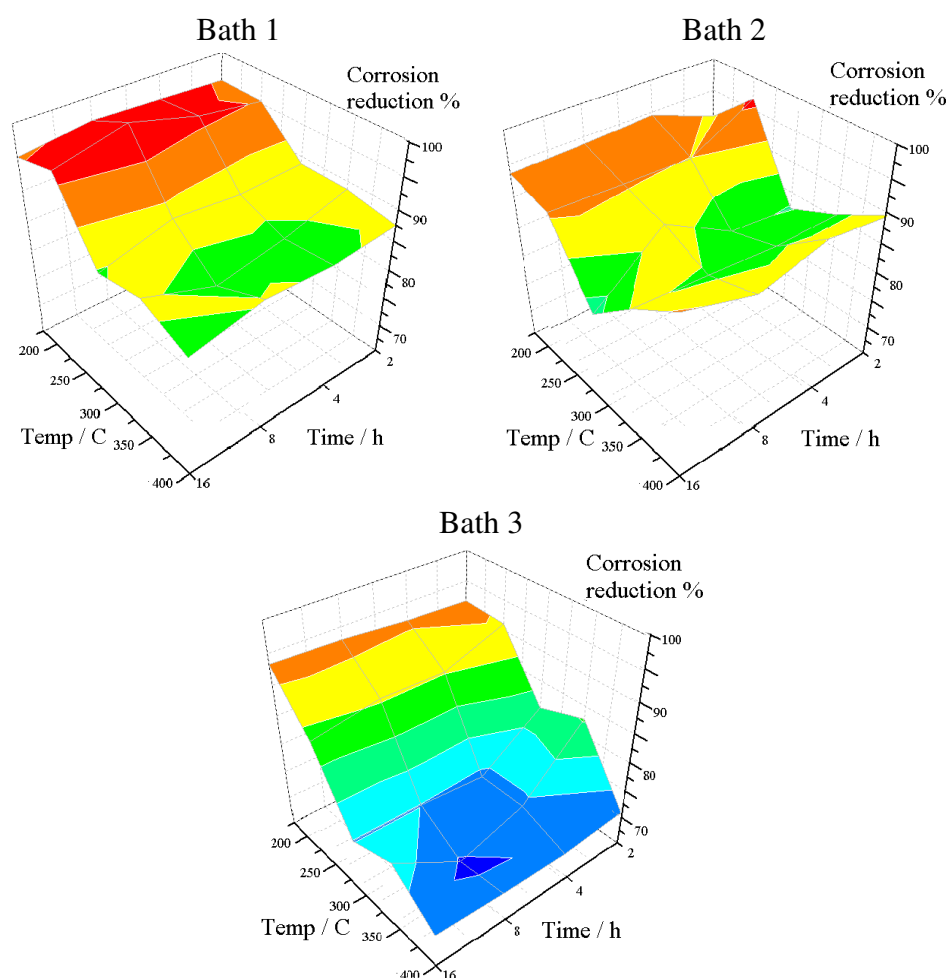


**Figure 4.9:** Corrosion data from three SBF baths showing temperature and time against corrosion rate as a percentage of the control. All three baths differ with the magnitude the heat treatment decreases corrosion rate as well as the optimal condition.

### Corrosion analysis

The optimum heat treatments were studied independently of the other treatments and alongside the standard condition. Hydrogen evolution in SBF shows the treated sample produces 40% less  $H_2$  than the standard, slightly less than the mass loss result. Electrochemistry of the two conditions (potentiodynamic polarisation curves shown in figure 4.11) show agreement with the mass loss, with the heat treated sample more noble than the standard. Tafel extrapolation of the curves, show  $I_{corr}$  is unaffected by the treatment, whereas  $E_{corr}$  raise from -1.88 mV to -1.77 mV). This means the potential for corrosion has been reduced while keeping the rate kinetics the same.

### Microstructure analysis

Optical analysis showed a change in microstructure, particularly around the grain boundaries. These appear coarsened and intergranular precipitates appear to have been emphasised. Using SEM with secondary electrons highlighted the differences in microstructures. Both samples are un-etched, but on the heat treated sample the grain boundaries are



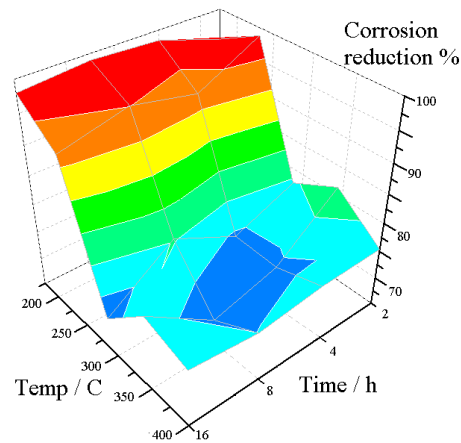


**Figure 4.10:** The mean from the data shown in figure 4.9. The optimum condition is shown to be 8 hours at 350 °C, which lowers corrosion rate by over 30%

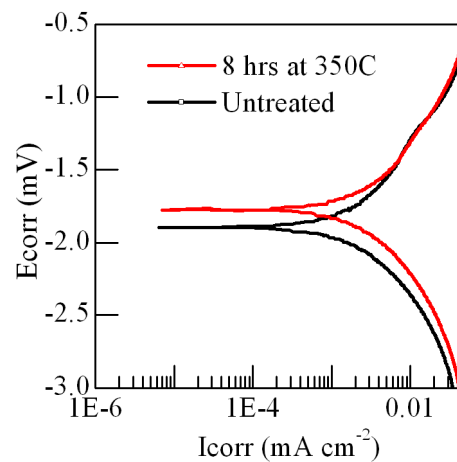


**Figure 4.11:** Potentiodynamic polarisation curves of the normal against heat treated condition (8 hours at 350 °C). The treatments positively shifts the Ecorr value.

visible.

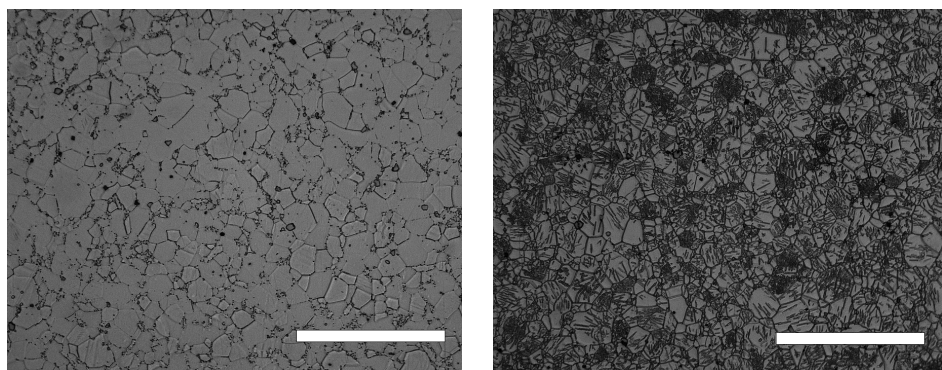


**Figure 4.12:** Optical micrographs of ML4 showing coarsening of the grain boundaries and twinning plans after 8 hours at 350 °C. Scale bar = 50  $\mu\text{m}$ .

The average grain size remained the same (5-10  $\mu\text{m}$ ) during the heat treatment. Fang found that additions of yttrium to magnesium-zinc alloys stopped grain growth during annealing as the yttrium forms grain boundary pinning particles that stop the movement of boundaries [146]. Instead of grain growth the thickening of the current ground bound-

aries is observed as well as twinning planes becoming emphasised. Lorimer reported in recrystallisation of WE43 occurred at grain boundaries, particles and deformation heterogeneities [147]. The change at grain boundaries and intergranular precipitates is possibly the coarsening of precipitates at the heterogeneities.

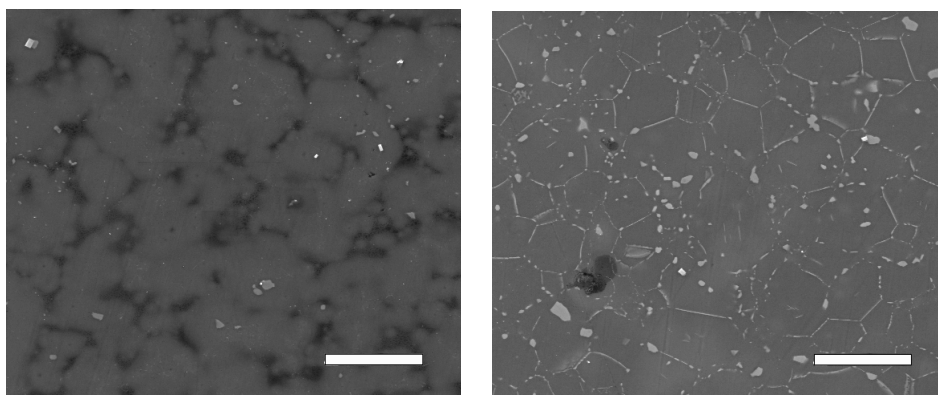


**Figure 4.13:** SEM using secondary electrons. After 8 hours at 350 °C ML4 appears to have the second phase aligned at the grain boundaries. Scale bar = 20  $\mu\text{m}$ .

Using SEM with backscattered electron detectors, which show differences in atomic number, the coarsened areas seen in the optical and secondary electron images were bright white, indicating they are dense with heavy elements. These areas were determined to be sites of new grain nucleation and are areas for the migration of heavy elements. These elements are much larger than magnesium in radius and therefore cause lattice strain in solid solution. Moving to areas of deformation such as new grain boundaries and twinning planes allows the larger elements to reduce the lattice energy.

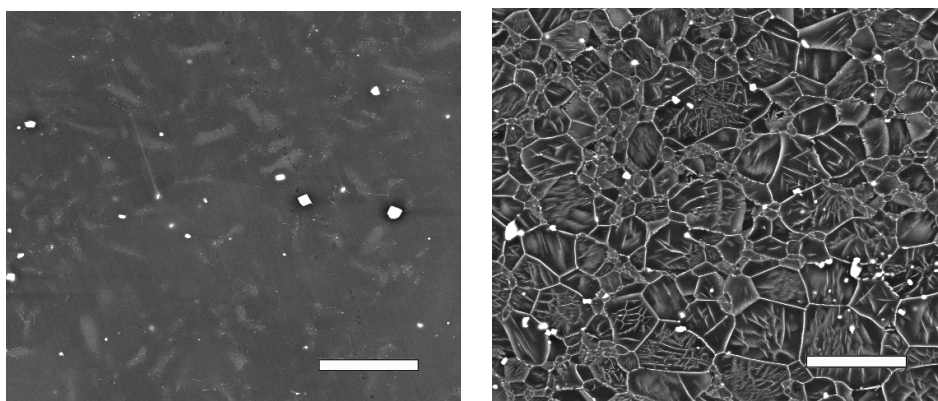


**Figure 4.14:** Back scattered electron micrographs show that the heavy elements (white) have migrated from within grains and the matrix to boundaries and stressed regions. Scale bar = 20  $\mu\text{m}$ .

The change in microstructure has had adverse effects, as these mid grain particles in solid solution or in the form of intermetallics, act to strengthen the alloy and is the reason for their inclusion. But by allowing the migration of these particles and their conglomeration, the strengthening effects are lowered. This is shown in table 4.6, where the 0.2% yield stress has lowered by 10 MPa from 185 to 175 MPa.

The standard condition (figure 4.14) shows the 'clouds' of heavy elements scattered around the structure rather than specific areas. The overall structure appears lighter than

**Table 4.6:** Mechanical properties before and after the heat treatment. The alloy strength lowers considerably

	0.2% Yield /MPa	UTS /MPa	Elongation /%
Standard	185	282	26
8 hours at 350C	175	265	23

the dark centres of the post treated grains. EDX of the standard structure showed that that Nd and Y were present almost uniformly (excluding the second phase crystals) throughout the structure, and hence the light grey microstructure seen in figure 4.14 (chemistries given by EDX are shown in table 4.7). The chemistry of the heat treated microstructure (spot locations shown in figure 4.15) reveals the composition of the light grain boundaries was rich in Nd and Y. Whereas the centre of the grains had much lower concentrations of heavy elements compared to the standard condition. This proves that heat treatment encourages the migration of heavy elements from their original position in solid solution or mid grain particles to heterogeneous regions. It should be also noted that the spot size used for the EDX was larger than the thickness of the light boundary, so the result would include a large quantity of the dark regions, meaning the difference in reality between the phase chemistries would be greater.

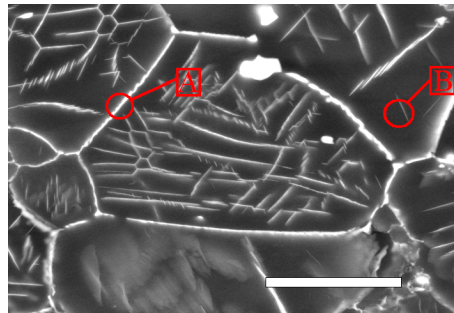


**Figure 4.15:** Positions from which the EDX values in table 4.7 were taken.

**Table 4.7:** Compositions found by EDX analysis of the heat treated sample.

Area	Mg	Y	Nd	Dy	Gd
A	85.1	7.1	2.9	1.2	1.9
B	94.1	3.7	0.7	0.2	0.4

The effects of the heat treated microstructure on corrosion rate in SBF are likely to be due to the movement of the cathodic regions and redistribution into less electrochemically active configurations. Magnesium corrosion in alloy form is well documented and occurs through the galvanic coupling of the anodic matrix, where magnesium is at its highest concentration and the cathodic regions made of elements much higher in the galvanic series. Corrosion occurs at the regions where the cathodic particles and phases meet with

anodic matrix. The anodic matrix loses cations while the cathode gains electrons, meaning magnesium is lost in the matrix while the second phases and particles are protected. An overview of this process in the WExx alloys is presented by Coy [148]. This new microstructure has moved the heavy elements from within the grain to grain boundaries and particles across the microstructure. This migration has effectively removed much of the surface area for cathode to anode contact, and therefore lowered the amount of the microstructure under corrosive attack. This is proved by the lowering in corrosion potential (figure 4.11). The microstructural effect has been shown previously, for instance, Anug used a heat treatment on AZ91D (420 °C for 24 hours) which was found to be effective in dissolving the  $\beta$ -precipitates. This improved corrosion resistance and the author concluded that this lowered the microgalvanic coupling between cathodic  $\beta$ -phase and anodic  $\alpha$ -matrix. This has since been studied by Zhou, by using T4 (445 °C for 24 hours) and T6 (200 °C for either 8, 16 or 24 hours) heat treatments on AZ91 and came to the same conclusion, albeit without such reductions in corrosion rates [149]. Using heat treatments specifically to improve corrosion resistance however are rare, most trials of heat treatment against corrosion are designed to show effects of the artificial aging processes, which for most alloys is carried out at 250 °C or below and as shown in figure 4.10 are ineffective in reducing corrosion rate. Authors investigating this have found as much [68][150].

In SBF solutions the corrosion reducing effect of this structure is made greater by the resistance offered by the phosphate and carbonate reactive film produced on magnesium alloys in SBF ([78][75] and chapters 7 and 5). This film protects the anodic regions from chloride attack which  $\text{Mg}(\text{OH})_2$  cannot do. The film is however is still undermined at the interfaces of anode and cathode so that it is peeled away and new matrix is revealed for corrosion. With the grains much lower in cathodic sites, this semi-passive film can offer far greater corrosion protection as the sites of undermining and peeling are lowered.

### **Post drawing heat treatments for stent tubing**

The magnesium alloy, ML4 has shown to give corrosion improvements of up to 30% when given a short ( $\sim 4\text{hr}$ ) annealing after extrusion at around 300-400 °C. For production into cardiovascular stents, the extruded 9mm rod as previously used in this section are drawn into thin walled tubes for laser machining into cardiovascular stents. After drawing a post treatment of 15 minutes at 450 °C (referred to as R91) was applied to the material to aid mechanical properties. As an alternative following from the improvements seen in this chapter, another heat treatment was applied; 350 °C for 45mins (referred to as V09). A much shorter time was used instead of the 8 hours previously, to take into account the samples relative thickness and size. These two treatments were tested using SBF by hydrogen evolution. Slightly lower corrosion rates were seen in the original R91 treatment (table 4.8). The respective microstructures are shown in figure 4.16 and show the coarse grain boundary structure associated with the corrosion resistance had not been accomplished with the V09 treatment. Therefore further treatments were conducted to try

and create this microstructure.

**Table 4.8:** Corrosion rates of stent tubing in R91 and V09 condition found by hydrogen evolution in SBF after 18 hours.

Condition	H <sub>2</sub> /mL
R91	0.0445
V09	0.0501

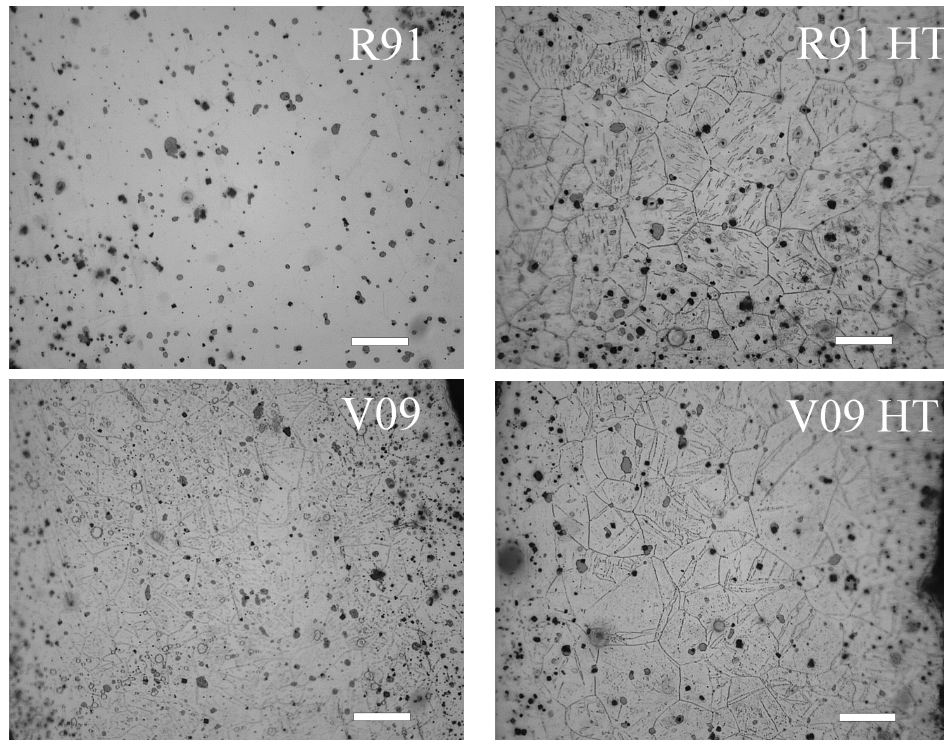


**Figure 4.16:** Original and post heat treatment microstructures, Scale bar = 10  $\mu\text{m}$ . The post treatment samples shown represent the best replication of the structure seen in figure 4.12 from a range of conditions trialled.

Stent tubing in both R91 and V09 condition was annealed for 2, 3 and 4 hours at either 300 °C or 400 °C. The coarsened deformation microstructures are most clearly seen in both respective starting conditions when R91 is treated at 400 °C for 2 hours and V09 at 300 °C for 3 hours (figure 4.16). When these stent tubes are corrosion tested by hydrogen evolution, improvements over their starting conditions was not achieved.

Explanations for this are most likely due to the microstructure, which although showed more coarsened grain boundaries than the original structures, were still different from the optimum structures achieved when the extruded cylinders were treated. The original microstructures were also different from that of the extruded rod used previously. Far greater work appears in the microstructure of the stent tubing, and this has been shown to stop the effects of the annealing process on corrosion; figure 4.7 in the previous section shows the improvement in corrosion rate for the standard microstructure, but not the worked microstructures. The annealing process enables the cathodic particles and elements to move

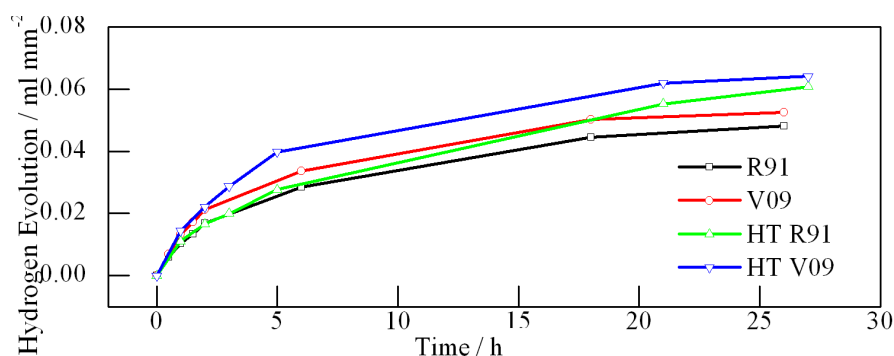


**Figure 4.17:** Hydrogen evolution in SBF for the stents in their post drawn state and after optimal heat treatments. No improvement is seen.

to sites of strain, which in a highly worked structure is throughout the majority of the grain, rather than just the grain boundaries.

### 4.3.3 Conclusions

The annealing effect seen in the previous section for the worked structure was shown to be real and this was optimised to achieve the best reductions in corrosion rate at 350 °C for 8 hours. The amount the annealing affects corrosion rate and microstructural changes is highly dependent on the original microstructure. Highly worked structures from poor extrusions or the drawing process do not achieve gains in corrosion resistance from annealing. The heat treatment gives recrystallisation by nucleation of new grains and precipitation of heavy elements to the heterogeneous sites (most commonly grain boundaries). This lowers the amount of galvanically coupled regions in the microstructure and therefore lowers the electrochemical potential for corrosion of the material. The heat treatment also increases the stability of the semi passive reaction film by lowering the amount of undermining and peeling that occurs.

### 4.3.4 Further Work

Detailed analysis of the mechanism of corrosion resistance offered by these heat treatment needs to be investigated. conducting studies in higher resolution so that the precipitation at the grain boundaries, both in terms of crystal structure and chemistry as been seen in detail. Techniques such as electron backscattered diffraction (EBSD) can be used to show grains and their orientation. Kelvin probe force microscopy (KPFM) can be used to show the corrosion potentials of the particles and microstructure features formed by the treatment, and thus prove if the theory of cathodic element conglomeration is accurate. Regarding future alloy development. The effects of these short, sub solidus treatments are investigated in the new biomedical alloys reported in chapter 5.

## 4.4 Stress corrosion cracking

Material used for biomedical testing by commercial partners was in some cases failing before the expected lifetime of the implant. It was put forward that this could be the result of stress corrosion cracking (SCC), and thus an investigation was set out to study if SCC was occurring in the alloys currently being trialled under biological conditions.

### 4.4.1 Materials and methods

The three magnesium alloys primarily under investigation were ML4 (DF9319), 675 (DF9400) and Elektron 21 with added gadolinium (DF9402). The material was made at Magnesium Elektron by the procedure outlined previously (section 4.2.1). The 9mm rod was machined into either single or double SCC testing samples (figure 4.18).

**Table 4.9:** Alloy compositions given by wt%. Total impurities (Fe, Ni, Cu) are less than 0.006 wt% for all three alloys.

	Y	Nd	Gd	HRE(misc)	Zr	Zn
Elektron 675	6	-	6.5-7.5	-	0.35-0.4	-
ML4	3.7-4.3	2-2.4	n/a	1	-	-
Elektron 21	-	2.7-3.1	7	-	0.3-0.9	0.2-0.43

**Table 4.10:** Ultimate tensile strength when tested in ambient air by static loading.

	Average UTS
WE43	409.5
675	467
Elektron 21 +7 wt% Gd	372

### Constant load static fatigue test

These tests were designed based upon ASTM F519-97. Constant load tests consisted of a single notched sample (schematic shown in figure 4.18) suspended in a frame. A lever arm connected the sample and the load (figure 3). Each sample was loaded to a pre-calculated stress. This stress was a known percentage of the notched ultimate tensile stress (UTS) of the material, previously tested. Loading consisted of weights suspended from the lever arm, which were all loaded within 5 minutes and without excessive movement to stop extra stress on the sample. The test was first conducted for each alloy at ambient air (roughly 20 °C with a relative humidity between 60 and 65%). The results of the ambient air test were used as the control for each material.

To analyse biological SCC, the same test was set up, but with the addition of a fluid reservoir around the notched tensile sample. The samples were loaded as previously,

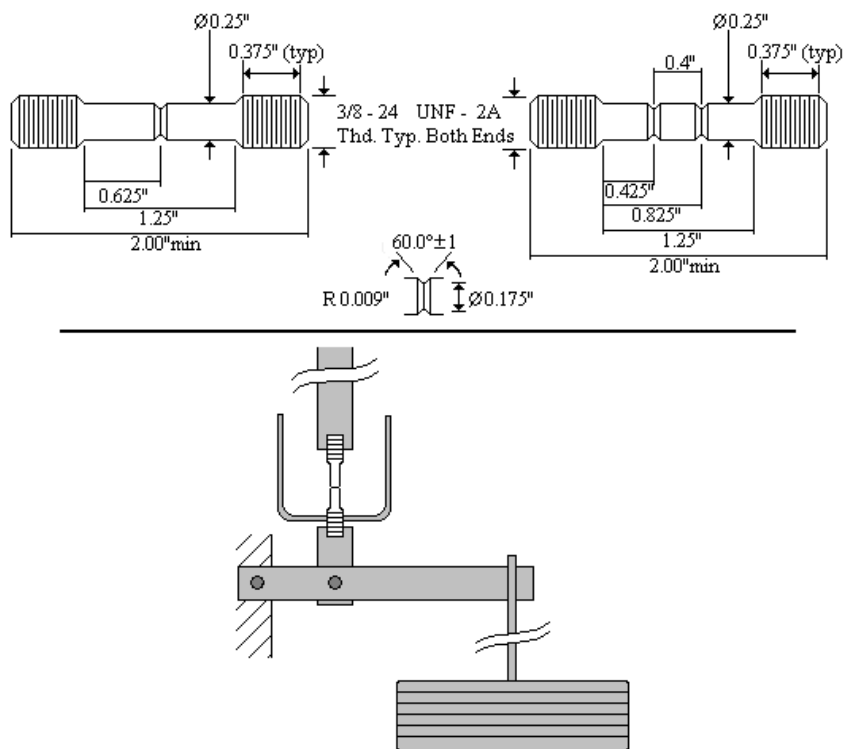


**Figure 4.18:** Top shows the design of both the single and double notched samples. Bottom; a schematic of the static load rig used to test both single and double notched samples.

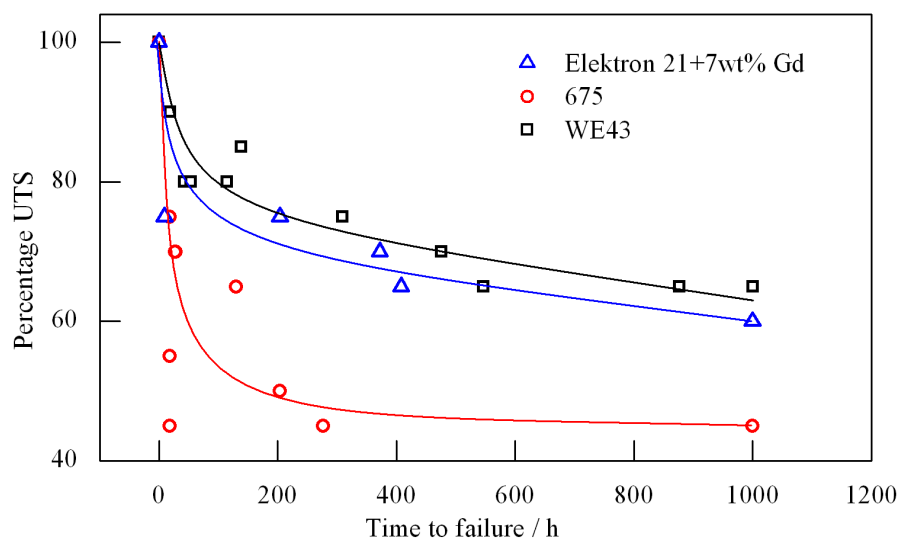


**Figure 4.19:** Time to failure against stress as a percentage of UTS while submerged in SBF. 675 fails at far lower % stress than WE43 and Elektron 21 + Gd. Samples marked as 1000 hours, were taken off test without failure.

then 150 ml of SBF solution was added to the reservoir. This covered the notch and approximately up to the bottom of the upper screw thread. Samples were loaded to a pre-calculated stress, which was a percentage of the UTS of the material previously tested (table 4.10).



### **Double notched samples**

For qualitative data, double notched samples (schematic shown in figure 4.18) were used in place of single notched, as this leaves an unfractured notch which replicates the fractured notch at the moments before failure. These were set up with the same method as above and loaded to stresses which would approximately last 200 hours before failure. Therefore ensuring SCC occurred where possible instead of cross sectional loss through corrosion (on test too long), or through standard failure from simply data spread of the ambient air fracture loads (tested too heavy).

## **4.4.2 Results and Discussion**

### **Static loading**

Work done by Magnesium Elektron had used static load testing with single notched tensile test samples in SBF to determine quantitatively the extent of failure in the alloys currently being trialed. Samples were loaded first in ambient air to as a control with 90% of their UTS. For all three alloys this resulted in the sample lasting beyond 4 weeks. For SBF testing, samples were loaded in decreasing stresses starting at 90% UTS, then down in 5% amounts until the samples lasted over 500 hours. This was deemed a crude approximation that SCC was not occurring if the samples were still maintaining stress after such a time period. The results of this investigation are shown in figure 4.19. The figure shows that all three alloys demonstrate some susceptibility to the combination of stress and corrosion. The alloys with 80-90% yield all break within 100 hours apart from one WE43 sample (85% UTS, 186 hours). To lose 80% of the UTS after less than 100 hours corrosion could mean the cross sectional area has been corroded by 80-90% by either pitting or general corrosion. Micrographs of the notched samples show extensive pitting, which support this explanation. True stress at failure however can only be calculated with three dimensional scanning so that all pits can be accounted for. WE43 and Elektron 21 + Gd, both appear resistant to failure at loads under 80% UTS. No failure is seen when loads drop below 65%. Alloy 675 however appears less resilient and still fails early until loads are dropped to well below 60%. Alloy 675 only survives the tests when the load is 45% UTS, and this is only in one out of the three samples.

It can be concluded from the initial study that 675 is highly susceptible to some form of SCC cracking as this is the highest strength alloy on test, but fails under the lowest loads. WE43 and Elektron 21 + Gd, however are inconclusive without further analysis.

### **Optical analysis**

Initially, analysis of the alloy performance under stress corrosion conditions used the single notched samples. These proved limited in the information they could give, as the fracture surface was immediately exposed to the SBF, meaning if failure occurred at night, the surfaces were corroded so that the surface was now usable. Some information however

was obtained. Figure 4.20 shows a selection of images taken at the edge of the fracture surface. Pitting is seen prevalent across the surface, with small cracks a rare occurrence in WE43 but pictured here.

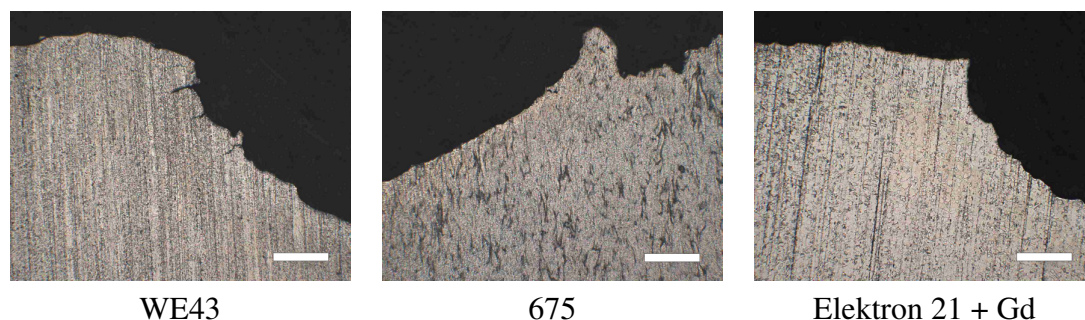


**Figure 4.20:** Optical micrographs taken at the edge of the fracture from three magnesium alloys. Scale bar = 200  $\mu\text{m}$ .

Double notched samples were used to show a replica of the notch moments before failure as the conditions of stress and corrosion are near identical to the failed notch. Figure 4.21 shows examples of the un-failed notches from the WE43 and 675. WE43 suffers from large pits throughout the notch. The pits look greater in severity within the notch compared to the surrounding material, indicating a correlation between stress and corrosion rate.

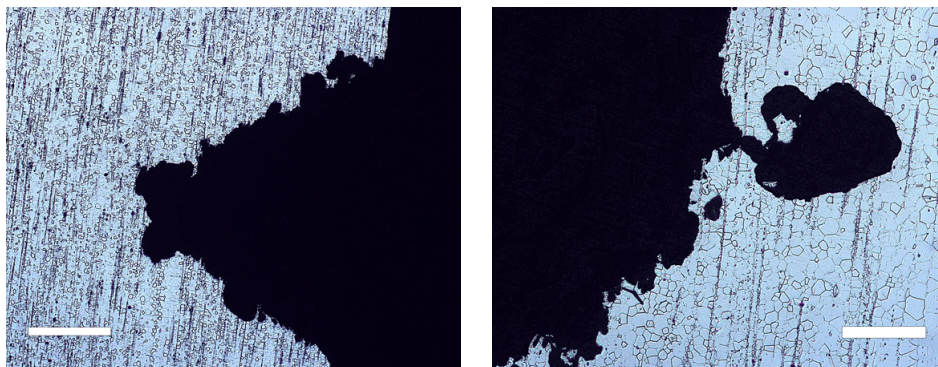


**Figure 4.21:** Pitting at the surviving notch from a double notched WE43 sample after corrosion in SBF. Scale bar = 100  $\mu\text{m}$ .

The failure mechanism in 675 is clear; figure 4.23 shows a crack nearly propagating across the entire width of the surviving notch. The notch also has less pitting corrosion than WE43, reflecting the alloy's lower time to failure and the inherent corrosion resistance in SBF comparative to WE43. Higher magnification images of the cracks reveal transgranular cracking, highlighted by the arrows in figure 4.22.

675 alloy's susceptibility to cracking under stress corrosion conditions explains why it yields at most stresses above 40% UTS in SBF whereas the other alloys seem to withstand stresses 60-65% UTS (which in fact is a poor estimate due to the large losses in cross sectional area due to pitting). It can be concluded that the mechanism of failure for WE43 and Elektron 21+Gd is the result of corrosion pits. The pits are seen to reduce the cross sectional area of the notch and therefore increase the overall stress within the remaining

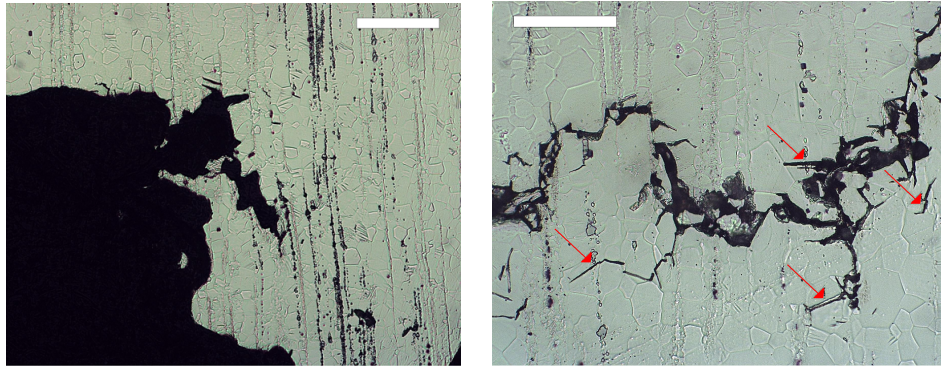


**Figure 4.22:** Transgranular cracking at the surviving notch from a double notched 675 sample after corrosion in SBF. Scale bar = 50  $\mu\text{m}$ .

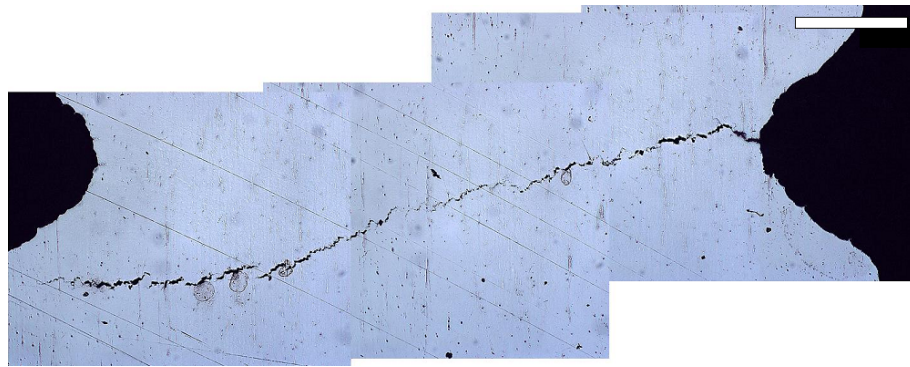


**Figure 4.23:** Four combined optical micrographs highlighting the extent of cracking in 675 alloy. Scale bar = 500  $\mu\text{m}$ .

material. Pits also act as local stress raisers, meaning fracture is initiated quicker and propagates faster, leading to catastrophic failure with less overall stress than a comparative smooth walled cylinder under similar loads.

Pitting corrosion alone however does not fully explain the failures seen in figures 4.20 and 4.21. WE43 is seen to crack in figure 4.20 not simply pit. Locations of pits are also seen in areas of higher stress rather than the thick stems of the tensile samples. Figure 4.21 reveals a deep subsurface pit at the thinnest point of the surviving notch. Analysis of the thicker sections of the sample show no deep pits, only shallow wide and elliptical pits. Pits are known to initiate at sites of physical damage which open the surface film or protective layer [151]. The large pits seen at the notch could therefore be the result of pitting corrosion stimulated by cracks. These cracks are most likely formed in a similar mechanism to the large cracks seen in 675, but with lower driving force for propagation. The cracks reveal unprotected magnesium alloy and pitting occur fast and engulfs the crack that started it. Therefore it is hypothesised that WE43 is also susceptible to SCC cracking, but with rates of crack growth lower than the rate of pitting corrosion stimulated by them. 675 under general corrosion is more resistive than WE43 in SBF, thus WE43 pits would be likely grow faster.

### Susceptibility to SCC

Alloy 675 demonstrated high susceptibility to SCC by transgranular cracking, causing the strongest, less corrosive alloy on test to fail at the lowest yields. WE43 was concluded to also crack by the SCC process, but for propagation to be slower than pitting corrosion growth. Elektron 21 + Gd however showed no signs of SCC only very high levels of generalised pitting, with no difference between high and low stress regions of the sample.

The cause of transgranular cracking (TC) in SCC circumstances is the cause of some debate, but where transgranular cracks are observed all the suggested mechanisms involve either cleavage fracture or hydrogen embrittlement (HE) [151][152][153]. Cleavage fracture, in all the proposed mechanisms involves a strain induced surface film crack, localised pit or dissociation to initiate a crack throughout the grain until the grain boundary halts the propagation. The fundamentals of hydrogen embrittlement are that it causes the material's resistance to crack propagation to lower at the site of the crack tip. The most prominent mechanism of HE suggested by researchers with magnesium alloys are the stress-induced hydride formation [152], but there are other mechanism commonly used to describe failure such as the hydrogen enhanced local plasticity process (HELP), absorption-induced dislocation emission (AIDE), and hydrogen enhanced decohesion (HEDE). These mechanisms and the disagreement between researchers and investigations is detailed by Winzer [151].

To determine why 675 fails with TG-SCC, the models above have to be placed in context with the results of this investigation. 675 showed high susceptibility, WE43 medium and Elektron 21 + Gd none. The chemistries of the alloys suggest a correlation with SCC and Y content. Gd (6wt% in 675) appears to have no effect as its high concentrations in the Elektron 21 alloy. Zirconium is also in all three alloys and has been shown to have little effect on SCC by Busk [151]. Therefore the high concentrations of Y (7wt%) in 675 and medium concentrations (4wt%) in WE43 could be the cause. Y is found within the grain in the form of the  $\alpha$ -matrix, but primarily forms precipitates. Particle and phase analysis for 675 has not been completed in the investigation, and therefore can only be assumed, unlike ML4. Thus a detailed explanation cannot be drawn, especially with the lack of published material on SCC mechanisms regarding Y or Gd based alloys. A likely cause would be the greater lattice strain caused by the larger Y atoms within the matrix and as small particles. The HELP model suggests that these become sites for the accumulation of hydrogen. The hydrogen as these regions eases the movement of dislocations when the external stress causes a drives force for lattice movement. Hydrogen does this by shielding the fields of stress of the dislocations against each other, meaning two dislocations which would normally repeal and cause local embrittlement, do not and therefore localized ductility and drop in yield stress occurs. This leads to a sliding localization which then forms a micro pore. Under shearing, the pore becomes a micro crack. Much greater work has to be completed to give a thorough hypothesis, not just for 675, but so that future alloy development is not hindered by SCC problems. However, this investigation has

shown that for future alloy development, high amounts of yttrium are to be avoided.

#### 4.4.3 Conclusions

The alloy 675 is highly susceptible to SCC. The mechanism of failure is mainly TG-SCC. Elektron 21 + Gd shows no SCC effects and WE43 is unclear, however the heterogeneous nature of the pitting suggests pitting flows initial cracks at high stress points, and there after these pits result in failure.

The cause of TC-SCC seen in 675 can only be hypothesised with such limited data, although hydrogen embrittlement seems a logical explanation, with the high yttrium content of the alloy fitting into the HELP model.

675 and development based on this alloying system have been stopped for use biomedically.

#### 4.4.4 Further Work

SCC and susceptibility will be continually be measured for all future alloys as SCC is fundamental to the working life time of any implant. Work on SCC will continue to be based on the static load method used in this chapter. This method is adequate for initial susceptibility trials, and the opticals can show important information, but static testing is limited for analysis into the true mechanisms and models of failure. Ideally, these need to be investigated, specifically for *in vitro* corrosion. However, detailed mechanisms and models of SCC failure in magnesium are widely disputed amongst its researchers [152] and thus for development purposes, investigating in detail the fracture mechanics seen under SBF conditions could be fruitless even with a large outlay in time. There is instead a need to link alloy susceptibility to chemistry and microstructure. Future alloy development would benefit from knowledge of what elements, microstructure features and conditions to avoid in order to stop SCC.



## NEW ALLOY COMPOSTIONS FOR BIOMEDICAL APPLICATIONS

### 5.1 Introduction

Previous work reported in chapter 4, *in vivo* studies by commercial partners, and external publications concluded that current magnesium alloys were too corrosive for implant applications. Witte reported hydrogen bubbles when magnesium pins were implanted into guinea pig femur [11]. Chapter 3 reported that high corrosion rates would lead to localised cell death by rise in pH. The commercial partners using the material required a longer working lifetime. Chapter 4 reported that using sub solidus heat treatments could lower the corrosion rate of the engineering alloy WE43 by 20-30%, but this came at a slight cost to the mechanical properties. Ideally an entirely new alloy would be created which performs specifically for *in vivo* applications.

This chapter outlines the use of the alloying additions to existing engineering alloy systems. Pre-existing systems were used to help to predict credible mechanical and corrosion properties beforehand. The systems used were Elektron 21 and Elektron WE43. The high strength and low corrosion 675 alloy was ruled out due to the problems with SCC, discussed in chapter 4.

The elements added to these systems were gadolinium, calcium and erbium. Gadolinium has been known to Magnesium Elektron as a means of increasing mechanical strength since the advent of WE43 and has recently been employed in the new Elektron 675 ultra high strength alloy and Elektron 21 casting alloy. Gadolinium's maximum solid solubility in magnesium is 23.49 % but falls to 4% at 200 °C, the typical aging temperature. Equilibrium precipitation when solid solubility is exceeded forms the beta phase  $Mg_5Gd$ . Keibus reported this  $\beta$  phase to be beneficial on corrosion rates [154]. The  $\beta$  phase precipitates take many forms according to the post casting aging mentioned but also due to the co-alloying amounts of Nd [155]. Addition of Nd to Gd containing alloys reduces the solid solubility of Gd meaning precipitates are formed with lower amounts of Gd. The precipitation sequence of these rare earths in magnesium, discussed by Apps occurs in four stages,  $Mg_{ssss} \rightarrow \beta'' \rightarrow \beta' \rightarrow \beta_1 \rightarrow \beta$  with the initial  $\beta''$  and  $\beta'$  phases being  $DO_{19}$



in structure and responsible for peak hardness. With further aging, the phase turns to  $\beta$  in its FCC form [156]. Elektron 21 uses this to its advantage alloying with low amounts of Nd and Gd so that precipitation concentrations are just met. Alloy 675 uses higher amounts of Gd (7wt%) but no Nd and therefore uses high amounts of Gd in solution.

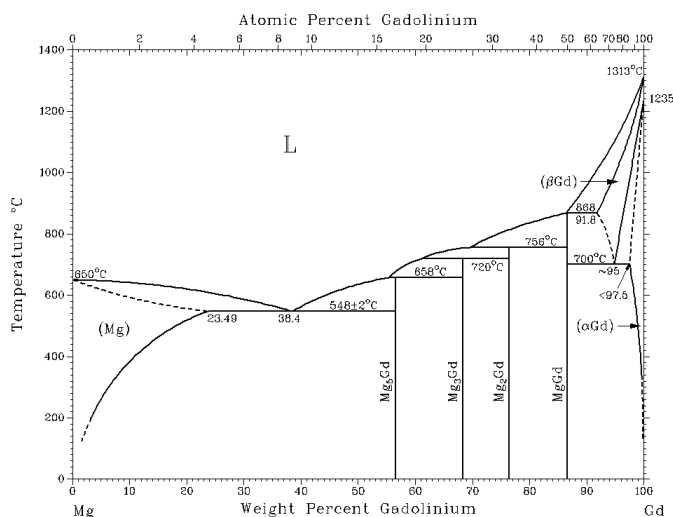


**Figure 5.1:** Phase diagram for magnesium and Gadolinium.

**Table 5.1:** Mass loss of various alloys based on Elektron 21 with added amounts of Gd. 1.3wt% is standard. Corrosion took place in cell culture media.

wt% Gd	Mass loss /mpy
1.3	43.0±8.1
6	28.7±5.6
8	27.2±4.7
12	23.9±6.7

Recently Magnesium Elektron had found that 675 was nearly 25% less corrosive than WE43 in SBF tests. Gadolinium was thought to be a potential cause of this and increasing the amount of Gd in Elektron 21 was confirmed by mass loss data (table 5.1). Gd was seen to have a direct effect on SBF corrosion rate. Although in Elektron 21 this was only seen in high amounts (>6 wt%). In this study, Gd has been added at 8 wt% and 12-15 wt% (exact amount unknown due to calibration on the spectrometric analysis apparatus) to Elektron 21 and at 4 wt% to ML4. A low amount was used in ML4 as this already contains Gd and has 2-2.4% Nd which as stated lowers the solubility.

Calcium has been the source of a large amount of alloy development work in the biomedical context of magnesium alloys. When this investigation was conceived, alloy development was in its infancy with the majority of publications still using current engineering alloys. Calcium containing alloys along with additions of zinc had been the only purpose made investigations for the *in vivo* application. Calcium seemed to be an obvious addition when considering the orthopaedic applications of the alloys and also the



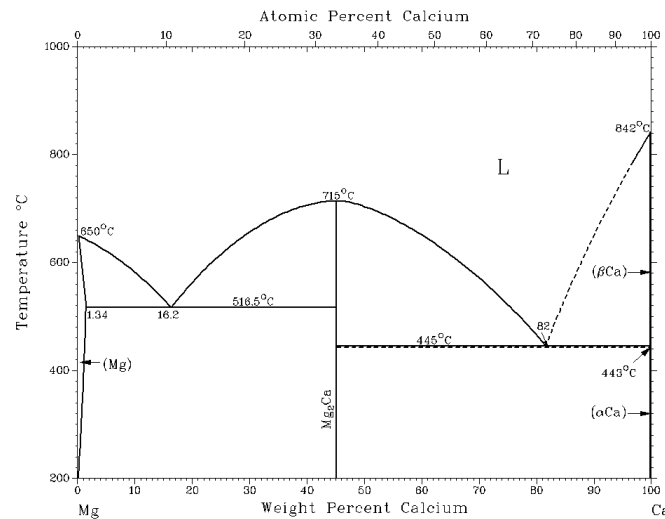


**Figure 5.2:** Phase diagram for magnesium and Calcium.

element's osteo-conductivity. This is cited as the reason for its introduction to alloys. However research with these alloys showed that Ca addition lowered corrosion rates *in vitro* and *in vivo* [27, 50, 96–101]. Albeit this came at the expense of mechanical properties [96, 97, 100]. Calcium's maximum solid solubility in magnesium is 1.34 wt% which lowers with temperature meaning only low about have to be added in order to precipitate out its equilibrium phase  $\text{Mg}_2\text{Ca}$ .

At the point of this investigation, conclusions as to how additions of calcium lowered corrosion rate had not been fully discussed, however Kannan, 2008 [96] reported that the polarization resistance of the surface film developed on the Ca alloys was 5 times greater than the non Ca alloy. A fair assumption at this point would be the formation of a calcium phosphate/carbonate layer aided the protection of the substrate material. Due to these results, Ca was added to both Elektron 21 and WE43 in 3 wt% quantities. Three wt% was used so that any potential osteoconductive effects could be seen, whereas a lower concentration might not be effective. Too much calcium however, is known to lower corrosion resistance by the formation of large quantities of  $\text{Mg}_2\text{Ca}$  which cause micro-galvanic couplings within the matrix [97].

Erbium was an unknown element in terms of addition to magnesium. It had been used within other specifications of other heavy rare earths, but rarely discussed independently for its effects either mechanically or on corrosion. Rosalbino in 2005 [157] was the sole publication to this author's knowledge regarding erbium additions to magnesium alloys (in this case AM60). Erbium is highly soluble in magnesium with a maximum solubility of 33.8 wt% and stays in solid solubility up to >15wt% when temperatures are lowered [158]. In binary form this leads to high strength and ductility [158]. For this investigation 8wt% was added to ML4. If solubility is exceeded however, the phase  $\text{Mg}_{24}\text{Er}_5$  is precipitated.

The aim of this investigation was therefore to evaluate the corrosion properties of these new alloys under *in vitro* conditions, determine the cause of any improvement in

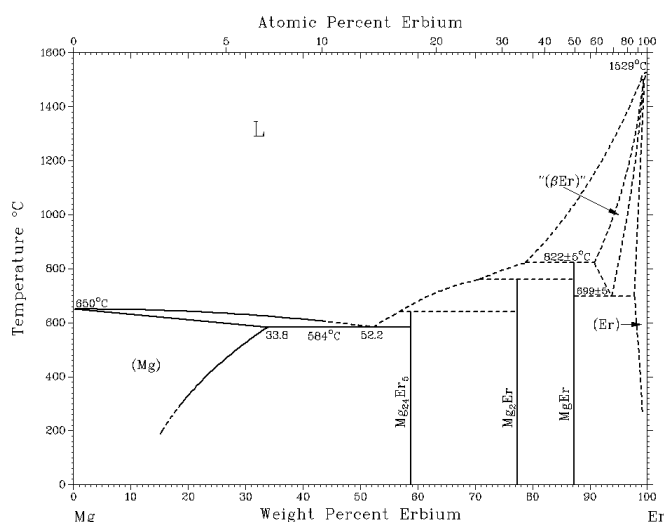


**Figure 5.3:** Phase diagram for magnesium and Erbium.

corrosion rate and thus an understanding for future alloy development.

## 5.2 Materials and methods

The six new alloys made for this investigation are listed in table 5.2. The material was made at Magnesium Elektron by melting pure magnesium ingot with the appropriate alloying elements. Once molten, the metal is stirred and a small casting was made for chemical analysis by Optical Emission Spectrometry (OES). If this falls within specifications the metal was ready to cast. Molten metal was then poured from the crucible into the mold. Once solidified and air cooled, the casting was machined into 75 mm diameter billets for extrusion.

The extrusion procedure required, pre heating of the billet, die and billet container to specified temperatures. The material was then extruded into 9 mm bar. For SBF corrosion baths, the rods were machined into 30 mm by 6 mm cylinders. For all other tests, the rods were machined into 9 mm diameter by 3 mm thick discs. The methods used in this chapter are all outlined in chapter 4 apart from the GDOS surface analysis technique.

### Glow emission discharge optical spectroscopy

Reaction layer cross sections were examined by glow emission discharge optical spectroscopy (GDOS) using a GD-Profilr 2 (Horiba Jobin Yvon). This operated in the rf-mode at 13.56 MHz. A 4 mm diameter copper anode and high purity argon gas was used. The emission responses from the excited sputtered elements were detected with a polychromator of focal length of 500 mm with 30 optical windows. The emission lines used were 130.21 nm for oxygen and 383.82 nm for magnesium. The yttrium or calcium response was recorded using a monochromator adjusted to the corresponding lines at 393.366 nm, 417.732 nm and 371.029 nm for Ca, Nd and Y respectively. The

**Table 5.2:** Alloy composition used in the chapter. Additions on Gd, Ca and Er were added to ML4 and Elektron 21. Heavy Rare Earths (HRE) are added combined in ML4. Total impurities (TI) equates to the sum of Fe, Ni and Cu.

Melt No.	Y	Nd	Gd	HRE	Zr	Zn	Er	Ca	TI
MI0009	3.7-4.3	2-2.4	n/a	1	-	-	-	-	0.003
MI0010	-	2.7-3.1	8	-	0.3-0.9	0.2-0.43	-	-	0.004
MI0011	-	2.7-3.1	12-15	-	0.3-0.9	0.2-0.43	-	-	0.000
MI0012	3.7-4.3	2-2.4	4	1	-	-	-	-	0.004
MI0013	3.7-4.3	2-2.4	n/a	1	-	-	-	3	0.004
MI0014	-	2.7-3.1	1.1-1.7	-	0.3-0.9	0.2-0.43	-	3	0.004
MI0029	3.7-4.3	2-2.4	n/a	1	-	-	8	-	0.011

monochromator allows monitoring of one element during measurements. The elemental depth profiling was carried out at argon pressure of 650 Pa and a power of 35 W, with a data acquisition time of 0.01 s. Prior depth profiling, pre-sputtering of a monocrystalline silicon wafer was undertaken to clean GD source. Data fitting analysis of the different elemental depth profiles was performed using a standard user-defined curve fitting function of IGOR Pro software (WaveMetrics).

## 5.3 Results and discussion

### 5.3.1 Characterisation

The new alloys were first examined by SEM (figure 5.4) to analyse the phases present within the microstructures. The ML4 (MI0009) reference material shows a clean sparsely populated structure, with phases that appear evenly dispersed and random in shape. Using EDX (figure 5.5) the large particles are shown to be a Nd-Mg particle rich in Nd. The smaller particles are either Y-Mg-Nd particles with high Y/Nd ratio or low Y/Nd ratio. The matrix material contains amounts of REs similar to the overall composition of the material.

MI0010 (figure 5.6) has far more particles than MI0009, and these look to be of two types, large angular phases, and randomly shaped smaller particles. Chemical analysis shows that the large crystal like phase is composed of Nd-Gd-Mg, although the most of the Mg consistent is likely to be from the surrounding matrix. Smaller phases look to have higher Gd/Nd ratios closer to 1:1. The majority of the Gd in the alloy, which is added at 8 wt%, appears in the matrix at 6.4 wt%, nearly as high as the particles analysed. The solubility of Gd in Mg is far below this, and therefore it is probably present in smaller particles not seen as the post-casting treatments for extrusion, such as the billet pre-heating and recrystallisation process during the extrusion would have allowed Gd to precipitate out of the matrix. Adding even greater quantities of Gd, as in MI0011 gives rise to a microstructure that looks densely packed with small second phase particles. The same

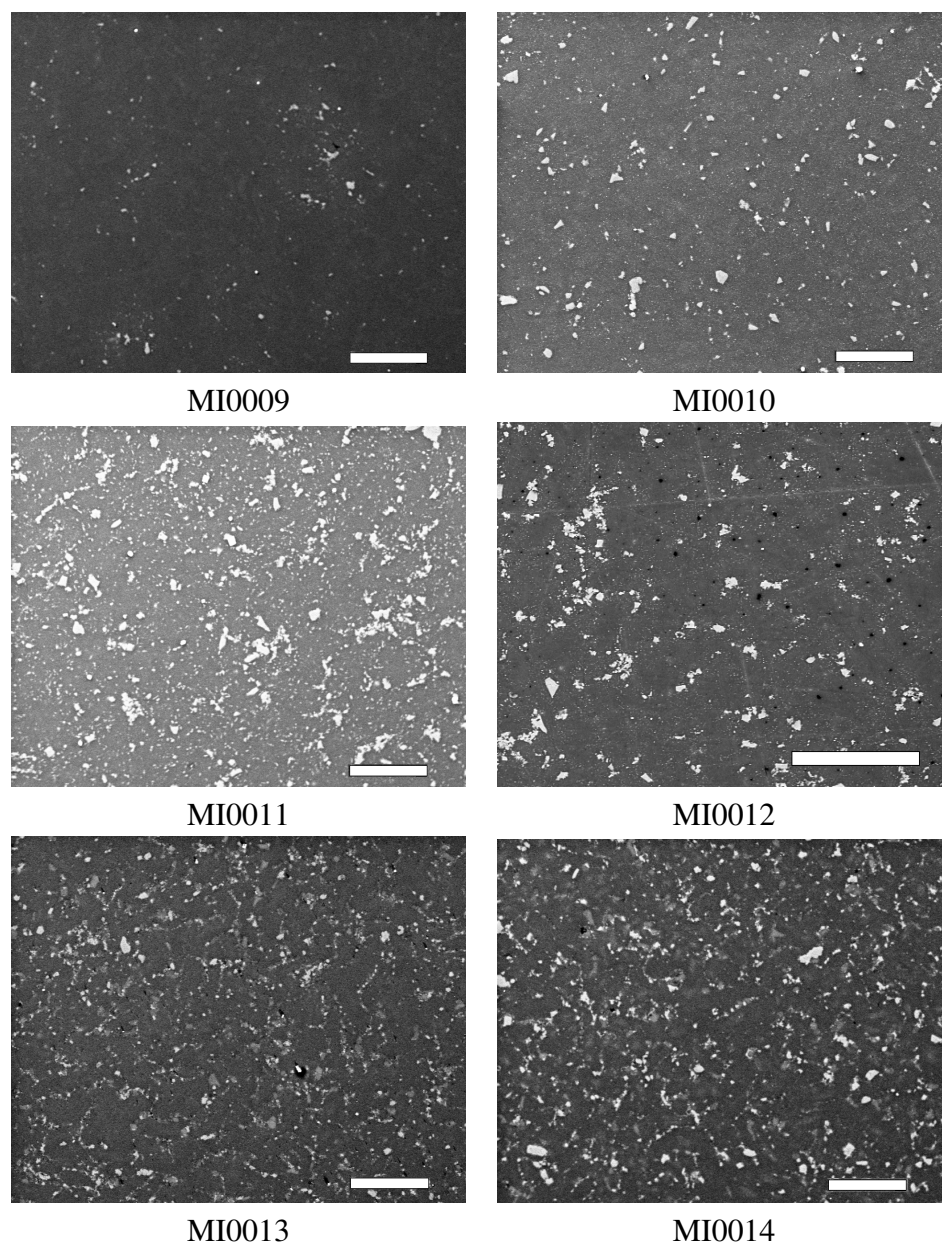
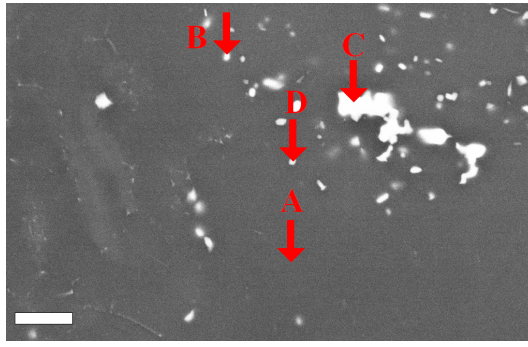


**Figure 5.4:** Scanning electron micrographs of the new alloys microstructure. Scale bar = 50  $\mu\text{m}$

general appearance of the particles (some angular others rounded and random) is seen in MI0010 but in greater density. The particles measured with EDX reveal much greater concentrations of Gd than in MI0010, with Gd/Nd ratios around 3:1 for the angular second phase, but almost totally Gd in the large rounded second phase. The matrix has also increased from 6.4 to 10.6 wt% Gd.

The effects of Gd in ML4, which is similar to Elektron 21 with added Yttrium, is a microstructure not dissimilar to MI0010 even though only 4 wt% Gd had been added. Under BSE the microstructure becomes dense with small micron sized particles which was not seen using secondary electron. These are too small to target with EDX. The larger second phase appear similar in shape and contrast under BSE. EDX on different particles reveals no distinction between spots, with all phases comprising of Nd, Y and Gd in a ratio of 4:3:2. Yttrium is more prevalent in the matrix than the other rare earths



Arrow	Element				
	Mg	Y	Nd	Dy	Gd
A	86.1	4.0	0.9	0.2	0.8
B	50.3	34.3	5.6	2.0	1.4
C	61.6	3.5	30.5	-	-
D	67.1	13.9	7.2	1.1	1.0

**Figure 5.5:** Microstructure of ML4(MI0009) taken by SEM with BSE, scale bar = 50 $\mu$ m. The table shows the chemistry in wt% of the spot points indicated by arrows A-D.

as seen in the ML4 control.

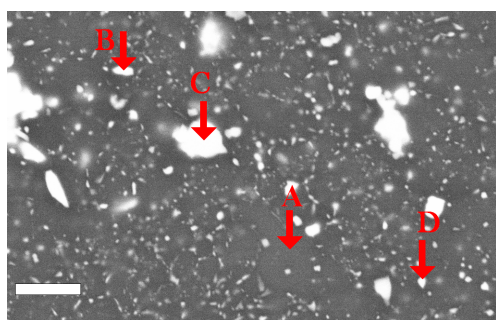
The two calcium alloys appear darker in contrast with dark and light areas of second phase. Under BSE it can be seen that these are not just optical effects and are differences in atomic weight. MI0014 had more lighter areas of second phase than MI0013. EDX analysis shows that the dark areas of second phase are rich in calcium. Arrow D on the large dark particle in MI0013 appears to be a Mg-Ca particle with a ratio of 3 or 4:1, taking into account the spot size of the electron beam and the unavoidable measurement of the matrix as well, this ratio could be nearer to the 2:1 of Mg<sub>2</sub>Ca. In MI0014, arrow C analyses the dark region and gives a ratio of 2:1 suggesting Mg<sub>2</sub>Ca. The light particles in MI0013 have high Y, Nd and Ca with a ratio of 2:4:3 and in MI0014 the light particles are higher in Nd with low amounts of Gd or Ca, indicating a particle mainly of Mg-Nd as seen in MI0009 but with the incorporation of Gd and Ca. The addition of Er is discussed in greater detail in chapter 7.

To summarise the new alloy's microstructures; the addition of Gd in Elektron 21 has formed large Mg-Gd-Nd particles and smaller dispersed Gd-Nd particles. These smaller particles have a ratio of 1:1 in the 8 wt% alloy and 3:1 when at 12-15 wt%. It is proposed that smaller Gd-Mg particles, unseen in these images, are also distributed throughout the matrix. Gd in ML4 combines in the Y-Nd particles observed in MI0009 to form Nd-Y-Gd phase with a ratio of 4:3:2.

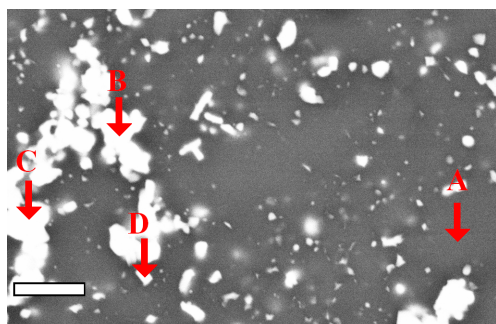
Calcium additions create large Mg<sub>2</sub>Ca particles in both ML4 and Elektron21. In ML4 Ca also makes incorporates into the Y-Nd particle seen in MI0009 to make Y-Nd-Ca particles.

### 5.3.2 Mechanical properties

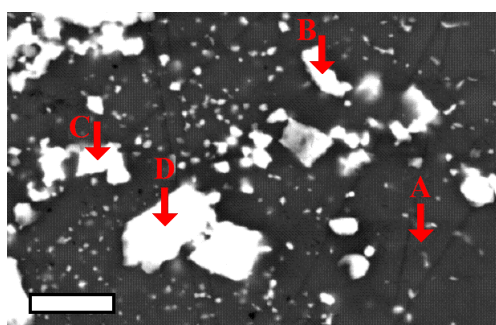
Initial analysis of the alloys was carried out by tensile fracture measurements, salt fog cabinet and SBF corrosion. Figure 5.7 shows the 0.2% yield stress, ultimate tensile stress (UTS) and elongation of the six new alloys alongside standard ML4. All the alloys have higher strengths, but appear less ductile. This is expected when adding elements forming the additional particles and second phase shown above as these particles cause precipitation hardening. This effect is shown neatly with 0.2% yield and UTS increasing with 8



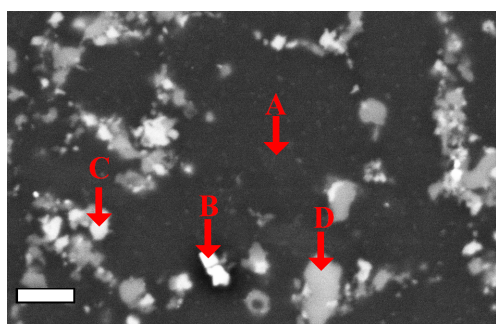
MI0010			
Arrow	Mg	Nd	Gd
A	87.6	1.8	6.42
B	77.1	11.8	7.5
C	70.4	19.95	7.91
D	83.2	6.1	6.6



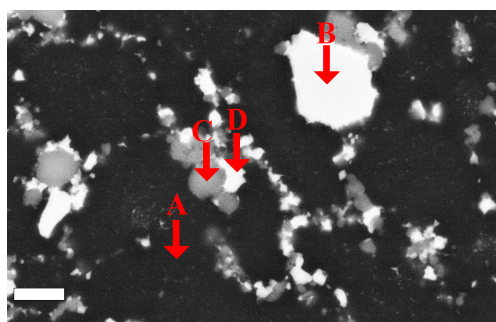
MI0011			
Arrow	Mg	Nd	Gd
A	85.1	1.4	10.6
B	2.5	4.21	85.51
C	47.5	14.06	34.5
D	57.9	11.1	30.1



MI0012				
Arrow	Mg	Nd	Y	Gd
A	86.2	6.8	4.2	1.7
B	58.1	20.4	10.8	7.7
C	61.2	16.3	11.5	7.1
D	57.2	17.3	13.9	8.0



MI0013					
Arrow	Mg	Nd	Y	Gd	Ca
A	86.1	4.1	0.78	-	0.5
B	68.9	5.2	9.9	-	8.4
C	74.5	4.9	12.6	1.2	6.8
D	72.5	5.6	4.9	-	19.9



MI0014				
Arrow	Mg	Nd	Gd	Ca
A	97.28	0.97	1.37	0.38
B	62.9	24.8	5.6	5.47
C	59.1	7.8	2.2	26.1
D	70.8	21.1	2.5	4.5

**Figure 5.6:** Microstructures of alloys MI0010-MI0014 taken by SEM with BSE, scale bar = 50 $\mu$ m. The table shows the corresponding chemistry in wt% at the spot points indicated by arrows A-D.

wt% Gd and further increasing with 12-15 wt%Gd, this goes hand-in-hand with the lowering of elongation with 8wt% and again further with 12-15wt%. The Gd in Elektron 21 has created large Mg-Gd-Nd particles and high quantities of smaller, well dispersed Gd-Nd particles. These smaller intermetallics are the likely cause of the increase in strength from standard Elektron 21. The precipitation of these particles is the desired outcome from the age hardening process normally given to Elektron 21 to increase strength.

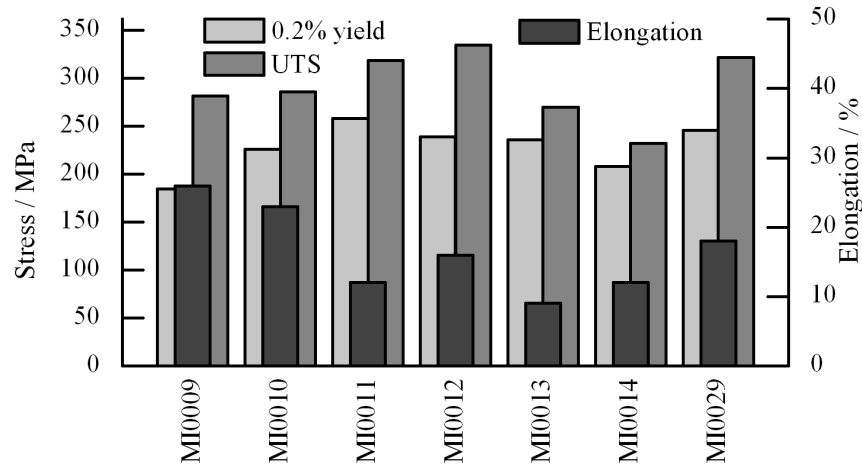


**Figure 5.7:** Tensile properties of MI0010-MI0029 against the ML4 standard.

Gd has had a similar effect on ML4, with increases in strength and brittleness. This is the result of the large numbers of small particles observed using BSE in figure 5.6, an example of precipitation hardening, along with the higher concentrations in matrix yttrium causing solution hardening.

Calcium alloys are low in UTS and ductility. This is attributed to  $Mg_2Ca$  particles throughout the microstructure which would create a strong but brittle alloy. Hence the high 0.2% yield but low UTS and elongation. Wu found that addition of Ca over the solubility limit (0.82wt%) caused the precipitation of calcium ( $Al_2Ca$  in this report), and lowered the UTS and elongation linearly with increasing Ca content [159].

Erbium has the effect of increasing both 0.2% yield and UTS with a drop in elongation. Microstructural analysis is reported in greater detail later (chapter 7). Erbium is highly soluble in magnesium and therefore mainly occupies the matrix. Strength is increased by solid solution strengthening whereby dislocation propagation is impeded, this increases strength, but lowers elongation as seen in figure 5.7.

### 5.3.3 Corrosion rates

Corrosion in salt fog is reported for completion of this report and Magnesium Elektron records. The data highlight the differences that can be seen when alloys are tested in SBF and NaCl solutions. In general, all the new alloys corrode at the same rate under salt fog conditions apart from MI0029 which is over 6 times more corrosive than MI0009. The true test for the biomedical alloys however is corrosion in a SBF bath. The outstanding

alloy is MI0029 which corrodes at over 8 times less than MI0009, in stark contrast to the salt fog results. This performance in SBF conditions, along with the more than adequate mechanical properties, has lead this alloying system being the focus of future development and is reported in greater detail in chapter 7. The remaining portion of this chapter will detail the other alloys as the information is useful for future alloying progress.

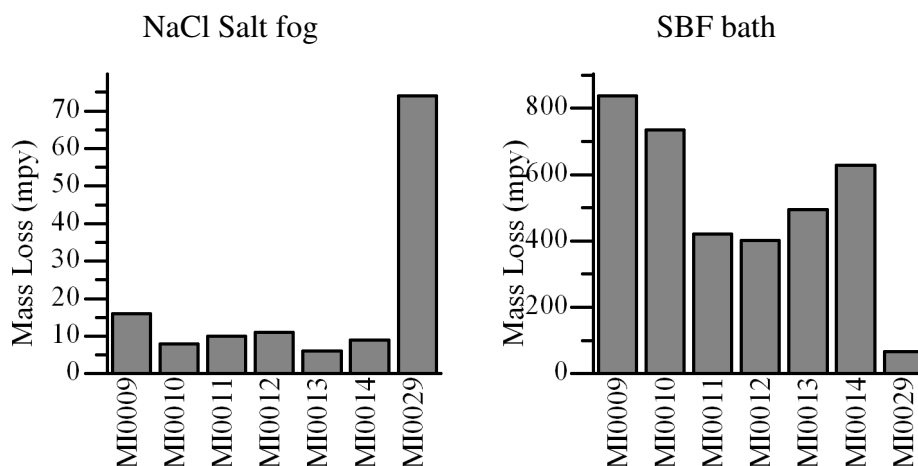


**Figure 5.8:** Mass loss after 7 days in either NaCl salt fog or SBF bath. MI0029 shows corrosion rates over 10 times less than ML4 in SBF.

Gd additions to Elektron 21 show a large increase in corrosion resistance as shown in table 5.1. In SBF the rate drops from 735mpy with 8wt% Gd to 421mpy with 12-15wt%Gd. Additions to ML4 of Gd give the lowest corrosion rate of the alloys except MI0029, with only 4 wt% compared to 12-15 wt% as in MI0011. Phases present when yttrium is combined with Gd must have a considerable effect on corrosion. EDX revealed MI0012 to be composed of the same second phase throughout the microstructure, although smaller intermetallics were also seen but not measured. MI0009 showed Nd rich Nd-Y particles and Y rich Nd-Y particles, the addition of Gd appears to have stabilised the precipitation so that a similar Nd-Y-Gd is produced throughout. The higher Nd/Y ratio along with Gd in these second phases, seems to provide the alloy with its corrosion resistance.

The addition of Ca also lowers corrosion rate in both Elektron 21 and ML4.  $Mg_2Ca$  particles are normally associated with galvanic coupling and therefore higher corrosion rates. To analyse why the corrosion rates changed with the alloying, electrochemical testing was used. GDOS was also employed to give cross sections of the respective reaction layers as the passivation layer appears to be of great importance when testing in SBF.

### 5.3.4 Corrosion analysis

Figure 5.10 shows the curves obtained via potentiodynamic polarization and table 5.3 lists the  $E_{corr}$  and  $I_{corr}$  values given by Tafel extrapolation. The first observation is that all the  $E_{corr}$  values at  $t=0$  hours are between -1.992 mV and -2.077 mV and therefore it



can be concluded that alloying has made little difference to the initial corrosion properties of the alloys. However with time, the  $E_{corr}$  values spread and correlate with the general corrosion data from the SBF bath. The corrosion rate appears to be highly dependent on the transformation of the alloy over time, most likely due to the formation of a reaction layer. Anodic shoulders are seen to develop on all potentiodynamic polarisation plots, but with different characteristics per alloy. Impedance data shown in figure 5.11 and listed in table 5.3 give more accurate values to represent any surface reaction layer formed on these alloys. There is a loose correlation between the overall corrosion rates seen in figure 5.11 and the polarisation resistance listed in table 5.3. In figure 5.9 it can be seen that the rise in surface film strength leads to a lowering of corrosion rate. Looking at the potentiodynamic polarisation plots, the rate at which corrosion protection is formed also seems relevant. Alloys such as MI0011 and MI0012 show plots at 2 hours more similar to the 24 hour than 0 hour plots, whereas the poor performing MI0009 is less similar. Overall, it seems that the prevailing factor affecting corrosion rate is the formation of a semi-stable reaction layer. The effects chemical composition has on corrosion and reaction layers are now discussed by alloying element and starting system.

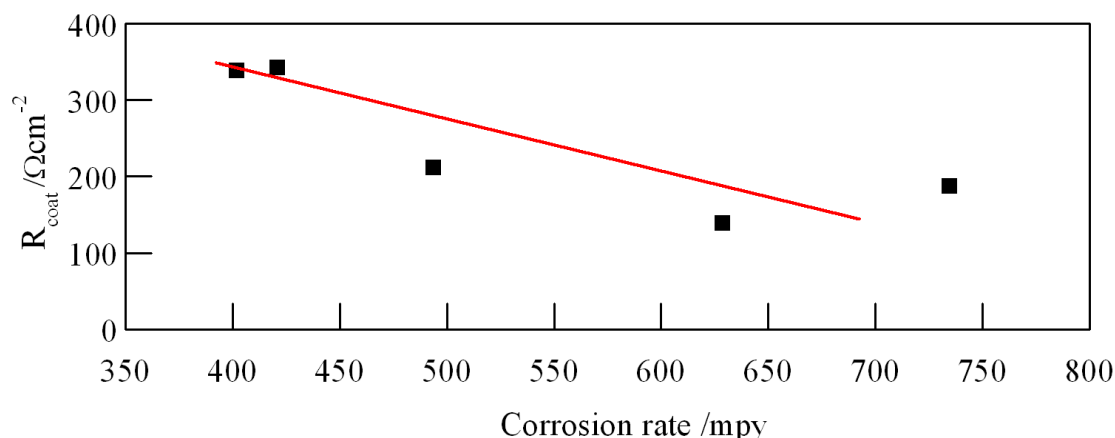


**Figure 5.9:** Polarisation resistance from the surface film off MI0010-MI0014 alloys after 24 hours in SBF (table 5.3) against mass loss from the SBF baths in figure 5.9. Note, a inverse relationship indicating strong surface films are an important aspect for lower corrosion rates.

#### Gadolinium increases to Elektron 21 and ML4

The microstructures obtained by added high amounts of gadolinium in MI0010-12 appear to be structures associated with higher corrosion. Large quantities of Gd-Nd particles throughout the matrix lead to high galvanic coupling. Keibus has shown that by solution treating Elektron 21 to remove these, corrosion rates are lowered, whereas precipitation hardening increases corrosion [154]. This data however is in NaCl, in SBF Hort reported increases in corrosion resistance up to 10% wt (he speculates that this would have been up to 15% if not for poor sample preparation) [160]. The report focuses mainly on the mechanical properties and offers little explanation as to why Gd is having a corrosion inhibiting effect. Hort did however state that the higher the Gd fraction the lower the grain

**Table 5.3:** Tafel extrapolation values from the potentiodynamic polarisation curves shown in figure 5.10 and polarisation resistances from medium and low frequency loops obtained from figure 5.11. All corrosion in SBF

Alloy	Time (h)	E <sub>corr</sub> (mV)	I <sub>corr</sub> (mAcm <sup>-2</sup> )	Rp(Ωcm <sup>-2</sup> )	
				R <sub>Corr</sub>	R <sub>Coat</sub>
MI0009	1	-2.053	2.12x10 <sup>-4</sup>	110.9	64.4
	2	-1.896	5.07x10 <sup>-5</sup>	167.0	100.7
	24	-1.711	2.98x10 <sup>-5</sup>	422.7	262.1
MI0010	1	-1.992	2.08x10 <sup>-4</sup>	102.0	21.9
	2	-1.732	1.44x10 <sup>-4</sup>	183.9	51.2
	24	-1.569	8.48x10 <sup>-5</sup>	418.9	187.7
MI0011	1	-2.023	1.52x10 <sup>-4</sup>	156.5	54.3
	2	-1.671	4.27x10 <sup>-5</sup>	573.8	267.1
	24	-1.506	1.13x10 <sup>-5</sup>	780.6	342.5
MI0012	1	-2.0457	6.45x10 <sup>-5</sup>	196.8	59.4
	2	-1.768	2.85x10 <sup>-5</sup>	464.2	160.2
	24	-1.692	1.38x10 <sup>-5</sup>	770.9	338.8
MI0013	1	-2.072	2.62x10 <sup>-4</sup>	202.9	52.8
	2	-1.883	1.88x10 <sup>-4</sup>	335.9	48.1
	24	-1.776	1.62x10 <sup>-5</sup>	666.3	211.4
MI0014	1	-2.077	8.29x10 <sup>-5</sup>	145.1	40.4
	2	-1.693	8.37x10 <sup>-5</sup>	205.7	46.9
	24	-1.613	3.97x10 <sup>-5</sup>	472.2	138.6

size and thus higher the grain boundary volume fraction. The cathodic Gd phase occupies these boundaries [160]. Possibly Hort is suggesting the large amount of cathode phase at the boundaries forms a wall to further corrosion of the anodic matrix. However the SBF corrosion in this investigation has shown that the reaction layer formed is of great importance (figure 5.9). MI0011 neatly demonstrates this with larger  $R_{coat}$  values than MI0010 that Gd increases with reaction layers protection. Large anodic shifts after 2 hours in all three Gd alloys indicate that a reaction film is formed quickly. For the Elektron 21 alloys these break down at 0.7 mV above the rest potential, but for the ML4 alloy at 24 hours, the film is very stable and breaks down at over 1.2 mV above the rest potential. Impedance data for MI0012 shows a  $R_{coat}$  value 80.4 Ωcm<sup>-2</sup> higher than MI0009 and also higher than the MI0013 Ca alloy.

Corrosion layers were analysed for chemical composition in cross section by GDOS. Figure 5.12 shows the cross sections of the reaction layers produced on MI0009 and MI0012 after 15 minutes corrosion in SBF. The added Gd might be expected to change reaction layer composition and thus explain the stable reaction layer seen by electrochemistry. However the GDOS results show Ca, O and P in the same distribution through the layer. What is shown is the difference between Mg concentration within the layer between alloys. MI0012 has far lower Mg counts throughout than MI0009, indicating that the P, Ca and O are chemically bound with an element other than Mg in MI0012. The Gd line

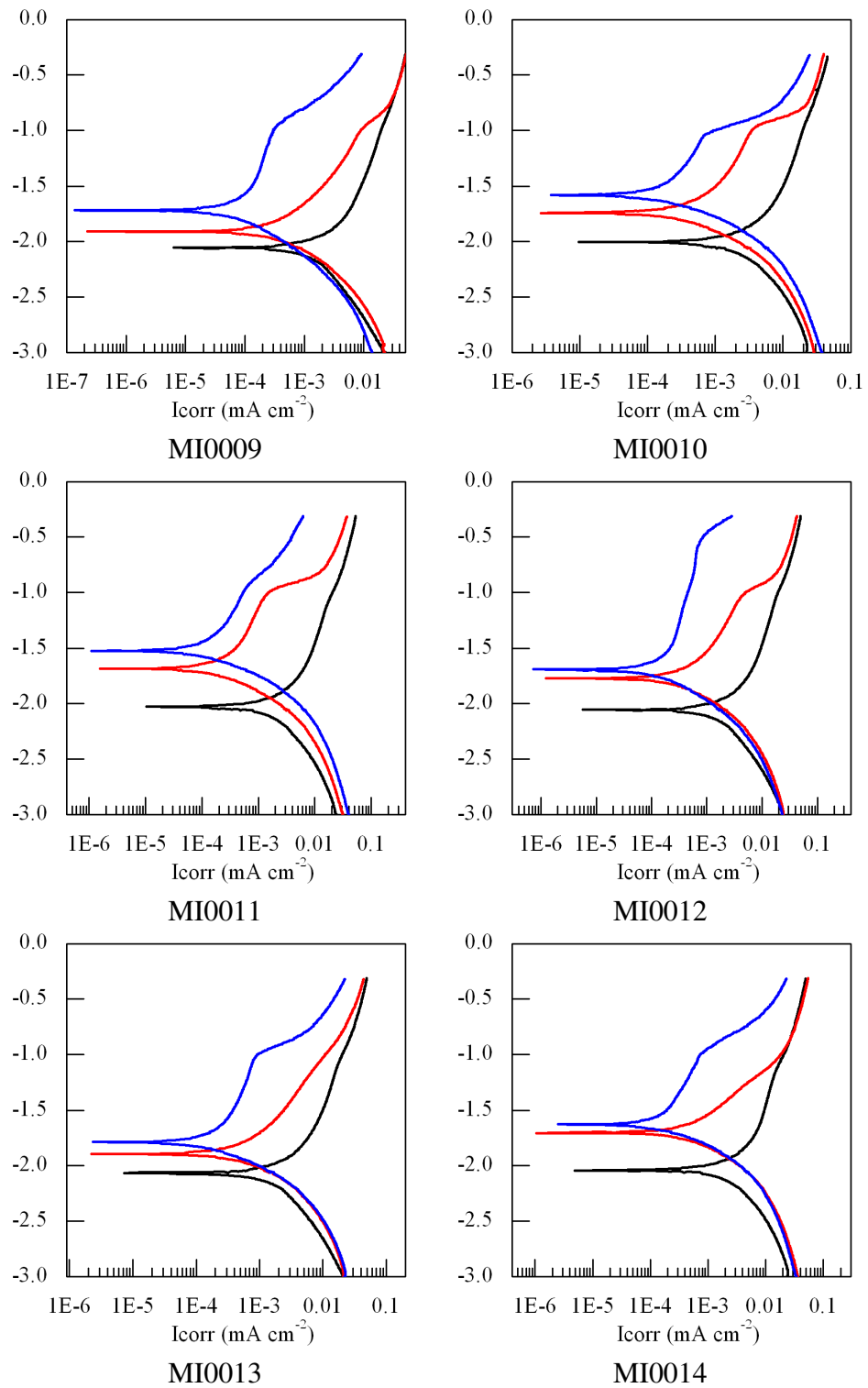


**Figure 5.10:** Potentiodynamic polarisation curves obtained in SBF from MI0009 to MI0014 alloys. Black = 0 hrs, red = 2 hrs and blue = 24 hrs.

was not obtained, as the Gd wavelength leaked giving false readings. The Nd line was obtained, and gave a reading in the substrate but not reaction layer for both alloys.

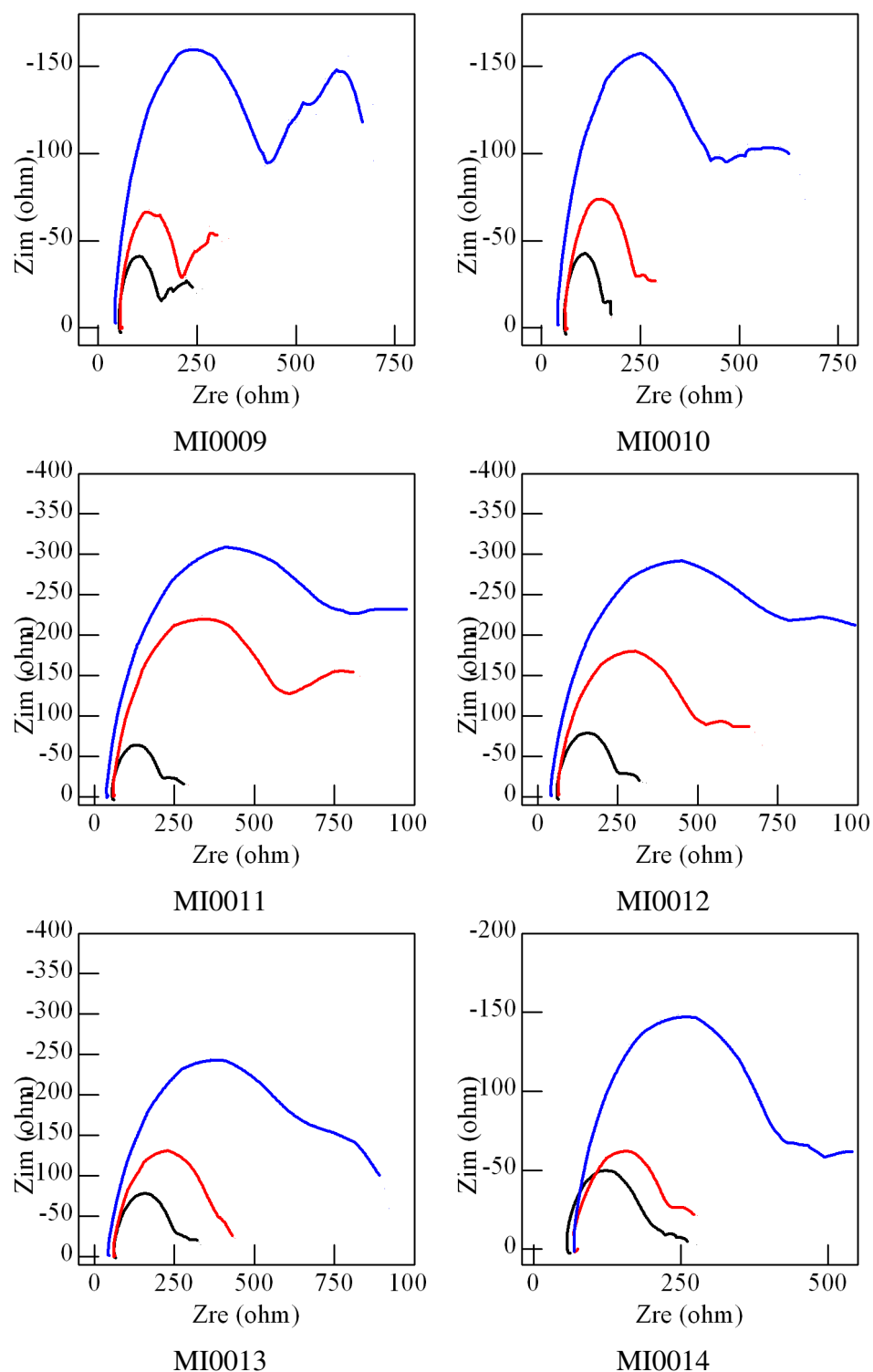


**Figure 5.11:** Nyquist plots obtained in SBF from MI0009 to MI0014 alloys. Black = 0 hrs, red = 2 hrs and blue = 24 hrs.

### Calcium additions

EDX of the calcium contacting alloys showed the presence of  $Mg_2Ca$  phase. Reports of far greater corrosion resistance seen by Kannen did not occur [96]. Kannen reported 5 times greater surface film polarization resistance than the non Ca alloy. Here table 5.3 shows that Ca actually lowers this. MI0009 give a  $R_{coat}$  value of  $262.1 \Omega cm^{-2}$  at 24 hours,

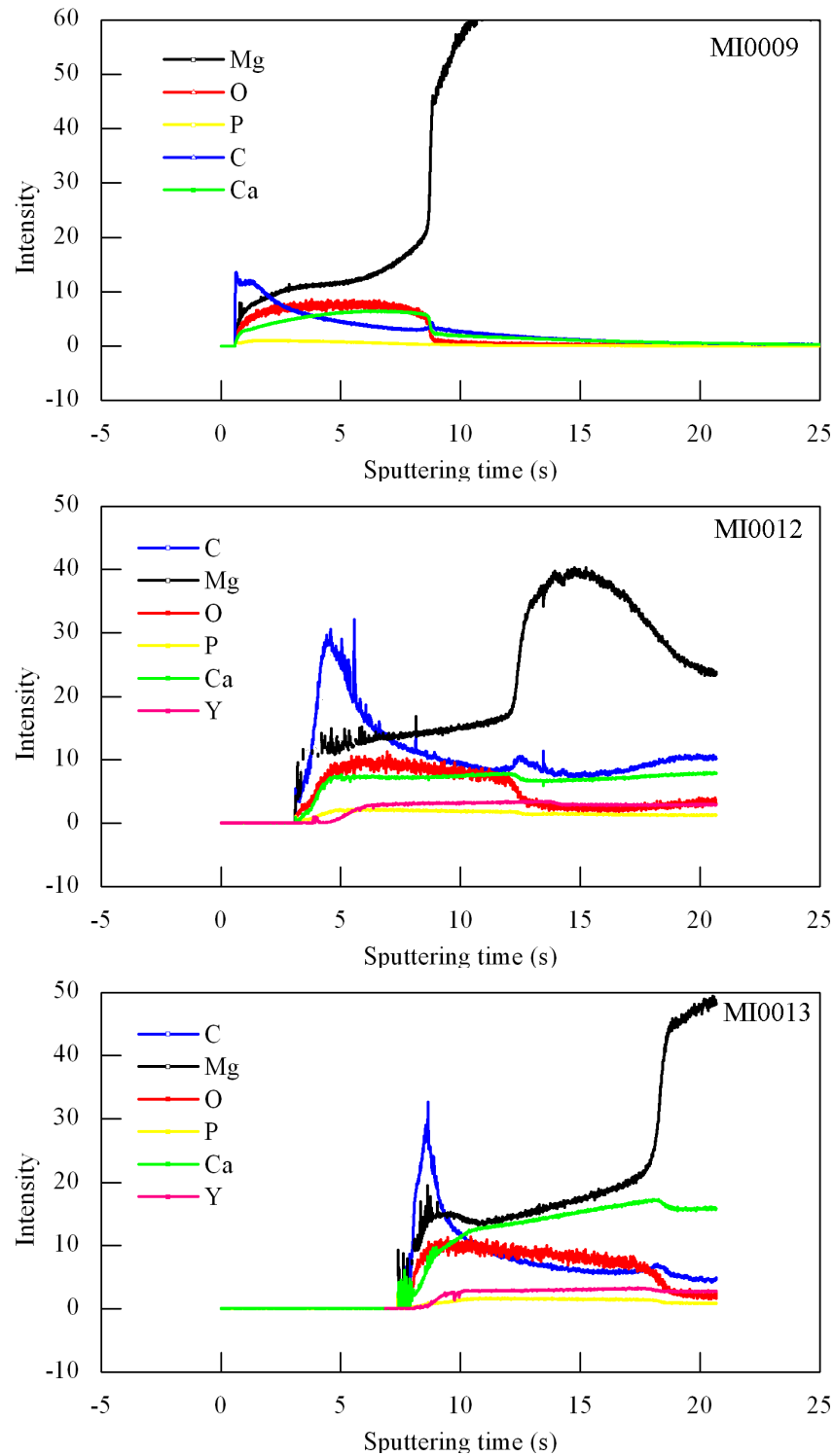


**Figure 5.12:** Chemical composition through the corrosion reaction layer investigated by GDOS. Corrosion occurred in SBF for 15 minutes. 0 sputtering time represents the expected surface.

whereas MI0013 is lower at  $211.4 \Omega\text{cm}^{-2}$ . This is probably due to the amounts of Ca used by Kannen (1wt%) and also the alloy difference (AZ91). Kirkland investigated Mg-Ca binary alloys with a range of Ca concentrations [161]. It was reported that increases of Ca content above a critical concentration of around 1.5wt% for corrosion rates. Detailed work was carried out on the role of Ca in Mg and specifically the precipitate  $\text{Mg}_2\text{Ca}$  which forms above 0.86 wt%. Kirkland showed by micro-polarisation tests that although the

phase has slightly less corrosive potential than pure Mg, it has a far greater rate of reaction (normally in Mg alloys the second phase is assumed the cathodic role, but here this is not the case) [161]. This effect on the binary alloys was to change the shape of the polarisation curves. With increasing Ca concentration the anodic regions were shifted dramatically, whereas the cathodic reaction appeared unaffected. Figure 5.10 shows similar results, with the plots for MI0013 and MI0014 demonstrating cathodic region not dissimilar to MI0009, but the anodic reaction shifts to higher currents at the same potential. Kirland concluded that this suggests that  $\text{Mg}_2\text{Ca}$  is a more efficient anode than  $\alpha\text{-Mg}$  [161]. It was also reported that the rate of oxygen produced at the surface was lower than the rate of metal consumed, meaning a magnesium oxide layer could not effectively be produced. If this was occurring in MI0013 and MI0014, it may explain the low  $R_{\text{coat}}$  values. The composition of reaction layers however has never been reported, only suggested in Mg-Ca investigations.

GDOS analysis of MI0013 (figure 5.12) shows that calcium is high in concentration throughout the reaction layer, at a ratio with Mg of nearly 1:1. MI0009 by comparison has a ratio more like 2:1 Mg to Ca. Calcium therefore is reacting with the  $\text{CO}_3$  and  $\text{PO}_4$  in SBF to form its Ca compounds alongside the  $\text{Mg}_2(\text{PO}_4)_2$  and  $\text{MgCO}_3$  forming in MI0009. This has been reported in publications when modifying the corrosion solution with amounts of calcium [74, 79] but not by the use of Mg-Ca alloys, although the principle of free  $\text{Ca}^{2+}$  ions at the corrosion surface to react is the same. Calcium intergration into the reaction layer resulting in lowering the layer stability however goes against previous work [96].

### 5.3.5 Heat treatment

Following on from work in chapter 4 where standard ML4 extrusions were heat treated for improved corrosion resistance, the new alloys were investigated similarly. The extrusions were cut into sections and heat treated at 300 °C, 350 °C, 400 °C and 450 °C for 4 and 8 hours. The sections were then machined into corrosion cylinders and tested by SBF bath. The results are shown in respect to the standard condition in figure 5.13.

Compared to ML4, none of the new alloys had the same dramatic effect when treated. Corrosion rates in ML4 lowered by an average of around 200 mpy at peak temperature and time. Here, the only corrosion improvements were observed in Elektron 21 with Gd, but these are minor. Peak conditions were 350 °C for 8 hrs which gave an -57.6 mpy improvement in MI0010 and -36.5 mpy for MI0011. All the other alloys showed increases or negligible changes.

MI0010 and MI0011 response to heat treatments is similar to that in the literature, but less pronounced [154]. Keibus concluded that corrosion rates lowered with short period aging due to the precipitation of the metastable  $\beta$  phase. As this study was conducted with low amounts of Gd (1.2 wt%), precipitation is needed as this is close to the solid solution limit at slightly higher temperatures. In MI0010 and MI0011, the Gd is most likely already in these phase as they are alloyed to well above the solution limit. This results in

only a small effect on the amount of the  $\beta$  phase and thus corrosion rate. Interestingly, the corrosion rate rises sharply when temperatures of 450 °C are used. At this temperature the concentrations of Gd used would place in the microstructure into a solution treatment range, whereby the metastable phase may dissolve into solution.

In ML4, the effects of heat treatment are negligible for all temperatures and times. Therefore the 4wt% Gd added to ML4 which previously showed great benefits from the treatments, must be pinning the movement of the Y and Nd and thus stopping their migration to grain boundaries and twinning plans, as with ML4.

MI0013's corrosion rate increases at the lower temperatures. A fair assumption would be the precipitation of further  $\text{Mg}_2\text{Ca}$  into the matrix causes to the higher corrosion rates, as seen when increasing Ca concentration. In Elektron 21 however, corrosion only increases when 450 °C is used as with the Elektron 21 + Gd alloys.

A more reliable hypothesis to explain the slight changes in corrosion rate has not been drawn. This would require EDX and analysis of the new microstructures and the allocation of resources to this were agreed wasteful as no real gain in corrosion resistance was obtained through these heat treatments. The corrosion rates obtained with the five new alloys here would have to improve by around 50% in order to be a greater prospect than MI0029 and this was not the case.

### 5.3.6 Cell culture

As shown in chapter 3, the effect alloys have on cells culture either upon or in the vicinity of the magnesium sample are hard to distinguish. Although Y was cited as being osteo conductive, this is a mild affect compared to other bioactive elements, such as calcium. Chapter 3 also showed that corrosion rates had only small affects on cell cultures after the initial corrosion spike. This could potentially mean that magnesium alloyed with bioactive elements even with corrosion differences could show improved biological properties.

To test osteoblast responses to the alloys, the DNA and alamar blue assays along with fluorescence imaging were carried out. The cells were seeded at 40,000 cells  $\text{ml}^{-1}$  and incubated for 2 weeks. The assays and imaging were carried out throughout the time period. The experimental procedures for this study are as detailed in chapter 3, using 1 day pre-corrosion and seeding the cells directly on to the material. As previously described the DNA and alamar blue are heavily influenced by the magnesium or pH from magnesium corrosion. The alamar blue results were therefore discarded. However, using cells from around the magnesium in the well plate and not on the surface (protocol explained in section 3.3.1) meant that the cells could be washed and tested without magnesium present for the DNA assay. The results at 14 days for this trial are shown in figure 5.14. Although this is a proliferation assay and not cell function, calcium would still be predicted to enable good cell growth, instead it seems to be the worst performer of all the samples. The FTIR phalloidin and DAPI stained images from the sample surface show a much

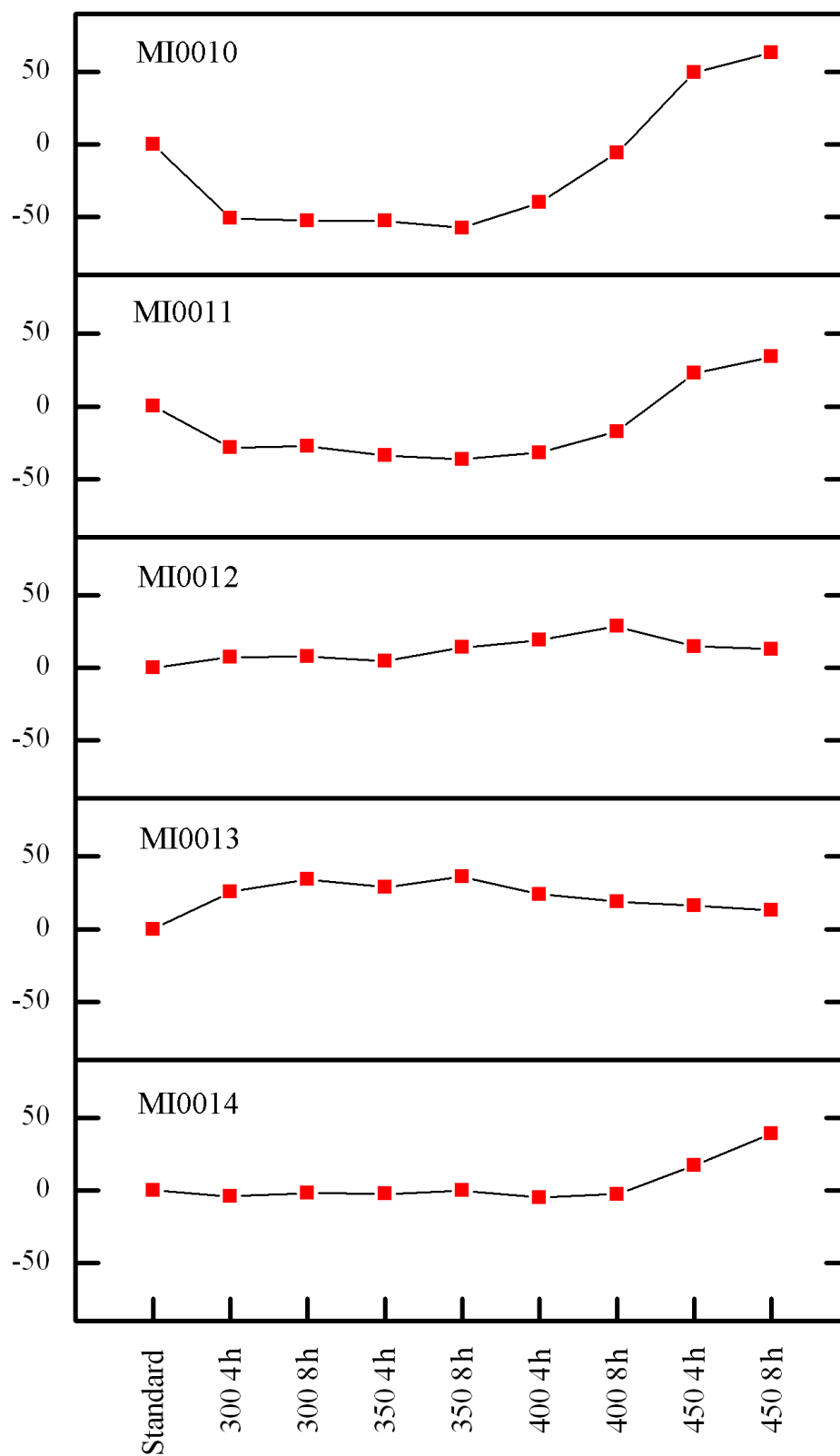


**Figure 5.13:** MI0010 to MI0014 heat treated for 4 and 8 hours 300-450°C in an attempt to further the corrosion rate loss as achieved by ML4 in Chapter 4



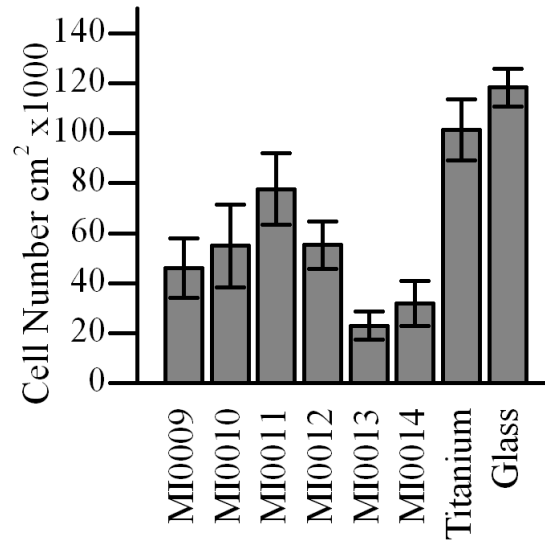


**Figure 5.14:** Cell density MI0009 to MI0029 compared to titanium and glass control. Calculated by DNA hoectsh staining after 14 days culture.  $n = 4$ , error = SD.

lower density than the MI0009 and glass control. The cells also appear less stretched than on the other magnesium alloys. The cause of this is unknown and not supported by cellular studies with Mg-Ca alloys in the literature [56] although Pietak used binary alloys and not RE and Y alloying systems. The DNA assay appears to show a positive effect of Gd on osteoblast growth. MI0011 shows greater density than MI0010 which in turn out performs MI0009. Images show highest cell density on the MI0011 and MI0012 alloys, notably the alloys with lowest corrosion rates. Cells on MI0009 to MI0012 in general look highly spread and well attached. Slight differences can be seen between osteoblasts on these alloys and glass, where the cells are a more equiaxed in shape. On the non Mg-Ca alloys, cells appear stretched in a linear fashion.

## 5.4 Conclusions

Additions of Gd, Ca and Er all have positive effects on the corrosion resistance of the magnesium alloys Elektron 21 and ML4. Additions of around 8 wt% Er appear the direction to take alloy development in the future. Gd additions appear to have a linear correlation with concentration and corrosion resistance. Calcium additions have less of an effect comparative to Gd and Er. Gd in ML4 is thought to owe its corrosion protection to the formation of a Nd-Y-Gd second phases, as well as a stable reaction film on its surface. This is speculated to be due to incorporation of Gd within the layer. Ca does not seem to produce a stable reaction layer to protect against corrosion. Corrosion of these alloys also has an adverse affect on cells grown on and around the alloys.

## 5.5 Further work

The majority of work should now focus on the development and understanding of the Er containing alloying systems. Although, the understanding of Gd and Ca alloying systems could be of importance in the future and therefore work on these alloy should not be overlooked. MI0012 appears to have good corrosion resistance, although not as high as MI0029, still a great improvement. Taking into account the superior strength and also gadonlium's apparent ability to reduce SCC cracking, could mean further work on this system regarding composition tuning would turn out to be promising. SCC testing should be carried out on all the alloys used in this investigation. Ca and Er's affect on SCC need to be studied.

Gadonlium's affects on cell culture need to be studied in depth. Results showing increases cell number on these alloys seems promising. The effect is not understood in current literature.

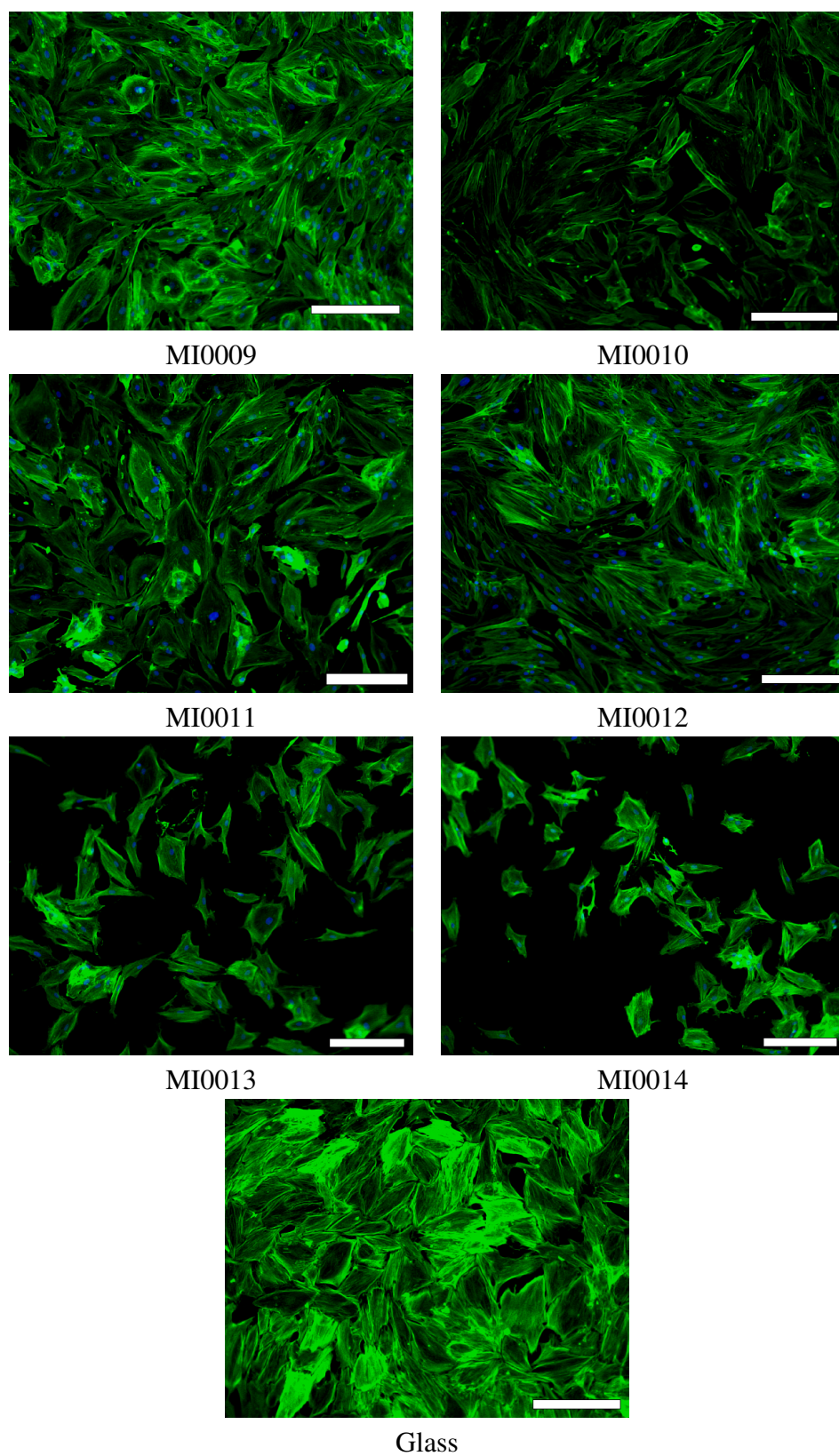


**Figure 5.15:** Fluorescence micrography of osteoblasts seeded on magnesium discs for 14 days, stained with phalloidin for F-actin and DAPI for the nuclei. Scale bar =  $200\mu\text{m}$



## STRATEGIES TO REDUCE INITIAL CORROSION RATE AND ALTER BIOCOMPATIBILITY USING SURFACE MODIFICATIONS

### 6.1 Introduction

The corrosion rates seen with standard commercial and even ML4 alloys have proved to be the limiting factor that Magnesium Elektron and their partners face with bringing this product to market due to low implant life and potential hydrogen build up problems. Progression from the WE43 alloy to ML4 has lowered corrosion rate slightly along with more stringent casting specifications. With further alloying and production protocol improvements, corrosion rates will most likely be lowered to a stage that the biomedical industry desires. Therefore other means of long term corrosion protection will be unnecessary in the future.

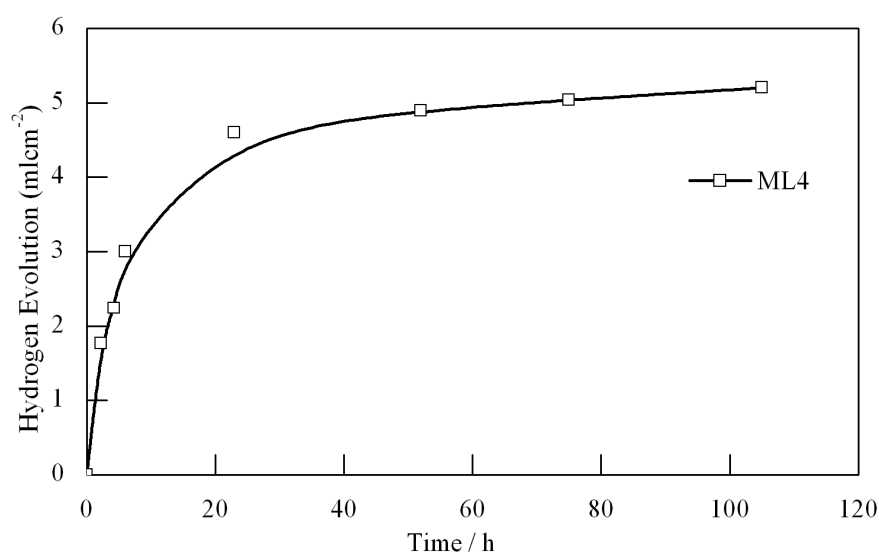


**Figure 6.1:** hydrogen evolution of ML4 discs in SBF at 37 °C

There is however a potential need for short term (<2 days) corrosion reduction. The dynamics of magnesium alloy corrosion rate is non linear regardless of alloy type. This

is due to the formation of a semi passive reaction layer, offering limited but important protection once formed. Hydrogen evolution studies of every alloy used in this and other investigations [75][83] show similar trends. Figure 6.1 shows a typical hydrogen evolution plot. The long term corrosion rate of the alloy is simply the gradient of the second stage of the alloy corrosion, normally after approximately 48 hours. The author believes this gradient will be lowered further and further by alloying changes, but the corrosion up until this point will always be present. This high initial corrosion is an important factor, as the rate of hydrogen evolution at this point could be above the threshold for the body to remove, meaning gas bubbles could be evolved. Figure 6.1 shows the initial (<6 hrs) corrosion rate to be 65 times greater than post 2 days. Controlling this initial corrosion spike is therefore necessary, and potentially could always be necessary due to the corrosion dynamics of magnesium *in vivo* and *in vitro*.

Corrosion protection via surface modifications is a feasible option. Potentially, surface coatings or modifications could offer short term protection while the magnesium alloy forms its semi-passive reaction layer. As discussed in section 2.5.1, the two most promising forms of surface protection are polymer or ceramic based. These coatings fit neatly into the two target markets for biodegradable magnesium alloys; cardiovascular stents and orthopaedic trauma fixation. Ceramic coatings appear to be a logical route for hydroxapatite based bone, and polymers potentially able to withstand the high elastic and elongation needs of balloon implanted stents. Polymer coatings could also be of use for orthopaedic applications.

For cardiovascular stents, a short term corrosion inhibitor would need to be easily attached to complex geometries, biocompatible with the chemical and biological processes within the blood, (i.e. not to increase the risk of thrombosis), and also to provide significant corrosion protection for the initial days of fixation. Another consideration, is that stents that are generally coated in biodegradable drug rich polymers. These are known as drug eluting stents, the metal stents are dip or spray coated with the polymer and release their payload drug which has been shown to lower neointimal growth [162]. Any surface treatment would have to be comparable with such coatings if the biomedical partners were to use the drug eluting stent method.

Orthopaedic implants are far less geometrically complex, but considerations still have to be made for 3D coatings. The implants are also generally forced into position, so adhesion of any coating is a concern. The type of coating however could be varied as long as it meets those criteria. A hydroxapatite-like coating would potentially be both corrosion resistant and biocompatible with the surrounding bone, but a polymer coating could potentially also demonstrate such attributes [118][131].

As previously discussed in the literature review, a number of solutions for the protection of magnesium have been put forward. With regard to ceramic coatings the most promising looks to be Cathodic arc deposition which showed corrosion rates lowered by 200 times [119] and also Micro arc oxidation which was shown to decrease corrosion

rates by 100 times [110]. Cathodic arc deposition gives good surface adhesion, but can only deposit simple oxides[106]. Micro Arc Oxidation can deposit tailored hydroxyapatite compounds, but has limited adhesion. Techniques able to combine both a strong adherent layer and one of hydroxyapatite are ion beam assisted deposition [163] and magnetron sputtering [124][164].

Polymer coatings have been less widely studied in biomedical magnesium corrosion protection. Although one of the best solutions came from Wong [133] who used plasma sprayed biodegradable polymers to coat magnesium which provided long term protection (>60 days). Aside from the biomedical research, self assembled monolayers (SAMs) were reported to be successful against NaCl solutions by Liu [165] and silane protection reported by Zurrchi [112][166]. Both solutions appear to be applicable to biomedical magnesium research.

## 6.2 Carboxyl Ended Self Assembled Monolayers

Lui reported in 2005 that the use of alkylcarboxylate based SAMs gave high corrosion resistance when measured with impedance spectroscopy in 0.2M NaCl solution [165]. The purpose of the following investigation is to review if this could be replicated and modified for *in vitro* conditions, as well as testing the corrosion results with more robust industrial corrosion techniques.

### 6.2.1 Materials and Methods

WE43 (DF9301) was supplied in 9 mm diameter rod. The material was made at Magnesium Elektron by melting pure magnesium ingot with the appropriate alloying elements. Once molten, the metal is stirred and a small casting was made for chemical analysis by Optical Emission Spectrometry (OES). If this falls within specifications the metal was ready to cast. Molten metal was then poured from the crucible into the mold. Once solidified and air cooled, the casting was machined into 75 mm diameter billets for extrusion.

The extrusion procedure required, pre heating of the billet, die and billet container to specified temperatures. The material was then extruded into 9 mm bar. These bars are then lathed into 9 mm by 3 mm discs for testing. The rod was machined into 3 mm thick discs.

Sodium Stearate (>99%), 10-Hydroxydecanoic acid (>99%) and 12-Aminododecanoic acid (>95%) were purchased from Sigma Aldrich (Gillingham, UK).

#### Preparation of carboxylate ion SAMs on Mg substrate

The WE43 discs were ground from grades 600 to 4000 then polished using colloidal silica (OPS) to a mirror finish. Cleaning was via a brief 5-10 second clean in 2% hy-

**Table 6.1:** Chemical composition of WE43 given by wt%. Total impurities equates to the combined composition of Fe, Ni and Cu.

Y	Nd	Zr	Hf	Total impurities
3.7-4.3	2.2-2.5	0.4-1.0	0.4-1.9	0.004

drofluoric acid, 15% hydrogen peroxide and 73% nitric acid, before being washed with deionised water and pure anhydrous ethanol. These were then immediately placed in the 0.01M of alkylcarboxylate solution for 48 hours. Followed by a wash with anhydrous ethanol and dried in the nitrogen-filled incubation cabinet. Solvents were pure anhydrous ethanol for sodium stearate and 10-hydroxydecanoic acid, and dimethylformamide (DMF) for 12-aminododecanoic acid.

### **Water contact angle**

Static water droplet contact angle measurements were performed using a type 2158 goniometer (The Precision Tool and Instrument Company Ltd.), and the sessile drop method was used throughout. A droplet of deionized water was formed on the end of the pipette tip and lowered onto the surface, and the pipette withdrawn until the drop detached. The contact angle was measured using a graduated eye piece where a tangent to the intersection was estimated after the drop had come to rest (approximately 2 sec). Both sides of three drops on different areas of each sample were measured (n=6), and the average was taken.

### **SAM stability**

Samples were coated with the alkylcarboxylate to form their monolayers. The water contact angles before and after SBF treatment were then compared to determine the extent of the coating removal over time. After submersion in SBF, the layers were washed in ethanol dried in nitrogen and had their water contact angles re-measured.

### **Mass loss**

One magnesium disc was submerged per 50ml of the various solutions for 1, 3 and 7 days at 37 °C. A polymer coating (Lacomit) was used to coat the bottom face of the discs. Post test, samples were washed in acetone and ethanol before a 10% chromium (VI) oxide bath (at 70 °C). The submersion time for the bath was determined to be sufficient when the oxide (stained yellow) had been visibly removed.

## **6.2.2 Results and Discussion**

Initially the SAM layer was tested with water contact angle to determine coating quality. Sodium stearate gave a very hydrophobic surface (shown figure 6.2), which in some



cases meant the water droplet rolled off the sample and could not be recorded. Average values (table 6.2) of  $147.5^\circ$  were recorded for sodium stearate which is statistically greater than Xin reported ( $131^\circ$ ), which could probably due to different alloy used. 10-hydroxydecanoic acid recorded a lower contact angle,  $78^\circ$ , due to its shorter carbon chain and hydroxyl end. 12-aminododecanoic acid which has a Shorter  $\text{NH}_2$  end gave a contact angle of  $120.7^\circ$ .

**Figure 6.2:** Water droplets on the surface of WE43 coated with sodium stearate (left and uncoated (right)).



**Table 6.2:** Mean water contact angles for silane modified magnesium surfaces.

Sodium Stearate	$147.5^\circ$	$\pm 2.12$
10-hydroxydecanoic Acid	$78^\circ$	$\pm 4.24$
012-Aminododecanoic Acid	$120.7^\circ$	$\pm 7.28$
Uncoated	$7.5^\circ$	$\pm 0.71$

Degrading the monolayers in deionised water over a period of 7 days showed that either the coatings were attached poorly or offered little protection to the magnesium substrate, meaning it could corrode beneath. After the first day, all but the sodium stearate had reverted back to their pre-coated hydrophobicities, and sodium stearate had lost nearly half its contact angle (figure 6.3). The poor coating adhesion in water meant that corrosion protection in SBF was very limited (figure 6.4).

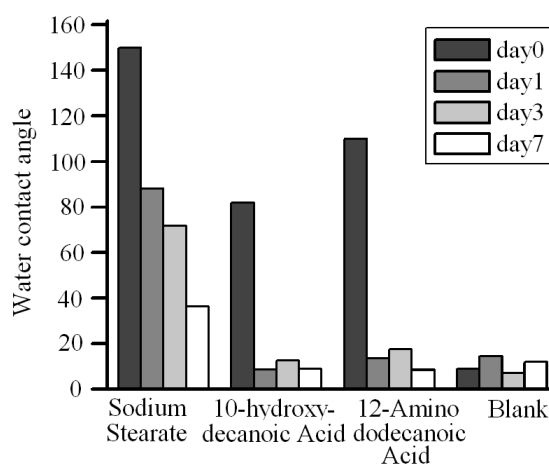


**Figure 6.3:** Water contact angle measurements after degradation in water. SAM coatings show poor adhesion

Mass loss showed no difference between any of the coatings and blank magnesium. These results are in great contrast to the work published by Liu [165]. Although, this is most likely due to the different time points and corrosion testing techniques used in this investigation compared to Liu's. Water contact angle measurements have shown that the monolayer was substantially effective at repelling water at shorter time points (<1 day). If impedance spectroscopy was performed at this early stage, the layer would be stable enough to inhibit the movement of ions through the double layer and therefore give greater polarisation resistance values. Liu did not report any values at longer time points. Mass loss is a more robust and realistic test of corrosion resistance and over 7 days it was shown that the use of carboxyl ended alkylcarboxylate chains is of no use biomedically for corrosion resistance.

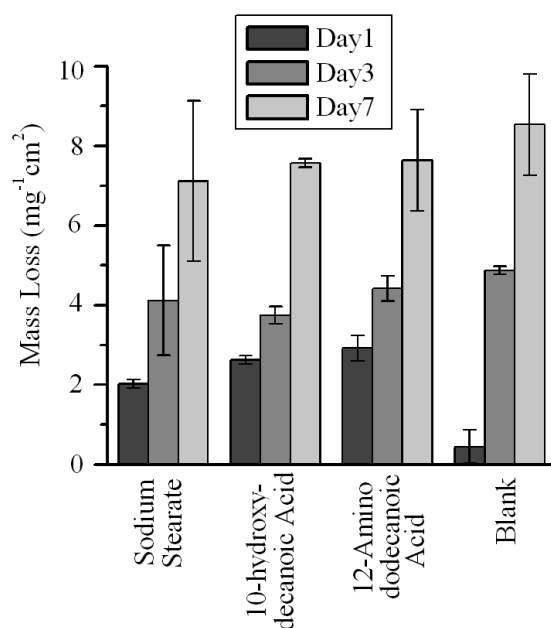


**Figure 6.4:** Mass loss of magnesium discs coated with SAMs in SBF over 7 days.  $n = 6$ , error = SD

## 6.3 Silanes

The use of SAMs as corrosion protection was limited due to its poor adhesion to the magnesium substrate. Silanes have been shown to bond covalently to metal hydroxides, potentially giving a surface with very high adhesion. Zurrchi used a long aliphatic chain silanes to chemical bond to WE43[166] and AZ31[112] surfaces giving protection against 0.1 M  $\text{Na}_2\text{SO}_4$  solution. This investigation examined whether this would be applicable to biomedical applications by testing *in vitro*.

### 6.3.1 Materials and Methods

ML4 (MI0009) was supplied in 9 mm diameter rod was made at Magnesium Elektron by the procedure outlined previously (section 6.2.1). The rod was machined into 3

mm thick discs. Octadecyl-trimethoxy-silane, 3-glycidoxypentyl tri-methoxysilane and 3-aminopropyltriethoxysilane were purchased from Sigma Aldrich. PEG-diamine powder with monomer repeats ( $n=18$ ) was purchased from Polypure (Oslo, Norway).

**Table 6.3:** Specification of ML4 and AZ31 given by wt%. Total impurities equates to the combined composition of Fe, Ni and Cu.

	Y	Nd	HfE(misc)	Al	Zn	Total impurities
ML4	3.7-4.3	2-2.4	1	-	-	0.003
AZ31	-	-	-	2.5-3.5	0.7-1.3	-

### Preparation of silane surfaces

Silane solutions were made to the following concentration 90/6/4 (v/v/v) absolute methanol, de ionised water and silane. The solution was then pH adjusted to pH 5 by  $H_2SO_4$ . 10 ml of silane solution was used per three magnesium discs. The solution and discs were placed in glass vials and stirred at room temperature for 1 hour. The discs were then cleaned in absolute methanol and dried at 70 °C for 30 mins.

### Poly (ethene glycol) attachment

Magnesium discs already treated with 3-glycidoxypentyl tri-methoxysilane (GOPTS) were placed on a glass slide with the upper surface coated with a fine layer of PEG-diamine powder. This was then left at 75 °C for 48 hours. The coverage of PEG was checked once melted and more powder is added if needed to ensure complete coverage. After 48 hours the surfaces were washed vigorously with water, then rinsed with methanol and dried at 70 °C.

### Attachment of carboxyl groups

Magnesium discs previously modified with 3-aminopropyltriethoxysilane (APS) were placed in the following solution for 24 hours at room temperature under stirring. The samples were then washed with pure DMF, methanol, then ethanol before being dried at 70 °C. The attached compounds were sodium stearate, Fmoc-arginine (Fmoc-Arg) and  $\alpha$ -lipoic acid, all purchased from Sigma Aldrich (Gillingham, UK).

0.2 mmols	Attachment compound
0.4 mmols	1-hydroxybenzotriazole (HOBt)
0.4 mmols	N,N-diisopropylcarbodiimide (DIC)
10 ml	N,N-dimethylformamide (DMF)

### Pierce protein adsorption assay

For the evaluation of protein density on surface, the Pierce BCA protein assay kit was used (Thermo scientific, IL, USA). Surfaces were submerged in cell culture media for a set time period to allow adsorption. Protein was then removed by placing surfaces in 1 mL 6M urea in dH<sub>2</sub>O for 30 minutes. This was sometimes diluted further to stop saturation of the test. The Pierce working reagent was made by mixing 50 parts reagent A to 1 part reagent B. 0.01 mL of the sample is then mixed with 0.2 mL working reagent. This was then read at 562 nm by spectrophotometer.

### 6.3.2 Results and discussion

The surfaces were characterised with FTIR to determine if silanes had successfully bonded to the magnesium. Figure 6.5 shows the peak data from uncoated ML4 and Octadecyl-trimethoxy-silane coated ML4. Labelled on the uncoated sample are 1522 cm<sup>-1</sup>, 1436 cm<sup>-1</sup> and 870 cm<sup>-1</sup> which are peaks for magnesium carbonate, the product of magnesium reacting with carbon dioxide in the atmosphere [112]. These peaks lower when the sample is coated and new peaks at 1462 cm<sup>-1</sup> (CH<sub>2</sub> stretching), 1196 cm<sup>-1</sup> (CH<sub>3</sub> Rock) and 1090 cm<sup>-1</sup> (Si-O-CH<sub>3</sub> stretching) appear [112].

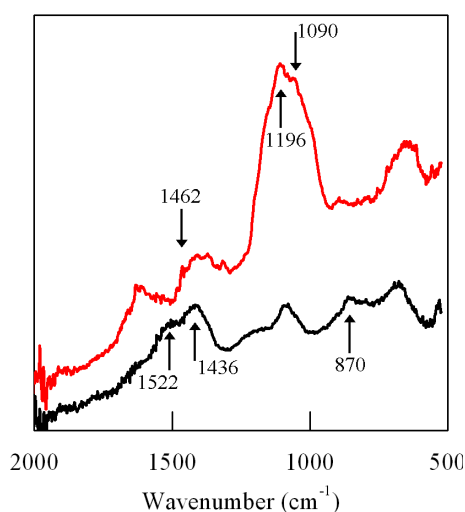


**Figure 6.5:** FTIR spectra for Octadecyl-trimethoxy-silane coated (red) and uncoated ML4 (black).

Attaching APS to magnesium gives Amine I peaks for C-N stretching (1550 cm<sup>-1</sup>) on all the surfaces. The peak is seen as much larger and broader on the Fmoc-Asp due to the extra amine groups on the amino acid. Fmoc-Asp also shows a peaks from the 660-900 cm<sup>-1</sup> and 1395-1440 cm<sup>-1</sup> range, the result of NH<sub>2</sub> wagging and carboxyl acid C-O-H bending respectively. The addition of Stearate acid is characterised by the strong CH<sub>2</sub> peaks due to the molecules large carbon chain length.  $\alpha$ -lipoic Acid is seen by it's disulphide bond, giving a broad peak around 500-540 cm<sup>-1</sup>. GOPTS (figure 6.7) gave only small peaks corresponding to CH<sub>2</sub> at 2960 cm<sup>-1</sup> and 2869 cm<sup>-1</sup> to differentiate

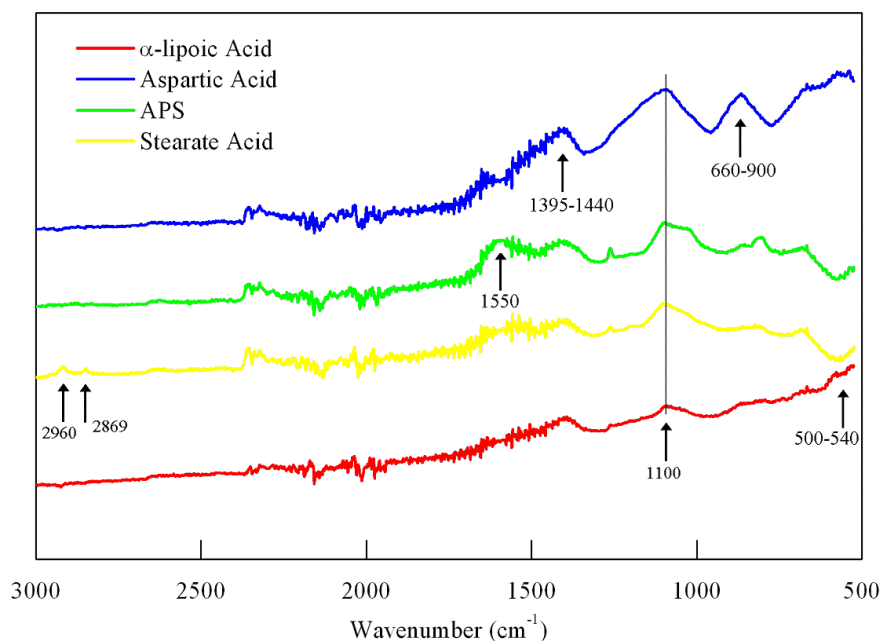


**Figure 6.6:** FTIR spectra for ML4 coated with APS, APS + stearate acid, APS + Fmoc-Asp and APS +  $\alpha$ -lipoic acid.

from the uncoated surface. This could be due to the silane having far less carbon than than the longer chain ODTMS in figure 6.5 or the result of poor coverage.

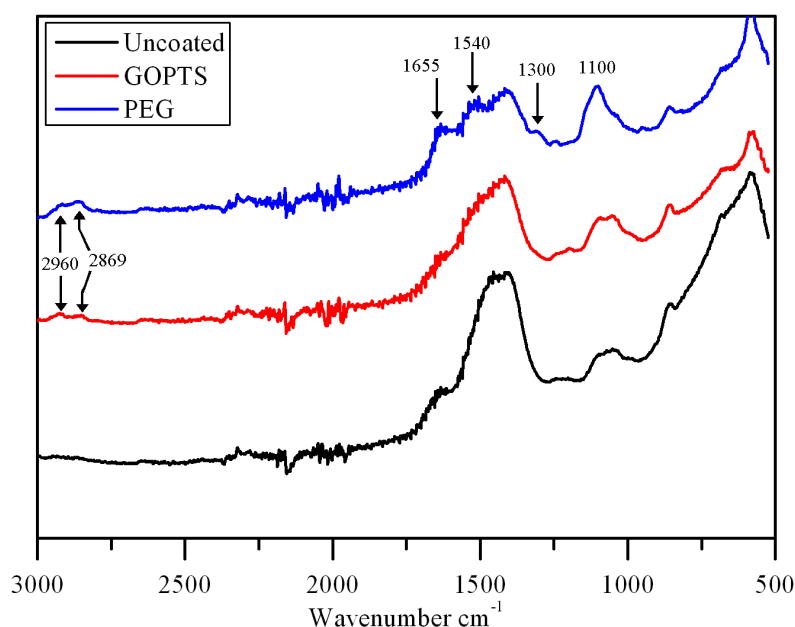


**Figure 6.7:** FTIR spectra for ML4 coated in GOPTS, GOPTS and PEG and uncoated

When PEG diamine is bonded to the surface, the peak data changes with lowering of the magnesium peaks and the addition of 4 more new peaks. Peaks at  $1655\text{ cm}^{-1}$  and  $1540\text{ cm}^{-1}$  correspond to amine I and amine II respectively [167].  $1300\text{ cm}^{-1}$  and  $1100\text{ cm}^{-1}$  are from stretching vibration the C-O-C bonds in the PEG monomers [168].

## Stability

To determine the stability of the silane layers, a range of silanes were coupled to magnesium ML4 discs and placed in GPS ethanol under stirred conditions for up to 9 days. These were periodically taken out, dried at 70 °C, tested using water contact angle and then replaced in ethanol. The silanes used were APS, GOPTS and ODTMS. APS and GOPTS were used due to their functional groups and ODTMS was used for its long alkane chains, which Zucchi had shown to be corrosion resistant [112].

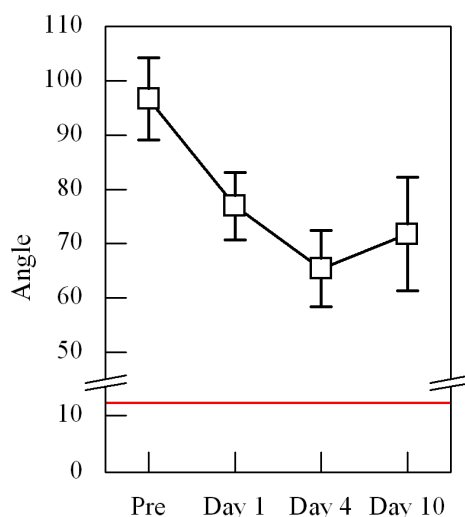


**Figure 6.8:** Degradation of octadecyltrimethoxysilane in ethanol over 9 days. Measured by contact angle  $n = 4$ , error = SD.

All three silanes showed stability after 9 days with their respective contact angles staying above the control. The drop in contact angle seen after the first day of submersion in ethanol indicates a proportion of the silane at the surface was not covalently attached. Zurrchi found that by altering the pH of the silane/methanol/water solution far greater surface strength was achieved [112].

Stability in a simulation body fluid was also tested. Magnesium discs were prepared and placed in SBF at 37 °C for 5 days. ODTMS gave a water contact angle of 43 °, a drop of around 60 °, but still demonstrating a presence on the surface comparative to the control (11 °).

## Corrosion

As the hydrophobic silane coating appeared to be stable in both ethanol and SBF, its corrosion protection was investigated with hydrogen evolution and 7 day mass loss.

Mass loss shows that with the silane coating a 50% reduction in corrosion could be achieved. The hydrogen evolution plot shows greater losses, but interestingly also demonstrates the protection of the layer over time. The plot (figure 6.10) can effectively be divided into the initial corrosion and steady state corrosion phases. The silane lowers the corrosion rate in the initial period (<24hours) by over 6 times. Given the aim of this chapter was set out to lower the amount of hydrogen production in this stage, it appears to

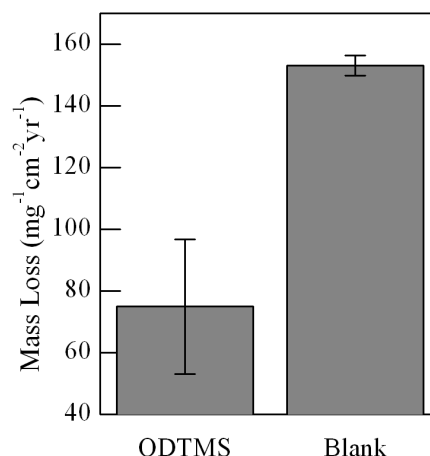


**Figure 6.9:** Mass loss of magnesium discs coated with octadecyltrimethoxysilane and uncoated after 7 days in SBF.  $n = 12$ , error = SD

be successful. After a 24 hours period, the both coated and uncoated samples steady, the coating still offers protection as the rates never become the same in this study.

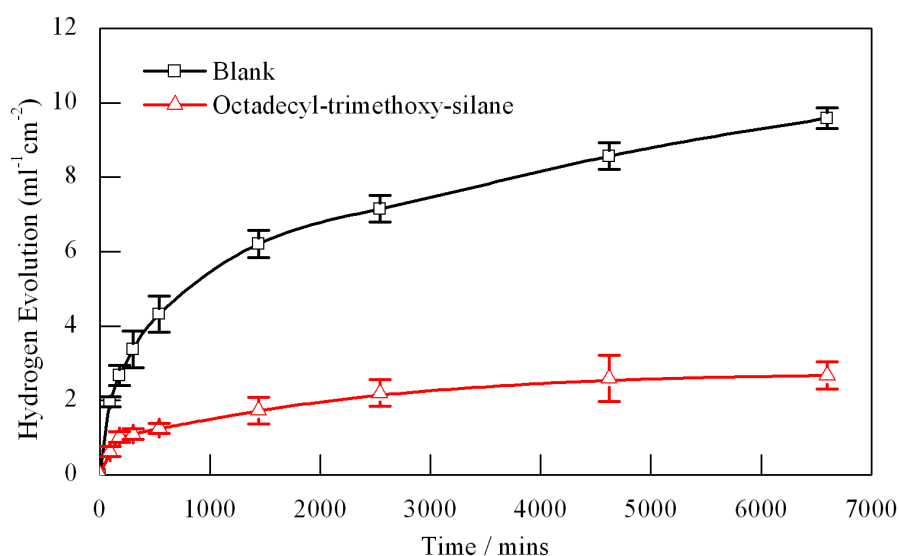


**Figure 6.10:** Hydrogen evolved from coated and uncoated magnesium discs in SBF at 37 °C.  $n = 12$ , error = SD

### Electrochemistry

The changing corrosion rate demonstrated by hydrogen evolution would suggest the coating is slowing corroding before 24 hours. Potentiodynamic polarization in SBF shows that the this effect is due to the inhibition of the anodic reaction. The two cathodic regions of the plots trace each other, but the anodic reaction is dominated by a shoulder, which moves the anodic reaction to over 10 times less current. The shoulder breaks down at around 0.5 mV above the rest potential which is around the same as expected for a stable magnesium film [75], which would suggest the coating breaks down at the point where the surface is stripped through such high anodic potential.

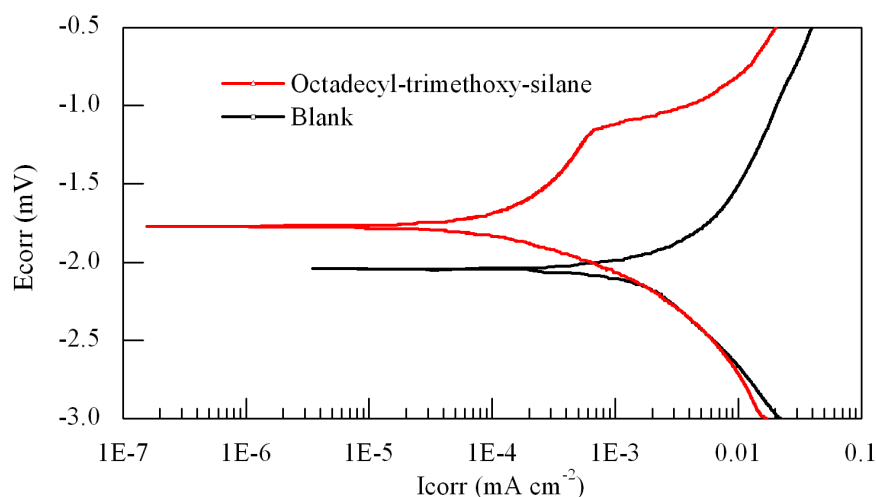


**Figure 6.11:** Potentiodynamic polarization in SBF after 5 minutes submersion. ODTMS shifts the rest potential less negative and to a lower current density.

The anodic shoulder is the result of the coating slowing the movement of electrolyte to the metal surface to cause the dissociation of magnesium metal into its  $2^+$  ion. The change in anodic behaviour is the same as seen by Zurrchi with the same coating on AZ31 in simple electrolytes [112] but also magnesium alloys with a passivating film [75]. Tafel extrapolation give current densities of  $0.99 \times 10^{-4} \text{ mA cm}^{-2}$  and  $3.46 \times 10^{-4} \text{ mA cm}^{-2}$  for the coated and un coated respectively, with the  $E_{\text{corr}}$  moving up from  $-2.041 \text{ mV}$  to  $-1.723 \text{ mV}$  with ODTMS coating.

Electrochemical impedance spectroscopy of the coating reveals an extra time constant at low frequency. Although in all the repeats this was not a well defined capacitance or inductive loop. A large capacitance loop at low frequency would suggest the coating was strong with only few pores to allow SBF through to the metal surface, resulting in two defined charge transfer regions. Here however, the method of corrosion inhibition seems to be at the medium frequency region. The silane is increasing polarisation resistance at the metal electrolyte interface by diffusion kinetics. The hydrophobic brushes could be creating a rate-limiting effect on the double layer.

### 6.3.3 Silane Modification

The use of long chain hydrophobic silanes to lower corrosion rate is one potential use of the coating. Silanes however can be readily purchased in many forms, for example with functional chemistry on their terminating group. Aminopropyltrimethoxy silane (APS) and 3-glycidoxypopyl tri-methoxy silane (GOPTS) can be attached with the same methodology as with octadecyl-trimethoxy-silane shown before. These present an amine group (APS) and a epoxy (GOPTS) at the end of their respective terminating group.

An amine functional group can be attached via a peptide bond to carboxyl acid groups, potentially meaning any molecule with this group can be attached covalently to the surface of a magnesium alloy via APS [169][170]. GOPTS offers a similar property as its epoxy can be chemically bonded to an amine.



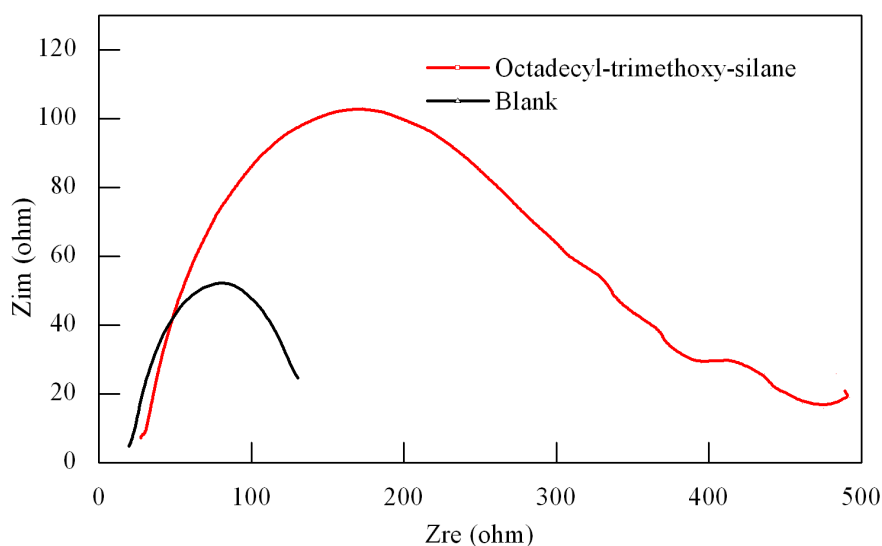


**Figure 6.12:** Nyquist Plot in SBF after 5 minutes of both samples. The uncoated shows only a single time phase, whereas the ODTMS coated shows a low frequency effect.

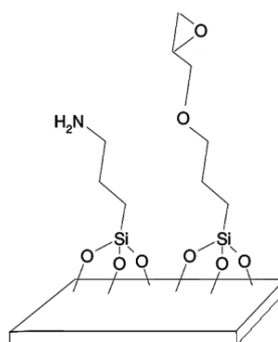


**Figure 6.13:** Chemical structures of APS (left) GOPTS (right). Note, the oxygen groups can react sideways with other silane molecules forming a 2D network in a monolayer.

### Aminopropyltrimethoxy silane

Using the previous method (Section 6.3.1), APS was attached to magnesium discs and tested with water contact angle. The mean contact angle achieved was  $54^\circ$  with the uncoated giving  $23^\circ$ . Various carboxyl ended molecules were then coupled to the APS via a peptide bond. These included long chain aliphatic molecules; sodium stearate and lauric acid, amino acids; arginine, glycine and aspartate in the sequence arg-gly-asp (RGD) and also  $\alpha$ -lipoic acid a potential anti restenosis drug.

Surfaces were characterised with FTIR (figure 6.6) after attachment. The long chain carboxyl acids were further tested for corrosion properties (table 6.4). The achievement of sodium stearate proved to be beneficial in the reduction of hydrogen evolution rates at the early stage in a similar fashion to that of the ODTMS coated samples previously. Although the sodium stearate and APS coated magnesium only demonstrated a 20% reduction over the blank.

The attachment of the tripeptide RGD was proposed to increase osteoblast response to the magnesium surfaces. RGD has long been recognised as the primary peptide sequence

**Table 6.4:** Hydrogen evolution after 7 days corrosion in SBF  $\text{mlcm}^{-1}$ .

Blank	12.67	$\pm 0.81$
APS + Stearate Acid	9.81	$\pm 1.23$

for cell attachment [171]. The attachment was in three stages, each amino acid being attached with blocking molecules on the amino end group and side chains to prevent unwanted side reactions. After attachment, these were removed, the sample washed and the next amino acid coupled. The process could not be completed however due to the final stage, which was the amine group blocking molecule (Fmoc) removal. Fmoc requires acidic conditions for removal, which destroys the magnesium surface and thus any coating attached.

$\alpha$ -lipoic acid coupling was attempted and again, measured by contact angle. Mean contact angles of  $53.4^\circ$  meant it was indistinguishable to the APS-magnesium surface it was coupled to ( $55.8^\circ$ ). FTIR proved its presence however, but it would need in vivo studies to prove its efficacy.

Further work regarding the attachment of these carboxyl ended molecules would be beneficial to determine if attachment was genuinely occurring. Surface investigation techniques such as XPS or ToF-Sims would determine the attachment and relative coverage. Meetings with Magnesium Elektron however, determined that this was not an avenue of research to follow.

### 3-glycidoxypropyl tri-methoxy silane

GOPTS surfaces were prepared and batch tested with water contact angle. Polyethylene glycol diamine powder was used to form a magnesium-GOPTS-PEG surface. Surface analysis was carried out by FTIR.

Polyethylene Glycol is a known protein repellent [172], and therefore stops the attachment of cells to an adsorbed protein layer and is effectively invisible to the body's immune system. To test this effect, osteoblasts were seeded onto surfaces prepared with no coating, GOPTS and GOPTS-PEG. Using DAPI and phalloidin fluorescent staining outlined in section 3.2, cells seeded at 40,000 cells/ml onto magnesium discs were cultured for 24 hours. Figure 6.14 shows the images of the three surfaces alongside a glass control. It can be seen that the uncoated magnesium supports adhesion. The slight alignment is due to the grinding process the discs underwent before seeding. Cells on the GOPTS surface appear to be less dense than the blank magnesium, but well attached, and highly spread. The reason for loss in cell number is unknown but consistent across samples. GOPTS shows good cell spreading, indicating osteoblasts are not under stress which might be assumed because of a loss of cell density. After PEG attachment to the surface, cells appear absent. Cells can be found in clusters by the surface edge where PEG attachment has been limited or damaged by handling. The centre of the sample (shown in figures 6.14) was consistent

across all the replicates as having low cell numbers or no cells present.

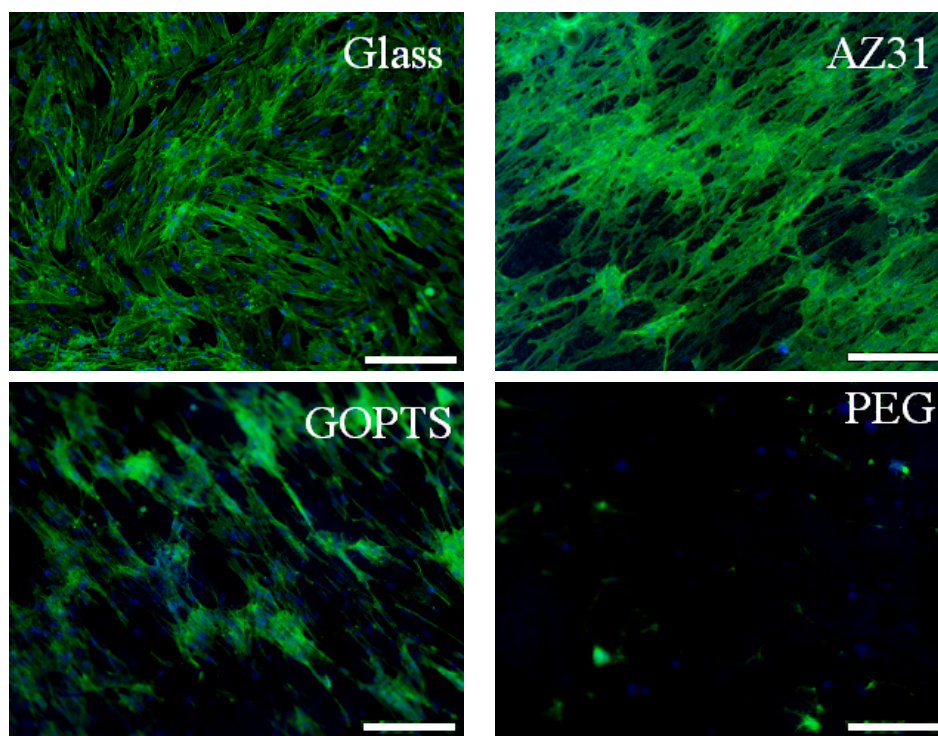


**Figure 6.14:** Osteoblasts seeded for 24 hours on four surfaces stained with Phalloidin for F-actin green and DAPI for nuclei (blue). The PEG coating demonstrates the non-fouling properties of this surface Scale bar = 200  $\mu\text{m}$ .

The mechanism for the cell repellent PEG has been attributed to its conformation. This is a spiral structure leading to very high dipole moment of the ethylene oxide repeats. The dipoles cause extensive hydration along the chains leading to osmotic repulsion of proteins. These chains are also conformed in such a way they cause elastic repulsion of proteins [173]. Protein adsorption was therefore also tested on the surfaces. The PEG modified surface has lower albumin adsorption than the uncoated or the GOPTS surface. Compared to studies using PEG modified titanium surfaces,  $0.155 \mu\text{cm}^{-2}$  is high. Protein concentrations of less than  $10 \text{ ncm}^{-2}$  have been shown on previous studies [173]. Considerations to the surface topography must be made, as the magnesium surfaces were ground to a 4000 grit finish, meaning the surface area is actually higher than recorded. The difference between the PEG coated and uncoated surfaces are also lower than other studies. This is most likely due to the processing and Pierce assay testing route. The PEG surface seemed to be inconsistent at the edges of the sample, this was visible by patches of cell growth. The Pierce assay tests indiscriminately over the total surface and protein is most likely in abundance at the poorly coated edges.

The potential importance of this PEG grafted surface has been demonstrated in coated stents previously. Shin [174] used a diamond like coating to modify Nitinol (TiNi) alloy discs meaning PEG could then be grafted to the surface. The TiNi-DLC-PEG and uncoated TiNi-DLC stents were implanted in rat muscle and skin. After 6 weeks, the PEG coated samples showed far less platelet adhesion, and substantially delayed fibrous tissue

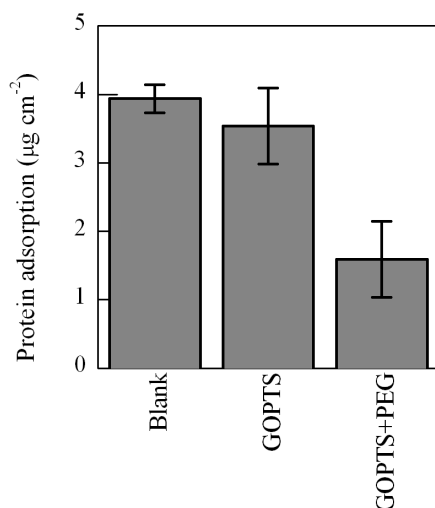


**Figure 6.15:** PEG repels proteins by steric hindrance. Protein adsorption using the Pierce protein assay shows lower adsorbed albumin than the uncoated samples.  $n = 4$ , error = SD

growth than uncoated samples. Billinger dip coated Poly(L-lysine)-graft-poly(ethylene glycol) to steel stents[175]. This gave a PEG polymer brush on the outer surface of the stent surface. After 6 weeks implantation in pig coronary arteries, neointimal were measured to be significantly smaller using PLL-g-PEG-coated stents: A neointimal area of 1.15 mm vs. 2.33 mm (decrease of 51%) and thickness; 0.16 mm vs. 0.31 mm (decrease of 48%) was recorded. Because of this luminal area was larger in PLL-g-PEG-coated stents; 2.91 mm vs. 2.04 mm. Histological restenosis was also significantly smaller in the coated (27%) than uncoated stents (52%)[175].

This work has demonstrated a successful method for the grafting of PEG onto the surface of magnesium alloys by the use of a GOPTS anchor. Its use on cardiovascular stents could potentially have the same impact as seen in the *in vivo* studies by Billinger[175]. Although considerations must be made to the longevity of the coating on a degradable stent compared to steel stents. Billinger's permanent stents were tested after 6 weeks implantation. No degradation studies of the PEG-GOPTS-Mg surface were conducted to determine the lifetime of the protein repellent nature of the surface. If a comparison is made with the water contact angle measurements of ODTMS degradation in SBF, the silane surface is present in this highly corrosive environment (more extreme than *in vivo*) for 5 days, showing a steady state at this point. The PEG coating would not have to give long term stability as with permanent titanium and steel stents due to magnesium being biodegradable. Therefore short term neointimal and histological restenosis reduction would be of great benefit.

At present, the coatings impact on neointimal and histological restenosis reduction can only be speculated. *In vivo* stent trials would have to be evaluated to determine the coatings real impact.

## 6.4 Magnetron Sputtered Hydroxyapatite

Thus far polymer based coatings have been used to lower corrosion and alter magnesium biocompatibility. In the use of silanes this has worked well, but these coatings are in the order of picometers thick and offer very limited adhesion or physical strength. Looking at the orthopaedic market which is being targeted as a potential end use for biodegradable magnesium alloys, the end products (for instance screws) have to take much greater physical demands as these are being inserted into mineralised bone rather than the soft tissue of the arteries. Therefore any surface coating has to be able to cope with the sheer loads and scratching likely to occur when forcing a screw into a bone.

Biocompatibility properties for orthopaedic coatings are different to those for blood-contacting devices. Where cardiovascular stents warranted low protein adhesion and tissue growth, the opposite is true for the orthopaedic applications. A coating for this application would be most successful if it enhanced the surrounding bone's ability to attach and grow into the corroding magnesium implant. Therefore osteoblast and osteoclast promotion is highly desirable to increase bone tissue dynamics.

Many solutions to the corrosion and biocompatibility demands have been proposed for orthopaedic implant applications. Various calcium phosphate coatings have been used on magnesium implants and have shown good corrosion resistance and biocompatibility. But these coatings, using cathodic electro-deposition, micro arc oxidation, thermal oxidation and cathodic arc only have limited adhesion to the bulk material. This potentially means during surgery, the coating could be peeled off or easily damaged.

Magnetron sputtering is a technique that has been used with great success on titanium surfaces to form extremely adherent hydroxyapatite coatings[118]. Magnetron sputtering forms an interface zone in which the coating is physically fused with the bulk material, meaning the coating is not simply on top of the metal. The technique can also be used to coat complex shapes, so is not limited if scaled up for its industrial purpose.

Magnetron sputtering of hydroxyapatite onto magnesium surfaces was considered the most promising coating technique for the corrosion protection and increased biocompatibility of orthopaedic implants. Previously, hydroxyapatite had only been sputtered onto titanium and other permanent metal surfaces [164]. Using magnesium as the substrate, only titanium nitride [126], chromium [127], nickel [128] have been used. So the combination of Hydroxyapatite onto magnesium is novel idea that could be beneficial in orthopaedics.

### 6.4.1 Materials and Methods

AZ31 was supplied in 25 mm rod and ML4 (DF9551) in 9mm diameter rod was machined into 9 mm diameter by 3 mm thick discs. AZ31 was supplied as Magnesium Elektron's commercial product. ML4 was made at Magnesium Elektron by the procedure outlined previously (section 6.2.1).

**Table 6.5:** Specification of ML4 and AZ31 given by wt%. Total impurities equates to the combined composition of Fe, Ni and Cu.

	Y	Nd	HfE(misc)	Al	Zn	Total impurities
ML4	3.7-4.3	2-2.4	1	-	-	0.004
AZ31	-	-	-	2.5-3.5	0.7-1.3	-

### Magnetron sputtering

Sputtering was carried out by Eminate, Nottingham UK. A HA target and ML4 disc were used, these were supplied polished by OPS and washed with acetone. The coating was created by a commercial physical vapour deposition (PVD) system (Teer Coatings UDP650) was used to generate Hydroxyapatite (HA) coatings for this work, comprising a vacuum chamber equipped with a serial pumping system (rotary and diffusion pumps). Gas pressure within the system was controlled using a feedback system comprising a capacitive manometer pressure transducer and piezo controlled mass flow control valve. Samples were held on a stainless steel jig, coupled to a pulsed direct current (DC) bias power supply. A 76.2 mm diameter thermally sprayed HA target was mounted on a magnetron on the sidewall of the vacuum chamber (such that it was immediately adjacent to the sample holder) and connected to a radio frequency (RF) power supply (13.56 MHz) with an automatic capacitive/inductive tuned matching network.

Before coating, the magnesium discs were rinsed in Acetone and dried in a Nitrogen gas stream prior to introduction into the vacuum chamber. Samples were placed in the chamber, on the stainless steel jig adjacent to the HA target, with a separation of circa 110 mm. The chamber was subsequently evacuated to a base pressure of circa  $5 \times 10^{-5}$  Torr.

Once base vacuum was achieved, a controlled flow of 41 sccm of Argon gas was introduced into the chamber via the aforementioned feedback system in order to raise the chamber partial pressure to circa  $1 \times 10^{-3}$  Torr. RF power at a density of  $3.8 \text{ Wcm}^{-2}$  was then applied to the HA target, whilst simultaneously a pulsed DC bias voltage of -25 V (frequency 250 kHz, pulse width 500 ns) was applied to the sample holder, thereby striking a plasma within the process chamber. Such conditions were maintained for a period of 14,400 s before DC and RF power were switched off and samples allowed to cool for a period of 900 s before the chamber was vented to atmosphere to facilitate sample removal.

### Glow emission discharge optical spectroscopy (GDOS)

Reaction layer cross sections were examined by (GDOS) using the same protocol as stated in the previous chapters (section 5.2). The monochromator was set up to detect Ca at 393.366 nm.

**Table 6.6:** Rp values in SBF for coated and uncoated AZ31 after a 430 °C sinter

	Uncoated $\Omega\text{cm}^{-2}$	HA coated $\Omega\text{cm}^{-2}$
1 hour	2649	1936
1 day	24110	13546
3 day	25860	22086

### Grazing incidence X-ray diffraction (XRD)

Surface crystal structure was investigated using a Philips X'Pert-MPD (PW 3040) instrument with a step size  $0.005^\circ$  and a scan range from  $5^\circ$  to  $85^\circ$  (in  $2\theta$ )

## 6.4.2 Results and Discussion

Initial trials for the coating were conducted with AZ31 alloy. This was due to confidentially concerns about sending out the new ML4 alloy to third parties. AZ31 is a world recognised alloy and available freely, but has a low solidus temperature comparative to the rare earth based alloys.

After coating the AZ31 discs were sintered at  $430^\circ\text{C}$  for 2 hours. This was the highest temperature the alloy could safely go to without risk of phases melting. Hydroxyapatite however is usually sintered for this purpose at the  $600\text{--}700^\circ\text{C}$  region.

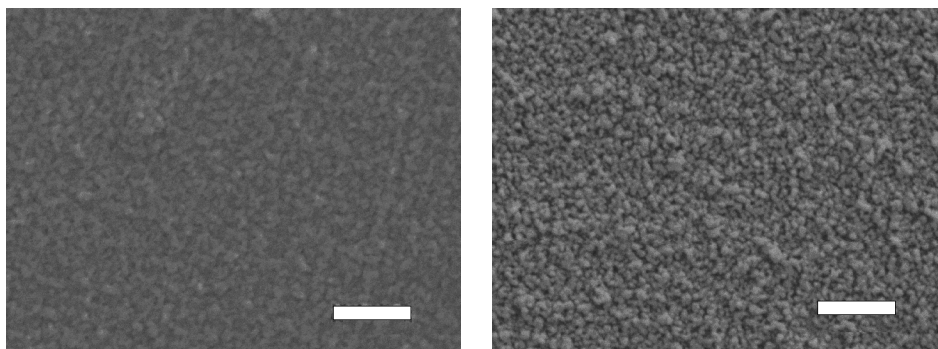


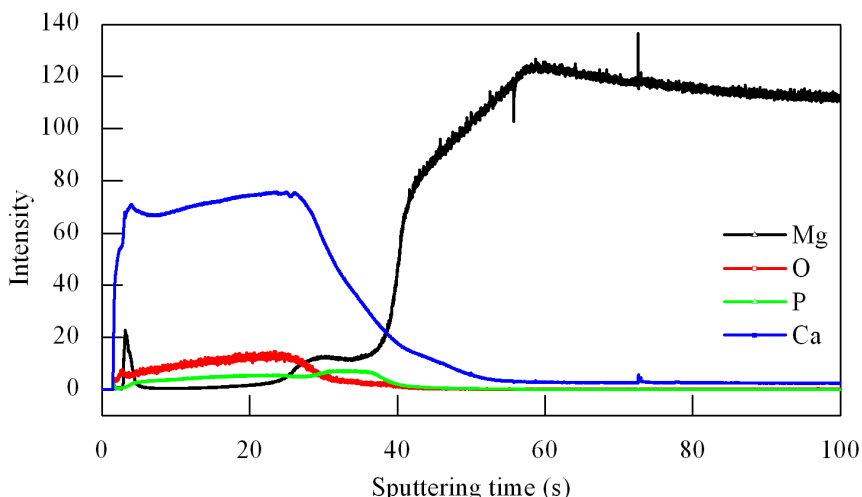
**Figure 6.16:** SEM images of both coated (right) and uncoated AZ31 (left). The surface shows no difference after the coating, with Magnesium oxide appearing over the surface of both samples Scale bar = 500 nm

SEM images (figure 6.16) of the surface revealed no visible difference between the coated and uncoated samples. Electrochemical impedance spectroscopy showed similar plots with Rp values (table 6.6) closely matched. The coating also gave a low frequency loop no bigger than the uncoated. XRD determined the surface to be magnesium oxide with no hydroxyapatite peaks. The conclusion from this initial study was that lower melting point alloys could not be used as a substrate.

ML4 was then coated and sintered at  $530^\circ\text{C}$ . WE43 based alloys are commonly solution treated at  $525^\circ\text{C}$  for improved mechanical properties. With ML4 being a high purity WE43, this temperature was deemed appropriate.

## Surface characterisation

After sintering the coating was characterised for composition and morphology. The magnetron sputter is meant to form an interface zone in which the coating slowly turns into the substrate. This was tested by GDOS which takes an average across the surface every few nanometres in depth giving an average cross section through the first micron of the surface.



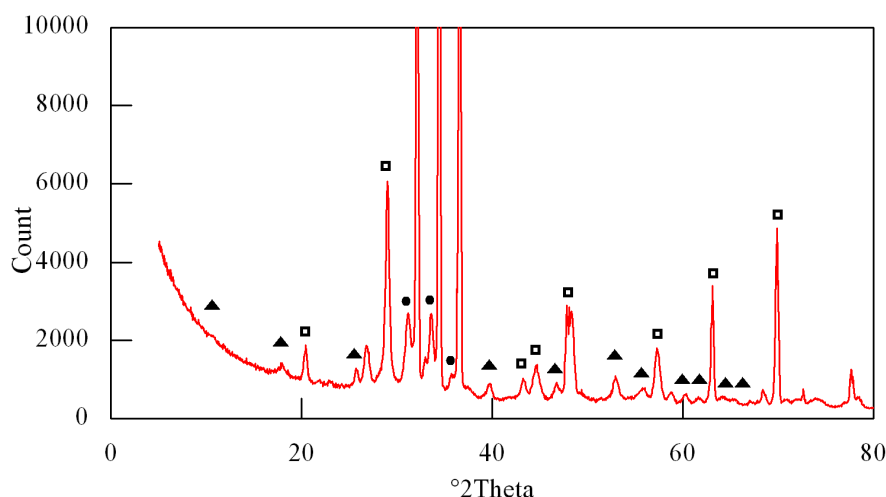
**Figure 6.17:** Cross Section through HA layer (left) to substrate (right) using GDOS.

Figure 6.17 shows the three distinct zones of the coating; The coating, the interface zone and the substrate. The specification to Eminate for the coating was a thickness of 300 nm, therefore the coating plus interface can be assumed to be just over this in thickness. No coating thickness calculation were carried out. The y-axis shown in figure 6.17 is intensity in arbitrary units. Therefore the results are qualitative and show no relation between intensities and atomic or weight percentage between the elements. What is shown however is that calcium and oxygen are fairly uniform through the coating and decrease steadily further into the interface zone. Phosphate however appears uniform throughout the coating but increases within the interface zone before a drop to the substrate.

XRD gives peaks for hydroxyapatite (figure 6.18), which shows the new sinter temperature has worked to a degree. The SEM image (figure 6.19) shows a compact non-porous coating. The crystal structures identified with XRD from the substrate were magnesium and yttrium neodymium second phase. Hydroxyapatite and  $Mg_2Ca$  intermetallics gave peaks which have come from the sputtering process. These intermetallics are most likely the result of the sputtered calcium penetrating into the magnesium, the 530 °C sinter is high enough for the liquid phase of  $Mg_2Ca$  at high magnesium concentrations. The magnesium-calcium phase diagram shows a liquid + HCP Mg phase at temperatures above 800K (526.85 °C) for concentrations 0.8 mole Mg or above. Therefore the formation of  $Mg_2Ca$  phase is thermodynamically favourable.

The hydroxyapatite peaks are faint but consistent in the XRD graph which is attributed to the crystallographic peak pattern of hydroxyapatite being a multitude of small peaks at





**Figure 6.18:** X ray diffraction of the coated sample after sintering at 530 °C for 3 hours. Unlabelled are the three large characteristic magnesium peaks. Labelled with ▲ are hydroxyapatite peaks, ● represent  $Mg_2Ca$ , and □ second phase yttrium and neodymium peaks.

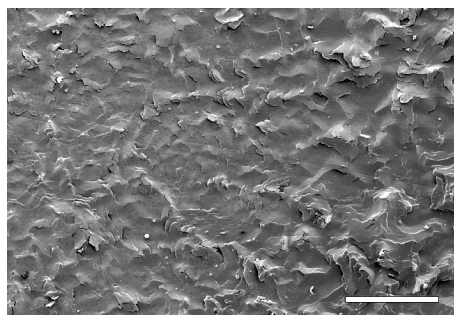


**Figure 6.19:** SEM of Magneton Sputtered HA on ML4 after 530 °C sinter. Scale bar = 50 μm.

most angles. Although the low X-ray count at the hydroxyapatite peaks could also be a low crystallinity as the sinter temperature is very low compared to the temperature which forms the highest density, 1300-1350 °C [176].

### Corrosion Properties

The coated samples when corroded in SBF showed large improvements in overall corrosion and also short term corrosion rate. Hydrogen evolution was negligible in the first 2 hours of submersion in SBF with the coating, whereas the uncoated alloy had produced  $2.2 \text{ ml cm}^{-2}$  (figure 6.20). The corrosion rate stays far lower than the uncoated for the first 24 hours. After which, the uncoated samples passivate and corrosion slows, and interestingly the coated samples increase in rate for the next 24 hours. After 24 hours the rate slows, but is still at a higher rate than the uncoated sample. Overall, the corrosion rate in the first 24 hours is lowered by 6 times. The reason for the changes in corrosion rate seen are indicated by the electrochemical data. Corrosion potential against time (figure 6.21) shows three phases on the coated layers protection. The layer starts with a potential of -1485 mV which drops to -1628 mV in the first 5 hours. From here it stays constant whereas the uncoated passivates, and at just after 33 hours the uncoated becomes more positive than the coated alloy.

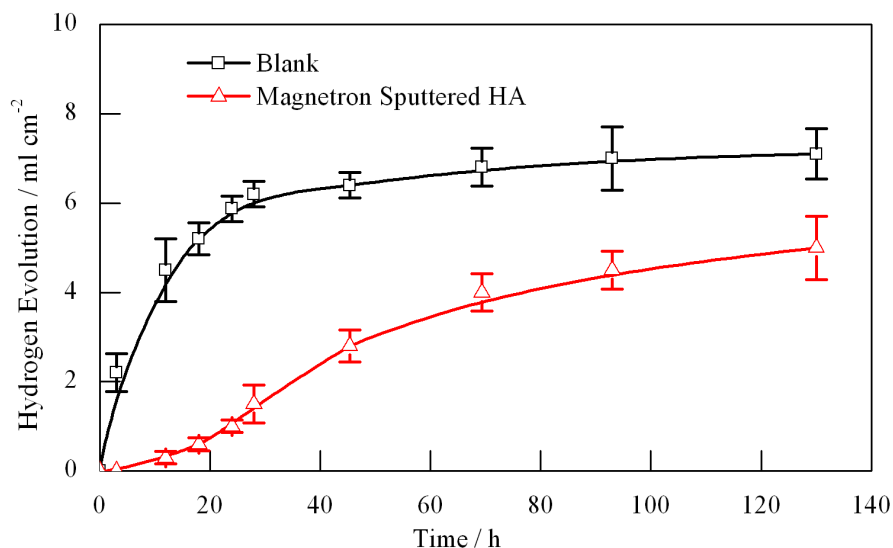


**Figure 6.20:** H<sub>2</sub> evolution against time with HA Coating and uncoated alloy when submerged in SBF. n = 6, error = SD

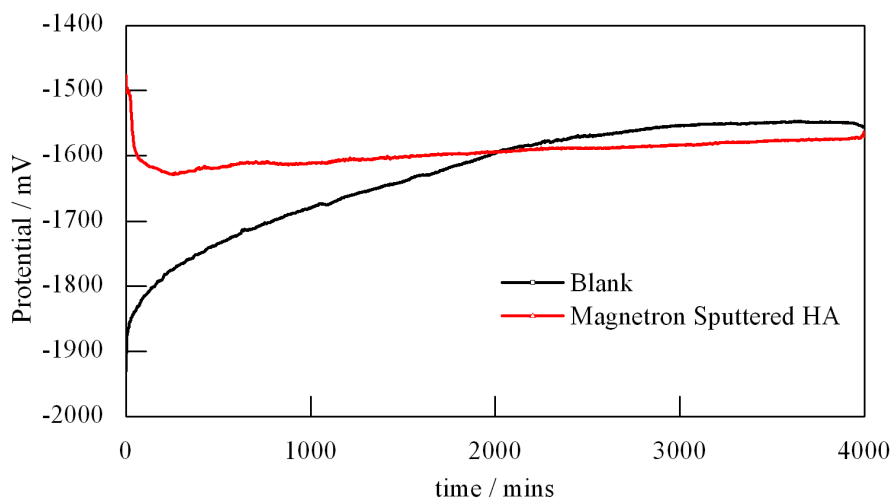


**Figure 6.21:** Potential against time for HA coated and uncoated alloy. The Uncoated shows the characteristic passivation with time. Whereas the HA coated sample shows a large increase in corrosion potential before staying constant.

Potentiodynamic polarisation of the coated sample shows a shift in potential from -2.041 mV to -1.387 mV and a slight reduction in current density from  $3.46 \times 10^{-4} \text{ mAcm}^{-2}$  to  $2.698 \times 10^{-5} \text{ mAcm}^{-2}$  (figure 6.22). With the current density only lowering by less than one order, the coating must be porous. The shift in potential will be the result of the pores leading to the interface zone and not naked magnesium alloy. The interface zone, mainly calcium and oxygen at the surface is far less corrosive than magnesium. The anodic region is flat, meaning the material is not passivating at this stage, another indication that magnesium is not heavily exposed by the pores.

Electrochemical impedance spectroscopy was used at various time periods in SBF (figure 6.23). The first plot at 1 hour shows two well defined time constants, the high frequency being the charge transfer at the metals surface and the low frequency the effect of the coating barrier which is in the form of an inductive loop rather than standard

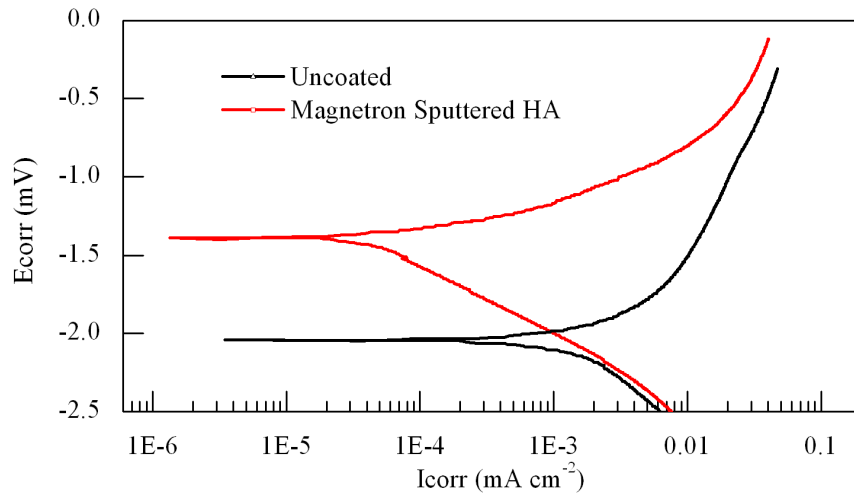


**Figure 6.22:** Electrochemical potentials for HA coating and uncoated sample in SBF. The coating shifts the rest potential over 0.6 mV less negative.

capacitance. Inductive loops are a trait of a stable coating layer. As time progresses the low frequency inductive loop disappears. After 20 hours, this becomes a low frequency capacitance loop, which is the trait of a failed coating, meaning the hydroxyapatite layer is now fully porous.

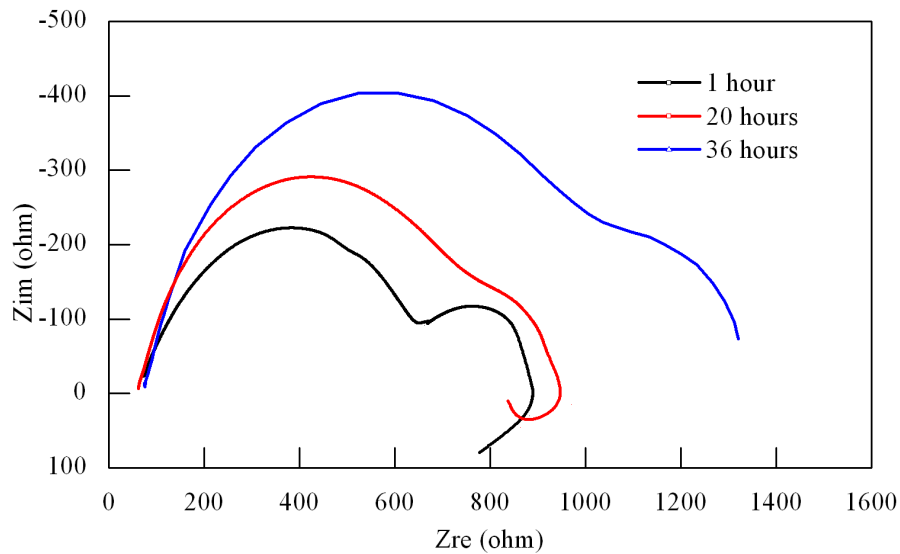


**Figure 6.23:** Nyquist Plot of the HA layer in SBF over time in SBF. The low frequency inductive loop becomes a capacitance loop as the surface coating breaks down.

The high frequency loop also shows two interesting points, firstly it is far larger than that of the uncoated sample and secondly it is ever increasing with time. The former point would mean that the charge transfer between the metal and electrolyte under the coating (HA or oxide film) is more resistive after the magnetron process. This is due to the fact that the process is not simply a coating, but modifies the magnesium beneath into an interface zone, which would have far less magnesium concentration compared to the uncoated sample. The magnesium exposed will slowly passivate as with the uncoated sample and therefore this high frequency loop increases with time.

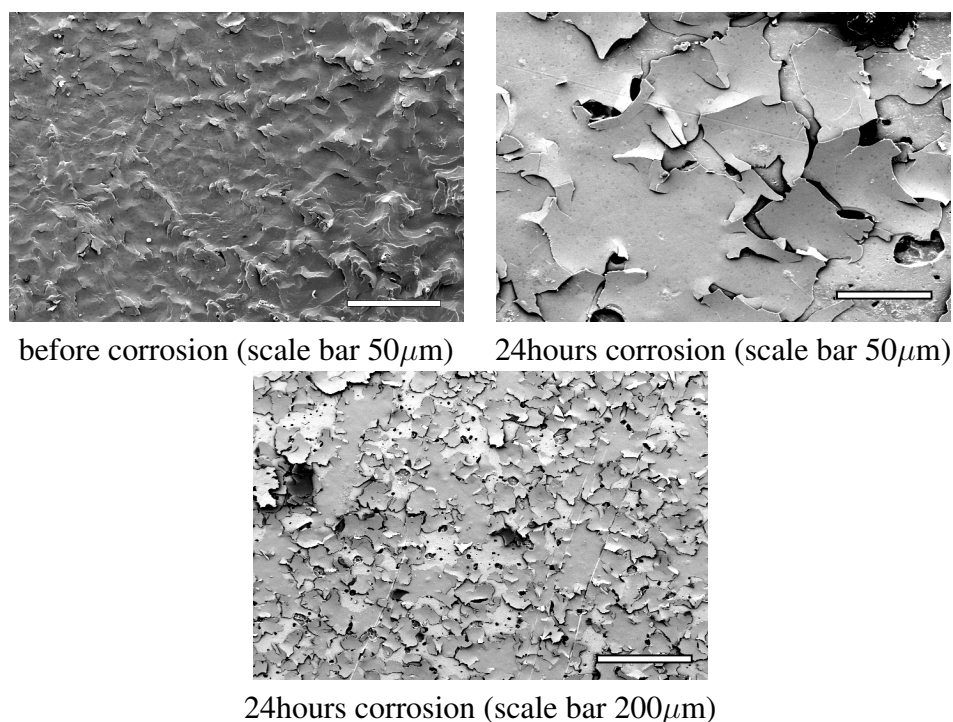


**Figure 6.24:** Degradation of the hydroxyapatite surface after 24 hours in cell culture media. The surface shows peeling of the coating, which appears to flake

From the electrochemical data it would appear the coating is broken down in three stages. Firstly the amorphous regions of the coating become detached and removed from the surfaces within the first 5-6 hours. This is shown by the sudden drop in potential in figure 6.21 and also the shrinking of the inductive loop from 1 hour and 20 hour in the Nyquist plots. This period would also explain the low production of hydrogen seen in the early period, as it is the coating breaking down rather than magnesium.

The coating is mainly the crystalline remains which would have small pores into the interface zone. These pores would have to be present for the production of hydrogen gas seen after 10 hours. SBF can attack these pores, but only slowly as magnesium at the outer region of the interface zone is visible in small concentrations as shown by the GDOS plots, hence corrosion rate begins low. These sites of corrosion become deeper and undermine the surrounding coating, meaning the coating starts to peel as seen in the SEM images. The corrosion pits grow at a speed determined by two rate limiting factors. Firstly, as they become deeper into the interface they are exposed to ever increasing amounts of magnesium (from both surface area and concentration of magnesium with depth) therefore speeding up corrosion, visible in the hydrogen evolution plots between 10 and 40 hours. The exposed magnesium then becomes rate limited, as with any uncoated magnesium in SBF, by the production of semi stable phosphate and carbonate based reaction layers (seen after 40 hours). This leaves the interface zone in state of attack from the SBF through large porous zones now only coated by a peeling top layer but in equilibrium with the the two rate limiting factors. The corrosion rate stays at a higher rate then that of blank magnesium after the equilibrium between corrosion pits and reaction

layer formation. This is due to the presence of  $Mg_2Ca$  and various other particles within the interface zone. These are slightly less galvanic than the magnesium alloy around them and thus promote coupling. Once the entire interface zone has been corroded, it is predicted that the corrosion rate would reach the same as for the uncoated samples at the same time point.

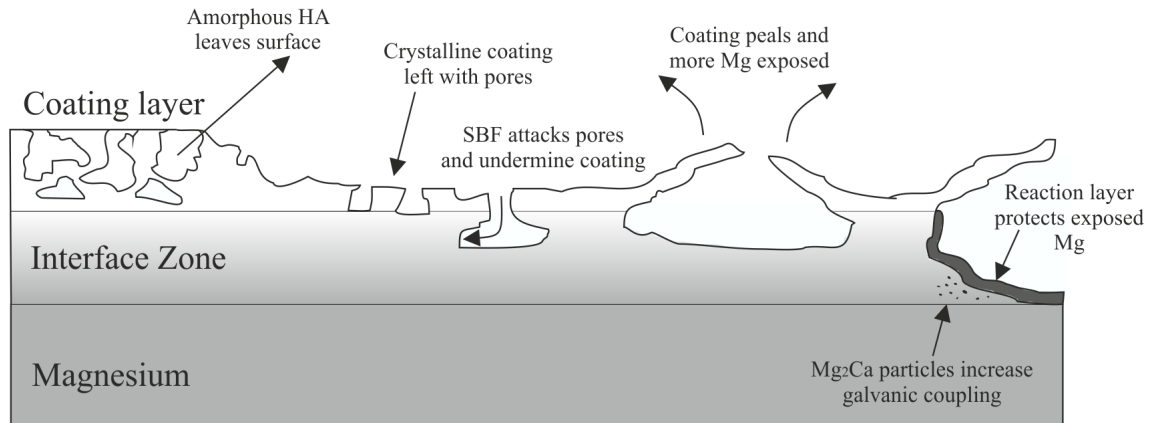


**Figure 6.25:** Schematic of the proposed breakdown of the HA coating, concluded from the various electrochemical and visual investigations above. Left hand side represents the point of exposure to SBF, with the stages of breakdown progressing further right with time.

### Biocompatibility

SEM was used to determine biocompatibility. Both samples were washed with PBS and cell culture media twice. The discs were then left in cell culture media for 3 hours. This was done to prevent the blank magnesium sample being too harsh for the cells, but representative of the conditions faced.

As seen in chapter 3, the cells seeded at early times points on bare magnesium alloys survive in good numbers, but far less than a pre corroded sample or a passive material like glass, titanium or steel, generally a survival rate of 40% was seen. The cells on magnesium generally appear well attached and this study was no different. SEM images of the hydroxyapatite coating shows the different environment the cells were introduced to. The uncoated sample is highly cracked, a product of the dehydration processing samples for SEM. This is the magnesium alloy's reaction layer, the surface on which the cells have to adhere, meaning the cells are at the point of hydrogen production, hydroxide formation and various other chemical reactions taking place. The hydroxyapatite coating looks to be more stable, with cells well spread, higher in density and showing no signs of stress. The reaction processes of the magnesium have been lowered in rate and also moved in relative position to the cells, which are now raised above the magnesium.

## 6.5 Conclusions

The aim of this chapter was to lower the initial corrosion rate of magnesium alloys in *in vitro* conditions with solutions that are applicable to the production of implants of

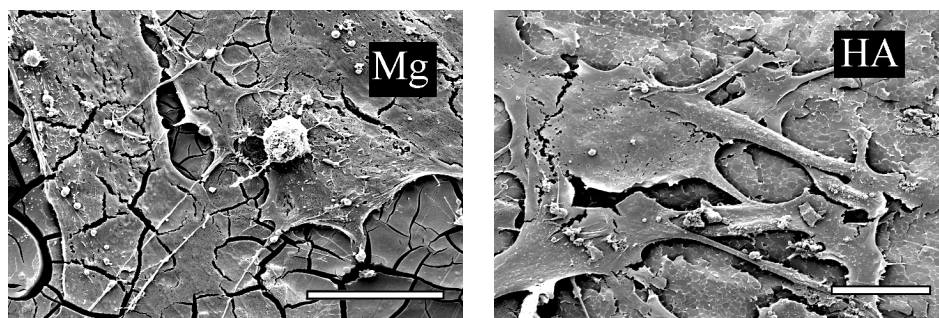


**Figure 6.26:** SEM images of osteoblasts on uncoated and magnetron sputtered hydroxyapatite coated magnesium after 24 hours culture, scale bar = 20 $\mu$ m

which bioresorbable magnesium is targeted. Therefore both successful techniques used here; organo-silanes and magnetron sputtering are credible options for the production of cardiovascular stents or orthopaedic trauma implants.

The use of organo-silanes protects magnesium well and for over 4 days (figure 6.10, giving reductions in corrosion rate of 6 times in the first hours.

Silanes successfully used as anchors for the grafting of polythene glycol, amino acids, alkylcarboxyl chains and  $\alpha$ -lipoic acid. The covalent attachment of PEG to the surface of magnesium is the first recorded and visibly lowers the adhesion of cells onto the surface. The practical benefits of this coating have been demonstrated by Billinger[175] and Shin [174].

Magnetron sputtered hydroxyapatite lowered corrosion rates by 6 times in the first 24 hours with no visible hydrogen gas being evolved in the first hours of submersion in SBF. The coating only proved protection for the first 2 days, but with increased deposition thickness, this is believed to improve. Biocompatibility of the surface with osteoblasts also improved.

## 6.6 Further Work

### 6.6.1 Silanes

From a development perspective the combination of the low corrosion properties of silanes and the non fouling property would be of great potential to the cardiovascular stent market. For this, long chain hydrophobic molecules would have to be attached with functional groups at the end, available for the attachment of PEG. Several molecules have been trialed for this purpose by the author, including Suberic acid, which is a 10 carbon chain with a carboxyl acid at either end.

The attachment of the peptide sequence RGD could also have significant benefits, especially if attached on top of a corrosion inhibiting silane layer. The attachment of this sequence is made impossible using peptide building methods as the side group blocking molecule, Fmoc cannot be removed without an acid treatment. One method to attach RGD to a silane layer would be the use of a pre made RGD sequence, but these still have

Fmoc blockers on the chain ends. Therefore a solution which has been considered is the attachment of RGDC. The cystine amino acid contains a thiol in its R-group. This can be bonded via maleimide to carboxyl groups. This method of production does not involve removal of Fmoc groups, meaning acid treatment is not needed. This is a feasible route to the functionalisation of a corrosion inhibiting silane layer with RGD for promoted cell attachment. Its use would be for orthopedic implants where fast and strong bone adhesion is needed for prevention implant failure.

*In vivo* testing of the PEG non fouling surface on stents would be a large step forward. The stent manufacturing partners were made aware of the PEG coating route but chose not to follow up with *in vivo* tests as they are persisting with the drug eluting method. Therefore *in vivo* trials will be carried out by future university funded projects. *In vitro* work on the surface such as platelet binding and blood studies would be a useful bridging step before this.

### 6.6.2 Magnetron Sputtered Hydroxyapatite

The coating used in this study was 300nm thick, which proved to be adequate in lowering corrosion rates for the first 2 days, but a thicker coating should be investigated. As the greater amount of hydroxyapatite on the surface would mean greater amounts of crystalline hydroxyapatite on the surface after sintering. This would lead to even lower corrosion rates.

Magnetron sputtering was used because previous authors had reported high adhesion strength onto the substrate [118]. This has not been tested, therefore thicker coatings produced should be investigated with scratch tests for example.

Mechanical properties of the sputtered magnesium needs to be investigated. It can be assumed the surface coating has modified the materials stress corrosion cracking properties as well as small changes in tensile strength.

Further *in vitro* studies on the new coating should be completed, fully investigating the long term affects of cell density comparative to uncoated magnesium and also regarding cell activity and function. Hydroxyapatite is known to stimulate bone intergration *in vivo* and affect osteoblast activity *in vitro* and could therefore change the characteristics of cells culture on its surface [177].

The final investigation would be the coating of a screw or plate and testing it *in vivo*. Coating strength could be analysed to see if surgical procedures are too robust for the coating and corrosion monitored to determine if is having a desired effect on implant longevity and hydrogen evolution.





## ERBIUM ADDITIONS TO YTTRIUM RARE EARTH ALLOYS FOR REDUCED CORROSION RATE

### 7.1 Introduction

The previous chapter demonstrated a promising alloy addition in the form of Erbium. The 8wt% addition of Er increased corrosion resistance by over seven times compared to the standard medical grade neodymium-yttrium alloy. This level of improvement in corrosion rate is encouraging. This chapter outlines the promising characteristics of the alloy and attempts to address why the alloy has such a low corrosion rate in biological solutions.

As an element Er is hexagonal close packed in crystal structure and soluble in Mg, with its maximum solid solubility being 3.5at%. The atomic radius of Er is 175.7 pm which is 29.2% more than that of Mg. Therefore Er addition should lead to solution strengthening in Mg.

### 7.2 Material and methods

The two alloys used in this chapter were ML4 as the control (MI0009) and ML4 + 8 wt% Er (MI0029) supplied in 9mm diameter rod. The material was made at Magnesium Elektron by melting pure magnesium ingot with the appropriate alloying elements. Once molten, the metal is stirred and a small casting was made for chemical analysis by Optical Emission Spectrometry (OES). If this falls within specifications the metal was ready to cast. Molten metal was then poured from the crucible into the mold. Once solidified and air cooled, the casting was machined into 75 mm diameter billets for extrusion

The extrusion procedure required, pre heating of the billet, die and billet container to specified temperatures. The material was then extruded into 9 mm bar. These bars are then lathed into 9 mm by 3 mm discs for testing.

**Table 7.1:** Alloy composition used of ML4 and ML4 + Er given in wt%. Total impurities equates to the combined composition of Fe, Ni and Cu.

Melt Number	Y	Nd	HRE(misc)	Er	Total impurities
MI0009	3.7-4.3	2-2.4	1	-	0.004
MI0029	3.7-4.3	2-2.4	1	8	0.011

## Surface Examination

The surfaces and cross sections of the coatings were examined by field emission gun scanning electron microscopy (FEG-SEM), using a Philips XL30 FEG SEM, equipped with energy-dispersive X-ray (EDX) analysis facilities. The cross sections were prepared by grinding, using successive grades of SiC paper, and polishing to  $1/4 \mu\text{m}$  diamond finish followed by colloidal silica (OPS). Crystal structure was investigated by X-ray diffraction (XRD), using a Philips X'Pert-MPD (PW 3040) instrument with a step size  $0.005^\circ$  and a scan range from  $5^\circ$  to  $85^\circ$  (in  $2\theta$ ). Reaction layer cross sections were examined by glow emission discharge optical spectroscopy (GDOS) using a GD-Profilier 2 (Horiba Jobin Yvon). This operated in the rf-mode at 13.56 MHz. A 4 mm diameter copper anode and high purity argon gas was used. The emission responses from the excited sputtered elements were detected with a polychromator of focal length of 500 mm with 30 optical windows. The emission lines used were 130.21 nm for oxygen and 383.82 nm for magnesium. The erbium or calcium response was recorded using a monochromator adjusted to the corresponding lines at 422.67 or 369.26 nm for Er or Ca respectively. Monochromator allows monitoring of one element during measurements. The elemental depth profiling was carried out at argon pressure of 650 Pa and a power of 35 W, with a data acquisition time of 0.01 s. Prior depth profiling, pre-sputtering of a monocrystalline silicon wafer was undertaken to clean GD source. Data fitting analysis of the different elemental depth profiles was performed using a standard user-defined curve fitting function of IGOR Pro software (WaveMetrics).

## Electrochemistry

Electrochemical measurements were conducted in aerated salt solutions at  $37^\circ\text{C}$ , using an ACM-instruments Gill AC computer-controlled potentiostat. A conventional three-electrode cell was employed with a platinum counter electrode and a saturated calomel reference electrode (SCE). The working electrode was the test material with an exposed area of  $0.64 \text{ cm}^2$ .

Initially the open circuit potential (OCP) time behaviour was examined. This was followed by anodic and cathodic potentiodynamic polarisations at a scan rate of  $0.3 \text{ mVs}^{-1}$ , commencing from  $-3 \text{ mV}$  or  $-0.3 \text{ mV}$  with respect to the OCP, respectively.

Electrochemical impedance spectroscopy (EIS) was performed with a three electrode cell incorporating a cylindrical platinum counter electrode and a saturated calomel elec-

trode. Data acquisition employed a combined frequency response analyser and potentiostat (Solartron 1280), with 'Z plot' software. The amplitude of the sinusoidal signal was 20 mV, with a frequency range of 20 kHz to 5 Hz. Data were analysed by 'Z view' software.

## 7.3 Results and Discussion

### Characterisation

Optical microscopy reveals a similar grain structure between the two alloys. The noticeable difference is more second phase which appears darker. Using SEM imaging, the two microstructures are set apart by the large increase in second phase and also with the addition of cube like particles. Using backscattered electrons at high energy, elemental differences across the microstructures can be seen. The second phase particles seen with the secondary electrons across both alloys all appear the same intensity of white indicating their chemistries are similar and made of heavy elements. The only distinction between the all the second phases present is the shape. Therefore the microstructures are split into three constituents; matrix, second phase and cuboid particles.

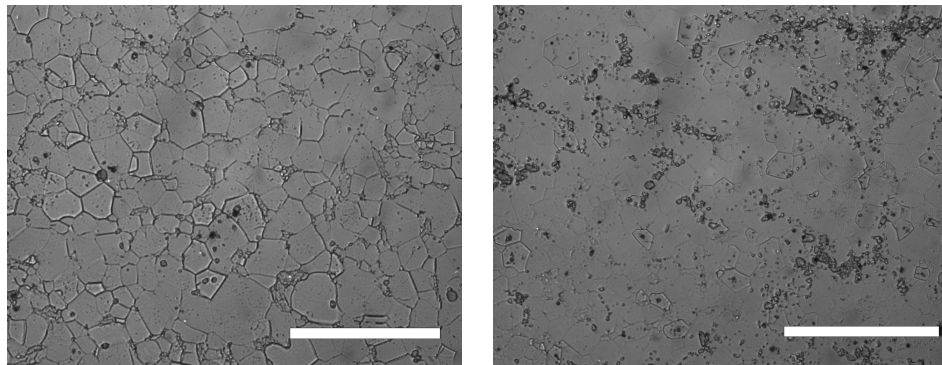


**Figure 7.1:** ML4 (left) and ML4+Er (right) microstructures shown with optical, etched in 5% Nitol, scale bar = 40  $\mu\text{m}$ .

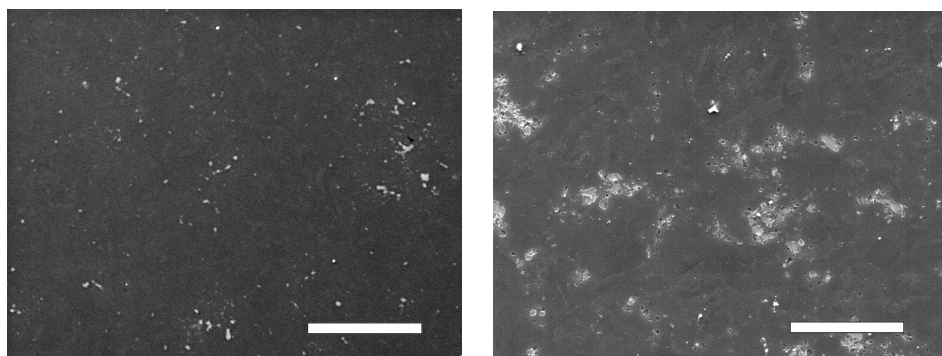


**Figure 7.2:** ML4 (left) and ML4+Er (right) using SEM Secondary Electrons, scale bar = 50  $\mu\text{m}$ .

Using EDX to analysis chemistries of the microstructure is can be seen that the Er affects most the features throughout the material; forming in the Mg matrix, RE second

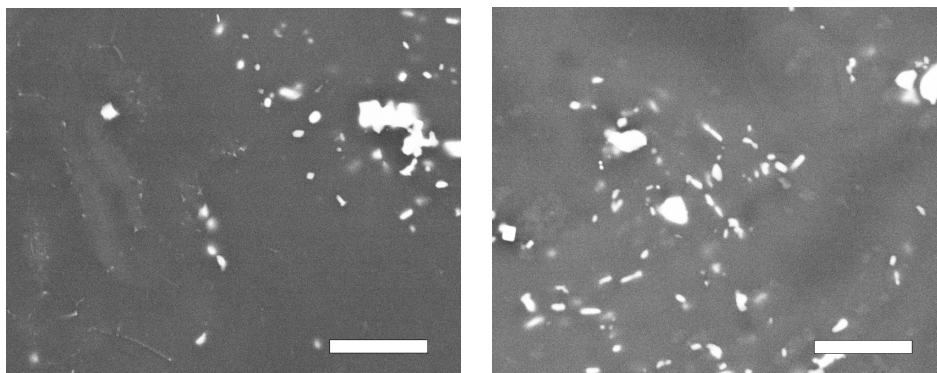


**Figure 7.3:** ML4 (left) and ML4+Er (right) microstructures shown with Back Scattered Electrons, scale bar = 10  $\mu\text{m}$ .

phases and a high Er cuboid particle. Er concentration within the matrix varies between 8 and 9wt% ( 1.4 at% and 1.7 at%), which is lower than the solid solution limit of Er within the Mg crystal structure. The second phase particles show higher amounts of Er (14.37 wt%) than the matrix so must therefore be present in an intermetallic with the neodymium and yttrium. The new particle not seen in MI0009 is an Yttrium-Er intermetallic cuboid particle (67.70wt%Er etc etc).

**Table 7.2:** Particle chemistry of MI0029 established by EDX in wt%. The area analysed by EDX is shown in figure 7.4.

Area	Mg	Y	Nd	Er
Matrix	85.48	4.07	2.17	8.29
Second Phase	57.06	11.40	18.19	13.35
Cube	2.63	28.10	1.57	67.70

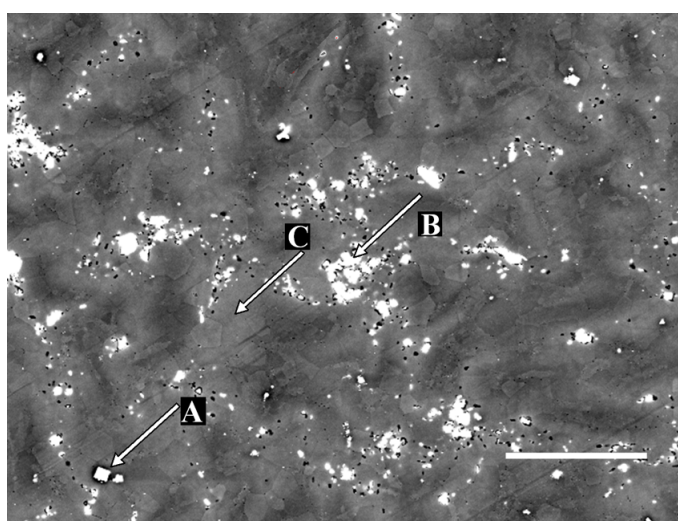


**Figure 7.4:** Back scattered electron image of MI0029 with EDX composition points. Arrow A; erbium cuboid particle. Arrow B; second phase. Arrow C; matrix.

X-ray diffraction confirmed a stretching of the matrix lattice most likely due to the inclusion of Er. This is determined by the shift in the triple peaks between  $32^\circ$  and  $37^\circ$

(Insert figure 7.5).  $\text{Mg}_2\text{Er}$  was also observed which also has a hexagonal structure and most is likely dispersed in the matrix. Both alloys were found to have the Mg-Nd crystal  $\text{Mg}_3\text{Nd}$ , a plate like face centred cubic particle commonly seen in WE43 alloys [178].

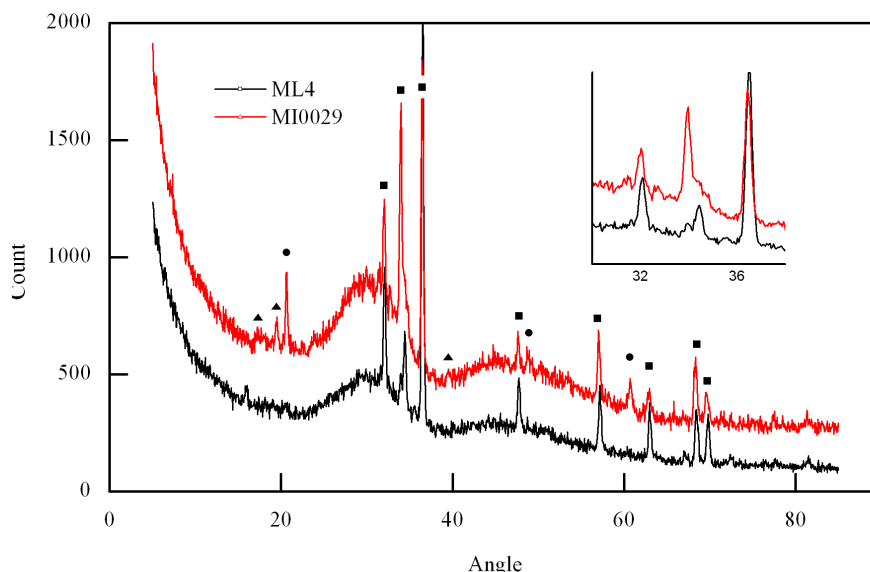


**Figure 7.5:** Grazing X-Ray Diffraction plots of MI0009 and MI0029. Insert highlights the triple Mg HCP lattice peaks and shows the shift in diffraction angle caused by lattice stretching due to Er. Labelled with  $\square$  representing magnesium,  $\blacktriangle$  for  $\text{Mg}_x\text{Nd}_y$  peaks and  $\bullet$  for  $\text{Mg}_x\text{Er}_y$  peaks.

Further work has to be completed to fully characterise the particles found in the Er containing alloys, but the important note is the confirmation of the distribution of Er within the Mg crystal lattice. A full particle analysis should be completed when the final alloy chemistry is finalised.

### Corrosion testing

Using SBF baths for mass loss and the gas displacement method for hydrogen evolution (figure 7.6), the corrosion rates of the two alloys were determined. Figure 5.8 in chapter 5 shows the mass loss of MI0029 to be less than a quarter of MI0009 (67 mpy compared to 837 mpy). The Er containing alloy evolved  $2.14 \text{ ml cm}^{-2}$  of hydrogen in the 7 days on test. The standard ML4 alloy evolved over 7 times as much with  $16.78 \text{ ml cm}^{-2}$ .

### Electrochemistry

The two alloys were tested over 7 days in SBF using potentiodynamic polarization (figure 7.3) and electrochemical impedance spectroscopy (figure 7.8). The Tafel exploration values reveal MI0029 to be more noble than ML4 ( $E_{\text{corr}}$ ;  $-2.043 \text{ mV}$  against  $-1.961 \text{ mV}$ ) and  $I_{\text{corr}}$  also lowered ( $3.46 \times 10^{-4} \text{ mA cm}^{-2}$  against  $0.768 \times 10^{-4} \text{ mA cm}^{-2}$ ), as expected for a less corrosive material. Two other observations can be made however; firstly MI0029 increases in nobility and shifts to lower current densities over time faster than MI0009. Secondly a large anodic shoulder is seen on the Er containing alloy in the first hours of submersion, whereas it takes 16 hours for the same to be seen on ML4. This

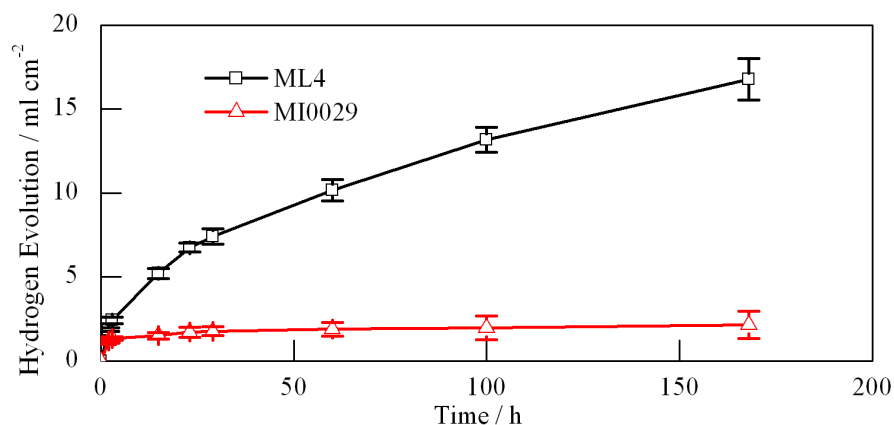


**Figure 7.6:** Hydrogen evolved from both alloys in SBF at 37 °C. MI0029 corrodes at 7 times less than ML4 over the 7 day period.  $n = 8$ , error = SD

means that the erbium is having not only an effect on corrosion potentials at the bare metal stage, indicated by the lower  $E_{corr}$  and  $I_{corr}$  values, but also by quickly providing protection with a semi-stable film, a process that the non-Er containing alloy takes far more time to replicate.

**Table 7.3:** Tafel exploration values from the potentiodynamic polarisation curves obtained in SBF from MI0009 and MI0029 alloys.

Time (h)	MI0009		MI0029	
	$E_{corr}$ (mV)	$I_{corr}$ (mAcm <sup>-2</sup> )	$E_{corr}$ (mV)	$I_{corr}$ (mAcm <sup>-2</sup> )
1	-1.975	$7.27 \times 10^{-4}$	-1.903	$2.19 \times 10^{-4}$
2	-1.858	$2.14 \times 10^{-4}$	-1.776	$6.98 \times 10^{-5}$
8	-1.784	$8.67 \times 10^{-5}$	-1.696	$5.01 \times 10^{-5}$
16	-1.718	$7.06 \times 10^{-5}$	-1.656	$1.11 \times 10^{-5}$
24	-1.658	$1.25 \times 10^{-5}$	-1.650	$1.09 \times 10^{-5}$

The impedance data reveals that protective film is far stronger on MI0029 than MI0009 as well as being made at earlier time points. The polarisation of the low frequency loop, assumed to be the semi passive reaction layer was  $17.43 \Omega\text{cm}^{-2}$  for MI0009 compared to  $56.28 \Omega\text{cm}^{-2}$  on MI0029 at 1 hour and  $95.9 \Omega\text{cm}^{-2}$  and  $400.50 \Omega\text{cm}^{-2}$  at 24 hours.  $R_p$  values for the medium frequency material interface loop (table 7.4), show resistances that start much higher and grow quicker for MI0029, starting at around 3 times greater than MI0009 with 1 hour submersion and rising to around 5 times greater after 7 days.

Both the polarisation and impedance plots reveal that the use of Er not only makes the alloy slightly more noble, but also helps to create a more stable semi passive reaction layer than formed without Er that is also produced with less time.

### The Effect of phosphates and carbonates

An interesting observation with MI0029 is its performance in salt solutions of NaCl. Considering its overwhelming performance in SBF against ML4 alloy MI0009, the same

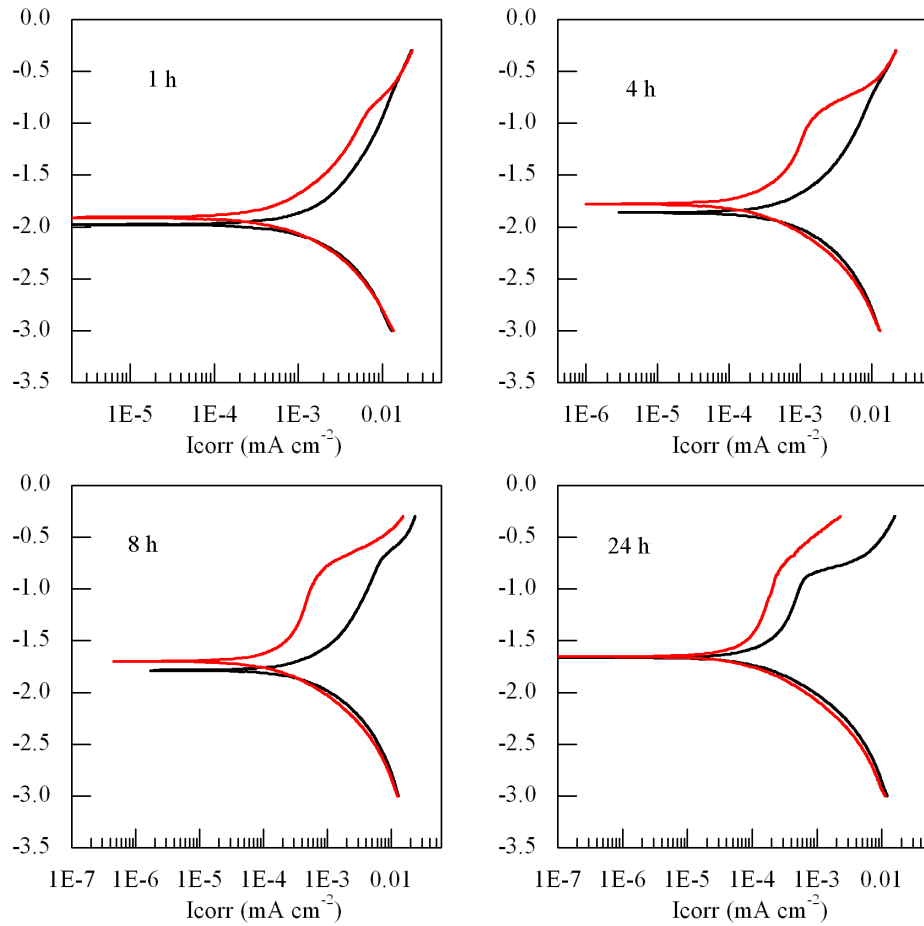


**Figure 7.7:** Potentiodynamic polarisation curves obtained in SBF over time with both alloys; MI0009 (black) and MI0029 (red). MI0029 grows an anodic shoulder within the first hours, ML4 takes 16 hours to replicate.

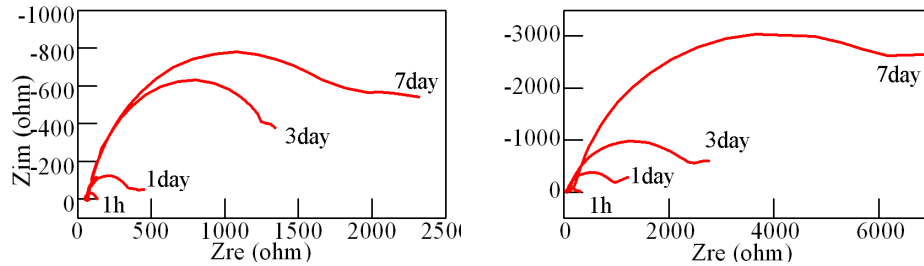


**Figure 7.8:** Nyquist plots of ML4 (left) and MI0029 (right) in SBF with increasing time.

might be expected in all solutions, but this is not the case. When tested in 0.1M NaCl solution (equal to the NaCl concentration of SBF) MI0029 performed similar or worse. Hydrogen evolution in the NaCl and SBF solutions (figure 7.9) shows the low corrosion as previously shown of MI0029 in SBF, but there is no difference in NaCl. MI0009 is showed to be nobler in NaCl than MI0029, but this nobility is switched in SBF. The same affect is seen in the polarisation resistance from the impedance plots (figure 7.10).

This effect seen with phosphates and carbonates is significant to the development of a Mg-Y-RE-Er alloy as it shows the Er is only having a positive influences in biological salt solutions. Rosalbino published work in 2004 [157], using small amounts (0.3 and 0.9 at%) of Er in an Mg-Al alloy and showed improved corrosion resistance in 0.05M  $H_3BO_3$

**Table 7.4:** Polarisation Resistance values obtained from figure 7.8.

Time (h)	Rp( $\Omega\text{cm}^{-2}$ )	
	MI0009	MI0029
1	60	177.7
24	300.4	986.9
72	1470	2643
168	1990	9830

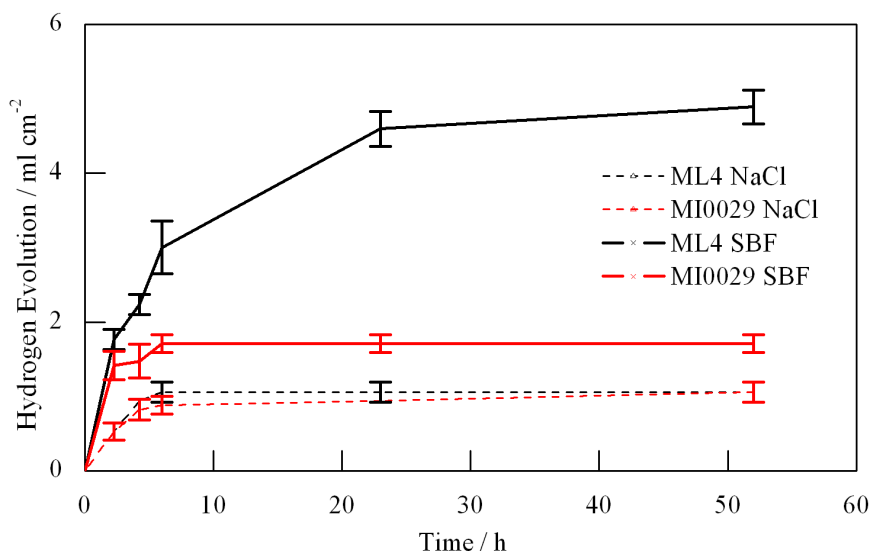


**Figure 7.9:** Hydrogen evolution for ML4 and MI0029 in both 0.1M NaCl and SBF. The curves show that MI0029 only offers greater corrosion resistance in SBF and not NaCl.  $n = 4$ , error = SD.

+ 0.075M  $\text{Na}_2\text{B}_4\text{O}_7$  solution, concluding that the incorporation of Er in the  $\text{Mg}(\text{OH})_2$  lattice was responsible for the improved corrosion behaviour of the Mg-Al-Er alloys.

This present work would indicate that Rosalbino's conclusion is not the same effect seen in SBF.  $\text{Mg}(\text{OH})_2$  is the predominate oxide state when corroded in NaCl solutions, thus if Rosalbino's statement was true, MI0029 would be nobler and have greater corrosion resistance in the NaCl solution.

A fair assumption would be that the Er is having an affect on reaction layer formed in the SBF solution. The two main components of this are phosphate and carbonate which have previously been show to incorporate into the reaction layer of Mg alloys in SBF type solutions [74]. A systematic approach of adding both the phosphate and carbonate consistent with the SBF composton to 0.1M NaCl was used to determine this. This gave the following solutions. 1mM  $\text{KH}_2\text{PO}_3$  + 0.1M NaCl and 28mM  $\text{NaHCO}_3$  + 0.1M NaCl.

The addition of phosphate and carbonate to the NaCl solution showed the same effect when comparing NaCl solution to SBF; MI0029 and MI0009 switch in their order of corrosion resistance. This is shown in both the impedance plots and polarisation curves (figure 7.12). If the 1mM  $\text{KH}_2\text{PO}_3$  + 0.1M NaCl plots to the curves gained in NaCl only (figure 7.10), Ecorr values for MI0029 have become more noble than MI0009, with MI0029 moving -0.04 mV from -1.602 mV to -1.6429 mV, whereas MI0009 shifted 5



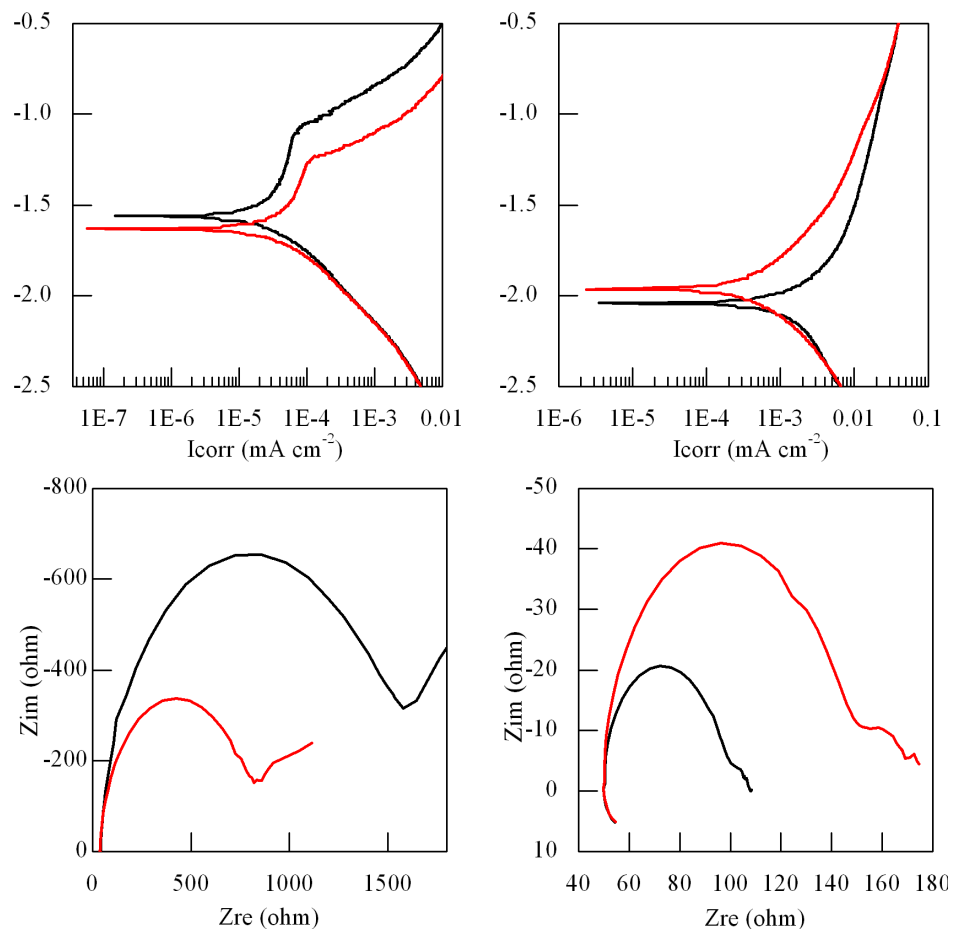


**Figure 7.10:** Polarisation and impedance plots for both alloys (ML4 black and MI0029 red) in NaCl (left) and SBF (right). MI0029 appears more corrosion resistant in NaCl, but less in SBF.

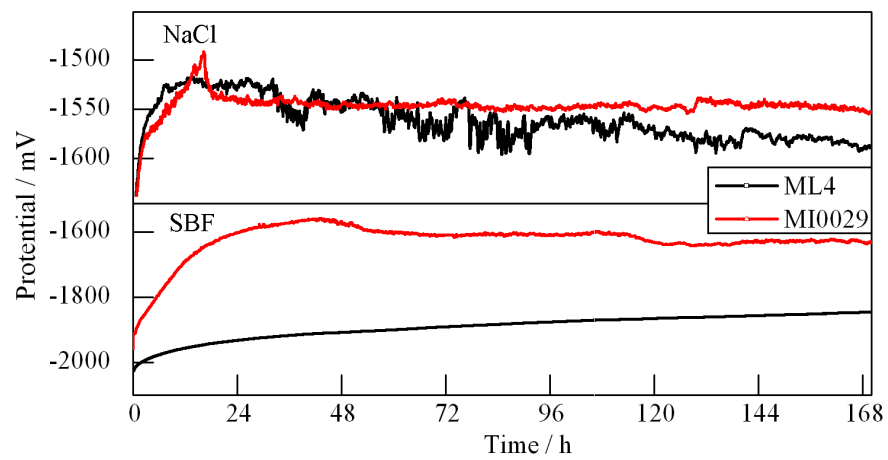


**Figure 7.11:** Rest potential against time of ML4 and MI0029 in NaCl and SBF.

times as much; -0.222 mV from -1.414 mV to -1.693 mV. Icorr values were similar in shift, both moving to higher current densities by around 2.5 times. Both alloys show a large shoulder on the anodic curve, but ML4 breaks down at higher potential comparative to rest than MI0029. This would indicate that the ML4 is forming a more stable layer at higher potentials with the added  $\text{HPO}_3^{2+}$  than MI0029. The Nyquist plots however show no definite low frequency activity, meaning a lack of a surface layer formed at rest potential, although MI0029 does show a small lip which could be a capacitance loop.

Both alloys showed an increase in  $R_p$  values, an effect which contradicts Xin's work [75]. This is most likely due to Xin using AZ31 as both concentrations of NaCl and  $\text{KH}_2\text{PO}_3$  are the same along with time point used. AZ alloys are known to produce  $\text{Al}_2\text{O}_3$  and  $\text{Mg}(\text{OH})_2$  at the surface, meaning the  $\text{HPO}_3^{2+}$  could be poorly incorporated into the reaction layer as potential explanation for Xin's negative phosphate data.

The effect of carbonate on both alloys shows the opposite trend to phosphate by lowering polarisation resistance comparative to NaCl solution. However, as with phosphate MI0029 demonstrates greater values than MI0009 which before the added  $\text{HPO}_3^{2+}$  was the reverse. Carbonate lowers the rest potential of MI0009 by -0.356 mV from -1.471 mV to -1.827 mV and lowers it by -0.069 mV from -1.601 mV to -1.670 mV in MI0029, meaning ML4 decreased potential 5 times more than the Er containing alloy. Both alloys show prominent anodic shoulders, but MI0029 appears to be far more stable than ML4 breaking down at over 1 mV greater than the rest potential ML4 appears to be around 0.75 mV. Carbonate in the solution has had a greater affect on the curves than phosphate. This could be due to the greater affect in stabilising the reaction layer with the formation of magnesium-carbonates, or the result of a greater concentration of  $\text{HCO}_3^+$  than  $\text{HPO}_3^{2+}$  used in the investigation. Nevertheless, carbonate appears to be the prominent ion in stabilising the RE based Mg alloys used here, and also the major reason MI0029 out performs MI0009 in SBF. This is shown in the impedance data, where the Er alloy is recorded with  $R_p$  values of  $250.7 \Omega\text{cm}^{-2}$  and ML4,  $114.3 \Omega\text{cm}^{-2}$ , 2.19 times the value. Whereas in the Phosphate, MI0029 has a polarisation resistance of  $2957 \Omega\text{cm}^{-2}$  and MI0009  $2042 \Omega\text{cm}^{-2}$ , only 1.44 times greater.

The results in figure 7.12 has effectively proved that Er's influence in the alloy is in its stabilisation of the reaction layer, in part agreeing with Rosalbino's conclusion. However as Er's influence was actually detrimental in NaCl solutions, where  $\text{Mg}(\text{OH})_2$  along with  $\text{MgCl}_2$  are products found within the reaction layer, Rosalbino's comments that Er is integrating into the  $\text{Mg}(\text{OH})_2$  lattice and enhancing its stability are not true in this case. Er is having a stabilising affect on this layer, but as seen with Figure 7.12, it's a product of carbonate and phosphate rather than hydroxide.

Using GDOS, cross sections of the reaction layer compositions can be accurately accessed. The first point to note, which is seen in both Figure 7.13 and 7.14 is that Er is in greater concentrations within the reaction layer than the substrate. At the right of all the images is the intensity given by Er in the bulk, but this sharply rises in the reaction

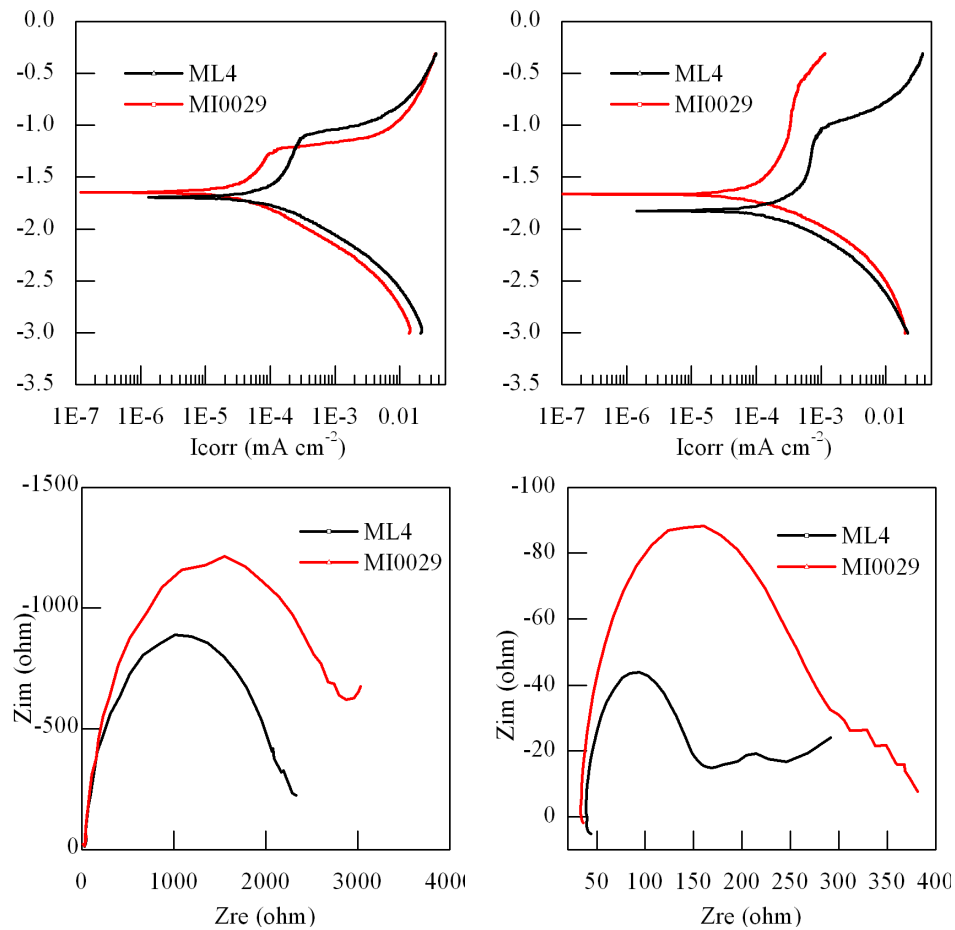


**Figure 7.12:** Polarisation and impedance plots in 1mM  $\text{KH}_2\text{PO}_3$  + 0.1M NaCl (left) 28mM  $\text{NaHCO}_3$  + 0.1M NaCl (right) for both alloys. MI0029 gives higher potentials and polarisation resistance in both solutions than ML4. The opposite seen in NaCl.

layer. This means Er is not leaching into the solution as with Mg, but staying within the oxides. Er will react with ions in NaCl and SBF solutions to form  $\text{Er(III)X}$  compounds, such as  $\text{ErCl}_3$ ,  $\text{Er}_2(\text{CO}_3)_3$  and  $\text{ErP}_5\text{O}_{14}$ . Erbium chloride is soluble in water as it easily forms its hexhydrate form,  $\text{ErCl}_3 \cdot 6\text{H}_2\text{O}$ . Erbium carbonate however is insoluble in water [179], as is Erbium phosphate [180]. This helps to explain Erbium's detrimental affect in NaCl, where it will be forming  $\text{ErCl}_3$ , which is of no use to passivity. Whereas in SBF the formation of  $\text{Er}_2(\text{CO}_3)_3$  and  $\text{ErP}_5\text{O}_{14}$  throughout the reaction layer is stable.

Why Er has such a stabilising affect on the reaction products is unknown. The solubilities of  $\text{Er}_2(\text{CO}_3)_3$  and  $\text{ErP}_5\text{O}_{14}$  are less than the corresponding Mg products. But this can be said for Nd, Gd and other heavy RE phosphates and carbonates [179][180]. The difference between other RE's used in alloying and Er is the crystal structure. Being hexagonal close packed, the same as Mg allows the RE to saturate the Mg matrix instead of just forming second phase. The reaction layer shown by XRD is amorphous, therefore a Er-Mg lattice is not an explanation for the stable reaction layer. It could be however that the distribution of Er being throughout the anodic Mg lattice rather than cathodic second phase as with other Heavy RE's, means Er is always at the corrosion front to form the phosphates and carbonates needed to protect the surface. Elements in the second phase

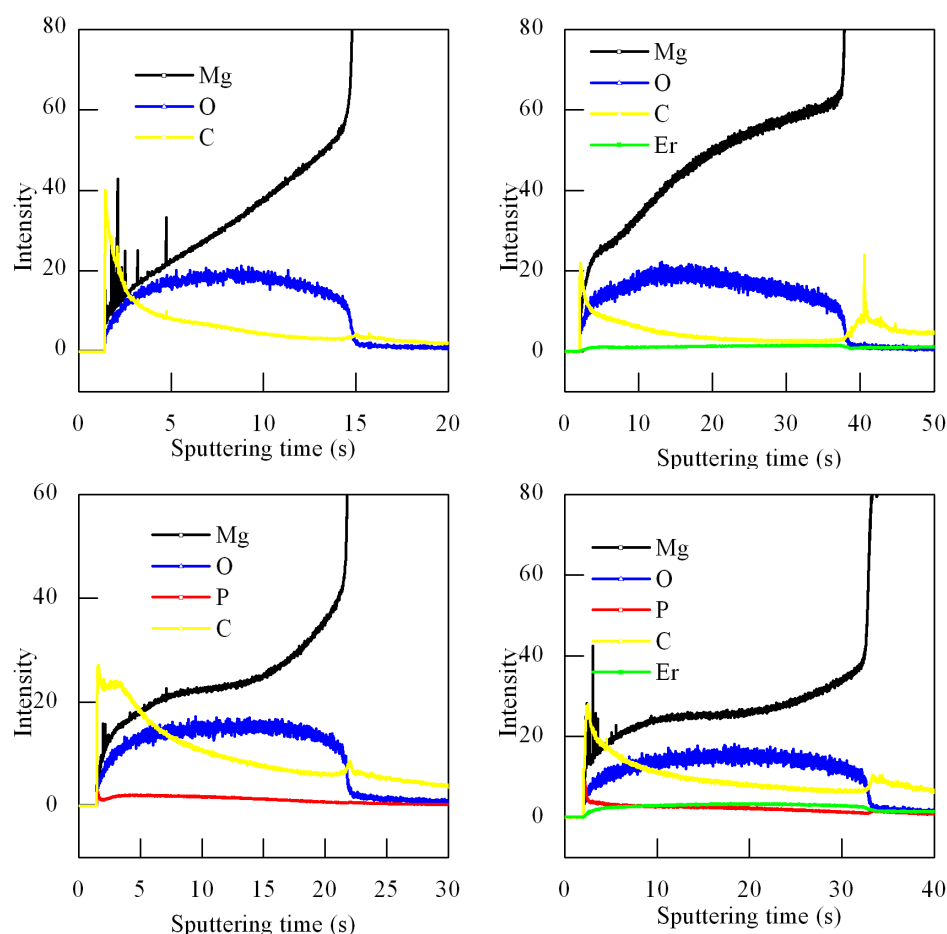


**Figure 7.13:** GDOS cross sections through MI0009 (left) and MI0029 (right) in NaCl (top) and SBF (bottom). The reaction layers in NaCl appear to consist of Mg, O and C from the atmosphere. In SBF phosphate is in the layer. Both MI0029 samples show the presence of Er within the layer as well.

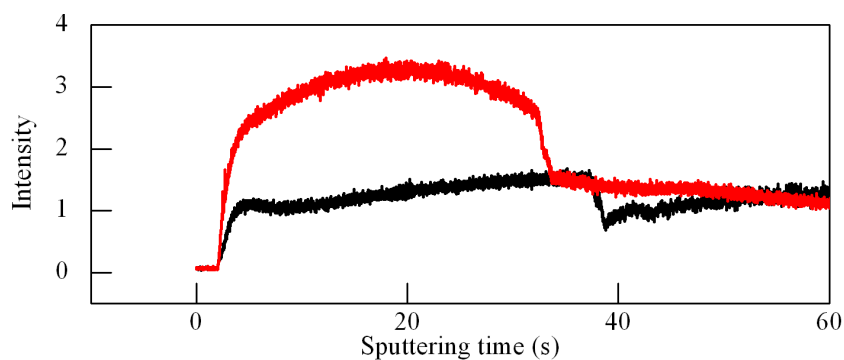


**Figure 7.14:** Cross section of Er through the reaction layer and substrate after corrosion in SBF (red) and NaCl (Black). Er is more intense when incorporated with the carbonate and phosphate of the SBF reaction layer.

are normally not reacted, but lost into solution by undermining of the anode around it.

## 7.4 Conclusions

Additions of around 8 wt% Er to the Mg-RE-Y system of ML4 results in a microstructure containing a  $\text{Mg}_{0.965}\text{Er}_{0.035}$  matrix, with Er incorporated into the second phase particles. Er-Y based cuboid crystals are also found.

The new alloy lowers corrosion rate in SBF by up to 7 times comparative to ML4, this has been shown to be the result of a stabilisation effect of Er with the carbonates and phosphates in the SBF. By proving this, Rosalbino's conclusions have been shown to be inapplicable to biomedical applications.

The stabilisation for carbonates and phosphates could be due to their reaction with Er to form insoluble compounds which are incorporated into the reaction layer.

This Mg-RE-Y-Er alloy has answered the original aim of this Doctorate and produced an Mg alloy specially designed for in vivo applications which satisfies the corrosion behaviour needs.

## 7.5 Further Work

The focus of future work will be the optimisation of this alloying system to further improve corrosion and mechanical properties. Process control and development for this alloy will be needed, so that it can be produced consistently to industry specifications.

In order to aid approval from governing bodies, the use of Er in vivo has to be studied in greater depth regarding its long term affects. The use of Mg for biomedical use is likely to be readily approved as it's already used or present within the body, but the alloying additions are the hurdle. In vitro testing of these with cell lines and tissue should be the first step, followed by long term in vivo studies especially regarding the heavy RE elements.



## FINAL CONCLUSION

At the advent of this doctorate, there was little knowledge about magnesium as a biomaterial, however at its conclusion, due to work by Magnesium Elektron and its partners, publications from external research groups and by this investigation, the extent of research in this area is expanding rapidly. This investigation reports through the rise in knowledge and product capability gained by the author and Magnesium Elektron in the 4 years undertaken.

The first stages of research were to form a general understanding of what occurs when magnesium is implanted into the body. This took the form of osteoblast trials which used cells cultured with magnesium to determine *in vitro* responses and effects on the magnesium alloys. These cell studies showed that high corrosion rates initially seen when magnesium alloys are placed in cell culture medium have a detrimental effect on cell numbers. Magnesium corrosion causes local pH rise and hydroscopic pressure. The effect is inherent to all magnesium alloys irrespective of their overall corrosion rate. However what was also noted is that after the initial corrosion spike, when the rate had lowered, surviving cells on the surface would proliferate and attach well. The attached cells on magnesium also showed a clear phenotype expression change compared to those on glass.

The outcome of this period of work was that *in vitro* testing was not useful for alloy development as this stage as no robust and reliable technique had been found which could distinguish between alloy to alloy effects. What had been noted was that a number of commonly used cell culture techniques were highly skewed by the effects of magnesium corrosion.

At the end of these cell culture investigations, work from commercial partners had highlighted the new direction progress needed to be made, and that was lowering the corrosion rate of the current magnesium alloys. From the commercial perspective this was to increase time until failure of the implant, but this also would resolve potential cell and tissue losses seen with the cell culture work. At this stage alloys used had been unaltered commercial engineering systems. Lowering corrosion rate was now the precedent for future work.

Initial steps towards lowering corrosion rate were modifications to current alloys. An-

nealing ML4 at 350 °C for 8 hours was found optimal and lowered corrosion rates by 20-30%. It was determined this was due to the migration of heavy elements to the deformation regions (most commonly grain boundaries and twinning planes), which lowered the amount of galvanically coupled regions in the microstructure which in turned lowered the corrosion rate.

Further work looked to modify alloys by changes to chemical composition. This offered greater potential for improving corrosion resistance. It was found that additions of 8wt% Er answered the problems given by corrosion *in vitro*. The alloy corroded at rates in SBF of around 6-8 times lower than ML4, it was concluded Er stabilised carbonate and phosphate integration into the reaction layer which served to protect the bulk. Additions of Ca and Gd were investigated. Gd in ML4 also gave low corrosion, around half the corrosion rate of ML4. Calcium additions only lowered corrosion rates slightly.

As well as bulk material changes, modifications to the surface were looked into, in order to lower the initial corrosion rate of magnesium alloys were *in vitro* and perhaps alter the biocompatibility of the alloys. Two successful techniques were found; organo-silanes and magnetron sputtering of hydroxyapatite. The use of organo-silanes protected magnesium well and for over 4 days, giving reductions in corrosion rate of 6 times in the first hours. Silanes were also successfully used as anchors to graft polythene glycol to create a non fouling surface. The covalent attachment of PEG to the surface of magnesium is the first recorded and visibly lowered the adhesion of cells onto the surface. The practical benefits of this coating were put forward for stent design in order to lower restenosis.

Magnetron sputtered hydroxyapatite lowered corrosion rates of ML4 by 6 times in the first 24 hours with no visible hydrogen gas being evolved in the first hours of submersion in SBF. The coating only proved protection for the first 2 days due to low deposition thickness. Biocompatibility of the surface with osteoblasts also improved. Therefore thicker layers will be investigated in future studies.

Manufacturing and alloy design issues were also investigated. The alloy 675 was found to be highly susceptible to SCC. The mechanism of failure was shown to be TG-SCC and it was hypothesised that the high yttrium content enabled hydrogen embrittlement. Due to this Magnesium Elektron altered its alloy development from this system.

In summary, this doctorate was designed to pave a route forward for further research, by gathering a basic understanding on all aspects of magnesium as a biomaterial. This was the first project on the subject by Magnesium Elektron and the University of Manchester. Overall, an understanding of magnesium alloy corrosion and cell interaction *in vitro* is now known along with a strong knowledge on methods to alter this and with regard to corrosion rate, lower this for commercial use. Reliable methods for testing this in future have been detailed so that future more detailed work can follow.



## BIBLIOGRAPHY

- [1] *Elektron RZ5 - Datasheet 452*. Tech. rep. Magnesium Elektron, 2006.
- [2] *Elektron WE43 Wrought alloy - Datasheet 478*. Tech. rep. Magnesium Elektron, 2006.
- [3] Duffy L, “**Magnesium Alloys - An Introduction**”, *Materials World*. 4, 127–130. (1996).
- [4] FIA. *Fomula One Technical Regulations*. FIA, 2006.
- [5] Huh WW Puleo DA, “**Acute toxicity of metal ions in cultures of osteogenic cells derived from bone marrow stromal cells**”, *Journal of Applied Biomaterials*. 6, 109 –116. (1995).
- [6] Van Noort R, “**Titanium - The implant material of today**”. English, *Journal of material science*. 22, 3801–3811. (1987).
- [7] Kalpana SK, “**Biomaterials in total joint replacement**”, *Colloids and Surfaces B: Biointerfaces*. 39, 133 –142. (2004).
- [8] Rozing PM Nagels J Stokdijk M, “**Stress shielding and bone resorption in shoulder arthroplasty**”, *Journal of Shoulder and Elbow Surgery*. 12, 35 –39. (2003).
- [9] Laurencin CT Nair LS, “**Biodegradable polymers as biomaterials**”. English, *Progress in Polymer Science*. 32, 762–798. (2007).
- [10] Tipton AJ Middleton JC, “**Synthetic biodegradable polymers as orthopedic devices**”, *Biomaterials*. 21, 2335 –2346. (2000).
- [11] Haferkamp H Switzer E Meyer-Lindenberg A Wirth CJ Windhagen H Witte F Kaese V, “**In vivo corrosion of four magnesium alloys and the associated bone response**”. English, *Biomaterials*. 26, 3557–3563. (2005).
- [12] KÄnig A, “**Influence of stent design and deployment technique on neointima formation and vascular remodeling**”, *Zeitschrift fÄr Kardiologie*. 91, 98–102. (2002).
- [13] Waksman R, “**Biodegradable Stents: They Do Their Job and Disappear**”, *The Journal of Invasive Cardiology*. 18, 70–74. (2006).

- [14] Tsuji T Kyo E Kosuga K Kawashima A Matsui S Komori H Motohara S Uehata H Takeuchi E Tamai H Igaki K, “**A biodegradable poly-L-lactic acid coronary stent in the porcine coronary artery**”. English, *Journal of interventional cardiology*. 12, 443–449. (1999).
- [15] Nanci A Puleo DA, “**Understanding and controlling the bone-implant interface**”, *Biomaterials*. 20, 2311–2321. (1999).
- [16] Anselme K, “**Osteoblast adhesion on biomaterials**”, *Biomaterials*. 21, 667–681. (2000).
- [17] Kao WH Schmidt DR Waldeck H. *Biological Interactions on Materials Surfaces. Understanding and Controlling Protein, Cell, and Tissue Response*. Ed. by Bizios R Puleo DA. Springer New York, 2009.
- [18] TH Herzlinger GA Nyilas E Chiu, “**Thermodynamics of native protein/foreign surface interactions. Calorimetry of the human  $\gamma$ -globulin/glass system**”, *American Society for Artificial Internal Organs*. 20, 480–490. (1974).
- [19] Davidson VJ Brash JL, “**Adsorption on glass and polyethylene from solutions of fibrinogen and albumin**”, *Thrombosis Research*. 9, 249–259. (1976).
- [20] Rogers C Edelman ER, “**Pathobiologic responses to stenting**”. 81, 4E–6E. (1998).
- [21] Cowan JA Maguire ME, “**Magnesium chemistry and biochemistry**”, *BioMetals*. 15, 203–210. (2002).
- [22] Vormann J, “**Magnesium: nutrition and metabolism**”, *Molecular Aspects of Medicine*. 24, 27–37. (2003).
- [23] Kerstan D Kang HS Cole D Quamme GA Dai LJ Ritchie G, “**Magnesium transport in the renal distal convoluted tubule**”. English, *Physiological Reviews*. 81, 51–84. (2001).
- [24] Quamme GA Cole D, “**Inherited disorders of renal magnesium handling**”. English, *Journal of the american society of nephrology*. 11, 1937–1947. (2000).
- [25] Shalhoub V Barone LM Wilming L Tassinari MS Kennedy MB Pockwinse S Lian JB Stein GS Owen TA Aronow M, “**Progressive development of the rat osteoblast phenotype in vitro: Reciprocal relationships in expression of genes associated with osteoblast proliferation and differentiation during formation of the bone extracellular matrix**”, *Journal of cellular physiology*. 143, 420–430. (1990).
- [26] Bissell MJ Roskelley CD Srebrow A, “**A hierarchy of ECM-mediated signalling regulates tissue-specific gene expression**”, *Current Opinion in Cell Biology*. 7, 736–747. (1995).

- [27] Lou S Zheng Y Li Z Gu X, “**The development of binary Mg-Ca alloys for use as biodegradable materials within bone**”. English, *Biomaterials*. 29, 1329–1344. (2008).
- [28] Vogt C Nellese J Meyer-Lindenberg A Windhagen H Thorey F Witte F Janning C Willbold E, “**Magnesium hydroxide temporarily enhancing osteoblast activity and decreasing the osteoclast number in peri-implant bone remodelling**”. English, *Acta Biomaterialia*. 6, 1861–1868. (2010).
- [29] Tan Z Schulz MJ Yun Y Dong Z, “**Development of an electrode cell impedance method to measure osteoblast cell activity in magnesium-conditioned media**”. English, *Analytical and bioanalytical chemistry*. 396, 3009–3015. (2010).
- [30] Moreau R. Abed E, “**Importance of melastatin-like transient receptor potential 7 and cations (magnesium, calcium) in human osteoblast-like cell proliferation**”. English, *cell proliferation*. 40, 849–865. (2007).
- [31] Odell R Noorman J Evans P Dalton BA Mcfarland C Steele JG Howlett CR Zreiqat H, “**The effect of magnesium-ion implantation into alumina upon the adhesion of human bone-derived cells**”. English, *Journal of materials science-Materials in medicine*. 5, 715–722. (1994).
- [32] Howlett CR Zreiqat H Evans P, “**Effect of surface chemical modification of bioceramic on phenotype of human bone-derived cells**”. English, *Journal of biomedical materials research*. 44, 389–396. (1999).
- [33] Zannettino A Evans P Schulze-Tanzil G Knabe C Shakibaei M Zreiqat H Howlett CR, “**Mechanisms of magnesium-stimulated adhesion of osteoblastic cells to commonly used orthopaedic implants**”. English, *Journal of biomedical materials research*. 62, 175–184. (2002).
- [34] Huadmai J Dias G Staiger MP Pietak AM, “**Magnesium and its alloys as orthopedic biomaterials: A review**”. English, *Biomaterials*. 27, 1728–1734. (2006).
- [35] McBride ED, “**Absorbable metal in bone surgery**”, *J Am Med Assoc*. 111, 2464–2467. (1938).
- [36] Tsitrin DN Troitskii VV, “**The resorbing metallic alloy as material for fastening broken bone**”, *Khirurgiia*. 8, 41–44. (1944).
- [37] Znamenskii MS, “**Metallic osteosynthesis by means of an apparatus made of resorbing metal**”, *Khirurgiia*. 12, 60–63. (1945).
- [38] Mikhailovich T Nina M Terekhova V Fedorovna V Stroganov GB Savitsky E. “**Magnesium-base alloys for use in bone surgery**”. Pat. 3,687,135, 1972.
- [39] Tighe B Amass W Amass A, “**A review of biodegradable polymers: Uses, current developments in the synthesis and characterization of biodegradable polyesters, blends of biodegradable polymers and recent advances in biodegradation studies**”. English, *polymer international*. 47, 89–144. (1998).

- [40] Song GL, “**Recent Progress in Corrosion and Protection of Magnesium Alloys**”, *Advanced Engineering Materials*. 7, 563–586. (2005).
- [41] Goktekin O Peeters N Verbist J Bosiers M Deloose K Heublein B Rohde R Kasese V Ilsley C Erbel R Mario C Hriffiths G, “**Drug-Eluting Bioabsorbable Magnesium Stent**”, *Journal of Interventional Cardiology*. 17, 391–395. (2004).
- [42] Resink TJ Erne P Schier M, “**The Road to Bioabsorbable Stents: Reaching Clinical Reality?**”, *CardioVascular and Interventional Radiology*. 29, 11–16. (2006).
- [43] Mueller PP Crostack HA Nellesen J Bach FW Bormann D Rudert M Witte F Reifenrath J, “**Cartilage repair on magnesium scaffolds used as a subchondral bone replacement**”. English, *Materialwissenschaft und werkstofftechnik*. 37, 504–508. (2006).
- [44] Nellesen J Crostack HA Kaese V Pisch A Beckmann F Windhagen H Witte F Fischer J, “**In vitro and in vivo corrosion measurements of magnesium alloys**”. English, *biomaterials*. 27, 1013–1018. (2006).
- [45] Nellesen J Beckmann F Witte F Fischer J. “**Microtomography of magnesium implants in bone and their degradation**”. English. In: *Developments in X-Ray Tomography 5*. 2006. ISBN: 0-8194-6397-3.
- [46] Kammal M Willumeit R Feyerabend F Witte F, “**Unphysiologically high magnesium concentrations support chondrocyte proliferation and redifferentiation**”. English, *Tissue Engineering*. 12, 3545–3556. (2006).
- [47] Tanik C Kaya AA Duygulu O Mutlu Z Zengin E Aydin Y Kaya RA Cavusoglu H, “**The effects of magnesium particles in posterolateral spinal fusion: an experimental in vivo study in a sheep model**”. English, *Journal of neurosurgery-spine*. 6, 141–149. (2007).
- [48] Weisbrode SE Litsky AS Bertone AL Waselau M Samii VE, “**Effects of a magnesium adhesive cement on bone stability and healing following a metatarsal osteotomy in horses**”. English, *American journal of veterinary research*. 68, 370–378. (2007).
- [49] Oktay G Kaya AA Duygulu O Kaya RA. “**Investigation on the potential of magnesium alloy AZ31 as a bone implant**”. English. In: *2006 BIMW: 2006 Beijing International Materials Week, Pts 1-4*. 2007. ISBN: 978-0-87849-432-3.
- [50] Bormann D Krause C Bach FW Windhagen H Meyer-Lindenberg A Krause A von der Hoeh N, “**Degradation behaviour and mechanical properties of magnesium implants in rabbit tibiae**”. English, *Journal of materials science*. 45, 624–632. (2010).

- [51] Rudert M Willbold E Witte F Ulrich H, “**Biodegradable magnesium scaffolds: Part I: Appropriate inflammatory response**”. English, *JOURNAL OF BIOMEDICAL MATERIALS RESEARCH PART A*. 81A, 748–756. (2007).
- [52] Yang K. Zhang B Ai H Zhang G Huang J, “**Experimental study of in vivo implantation of a magnesium alloy at early stage**”. Chinese, *ACTA METALLURGICA SINICA*. 43, 1186–1190. (2007).
- [53] Palm C Willbold E Witte F Ulrich H, “**Biodegradable magnesium scaffolds: Part II: Peri-implant bone remodeling**”. English, *Journal of biomedical materials research part A*. 81A, 757–765. (2007).
- [54] Zhang Y Jiang Y Zhang S Zhao C Li J Zhang B Song Zhang X He Y Tao H, “**Biocompatibility of bio-Mg-Zn alloy within bone with heart, liver, kidney and spleen**”. English, *Chinese science bulletin*. 54, 484–491. (2009).
- [55] Bianco P Bonucci E Silvestrini G, “**Extracellular alkaline phosphatase activity in mineralizing matrices of cartilage and bone: ultrastructural localization using a cerium-based method**”, *Histochemistry and Cell Biology*. 97, 323–327. (1992).
- [56] Dias GJ Staiger PM Pietak A Mahoney P, “**Bone-like matrix formation on magnesium and magnesium alloys**”, *Journal of Materials Science: Materials in Medicine*. 19, 407–415. (2007).
- [57] Tian TY Lee WH Lu SK Yeh HI. “**Degradation of magnesium alloys in biological solutions and reduced phenotypic expression of endothelial cell grown on these alloys**”. English. In: *3rd Kuala Lumpur International Conference on Biomedical Engineering 2006*. 2007. ISBN: 978-3-540-68016-1.
- [58] Tian TY Chen CH Yeh HI Lu SK Lee WH. “**Expression of Smooth Muscle Cells Grown on Magnesium Alloys**”. English. In: *11th mediterranean Conference on medical and biological engineering and computing*. 2007. ISBN: 978-3-540-73043-9.
- [59] Holtz J Witte F Willumeit R Dracker H Vogt C Hort N Feyerabend F Fischer J, “**Evaluation of short-term effects of rare earth and other elements used in magnesium alloys on primary cells and cell lines**”, *Acta Biomaterialia*. 6, 1834–1842. (2010).
- [60] Braun N Peuster M Drynda A Deinet N, “**Rare earth metals used in biodegradable magnesium-based stents do not interfere with proliferation of smooth muscle cells but do induce the upregulation of inflammatory genes**”, *Journal of Biomedical Materials Research*. 91A, 360–369. (2008).

- [61] Song Y Zhao C Zhang X Xie C Zhang Y Tao H He Y Jiang Y Bian Y Zhang S Li J, “**In vitro degradation, hemolysis and MC3T3-E1 cell adhesion of biodegradable Mg-Zn alloy**”, *Materials Science and Engineering: C*. 29, 1907–1912. (2009).
- [62] Atrens A Song GL, “**Corrosion Mechanisms of Magnesium Alloys**”, *Advanced Engineering Materials*. 1, 11–33. (1999).
- [63] Shaw BA, “**Corrosion Resistance of Magnesium Alloys**”, *ASM Handbook*. 13A, 696–696. (2003).
- [64] Atrens A Song GL, “**Understanding Magnesium Corrosion - A Framework for Improved Alloy Performance**”, *Advanced Engineering Materials*. 5, 837–858. (2004).
- [65] Peloubet JA Hanawalt JD Nelson CE, “**Corrosion Studies of Magnesium and its Alloys**”, *Trans AIME*. 147, 273–299. (1942).
- [66] Kiećbus A Rzychoń T Michalska J, “**Corrosion resistance of Mg-RE-Zr alloys**”, *Journal of Achievements in Materials and Manufacturing Engineering*. 21, 51–54. (2007).
- [67] Kojima Y Ninomiya R Kubota K Nakatsugawa I Kamado S, “**Corrosion of magnesium alloys containing rare earth elements**”, *Corrosion Review*. 16, 139–157. (1998).
- [68] Huang WJ Dietzal W Kainer KU Blawart C Ke W Zeng RC Zhang J, “**Review of studies on corrosion of magnesium alloys**”, *Transactions of Nonferrous Metals Society of China*. 16, 763–771. (2006).
- [69] Macci D Saccone A Delfino S Rosalbino F Angelini E, “**Influence of rare earths addition on the corrosion behaviour of Zn-5Al alloy in neutral aerated sodium sulphate solution**”, *Electrochimica Acta*. 52, 7107–7114. (2007).
- [70] Uggowitzer PJ Song G Atrens A Liu M Schmutz P, “**The influence of yttrium on the corrosion of Mg-Y binary alloys**”, *Corrosion Science*. 52, 3687–3701. (2010).
- [71] Tas CA Jalota S Bhaduri SB, “**Using a synthetic body fluid solution of 27mM HCO<sub>3</sub> to make bone substitutes more osteointegrative**”, *Materials Science and Engineering*. 28, 129–140. (2008).
- [72] Escobedo S Mantovani D Lopez HY Cortes DA. “**In vitro bioactivity assessment of metallic magnesium**”. English. In: *Bioceramics 18, parts 1 and 2*. 2006. ISBN: 0-87849-992-X.
- [73] Song SZ Song GL, “**Corrosion behaviour of pure magnesium in a simulated body fluid**”. Chinese, *Acta Physico-chimica sinica*. 22, 1222–1226. (2006).

- [74] Virtanen S Rettig R, “**Composition of corrosion layers on a magnesium rare-earth alloy in simulated body fluids**”. English, *journal of biomedical materials research Part A*. 88A, 359–369. (2009).
- [75] Tao H Tang G Chu PK Xin Y Huo K, “**Influence of aggressive ions on the degradation behavior of biomedical magnesium alloy in physiological environment**”. English, *acta biomaterials*. 4, 2008–2015. (2008).
- [76] Chen R Zhang F Han EH Song Y Shan D, “**Biodegradable behaviors of AZ31 magnesium alloy in simulated body fluid**”. English, *Materials science and engineering C-biomimetic and supramolecular systems*. 29, 1039–1045. (2009).
- [77] Liu C, Xin Y, and Chu PK Tian X, “**Degradation susceptibility of surgical magnesium alloy in artificial biological fluid containing albumin**”. English, *Journal of materials research*. 22, 1806–1814. (2007).
- [78] Virtanen S Rettig R, “**Time-dependent electrochemical characterization of the corrosion of a magnesium rare-earth alloy in simulated body fluids**”. English, *Journal of biomedical materials research Part A*. 85A, 167–175. (2008).
- [79] Hu T Tang G Chu PK Xin Y Huo K, “**Corrosion products on biomedical magnesium alloy soaked in simulated body fluids**”. English, *Journal of materials research*. 24, 2711–2719. (2009).
- [80] Schmutz P Quach NC Uggowitzer PJ, “**Corrosion behaviour of an Mg-Y-RE alloy used in biomedical applications studied by electrochemical techniques**”. English, *Comptes rendus chimie*. 11, 1043–1054. (2008).
- [81] Mantovani D Cortes DA Lopez HY. “**Spontaneous and biomimetic apatite formation on pure magnesium**”. English. In: *Thermec*. 2007. ISBN: 978-0-87849-428-6.
- [82] Zhang E Yang L, “**Biocorrosion behavior of magnesium alloy in different simulated fluids for biomedical application**”. English, *Materials science and engineering C-biomimetic and supramolecular systems*. 29, 1691–1696. (2009).
- [83] Zhang X Tang G Tian X. Chu PK Xin Y Lui C, “**Corrosion behavior of biomedical AZ91 magnesium alloy in simulated body fluids**”. English, *Journal of materials research*. 22, 2004–2011. (2007).
- [84] Tang G Chu PK Liu C Xin Y, “**Corrosion behavior of AZ91 magnesium alloy treated by plasma immersion ion implantation and deposition in artificial physiological fluids**”. English, *Thin solid films*. 516, 422–427. (2007).
- [85] Dietzel W Hort N Kainer K. U. Zeng Rong-chang Chen Jun, “**Electrochemical behavior of magnesium alloys in simulated body fluids**”. English, *transaction of nonferrous metals society of china*. 17, S166–S170. (2007).
- [86] Gao J Hu J Zhang Y Wang Y Wei M, “**Corrosion process of pure magnesium in simulated body fluid**”. English, *Materials technology*. 62, 2181–2184. (2008).

- [87] Song GL, “**Control of biodegradation of biocompatible magnesium alloys**”. English, *Corrosion science*. 49, 1696–1701. (2007).
- [88] Chen LJ Gu X Zheng YF, “**Influence of artificial biological fluid composition on the biocorrosion of potential orthopedic Mg–Ca, AZ31, AZ91 alloys**”, *Biomedical Materials*. 4, 065011. (2009).
- [89] Hiromoto S Yamamoto A, “**Effect of inorganic salts, amino acids and proteins on the degradation of pure magnesium in vitro**”, *Materials Science and Engineering: C*. 29, 1559 –1568. (2009).
- [90] Malavolti R Krajewski A Piancastelli A, “**Albumin adhesion on ceramics and correlation with their Z-potential**”, *Biomaterials*. 19, 637 –641. (1998).
- [91] Kulekci MK, “**Magnesium and its alloys applications in automotive industry**”, *The International Journal of Advanced Manufacturing Technology*. 37, 851–865. (2007).
- [92] Lyons P, “**New magnesium alloy for aerospace and speciality applications**”, *Magnesium Technology*, 311–315. (2004).
- [93] Vogt C Cohen S Kainer CU Willumeit R Feyerabend F Witte F Hort N, “**Degradable biomaterials based on magnesium corrosion**”, *Current Opinion in Solid State and Materials Science*. 12, 63 –72. (2008).
- [94] Braun N Peuster M Drynda A Deinet N, “**Rare earth metals used in biodegradable magnesium-based stents do not interfere with proliferation of smooth muscle cells but do induce the upregulation of inflammatory genes**”. English, *Journal of Biomedical Materials Research*. 91A, 360–369. (2009).
- [95] Nellesen J Vogt C Vogt J Donath T Beckmann F Witte F Fischer J, “**In vivo corrosion and corrosion protection of magnesium alloy LAE442**”, *Acta Biomaterialia*. 6, 1792 –1799. (2010).
- [96] Raman RKS Kannan MB, “**In vitro degradation and mechanical integrity of calcium-containing magnesium alloys in modified-simulated body fluid**”. English, *Biomaterials*. 29, 2306–2314. (2008).
- [97] Lee JY Seok HK Kim WC Kim JG, “**Influence of Ca on the corrosion properties of magnesium for biomaterials**”. English, *Materials letters*. 62, 4146–4148. (2008).
- [98] Bormann D von der Hoeh N Windhagen H Meyer-Lindenberg A Thomann M Krause Ch, “**Comparison of the resorbable magnesium alloys LAE442 und MgCa0.8 concerning their mechanical properties, their progress of degradation and the bone-implant-contact after 12 months implantation duration in a rabbit model**”. English, *Materialwissenschaft und werkstofftechnik*. 40, 82–87. (2009).



- [99] Hackenbroich CH Bormann D Lucas A Meyer-Lindenberg A Von der Hoeh N Krause A, “**Influence of different surface machining treatments of resorbable implants of different magnesium alloys - a primary study in rabbits.**” German, *Deutsche tierärztliche wochenschrift*. 113, 439–446. (2006).
- [100] Yang L Zhang G, “**Microstructure, mechanical properties and bio-corrosion properties of Mg-Zn-Mn-Ca alloy for biomedical application**”. English, *Materials science and engineering A Structural materials properties microstructure and processing*. 497, 111–118. (2008).
- [101] Xu J Chen H Zhang E Yang L, “**Microstructure, mechanical properties and bio-corrosion properties of Mg-Si(-Ca, Zn) alloy for biomedical application**”, *Acta Biomaterialia*. 6, 1756–1762. (2010).
- [102] Du H Yang K Zhang E He W, “**Microstructure, mechanical properties and corrosion properties of Mg-Zn-Y alloys with low Zn content**”. English, *Materials science and engineering A Structural materials properties microstructure and processing*. 488, 102–111. (2008).
- [103] Zeng Song-yan Yin Dong-song Zhang Er-lin, “**Effect of Zn on mechanical property and corrosion property of extruded Mg-Zn-Mn alloy**”. English, *transaction of nonferrous metals society of china*. 18, 763–768. (2008).
- [104] Yang K He W Zhang E, “**Effect of Y on the bio-corrosion behavior of extruded Mg-Zn-Mn alloy in Hank’s solution**”. English, *Materials science and engineering C-materials for biological applications*. 30, 167–174. (2010).
- [105] Witte F Hort N-Blawert C Zeng R Dietzel W, “**Progress and challenge for magnesium alloys as biomaterials**”. English, *Advanced Engineering Materials*. 10, B3–B14. (2008).
- [106] Luan B Gray JE, “**Protective coatings on magnesium and its alloys - a critical review**”. English, *Journal of alloys and compounds*. 336, 88–113. (2002).
- [107] Lyons P. *Surface Treatments for Magnesium alloys in Aerospace and Defence - Datasheet 256*. Tech. rep. Magnesium Elektron, 2006.
- [108] Wong MH Cheng FT Shi P Ng WF, “**Improvement of corrosion resistance of pure magnesium in Hanks’ solution by microarc oxidation with sol-gel TiO<sub>2</sub> sealing**”, *Journal of Alloys and Compounds*. 469, 286–292. (2009).
- [109] Jiang Z Yao Z Li L, “**Adjustment of the ratio of Ca/P in the ceramic coating on Mg alloy by plasma electrolytic oxidation**”. English, *Applied surface science*. 255, 6724–6728. (2009).
- [110] Xu MJ Zhao B-Guo LX Ouyang JH Wang YM Wang FH, “**Microstructure and corrosion behavior of coated AZ91 alloy by microarc oxidation for biomedical application**”. English, *Applied surface science*. 255, 9124–9131. (2009).

- [111] Zhang J Wu C, “**Corrosion protection of Mg alloys by cathodic electrodeposition coating pretreated with silane**”, *Journal of Coatings Technology and Research*. (2010).
- [112] Grassi V Balbo A-Trabanelli G Zucchi F Frignani A, “**Organo-silane coatings for AZ31 magnesium alloy corrosion protection**”, *Materials Chemistry and Physics*. 110, 263–268. (2008).
- [113] Yang K Xu L Zhang E, “**Phosphating treatment and corrosion properties of Mg-Mn-Zn alloy for biomedical application**”. English, *Journal of materials science- Materials in medicine*. 20, 859–867. (2009).
- [114] Kollmannsberger P Jaafar L-Fabry B Virtanen S Lorenz C Brunner JG, “**Effect of surface pre-treatments on biocompatibility of magnesium**”. English, *Acta Biomaterialia*. 5, 2783–2789. (2009).
- [115] Cheng Y Zheng YF Gu X Zheng W, “**A study on alkaline heat treated Mg-Ca alloy for the control of the biocorrosion rate**”. English, *Acta Biomaterialia*. 5, 2790–2799. (2009).
- [116] Lucas A Denkena B, “**Biocompatible magnesium alloys as absorbable implant materials - Adjusted surface and subsurface properties by machining processes**”. English, *CIRP annals-manufacturing technology*. 56, 113–116. (2007).
- [117] Chida N Yoshinari M-Sumii T Drand T Ohtsuka Y Matsuura M, “**Formation of hydroxyapatite coating on pure titanium substrates by ion beam dynamic mixing**”, *Surface and Coatings Technology*. 65, 224–230. (1994).
- [118] Ding CX Liu XY Chu PK, “**Surface modification of titanium, titanium alloys, and related materials for biomedical applications**”. English, *Materials science and engineering R-reports*. 47, 49–121. (2004).
- [119] Zhang W Jiang J-Tang G Tian X. Chu PK Xin Y Lui C, “**Electrochemical behavior Al<sub>2</sub>O<sub>3</sub>/Al coated surgical AZ91 magnesium alloy in simulated body fluids**”. English, *Journal of the electrochemical society*. 155, C178–C182. (2008).
- [120] Kaifu H Tang G-Tian X. Chu PK Xin Y Lui C, “**Corrosion behavior of ZrN/Zr coated biomedical AZ91 magnesium alloy**”. English, *surface and coating technology*. 203, 2554–2557. (2009).
- [121] Biswas A Manna I Majumdar JD Bhattacharyya U, “**Studies on thermal oxidation of Mg-alloy (AZ91) for improving corrosion and wear resistance**”. English, *Surface and Coatings Technology*. 202, 3638–3642. (2008).
- [122] Peng L Ren C-Wang X Hu Z Wen C Guan S, “**Characterization and degradation behavior of AZ31 alloy surface modified by bone-like hydroxyapatite for implant applications**”, *Applied Surface Science*. 255, 6433–6438. (2009).

- [123] Han EH. Song YW Shan DY, “**Electrodeposition of hydroxyapatite coating on AZ91D magnesium alloy for biomaterial application**”. English, *Materials letters*. 62, 3276–3279. (2008).
- [124] Chu YH Ding SJ Lee TY, “**Environmental effect on bond strength of magnetron-sputtered hydroxyapatite/titanium coatings**”, *Journal of Materials Science Letters*. 22, 479–482. (2004).
- [125] Lee GH Choi SH-Chung SM Lee IS Zhao B, “**Industrial application of ion beam assisted deposition on medical implants**”, *Surface and Coatings Technology*. 201, 5132–5137. (2007).
- [126] Yao S Zeng X Wu G, “**Formation by reactive magnetron sputtering of TiN coating on Ti-implanted magnesium alloy**”, *Materials Letters*. 60, 2252–2255. (2006).
- [127] Ding KJ Xu CY-Dai W Xu AJ Wu GS Wang AY, “**Fabrication of Cr coating on AZ31 magnesium alloy by magnetron sputtering**”, *Trans. Nonferrous Met. Soc. China*. 18, 329–333. (2008).
- [128] Chou TS Wu SK Yen SC, “**A study of r.f.-sputtered Al and Ni thin films on AZ91D magnesium alloy**”, *Surface and Coatings Technology*. 200, 2769–2774. (2006).
- [129] Li G Yao S-Wang X Wu G Zeng X, “**Preparation and characterization of ceramic/metal duplex coatings deposited on AZ31 magnesium alloy by multi-magnetron sputtering**”, *Materials Letters*. 60, 674–678. (2006).
- [130] Huo K Tang G-Tian X. Chu PK Xin Y Jiang J, “**Corrosion resistance and cytocompatibility of biodegradable surgical magnesium alloy coated with hydrogenated amorphous silicon**”. English, *journal of biomedical materials research part A*. 89A, 717–726. (2009).
- [131] Luethen F Nebe JB-Rychly J Liefelth K Bader R Walschus U Lucke S Schlosser M Neumann HG Ohl A Weltmann KD Finke B Schroeder K. “**Plasma Polymer Coating of Titanium for Improved Bone Implants**”. English. In: *14th Nordic-Baltic conference on biomedical engineering and medical physics*. 2008. ISBN: 978-3-540-69366-6.
- [132] Colucci S Zambonin G De Giglio E Sabbatini L, “**Synthesis, analytical characterization, and osteoblast adhesion properties on RGD-grafted polypyrrole coatings on titanium substrates**”. English, *journal of biomaterials science-polymer edition*. 11, 1073–1083. (2000).
- [133] Lam K Tam V Chu P Luk K Cheung K Wong HM Yeung K, “**A biodegradable polymer-based coating to control the performance of magnesium alloy orthopaedic implants**”, *Biomaterials*. 31, 2084–2096. (2010).

- [134] Cheng FT Ng WF Wong MH, “**Stearic acid coating on magnesium for enhancing corrosion resistance in Hanks’ solution**”, *Surface and Coatings Technology*. 204, 1823–1830. (2010).
- [135] Aslani A Kalkhoran NM Slamovich EB Webster TJ Sato M Sambito MA, “**Increased osteoblast functions on undoped and yttrium-doped nanocrystalline hydroxyapatite coatings on titanium**”, *Biomaterials*. 27, 2358–2369. (2006).
- [136] Boccaccini AR Gerhardt LC, “**Bioactive Glass and Glass-Ceramic Scaffolds for Bone Tissue Engineering**”, *Materials*. 3(7), 3867–3910. (2010).
- [137] Bertolotti SJ Porcal GV Previtali CM, “**Photophysics of the phenoxazine dyes resazurin and resorufin in direct and reverse micelles**”, *Dyes and Pigments*. 80, 206–211. (2009).
- [138] Wang J Yu W Wang W Ma X Xiao J Zhang Y, “**Monitoring of Cell Viability and Proliferation in Hydrogel-Encapsulated System by Resazurin Assay**”, *Applied Biochemistry and Biotechnology*. 162, 1996–2007. (2010).
- [139] McWhinnie SLW Maidwell NL Roeschlaub CA Sammes PG Whittlesey R Candeias LP MacFarlane DPS, “**The catalysed NADH reduction of resazurin to resorufin**”, *Journal Chemistry Society, Perkin Trans. 2*, 2333–2334. (1998).
- [140] Partensky F Marie D Vaulot D, “**Application of the novel nucleic acid dyes YOYO-1, YO-PRO-1, and PicoGreen for flow cytometric analysis of marine prokaryotes**”. English, *APPLIED AND ENVIRONMENTAL MICROBIOLOGY*. 62, 1649–1655. (1996).
- [141] Dolezel J, “**Flow cytometric analysis of nuclear-dna content in higher-plants**”. English, *Phytochemical analysis*. 2, 143–154. (1991).
- [142] Cowan JA, “**Magnesium activation of nuclease enzymes—the importance of water**”, *Inorganica Chimica Acta*. 275-276, 24–27. (1998).
- [143] Spigarelli S Evangelista E Rosen GI El Mehtedi M Balloni L, “**Hot Workability and Constitutive Equations of ZM21 Magnesium Alloy**”, *Key Engineering Materials*. 367, 79–86. (2008).
- [144] Duszczek J Leeflang MA Zhou J, “**Effect of Billet Temperature and Ram Speed on the Behavior of AZ31 During Extrusion**”, *K.U.Kainer, Eds. Magnesium. Proceedings of the 7th International Conference on Magnesium*. 7, 414–419. (2007).
- [145] Peng J Zhai C Ding W Chen Y Wang Q, “**Effects of extrusion ratio on the microstructure and mechanical properties of AZ31 Mg alloy**”, *Journal of Materials Processing Technology*. 182, 281–285. (2007).
- [146] Luo W Wang B Wang B Zhang X Zheng F Fang X Yi D, “**Effects of yttrium on recrystallization and grain growth of Mg-4.9Zn-0.7Zr alloy**”, *Journal of Rare Earths*. 26, 392–397. (2008).

- [147] Humphreys JF Wilks T Lorimer GW Mackenzie LWF, “**The Recrystallization Behavior of AZ31 and WE43**”, *Materials Science Forum*. 488 - 489, 99–102. (2005).
- [148] Skeldon P Thompson GE Coy AE Viejo F, “**Susceptibility of rare-earth-magnesium alloys to micro-galvanic corrosion**”, *Corrosion Science*. 52, 3896–3906. (2010).
- [149] Aung NN Zhou W Shen T, “**Effect of heat treatment on corrosion behaviour of magnesium alloy AZ91D in simulated body fluid**”, *Corrosion Science*. 52, 1035–1041. (2010).
- [150] Song YW Han EH Liu XB Shan DY, “**Effects of heat treatment on corrosion behaviors of Mg-3Zn magnesium alloy**”, *Transactions of Nonferrous Metals Society of China*. 20, 1345–1350. (2010).
- [151] Song G Ghalie E Dietzel W Kainer KU Hort N Blawert C Winzer NA Atrens A, “**A critical review of the stress corrosion cracking (SCC) of magnesium alloys**”, *Advanced Engineering Materials*. 7, 659–693. (2005).
- [152] Dietzel W Song G Kainer KU Winzer NA Atrens A, “**Stress corrosion cracking in magnesium alloys: Characterization and prevention**”, *Journal of the Minerals, Metals and Materials Society*. 59, 49–53. (2007).
- [153] Blawert C Dietzel W Song R Fand Y, “**Behavior of stress corrosion cracking in a magnesium alloy**”, *Journal of Wuhan University of Technology–Materials Science Edition*. 24, 111–113. (2009).
- [154] Keibus, “**Microstructure and mechanical properties of Elektron 21 alloy after heat treatment**”, *Journal of Achievements in Materials and Manufacturing Engineering*. 20, 2007. (2007).
- [155] Heaney S Lyons P Syed I, “**Elektron 21 – An Aerospace Magnesium Alloy for Sand Cast and Investment Cast Applications**”, *Advanced Engineering Materials*. 9, 793–798. (2007).
- [156] King JF Lorimer G Apps PJ Karimzadeh H, “**Precipitation reactions in Magnesium-rare earth alloys containing Yttrium, Gadolinium or Dysprosium**”, *Scripta Materialia*. 48, 1023–1028. (2003).
- [157] Negri SD Saccone A Delfino S Rosalbino F Angelini E, “**Effect of erbium addition on the corrosion behaviour of Mg-Al alloys**”, *Intermetallics*. 13, 55–60. (2005).
- [158] Zolina ZK Rokhlin LL Nikitina NI, “**Magnesium alloys with erbium**”, *Metal Science and Heat Treatment*. 20, 529–531. (1978).
- [159] Gao H Zhai C Zhu YP Wu G Fan Y, “**The effect of Ca and rare earth elements on the microstructure, mechanical properties and corrosion behavior of AZ91D**”, *Materials Science and Engineering: A*. 408, 255–263. (2005).

- [160] Stormer M Blawert C Witte F Vogt C Dracker C Willumeit R Kainer KW Feyerabend F Hort N Huang Y Fechner D, “**Magnesium alloys as implant materials - Principles of property design for Mg-RE alloys**”, *Acta Biomaterialia*. 6, 1714–1725. (2010).
- [161] Walker J Woodfield T Dias GT Staiger MP Kirkland NT Birbilis N, “**In-vitro dissolution of magnesium–calcium binary alloys: Clarifying the unique role of calcium additions in bioresorbable magnesium implant alloys**”, *Journal of Biomedical Materials Research*. 95B, 91–100. (2010).
- [162] Marks AR Cooper Woods T, “**Drug-Eluting Stents**”, *Annual Review of Medicine*. 55, 169–178. (2004).
- [163] Cui FZ Lee IS Yin QS Zhang Y Yang JX Jiao JP, “**Modification of degradation behavior of magnesium alloy by IBAD coating of calcium phosphate**”, *Surface and Coatings Technology*. 202, 5733–5736. (2008).
- [164] Hikawa J Lee JH Wan T Aoki H, “**RF-magnetron sputtering technique for producing hydroxyapatite coating film on various substrates**”, *Biomedical Materials and Engineering*. 17, 291–297. (2007).
- [165] Zhou S Wu L Liu Y Yu Z, “**Self-assembled monolayers on magnesium alloy surfaces from carboxylate ions**”, *Applied Surface Science*. 252, 3818–3827. (2006).
- [166] Grassi V Monticelli C Trabanelli G Zucchi F Frignani A, “**Influence of a silane treatment on the corrosion resistance of a WE43 magnesium alloy**”, *Surface and Coatings Technology*. 200, 4136–4143. (2006).
- [167] Ko SW Kim KJ, “**Degradation mechanism and morphological change of PET by poly(ethylene glycol) diamine**”. English, *Journal of applied polymer science*. 37, 2855–2871. (1989).
- [168] Wu Q Ren J Zhao P Liu W, “**Preparation, Mechanical, and Thermal Properties of Biodegradable Polyesters/Poly(Lactic Acid) Blends**”. English, *Journal of nanomaterials*. (2010).
- [169] Alexander MR Ulijn RV Todd SJ. Scurr DJ Gough JE, “**Enzyme-Activated RGD Ligands on Functionalized Poly(ethylene glycol) Monolayers: Surface Analysis and Cellular Response**”. English, *Langmuir*. 25, 7533–7539. (2009).
- [170] Valiokas R Liedberg B Gauglitz G Piehler J Brecht A, “**A high-density poly(ethylene glycol) polymer brush for immobilization on glass-type surfaces**”. English, *Biosensors and bioelectronics*. 15, 473–481. (2000).
- [171] Kao WYJ, “**Evaluation of protein-modulated macrophage behavior on biomaterials: designing biomimetic materials for cellular engineering**”. English, *Biomaterials*. 20, 2213–2221. (1999).

- [172] Ratner BD Castner DG, “**Biomedical surface science: Foundations to frontiers**”. English, *surface science*. 500, 28–60. (2002).
- [173] Griesser HJ Kingshott P Thissen H, “**Effects of cloud-point grafting, chain length, and density of PEG layers on competitive adsorption of ocular proteins**”, *Biomaterials*. 23, 2043 –2056. (2002).
- [174] Kim JH Kim JJ Han DK Moon MW Lee KR Shin JH Shin HS Park, “**Biocompatible PEG Grafting on DLC-coated Nitinol Alloy for Vascular Stents**”. English, *journal of bioactive and compatible polymers*. 24, 316–328. (2009).
- [175] Hubbell J Elbert DJ Schaffner T Mettler D Windecker S Meier B Hess O Billinger M Buddeberg F, “**Polymer Stent Coating for Prevention of Neointimal Hyperplasia**”, *Journal of Invasive Cardiology*. 18, 423–426. (2006).
- [176] Wang K Bordia RK Basu B Nath S Biswas K, “**Sintering, Phase Stability, and Properties of Calcium Phosphate-Mullite Composites**”. English, *Journal of the american ceramic society*. 93, 1639–1649. (2010).
- [177] Wang M, “**Developing bioactive composite materials for tissue replacement**”, *Biomaterials*. 24, 2133 –2151. (2003).
- [178] Stullikov I Smola B, “**Equilibrium and transient phases in Mg-Y-Nd ternary alloys**”, *Journal of Alloys and Compounds*. 381, L1 –L2. (2004).
- [179] Mohammadzadei J Firsching FH, “**Solubility products of the rare-earth carbonates**”, *Journal of Chemical and Engineering Data*. 31, 40–42. eprint: <http://pubs.acs.org/doi/pdf/10.1021/je00043a013> (1986).
- [180] Brune SN Firsching FH, “**Solubility products of the trivalent rare-earth phosphates**”, *Journal of Chemical & Engineering Data*. 36, 93–95. eprint: <http://pubs.acs.org/doi/pdf/10.1021/je00001a028> (1991).